

Dissertation
submitted to the
Combined Faculties for the Natural Sciences and for Mathematics
of the Ruperto-Carola University of Heidelberg, Germany
for the degree of
Doctor of Natural Sciences

Put forward by
Dipl.-Phys.: Robert Holla
Born in: Worms

Oral examination: 07.02.2012

Reactive Halogen Species above Salt Lakes and Salt Pans

Referees: Prof. Dr. Ulrich Platt
Prof. Dr. Bernd Jähne

Reaktive Halogenverbindungen über Salzseen und Salzpfannen

Die vorliegende Arbeit beschäftigt sich mit den Vorkommen von reaktiven Halogenverbindungen (RHS) über Salzseen und salinen Böden, um ihre Bedeutung für die troposphärische Chemie der planetaren Grenzschicht einschätzen zu können. Salzseen kommen auf der ganzen Welt vor und saline Böden bedecken 2.5% der Landoberfläche der Erde (FAO, 2012). An mehreren Salzseen und anderen Orten mit hohem Halogengehalt wurden bodengestützte MAX-DOAS- und LP-DOAS-Messungen durchgeführt. Im Vorfeld dieser Arbeit waren an drei Salzseen RHS in Mischungsverhältnissen von einigen pptv bis zu über 100 pptv gefunden worden. Die Datengrundlage zu RHS über Salzseen konnte so deutlich vergrößert werden. Sowohl verschiedene passive, als auch ein aktives DOAS System wurden benutzt, um die horizontale und vertikale Verteilung von BrO im Tal des Toten Meeres zu ermitteln und so Freisetzungsprozesse zu identifizieren und ihren Beitrag zu den hohen BrO-Konzentrationen am Toten Meer einschätzen zu können. Mithilfe von MAX-DOAS wurden an zwei benachbarten Messorten am Toten Meer Vertikalprofile von Aerosol, BrO und NO₂ gemessen. So konnten zum ersten mal Vertikalprofile von BrO und NO₂ am Toten Meer bestimmt und hinsichtlich der Meteorologie interpretiert werden. Die daraus folgenden Bodenwerte von BrO und NO₂ konnten mithilfe von LP-DOAS-Messungen bestätigt werden. Die in dieser Arbeit vorgestellten Feldstudien zeigen, dass mehr Voraussetzungen für das Auftreten von RHS über Salzseen erfüllt sein müssen als man auf Basis der vorangegangenen Messungen hätte annehmen können.

Reactive Halogen Species above Salt Lakes and Salt Pans

Salt lakes can be found on all continents and saline soils cover 2.5% of the land surface of the earth (FAO, 2012). This thesis investigates the presence of reactive halogen species (RHS) above salt lakes and saline soils to evaluate their relevance for tropospheric chemistry of the planetary boundary layer. Ground-based MAX-DOAS and LP-DOAS measurements were conducted at salt lakes and two other sites with high halogen content. Prior to this work, RHS were found at three salt lakes with mixing ratios ranging from several pptv up to more than 100 pptv. On the basis of this work the data base on reactive halogen release from salt lakes was significantly expanded. Passive DOAS and active DOAS systems were used to examine the vertical as well as the horizontal distribution of BrO in the Dead Sea Valley. Vertical profiles of aerosols, BrO and NO₂ were measured at two adjacent sites at the Dead Sea using MAX-DOAS. The first time vertical profiles of BrO and NO₂ at the Dead Sea were determined and interpreted in terms of the special atmospheric dynamics in the Dead Sea Valley. The resulting ground values of BrO and NO₂ at one measurement site were validated by LP-DOAS and show very good agreement. The field studies presented in this work showed, that the release of RHS in those regions is less widespread than previously assumed.

Contents

1	Introduction	1
2	Reactive Halogen Species	3
2.1	Sources and Sinks of RHS in the Atmosphere	5
2.1.1	Release processes of RHS	5
2.1.2	Sinks of RHS	6
2.2	Tropospheric Halogen Chemistry	6
2.2.1	Impact of RHS on Tropospheric Chemistry	7
2.2.2	Bromine Chemistry	8
3	Radiative Transfer in the Atmosphere	11
3.1	Radiative Transfer Equation	11
3.2	Scattering Processes in the Atmosphere	12
3.2.1	Rayleigh Scattering	12
3.2.2	Mie Scattering	13
3.2.3	Raman Scattering	14
3.2.4	Aerosol Optical Properties	16
3.3	The Air Mass Factor Concept	16
3.4	Radiative Transfer Modeling	17
3.4.1	SCIATRAN 2	18
3.4.2	Model Parameters	18
4	Absorption Spectroscopy	19
4.1	DOAS	19
4.2	MAX-DOAS	22
5	Atmospheric Retrievals	25
5.1	Characteristical Light Path	25
5.2	Inversion	27
5.2.1	Basic Inversion Principle	27
5.2.2	Retrieval Properties	29
5.2.3	Retrieval Procedure	30
5.2.4	Retrieval Errors	31
5.3	User Interface HEROE	31

6	Instrumentation	33
6.1	Spectrographs	33
6.2	MAX-DOAS South Russia and Mauritania	34
6.3	MAX-DOAS Cape Verde and Australia	35
6.4	MAX-DOAS Masada 2002	37
6.5	MAX-DOAS Masada 2012	38
6.5.1	Offset and Dark Current	40
6.5.2	Instrument Function	41
6.5.3	Field of View	42
6.6	MAX-DOAS Ein Bokek	44
6.7	LP-DOAS Ein Bokek	45
6.8	IMK Weather Station	46
7	Field Studies	49
7.1	Salt Lakes and Salt Pans	50
7.1.1	Botswana 2008	50
7.1.2	South Russia 2009	50
7.1.3	Mauritania 2009	52
7.1.4	Cape Verde 2010	55
7.1.5	Australia 2011	56
7.1.6	Israel 2002 and 2012	61
7.2	Other Areas with High Salt Content	70
7.2.1	Bourtanger Moor 2011	70
7.2.2	Kali Dump 2011	71
8	Data analysis	73
8.1	Spectral Evaluation	73
8.2	Measurement Error and Detection Limit	77
8.3	Retrieval of Vertical Profiles	79
8.3.1	Profile Retrieval Parameters	79
8.3.2	Profile Retrieval Errors	81
8.3.3	Sensitivity Studies of Profile Retrievals	81
8.3.4	Intercomparison of measurements at Masada and Ein Bokek	85
9	Results and Discussion	87
9.1	Results from Israel 2002 and 2012	87
9.1.1	MAX-DOAS measurements in 2002	87
9.1.2	MAX-DOAS and LP-DOAS measurements in 2012	93
9.1.3	Car-DOAS measurements in 2012	107
9.1.4	Discussion	110
9.1.5	Approximation of the Uptake of BrONO ₂ on Aerosol	116
9.1.6	Gas Phase Mixing Ratio of BrONO ₂ in Equilibrium	117
9.2	Results from other measurement sites	119
9.2.1	Discussion	123
10	Conclusion and Outlook	129

A Data Charts	133
A.1 Israel 2012	134
A.2 Botswana 2008	137
A.3 South Russia 2009	141
A.4 Cape Verde 2010	145
A.5 South West Australia 2011	149
A.6 Kali Dump Heringen 2011	153
A.7 Bourtanger Moor 2011	157
List of Figures	161
List of Tables	171
Bibliography	173
B Acknowledgements	190

Chapter 1

Introduction

The atmosphere of Earth is a prerequisite for the development of the present-day life and sustains its permanent existence in many aspects. Although its physical influence reaches to altitudes of several hundred kilometers, in terms of mass, around 90% of the atmosphere is located in the lowermost 20 km. In other words, the atmospheric composition is mainly influenced by chemical processes occurring in the troposphere and stratosphere. Beside its main constituents oxygen and nitrogen, also trace gases abundant in fractions of less than a half per mille, or even several orders of magnitude less, can have significant impacts on physical and chemical processes in the atmosphere. This has become evident at least in the case of ozone layer depletion or global warming. Beside direct effects, also indirect effects of constituents have to be regarded, which make reliable predictions very complicated. Therefore an accurate knowledge of the atmospheric composition and processes determining and controlling the atmosphere is vital.

The impact of reactive halogens (RHS) on atmospheric processes is manifold. It is known that they can readily destroy tropospheric ozone, have an impact on the oxidation capacity of the atmosphere and on the atmospheric cycle of mercury (e.g., Peleg et al., 2007) and induce particle formation (e.g., O'Dowd et al., 2002; Saiz-Lopez et al., 2012). Known sources of RHS include the oceans, polar regions, volcanoes, biomass burning, industry and salt lakes.

The aim of this work was to study the relevance of salt lakes and saline soil enclosing salt lakes, often by a wide area of several hundred square kilometers.

In literature different definitions of salt lakes (or saline lakes) can be found. Williams (1981) regards lakes with mass fractions of total dissolved solids greater than 3 per mille as saline lakes.

Salt lakes are distributed all over the world (see Figure 1.1). Inland salt lakes develop in drainage basins where hydrological inputs and outputs are balanced. Depending on seasonal, annual or longer term variations these salt lakes can be transitory (called *ephemeral*) or permanent. For salt lakes without water bodies, often the term *salt pan* is used. Competing hydrological inputs and outputs occur in arid and semi-arid regions (around one-third of total world land area (Williams, 2002)) more often, but salt lakes also occur in high mountain regions behind atmospheric water divides, in coastal areas under marine influence or even in the Antarctic (Matsubaya et al.,

1978).

However, saline soils tend to occur within arid to semi-arid regions. They are usually defined as consisting of an exchangeable sodium percentage greater than 15% and their pH is usually less than 8.5 (AAFC, 2011).

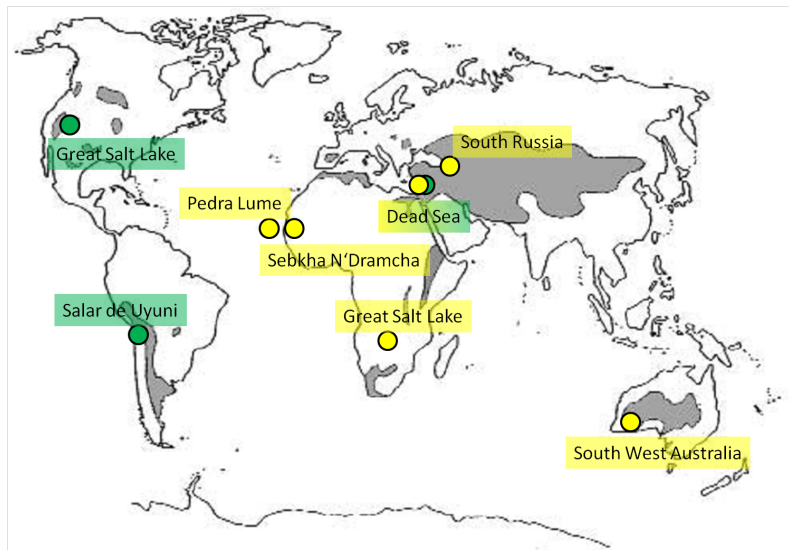


Figure 1.1: *Shaded areas indicate the distribution of salt lakes around the world. Salt lakes occur also outside of these areas, but less frequent. The circles indicate the locations of the salt lakes which were known to emit RHS prior to this work (green circles) and the salt lakes examined in the scope of this work (yellow circles), cf. Table 9.2. Adapted from Williams (2002).*

According to (Saiz-Lopez and von Glasow, 2012; FAO, 2012) "globally, about 2.5% of the land surface is covered by saline soils implying that halogen release might be relevant on a rather large part of the continents and not only over the comparatively small areas of salt lakes."

Chapter 2

Reactive Halogen Species in the Atmospheric Boundary Layer

Halogens¹ form the seventh group in the periodic table of elements. They lack only one electron to fill their outermost shell, and thus they are very reactive in their elemental form. Halogens comprise the natural-occurring elements fluorine (F), chlorine (Cl), bromine (Br), iodine (I) and astatine (At).

For atmospheric chemistry mainly chlorine, bromine and iodine are relevant. With regard to the mass Cl dominates within the atmosphere in the form of NaCl in sea salt. Compared to chlorine, fluorine, bromine and iodine are present in sea salt in analogous compounds in mass fractions of 68 ppm, 0.34% and 3 ppm (Möller, 2003), respectively. Fluorine reacts with water vapor to hydrogen fluoride HF and is rapidly wet deposited. It plays a minor role in atmospheric chemistry and is mainly present in the form of degradation products of organic anthropogenic precursors (Finlayson-Pitts, 2000). Sulfur hexafluoride (SF₆) originates exclusively from anthropogenic sources and has the longest known atmospheric lifetime ($\tau \approx 3200$ years) (Möller, 2003).

Beside elemental halogens X₂, a series of other halogen compounds are reactive within the atmosphere. The term Reactive Halogen Species (RHS) refers to halogen radicals X, halogen molecules X₂ and XY, halogen oxide radicals XO, hypohalous acid HOX, halogen nitrate XONO₂ and hydrogen halide HX, where X= Cl, Br, I (Platt and Stutz, 2008). Hydrogen halide HX is quite stable within the atmosphere and can act as a reservoir gas or even as the most important sink for RHS due to its wet deposition. Sources and sinks of RHS will be discussed in section 2.1.

The importance of halogen species for the atmospheric chemistry is manifold. Halogen compounds with atmospheric lifetimes which are long against the timescales of global circulation reach the stratosphere where they can destroy ozone. This was first discovered by Molina and Rowland (1974) and finally led to the adoption of the Montreal Protocol in 1987, whose members commit to restrict the production of halogenated hydrocarbons which have been shown to play a role in ozone depletion. RHS can readily destroy tropospheric ozone, have an impact on the oxidation capacity of the atmosphere and on the atmospheric cycle of mercury (e.g., Peleg et al., 2007), and can induce particle formation (e.g., O'Dowd et al., 2002). These aspects

¹from Greek: *halos*, "salt" and *gennáo* "creator"

will be discussed in more detail in section 2.2.1.

In section 2.2.2 photochemical processes including bromine will be discussed.

RHS were found at numerous sites (cf. Figure 1.1) using the DOAS technique (see chapter 4) in recent years: In polar troposphere, enhanced BrO concentrations were found in the boundary layer during ozone depletion events (Sihler, 2012), in the Arctic (Hausmann and Platt, 1992; Hönninger, 2002; Pöhler, 2010), as well as in the Antarctic (Friess et al., 2004; Wagner et al., 2007; Saiz-Lopez et al., 2007b).

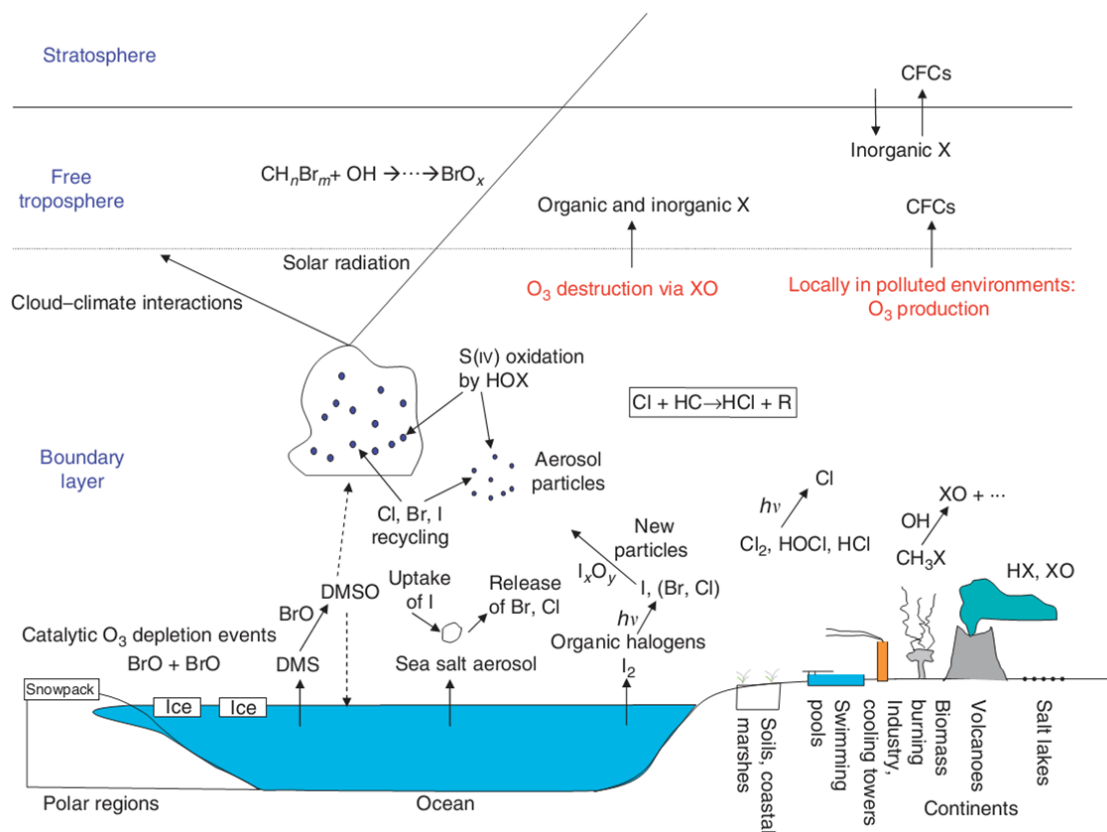


Figure 2.1: Overview of the main atmospheric domains and processes involving halogens. Adapted from von Glasow (2007).

Measurements of BrO in the marine boundary layer were performed by Leser et al. (2003) and Martin (2009) south of the Canary Islands, by Saiz-Lopez et al. (2006) at the Mace Head observatory on the west coast of Ireland as well as by Read et al. (2008) at the Cape Verdian island Sao Vicente.

Beside polar regions and the marine boundary layer, also at terrestrial sites at mid-latitudes increased BrO mixing ratios were detected: At salt lakes (see sections 9.2 and 9.2.1) and in volcanic plumes by Bobrowski (2003) and Kern (2009).

IO was detected above Spitzbergen by Wittrock et al. (2000) and in the Antarctic by Friess (2001) as well as at the Irish West coast by Seitz et al. (2010). From satellite, Saiz-Lopez et al. (2007a) observed enhanced IO column densities around the Antarctic coast and Schönhardt (2009) measured enhanced IO column densities over the Antarctic region and over the upwelling region in the Eastern Pacific. A

more elaborate list of ground-based observations of RHS in the troposphere using active and passive DOAS can be found in literature (e.g., Saiz-Lopez and von Glasow, 2012; Grossmann, 2010).

2.1 Sources and Sinks of RHS in the Atmosphere

2.1.1 Release processes of RHS

Reaction paths forming reactive halogen species can be classified into two main types:

1. The first type are abiotic reactions which can occur on air-solid or air-water interfaces. In the environment, surfaces rich of halogen salts are mainly provided by sea salt aerosols, salt water (i.e. the oceans and salt lakes), crystallized salt surfaces (salt crusts at salt lakes or salt pans), saline soil (depending on their composition denoted as *solonchaks* or *solonetz* (FAO, 2012)) and salt marshes.
 - The so-called "bromine explosion" is regularly observed in polar regions, especially during spring. The underlying process is an autocatalytic release of reactive bromine from sea salt water deposits or from frost flowers on sea ice. When sea water freezes, the sea salt concentrates at the surface and leads to an enhanced release of bromine and chlorine. The high BrO mixing ratios consequently can cause ozone depletion events (ODEs) (Friess et al., 2004). Bromine explosions and associated ODEs are also observed recurrently at the Dead Sea, see section 9.1.
 - Strong acids can release HCl (but not HBr) from sea salt halides. Under certain conditions HX can be converted to more reactive forms (Platt and Stutz, 2008), see below.
 - At high NO₂ levels (ppm) nitrogen oxides can react with dry halide to form ClNO₂ and BrNO₂ (Finlayson-Pitts and Johnson, 1988; Finlayson-Pitts et al., 1989).
 - Cl⁻, Br⁻ and I⁻ can be converted to Br₂, BrCl, ICl or IBr with oxidants like HOX (Platt and Stutz, 2008).
 - Methyl iodide (CH₃I) can be released from sea water containing dust aerosols (Williams et al., 2007).
 - The reaction of marine dissolved organic matter with hypoiodous acid and molecular iodine, which are formed at the sea surface when ozone reacts with dissolved iodide, can produce CH₂I₂, CHClI₂ and CHI₃ (Martino et al., 2009).
 - The main anthropogenic sources of halogens are biomass burning or industrial processes (Seitz, 2009).
 - Large mixing ratios of BrO and ClO are observed in gas plumes emitted by volcanoes (e.g., Bobrowski, 2005).

2. The second type of reaction paths is the photochemical degradation of organohalogens.

The photolytic lifetimes of most of the organic chlorine and bromine compounds are in the order of months, however iodine compounds can have lifetimes of minutes or hours. Organohalogens are produced by industry but also naturally. Biogenic organohalogens can be produced by organisms (bacteria, fungi, plants, marine organisms, higher animals), abiogenic organohalogens are formed during geothermal processes from chloride, fluoride and bromide salts and organic matter. Methyl halides (CH_3X) or polyhalogenated hydrocarbons as CH_2X_2 or CHX_3 are a main source of RHS. They are emitted by macroalgae (seaweed) at coastal sites and microalgae (phytoplankton) in the ocean and are photolyzed in the troposphere to form RHS (Grossmann, 2010). The quantities of some natural organohalogens even exceed the identical anthropogenic organohalogens (Gribble, 2004). Beside biotic formation of organohalogens there is also evidence of abiotic formation in soils involving humic substances and iron (e.g., Keppler et al., 2000; Huber et al., 2009).

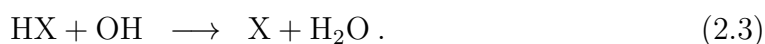
2.1.2 Sinks of RHS

The typical atmospheric lifetimes of individual XO molecules are only seconds (IO) to hours (ClO). Yet, in the combination with X the lifetime can be several hours. The most important loss processes of reactive halogen species are the reactions:



where R represents an organic molecule, e.g. HCHO.

The only relevant process which could reactivate HX within the gas phase is the reaction (Platt and Stutz, 2008):



The lifetime of HX against this reaction is in the order of magnitude of a day and therefore, it is too slow to recycle HX efficiently.

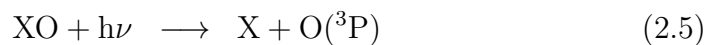
A further, although temporary, sink are the reactions with NO_2 (e.g. reaction 2.29), see sections 2.2.2 and 9.1.4.

2.2 Tropospheric Halogen Chemistry

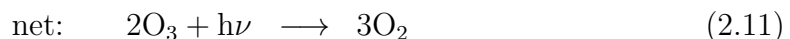
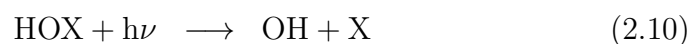
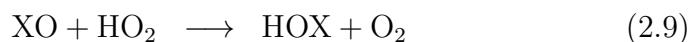
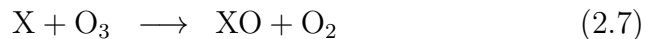
In this section, the relevance of RHS for atmospheric processes (section 2.2.1) and the photochemistry of bromine will be summarized. A more detailed description of bromine chemistry and the chemistry of iodine and chlorine species is given by e.g. Saiz-Lopez and von Glasow (2012), Simpson et al. (2007) and von Glasow (2007).

2.2.1 Impact of RHS on Tropospheric Chemistry

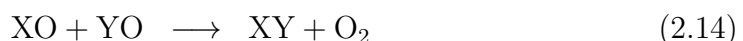
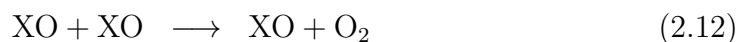
- RHS, in particular reactive bromine and iodine, can catalytically destroy tropospheric ozone. Even very small amounts of RHS (several ppt) can reduce ozone abundances of several ten ppb. The reaction of a halogen atom and an ozone molecule (equation 2.7) is very fast. With a typical ozone concentration of 50 ppb the lifetimes of individual halogen atoms are: $\tau_{\text{Cl}} = 0.13$ s, $\tau_{\text{Br}} = 1.3$ s and $\tau_{\text{I}} = 1.3$ s (Seitz, 2009). If XO gets photolyzed (equation 2.5), a single oxygen atom $\text{O}(^3\text{P})$ is produced and can react with molecular oxygen to form ozone (equation 2.6). In net terms this cycle does not destroy ozone.



M denotes a collision partner which is most likely a nitrogen or oxygen molecule. Taking into account the presence of the hydroxyl radical OH and the formation of hydroperoxyl HO_2 (equation 2.8) leads to a cycle which catalytically destroys ozone:



This cycle is dominant for low concentrations of RHS, e.g. in the marine boundary layer. At higher levels of RHS, e.g. at the Dead Sea, self reactions of halogen monoxides become relevant:



where Y denotes another halogen type. Reactions 2.12 to 2.14 lead to a further destruction of ozone. Meanwhile, the formation of a halogen dioxide (reaction 2.15) reduces the destruction of ozone due to photolysis and the resulting atomic oxygen:

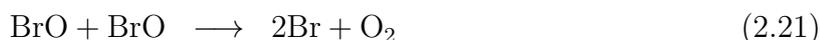


However, in the case of OIO the photolysis can also result in $\text{I} + \text{O}_2$ (Ashworth et al., 2002) which leads to an increase in the ozone destruction.

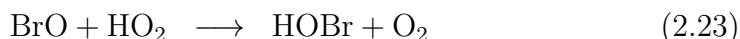
- Reactions 2.9 and 2.10 lead to the conversion of HO_2 to OH . A reduced HO_2/OH ratio influences the atmospheric oxidation capacity. The atmospheric oxidation capacity refers to the capability of the atmosphere to oxidize trace gas species in it and can be regarded as the "self-cleaning" capacity of the atmosphere (Platt and Stutz, 2008).
- Chlorine atoms, and to a lesser extent bromine atoms, have a direct impact on the oxidation capacity of the troposphere (Platt and Stutz, 2008).
- A further impact of RHS on the marine boundary layer is the oxidation of dimethyl sulfide (DMS). DMS is a sulfur compound that is emitted by phytoplankton and can be oxidized by BrO . See e.g. Platt and Stutz (2008); Grossmann (2010) and references therein.
- Iodine species are involved in particle formation (Hoffmann et al., 2001; O'Dowd et al., 2002; Jimenez, 2003; O'Dowd and Hoffmann, 2005; McFiggans, 2005; Saiz-Lopez et al., 2012).
- Reactive bromine species oxidize gaseous elemental mercury, enhancing the deposition of mercury. Bromine-induced mercury oxidation may be an important source of mercury to the oceans (Obrist et al., 2010). Bromine-induced mercury depletion has been observed in polar regions (Barrie and Platt, 1997; Schroeder et al., 1998) as well as at the Dead Sea (Peleg et al., 2007; Tas et al., 2011; Ariya, 2011).

2.2.2 Bromine Chemistry

Two main chemical mechanisms have been proposed as being responsible for the catalytic destruction of ozone in the boundary layer. The first mechanism is driven by the self reaction of BrO and the photolysis of Br_2 :

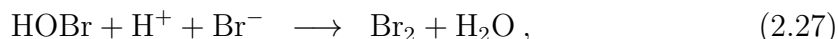


The second mechanism is initiated by the hydroperoxyl radical:

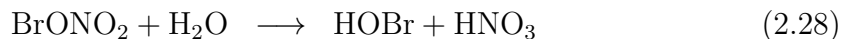


For O_3 volume mixing ratios higher than $\sim 1\text{-}2$ ppb the rate limiting steps in these cycles are reactions 2.21 and 2.23, respectively. The first cycle is quadratically dependent on the concentration of BrO, whereas the second cycle is linearly dependent. Thus, at high BrO levels, as observed at the Dead Sea, the first cycle should dominate (Tas et al., 2006).

Probably the most important mechanism for BrO production at the Dead Sea is the heterogeneous "bromine explosion" mechanism:



where one HOBr molecule in the liquid phase initiates the emission of two Br atoms in the form of Br_2 . HOBr can be formed by reaction 2.23 or by the hydrolysis of bromine nitrate BrONO_2 :

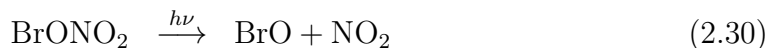


BrONO_2 , in turn, is formed by the reaction:



Thus, at high NO_2 levels reactions 2.29 and 2.28 might be an efficient alternative pathway to reaction 2.23 sustaining the autocatalytic release process of BrO, see Figure 2.2. However, the prerequisite for the hydrolysis of BrONO_2 is the uptake into the liquid phase. This can be lake water, aerosol or micro layers on top of salt surfaces, see (Buxmann, 2012a).

Important reactions which compete with the uptake are the photolysis and thermal decay of BrONO_2 in the gas phase:



This will be discussed for the case of the Dead Sea in section 9.1.4.

Also nitryl bromide (BrNO_2) can be produced and photolyzed in the gas phase:

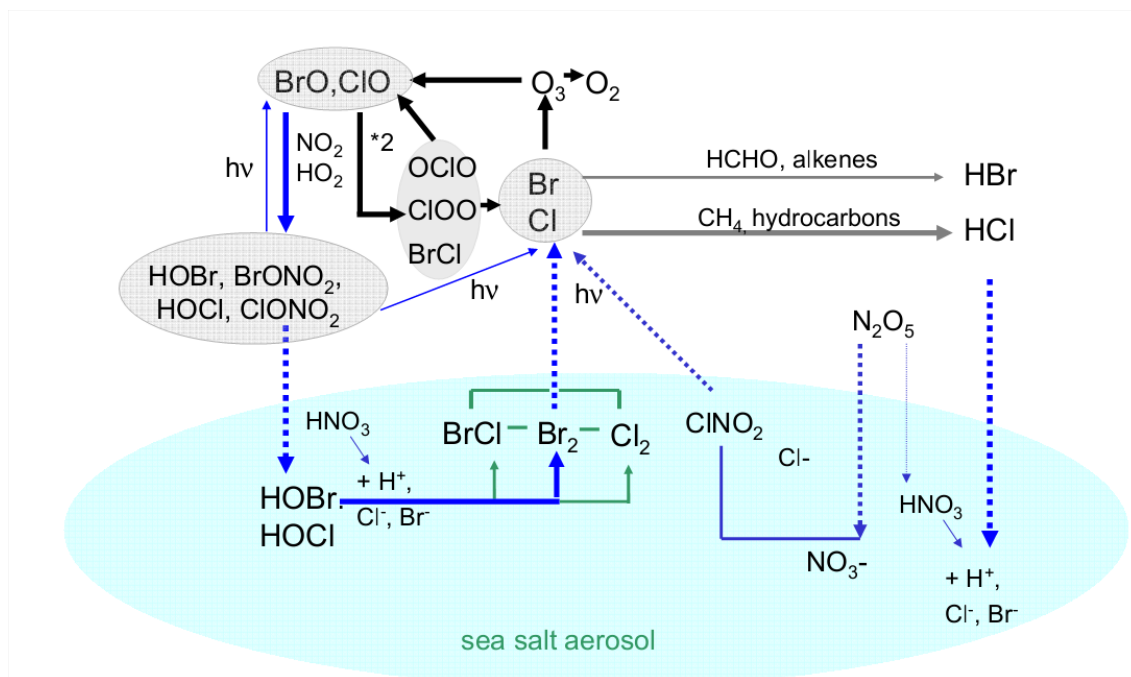
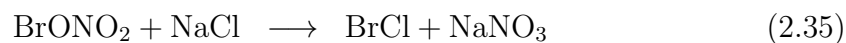


Figure 2.2: Sketch of important reactions of Cl and Br chemistry. Gas phase reactions, as well as aqueous phase are indicated by full arrows. Interaction with organics (grey arrows) possibly inhibits the release mechanisms by formation of soluble HBr and HCl. Dotted arrows show possible pathways for heterogeneous reactions. (Buxmann, 2012a)



Beside hydrolysis, also reactions



are possible on aerosols (Aguzzi and Rossi, 1999).

Chapter 3

Radiative Transfer in the Atmosphere

In this chapter, an introduction on the propagation of radiation within the atmosphere is provided. The sun is the dominating source of primary radiation in the atmosphere. The solar spectrum can be described approximately by the radiation curve of a black body according to Planck's law with the maximum of its energy distribution at around 500 nm. Radiation transmitted through the atmosphere is filtered by different absorption and scattering processes (see section 3.2) so that mainly radiation in UV ($\gtrsim 350$ nm), Vis, IR and in microwave and radar wavelength ranges remains in the troposphere. In the scope of this work only radiation in the UV and visible wavelength ranges is relevant, therefore the term *radiation* is used synonymously with the term *light* in the following. The knowledge of the light path of UV and visible light through the atmosphere is crucial to interpret the differential slant column density ΔS (see section 4.2) of a certain trace gas obtained by MAX-DOAS measurements. The propagation of light is determined by molecular absorption and different scattering processes which occur on air molecules (i.e. mainly N_2 and O_2 molecules) and aerosols. These processes will be described in section 3.2.

The formal treatment of terrestrial radiation using the radiative transfer equation (RTE) will be presented in section 3.1.

The differential slant column density ΔS of an atmospherical constituent measured with MAX-DOAS depends on the most probable light paths of the photons reaching the instrument. The Air Mass Factor (AMF) which is the factor by which an absorbers differential slant column density is enhanced by the geometry of the light path compared to a reference light path will be introduced in section 3.3. Parts of this chapter are adapted from Yilmaz (2012a).

3.1 Radiative Transfer Equation

The propagation of light within the atmosphere is described by the (integro-differential) radiative transfer equation (RTE). In its differential form for terrestrial

radiation it is:

$$\frac{dI(\lambda)}{ds} = \underbrace{-[\epsilon_a(\lambda) + \epsilon_s(\lambda)] \cdot I(\lambda)}_1 + \underbrace{\epsilon_s(\lambda) \int_0^\pi \int_0^{2\pi} I^*(\lambda, \vartheta, \phi) \cdot \frac{\Phi(\vartheta, \phi)}{4\pi} d\phi \cdot \sin \vartheta d\vartheta}_2, \quad (3.1)$$

with ϵ_s and ϵ_a being the scattering coefficient and absorption coefficient, respectively. Equation 3.1 describes the change of the radiance $dI(\lambda)$ after crossing an infinitesimal volume dV with length ds . The initial radiance $I(\lambda)$ is attenuated by scattering and absorption, denoted by the first term on the right hand side. The second term accounts for the radiance added to the direction of propagation by scattering from the diffuse radiation field $I^*(\vartheta^*, \phi^*)$ from any direction in space, indicated by the scattering angle ϑ^* and the azimuthal angle ϕ^* .

The dimensionless function $\Phi(\vartheta, \phi)$ (denoted as distribution or redistribution function) accounts for the anisotropy of the scattering processes and is defined by:

$$\Phi(\vartheta, \phi) := 4\pi \cdot \frac{1}{\sigma_s(\lambda)} \cdot \frac{d\sigma_s(\lambda)}{d\Omega}, \quad (3.2)$$

with the scattering cross section σ_s and solid angle $d\Omega$. For isotropic scattering it is $\Phi = 1$. More details and a derivation of the RTE can be found in literature (e.g., Roedel, 2000; Deutschmann, 2009).

For a more detailed interpretation of differential slant column densities ΔS or dS (see chapter 4) obtained by MAX-DOAS measurements, methods dissolving this equation numerically are applied. In the scope of this work for this purpose the radiative transfer model SCIATRAN 2 is used, which will be introduced in chapter 5.

3.2 Scattering Processes in the Atmosphere

Light is scattered in the atmosphere by three different kinds of scattering processes. The elastic Rayleigh and Mie scattering change the propagation direction of light, but conserve its energy. Inelastic Raman scattering also changes the photon energy resulting in a wavelength shift of the scattered light. Yet the cross sections of Raman scattering are in the range of at most several hundredth of the cross section of Rayleigh scattering (Bussemer, 1993, and references therein). Therefore inelastic scattering is not included in the radiative transfer model used for this thesis.

3.2.1 Rayleigh Scattering

Rayleigh scattering occurs on polarizable scattering centers being significantly smaller than the wavelength of the scattered light. The physical process can be described as the forced oscillation of an electrical dipole induced by incoming radiation (Roedel, 2000). It is an elastic type of scattering. In the atmosphere these electrical dipoles

are represented mainly by N_2 and O_2 molecules. The cross section of Rayleigh scattering σ_R can be approximated by:

$$\sigma_R \approx \frac{8\pi^3}{3\lambda^4 N_{air}^2} \cdot (n_0(\lambda)^2 - 1)^2 \cdot F_K(\lambda), \quad (3.3)$$

with λ denoting the wavelength, $n_0(\lambda)$ is the wavelength dependent refraction index of air, N_{air}^2 is the number density of air, and $F_K(\lambda)$ is a correction factor for anisotropic polarizability of air molecules.

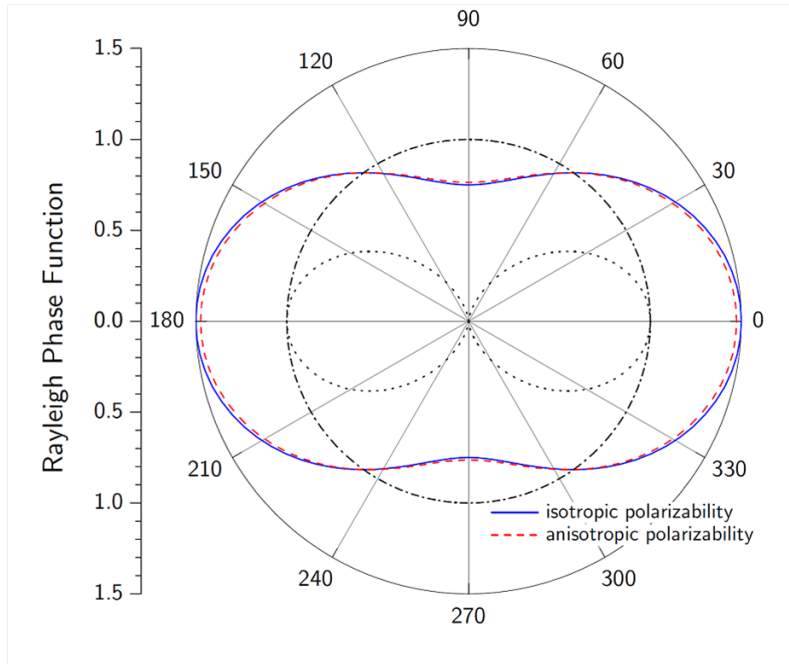


Figure 3.1: Polar diagram of the Rayleigh phase function $\Phi_R(\vartheta)$ for unpolarized incoming light. The dotted line represents the contribution of light polarized parallel to the scattering plane and the dashed line shows the contribution of light polarized perpendicular to the scattering plane. Adapted from Hönninger (2002).

The polar diagram in Figure 3.1 shows the phase function $\Phi_R(\vartheta)$ for unpolarized light, where ϑ denotes the angle between incoming and scattered light. Compared to scattering on large particles (see section 3.2.2), the angular dependency of the Rayleigh phase function Φ_R is comparatively small. In contrast, the wavelength dependency of the Rayleigh scattering cross section is very strong with

$$\sigma_R \propto \lambda^{-4}, \quad (3.4)$$

which is the reason for the blue color of the sky. The Rayleigh extinction coefficient ϵ_R is given by $\epsilon_R = N_{air} \cdot \sigma_R$.

3.2.2 Mie Scattering

The Mie theory describes the scattering of light on a particle significantly larger than the light's wavelength. The physical process of Mie scattering is the diffraction

on a pinhole, which is equivalent to diffraction on an opaque body of the same size and shape according to Babinet's principle. The ratio of the particle's radius r and the wavelength λ is crucial for the scattering properties of the particle. Often this ratio is described by the aerosol size parameter x :

$$x := \frac{2\pi r}{\lambda} \quad (3.5)$$

Following Van de Hulst (\sim p.129 1981) for incoming light $I_0(\text{W}/\text{m}^2)$ the intensity (W/m^2) distribution of light scattered on a spherical particle is described by:

$$I_{Mie}(\vartheta) = \frac{I_0(i_1(\vartheta) + i_2(\vartheta))\lambda^2}{8\pi^2 r^2}. \quad (3.6)$$

$i_1(\vartheta)$ denotes the intensity of light polarized perpendicular to the scattering plane, $i_2(\vartheta)$ denotes the intensity of light polarized parallel to the scattering plane. $i_1(\vartheta)$ and $i_2(\vartheta)$ depend on the scattering angle ϑ and on x . r is the distance to the scattering center. The scattered light in any direction has a partial linear polarization. The average of intensity of scattering over both directions of polarization for a given scattering angle is given by the phase function $\Phi_{Mie}(\vartheta)$.

Mie scattering phase functions for water droplets of three different $x = 1, 3$ and 10 are shown in Figure 3.2. The larger the aerosol size parameter x , the more the scattering process is dominated by forward scattering.

However, atmospheric aerosols consist of solid, liquid or mixed particles with different sizes, shapes and chemical composition. Within the Mie theory the bulk scattering properties are therefore described by integrating the single scattering properties of aerosols over their entire size distribution. By doing so, the dependency of Mie scattered light intensity on the scattering angle can be approximated by the Henyey-Greenstein parameterization (Henyey and Greenstein, 1941):

$$\Phi_{HG}(\vartheta) = \frac{1 - g^2}{4\pi \cdot (1 + g^2 - 2g \cos \vartheta)^{\frac{3}{2}}}, \quad (3.7)$$

where g is the average cosine of the scattering function $g = \langle \cos \vartheta \rangle$. g is denoted as asymmetry parameter and typically ranges between 0.6 and 0.7 for atmospheric aerosol (Perliski, 1992).

The degree of wavelength dependency of Mie-Scattering depends on the aerosol's size distribution. For a typical aerosol size distribution (e.g., for the Junge distribution) in the atmosphere the scattering cross section of Mie scattering is

$$\sigma_{Mie} \propto \lambda^{-1.3}, \quad (3.8)$$

which explains the white color of clouds or fog, for example (Roedel, 2000).

3.2.3 Raman Scattering

Like Rayleigh scattering, Raman scattering is a type of molecular scattering, but energy is transferred between the scattering molecule and the photon. The rotational and/or vibrational state of the scattering molecule changes during the scattering process. The energy difference is assigned to the scattered light according to a

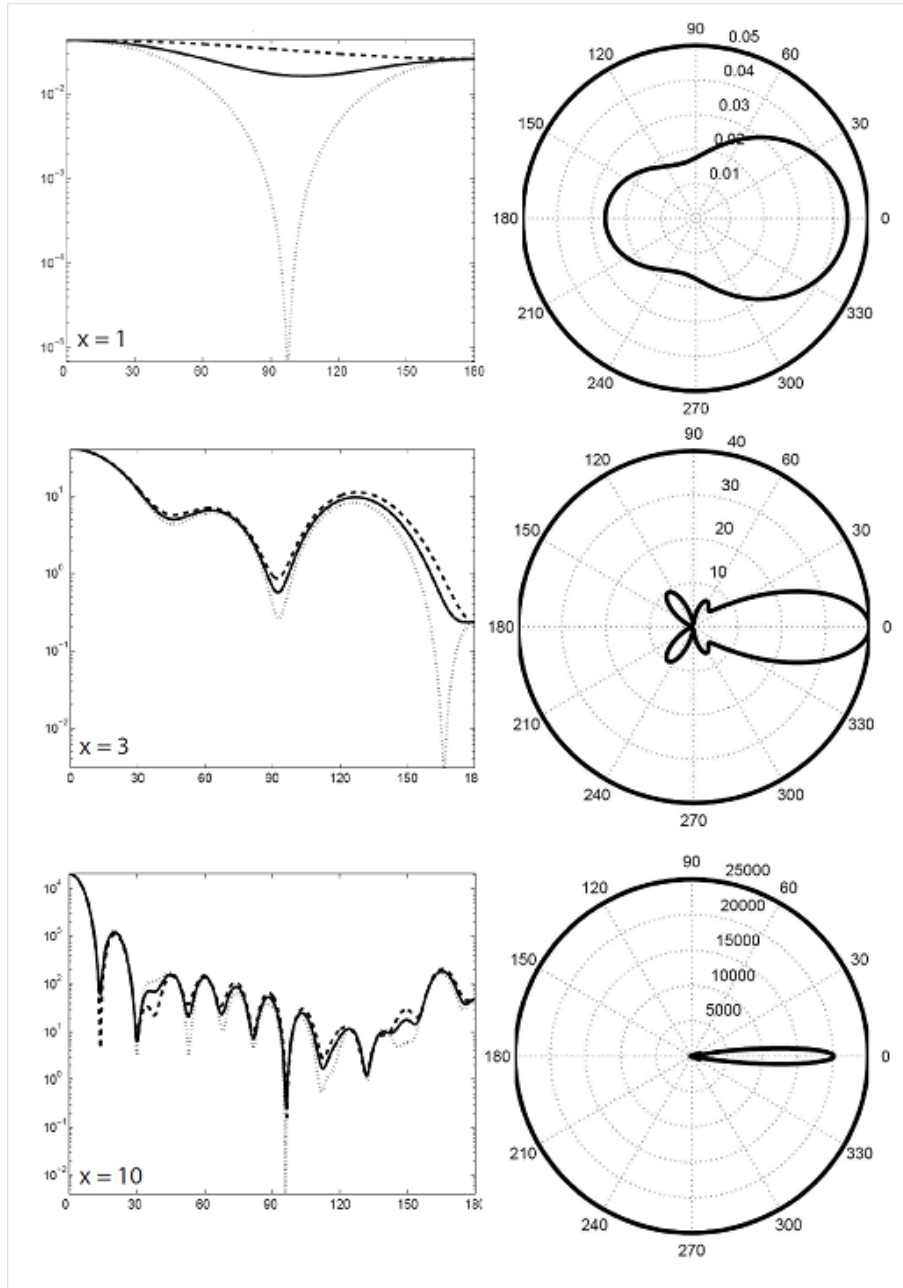


Figure 3.2: *Mie scattering phase functions at 550 nm for water droplets with aerosol size parameters $x=1,3$ and 10 . Left column: Phase function on logarithmic scale; Right column: Polar diagrams of the same phase functions on linear scale. It becomes apparent that forward scattering dominates with increasing particle size. Adapted from Sanghavi (2003). Ordinates give the scattering angle ϑ , abscissae the phase function $\Phi_{Mie}(\vartheta)$.*

Stokes (Stokes $\Delta J = +2$, S-branch) or Anti-Stokes shift (Anti-Stokes $\Delta J = -2$, O-branch) changing the light's wavelength, with ΔJ denoting the difference in the total angular momentum quantum number of the molecule. The cross section for (rotational-)vibrational Raman scattering (RVRS) is only a thousandth of the

Rayleigh scattering cross section and therefore one order of magnitude lower than rotational Raman scattering (RRS). Although the contribution of Raman scattering on radiative transfer is small, it has an important impact on the differential spectral structure of scattered light, referred to as the *Ring effect* (Grainger and Ring, 1962). Further details on Raman scattering and the Ring effect can be found in the literature (e.g., Chance and Spurr, 1997; Haug, 1996; Bussemer, 1993).

3.2.4 Aerosol Optical Properties

For the Mie theory described in section 3.2.2 aerosols are regarded as opaque bodies. However, actual atmospheric aerosol is characterized also by the optical properties of individual particles, which depend on their chemical composition. Besides scattering, also absorption of light by aerosol contributes to the extinction coefficient ϵ_M , which indicates the strength of exponential attenuation of light due to aerosol per unit of distance. The ratio of extinction due to scattering ϵ_s and total extinction $\epsilon_M = \epsilon_s(\lambda) + \epsilon_a(\lambda)$ is described by the dimensionless single scattering albedo (SSA):

$$\omega_0(\lambda) = \frac{\epsilon_s(\lambda)}{\epsilon_M(\lambda)} \quad \text{with} \quad \epsilon_M(\lambda) = \epsilon_s(\lambda) + \epsilon_a(\lambda). \quad (3.9)$$

The SSA ranges between 1 for aerosol only scattering and 0 for aerosol completely absorbing incoming light. The wavelength dependency of ϵ_M can be approximated by the Ångström exponent α_M :

$$\epsilon_M(\lambda) = \epsilon_M(\lambda_0) \cdot \left(\frac{\lambda}{\lambda_0} \right)^{-\alpha_M}, \quad (3.10)$$

whith $\epsilon_M(\lambda_0)$ being the extinction coefficient at the reference wavelength λ_0 . More details on the Ångström exponent can be found in literature (e.g., Yilmaz, 2012a; Ångström, 1929).

3.3 The Air Mass Factor Concept

As outlined in chapter 4, in general MAX-DOAS measurements yield differential slant column densities, which can be defined as ΔS , see section 4.2. Due to the stratification of the atmosphere and turbulent mixing, it is appropriate in many cases to assume a layer-like, homogeneous distribution of an atmospherical absorber. With a given concentration c_A of an absorber A within a layer the slant column density S along an arbitrary light path s which is detected by a MAX-DOAS instrument is given by:

$$S(\lambda, \vartheta, \alpha, \phi) = \int_0^{\infty} c(s) ds. \quad (3.11)$$

To obtain comparable quantities for a given absorber layer, the vertical slant column density V is defined, which corresponds to the concentration in the layer integrated

along a vertical light path of the length of the layer height:

$$V(\lambda, \vartheta, \alpha, \phi) = \int_{z=0}^{\infty} c(z) dz, \quad (3.12)$$

with the wavelength λ , solar zenith angle ϑ , elevation angle of the instrument's line of sight α , the relative solar azimuth angle ϕ and the altitude z . The factor A between S and V is called air mass factor (AMF). For horizontally homogeneous atmospheric layers the height dependence of the AMF can be described by dividing the atmosphere along its vertical axis into layers of height h_i , called boxes. Each box i is described by an individual Box-AMF A_i , defined by:

$$A_i := \frac{dS}{dV_i}, \quad (3.13)$$

with V_i being the vertical column density in box i . The Box-AMF quantifies how the measured slant column density changes with an alteration of the vertical column density in a certain box. Box-AMFs can be used in the retrieval of trace gas vertical profiles (see chapter 5). In the case of weak absorbers, the inversion problem of the profile retrieval is linear, since the Box-AMFs do not depend on the corresponding trace gas profile. In contrast, strong absorbers influence the Box-AMFs, causing the inversion problem to become non-linear. The total AMF can be calculated from the Box-AMFs and the respective trace gas profile by adding the Box-AMFs over the whole atmosphere, weighted with the partial trace gas vertical columns:

$$A = \frac{\sum_i A_i \cdot V_i}{\sum_i V_i}. \quad (3.14)$$

3.4 Radiative Transfer Modeling

Radiative transfer simulations in the atmosphere require the solution of the RTE (equation (3.1)). Since the RTE has no analytical solution, radiative transfer models (RTM) are required. In general, two different numerical approaches are commonly applied in RTMs. On the one hand, numerical methods, e.g. the Discrete Ordinate Method, which applies a discretization for the ordinates and directions, are implemented for the calculation of the resulting radiation field. On the other hand, the paths of an ensemble of individual photons, with randomly chosen parameters, through the atmosphere are calculated in a statistical approach using e.g. Monte Carlo Methods. Examples for the former approach are DISORT (Stamnes et al., 1988) and SCIATRAN 2 (Rozanov et al., 2005). The latter approach is used e.g. by TRACY (von Friedeburg, 2003) and McArtim (Deutschmann et al., 2011). SCIATRAN 2 (Rozanov et al., 2005) was used for the calculations performed within this work.

3.4.1 SCIATRAN 2

The radiative transfer model SCIATRAN 2 applies the Discrete Ordinate Method to solve numerically the RTE for monochromatic unpolarized radiation in a spherical atmosphere (Rozanov et al., 2005). Thereby, the second term in equation (3.1) is separated in a part, contributing due to single scattering, and a part for the contribution due to multiple scattering. The resulting combined integro-differential equations are then solved using the Finite Difference Method and the Picard iterative approximation for the multiple scattering term (Rozanov et al., 2000, 2001). Furthermore, both the azimuthal dependence of the radiation field and the scattering phase function are developed in Fourier series in combination with Legendre polynomials. The solar zenith angle dependency is discretized and the according integrals are replaced by Gaussian quadratures. Also the height coordinate is discretized. Finally, the approximations and discretization result in a set of equations, which are solved by matrix inversion for each harmonic of the Fourier expansion separately.

3.4.2 Model Parameters

SCIATRAN 2 provides the calculation of radiances, total AMFs and Box-AMFs for an arbitrary output altitude. The atmosphere is subdivided in layers defined by the altitude grid. Atmospheric properties are assumed to be homogeneous within these layers. The temperature and pressure profile can either be provided by the user, e.g. radiosonde measurements, or adapted from a climatological data base. The climatology data included in SCIATRAN 2 has been obtained using a two dimensional chemo-dynamical model developed at the Max Planck Institute for Chemistry in Mainz (Brühl and Crutzen, 1993). The same applies for the trace gas profiles. The trace gas absorption cross sections are provided by the user and consist of several cross sections at different temperatures to account for the temperature dependence. The optical properties of aerosols are quantified by the vertical distribution of the extinction coefficient, single scattering albedo and asymmetry parameter of the Henyey-Greenstein parametrization (see section 3.2.2) of the phase function. The provided profiles are interpolated on the altitude grid using Akima interpolation (Akima, 1970). Furthermore, the surface albedo and the wavelength for the calculations are selected by the user. SCIATRAN 2 allows for the consideration of several viewing geometries in a single program run. Each viewing geometry is determined by the solar zenith and relative azimuth angle, and the elevation angle of the observer's line of sight.

Chapter 4

Absorption Spectroscopy

Atmospheric spectroscopy is based on the interaction of light with molecules in the air. As described in chapter 3, one possible interaction is the absorption of light: A single photon transfers its energy completely, exciting an electronic rotational and/or vibrational energy state of a molecule. The energy of such a state corresponds to an absorption line which gets apparent in a spectral analysis. The entirety of interacting energy states and thus of absorption lines at different wavelengths is characteristic for a molecule type, i.e. the absorbing gas species. Therefore the knowledge of the wavelength dependent absorption coefficient (cf. equation 3.1) of a given absorbing gas species can allow for the assessment of its concentration.

A very powerful analytical variant of atmospheric spectroscopy is DOAS, which was used for the spectral retrievals of trace gases presented in this work. The basic DOAS principle is outlined in section 4.1.

In section 4.2, the basic quantities used in the spectral retrieval of spectra obtained by the MAX-DOAS technique will be defined.

A very detailed description of the theory and applications of DOAS can be found in (Platt and Stutz, 2008).

4.1 DOAS

In a continuous spectrum, as in the case of the solar spectrum or a certain lamp spectrum, the superimposition of single, neighboring absorption lines causes so-called absorption bands. The DOAS method (Differential Optical Absorption Spectroscopy), first introduced by Perner et al. (1976); Platt et al. (1979), takes advantage of that the absorption bands of many atmospheric constituents are narrow, compared to extinction by scattering processes (cf. chapter 3). DOAS allows for the simultaneous detection of trace gases with mixing ratios of several pptv without impacting the atmospheric chemistry, as for example by titration on inlet-surfaces, or the exposure to strong radiation.

A solution of the terrestrial form of the radiative transfer equation presented in section 3.1 is given by the Lambert-Beer law, which describes the attenuation of

light by an absorbing medium along the light path:

$$I(\lambda, L) = I_0(\lambda) \exp \left(- \int_0^L \left(\epsilon_R(\lambda, L) + \epsilon_M(\lambda, L) + \sum_i \sigma_i(\lambda, p, T) \cdot c_i(s) \right) dl \right) . \quad (4.1)$$

with

$I(\lambda)$	Radiance of light after having travelled a path of length L through the atmosphere
$I_0(\lambda)$	Initial radiance
λ	wavelength
ϵ_R	extinction coefficient for Rayleigh scattering
ϵ_M	extinction coefficient for Mie scattering
σ_i	absorption cross section of absorber i , quantifying the probability of absorption
c_i	concentration of absorber i
p	pressure
T	temperature
L	Length of the light path s

Equation 4.1 implies an initial radiance I_0 and the radiance I . The quotient

$$\tau(\lambda) = \ln \frac{I_0(\lambda)}{I(\lambda)} = \ln I_0(\lambda) - I(\lambda) \quad (4.2)$$

contains the information on total extinction along the light path difference between I_0 and I . The basic principle of DOAS is the separation of broad and narrow band (also called differential) spectral structures in an absorption spectrum to isolate the narrow trace gas absorptions.

Therefore the exponent of equation 4.1 can be rewritten as an optical density τ :

$$\tau = \tau_b + \tau' , \quad (4.3)$$

whith τ_b and τ' representing the broad band and narrow band extinction, respectively. In practice, τ_b can be represented by a polynomial $P_r(\lambda)$ of degree r , yielding:

$$\tau = \int_0^L \sum_i \sigma'_i(\lambda) c_i(s) ds + P_r(\lambda) . \quad (4.4)$$

The aim of a DOAS fitting procedure is to retrieve the slant column densities

$$S_i = \int_0^L \sum_i c_i(s) ds \quad (4.5)$$

of the absorbers i within a given wavelength interval. For details on analytical methods see (Platt and Stutz, 2008). For the determination of the integrated concentrations $c_i(s)$ also the knowledge of the light path difference between I and I_0 is

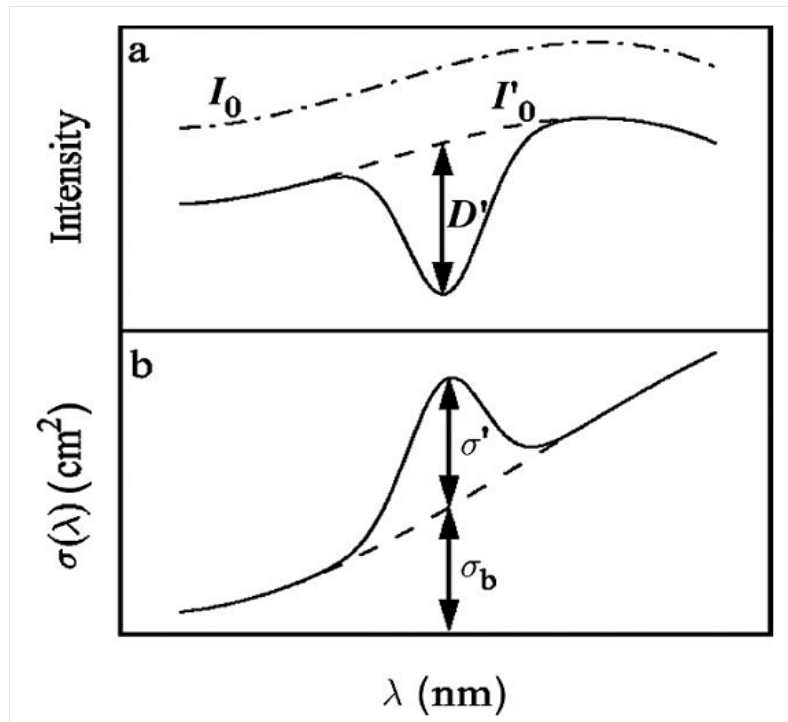


Figure 4.1: Principle of DOAS: I_0 and σ are separated by an adequate filtering procedure into a narrow-band (D' and σ') and broad-band part (I'_0 and σ_b). (Platt and Stutz, 2008)

required.

4.2 MAX-DOAS

Multi-AXis-DOAS is a passive variant of DOAS, meaning that no artificial light source is used to gain I and I_0 . Instead, scattered sunlight is measured reaching the instrument from different viewing directions, see Figure 4.2. MAX-DOAS is based on a comparable uncomplex instrumental set up, in contrast to active DOAS variants, as Long-Path DOAS or Folded-Path DOAS variants, for example.

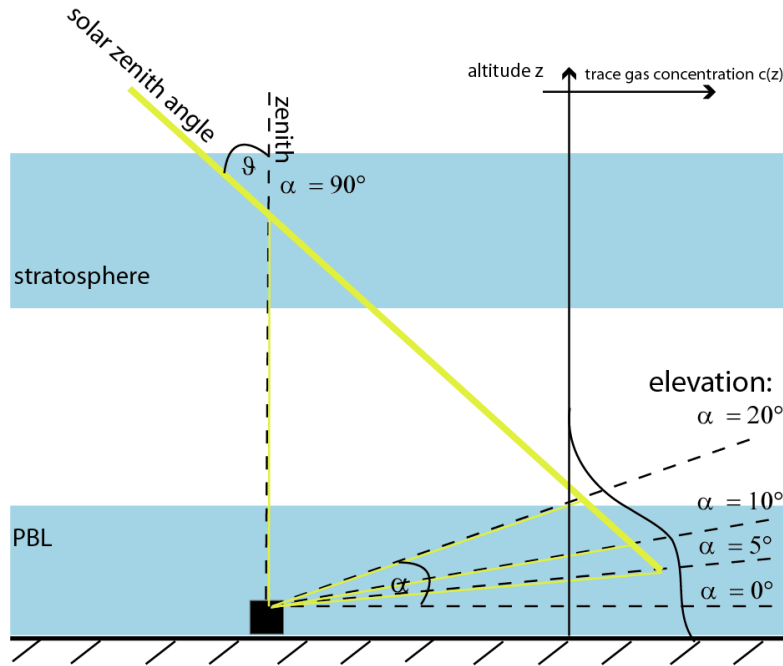


Figure 4.2: Sketch of a typical MAX-DOAS measurement in the single scattering case. Incoming sun light becomes scattered into the field of view of the instrument's telescope which is pointing sequentially at different elevation angles including the zenith.

Ground based MAX-DOAS systems are most sensitive within the lowest several hundred meters of the planetary boundary layer (PBL) (cf. sections 5.2.2 and 8.3.2). The simplified MAX-DOAS measurement principle is sketched in Figure 4.2 for the case of single scattering, cf. section 5.1: Light detected at lower telescope elevation angles α contains a larger contribution of light which passed a longer path through the boundary layer than that at higher telescope elevation angles. Therefore trace gas layers close to the ground should lead to a distinct increase of the absorber signal with decreasing telescope elevation angle.

As described above, the information of absorption is contained in the quotient of $I_0(\lambda)$ and $I(\lambda)$. Therefore slant column densities S of absorber species obtained by the use of a DOAS fitting procedure represent the difference $S(I) - S(I_0)$.

In terms of DOAS, $I_0(\lambda)$ is usually called reference spectrum. Principally an arbitrary measured spectrum can be used as reference spectrum for a DOAS measurement. In the scope of this work, for the spectral retrieval of data obtained by

MAX-DOAS and Car-DOAS, which is none other than a variation of MAX-DOAS with fixed elevation angle, two definitions of $S(I)-S(I_0)$ were used:

1. The MAX-DOAS slant column densities of absorbers i presented in sections 9.1 and 9.2 are defined by

$$\Delta S_i(\vartheta, \alpha) := S_i(\vartheta, \alpha) - S_i(\vartheta, \alpha_{ref} = 90^\circ), \quad (4.6)$$

where the reference $S_i(\vartheta, \alpha_{ref} = 90^\circ)$ points to zenith and is measured at approximately the same solar zenith angle ϑ as the measurement at the elevation angle α . In terms of MAX-DOAS, $S_i(\vartheta, \alpha_{ref} = 90^\circ)$ is also called Fraunhofer Reference Spectrum (FRS). The reason for the choice of $\alpha_{ref} = 90^\circ$ becomes clear considering the light path through the planetary boundary layer (PBL): In the case of single scattering, at $\alpha_{ref}=90^\circ$ the order of magnitude of the light path length within the PBL is in the order of magnitude of 1 km, compared to a characteristic light path in the order of magnitude of 10 km at low ($< 5^\circ$) α (see section 5.1). So, the initially unknown, contribution of an absorber signal to the reference S_{FRS} is only in the order of magnitude of $\sim 10\%$ of the measurement spectra S_i , assuming a homogeneous distribution of the absorber. To assess S_{FRS} radiative transfer models (see section 3.4) or sometimes also the Langley plot are used. A description of the Langley plot method is given by e.g. Hönninger (2002), Sinreich (2008) and Platt and Stutz (2008).

2. The Car-DOAS slant column densities presented in section 9.1 are defined by

$$dS_{BrO}(\vartheta, \phi) := S_{BrO}(\vartheta, \alpha = 20^\circ, \phi) - S_{BrO}(\vartheta_{ref}, \alpha = 20^\circ, \phi_{ref}), \quad (4.7)$$

where the reference is an arbitrary measurement $S_{BrO}(\vartheta_{ref}, \phi_{ref})$ from the same exploratory ride pointing perpendicular to the street at solar zenith angle ϑ_{ref} , azimuth ϕ_{ref} and $\alpha=20^\circ$ relative to the lateral inclination of the car (see Figure 7.15). $S_{BrO}(\vartheta, \alpha = 20^\circ, \phi)$ represent the individual measurements during the exploratory ride.

Chapter 5

Retrievals of Vertical Profiles in the Atmosphere by Inversion

In contrast to LP-DOAS, for MAX-DOAS measurements the light path within an absorber is not well-defined. In fact, it is not appropriate to speak about 'a light path', as the light reaching the MAX-DOAS instrument is a superposition of photons with individual light paths. Yet it is possible to make some considerations about the most probable, or also called 'characteristical', light path. This will be done in section 5.1. In section 5.2 the principle of inversion applied on MAX-DOAS data in the scope of this work will be introduced and the software package which was used for that purpose is summarized in 5.3.

5.1 Light Paths of MAX-DOAS Measurements - A Simple Approach

MAX-DOAS measurements (i.e. passive DOAS measurements at different telescope elevation angles, see section 4.1) can yield information on the vertical distribution of an atmospheric absorber. For example, under typical atmospheric conditions without aerosol, it can be assumed that the path of the light reaching the instruments aperture at low telescope elevation angles α is mainly located in lower altitudes. Therefore differential slant column densities $\Delta S(\alpha)$ increasing with decreasing telescope elevation angles would indicate an absorber situated close to the ground within the troposphere.

Light reaching the telescope of a MAX-DOAS instrument has been attenuated along its way according to Lambert-Beer's law, see chapter 4. In the troposphere the total extinction is dominated by scattering processes on aerosols rather than absorption by trace gases. Therefore the range of sensitivity can be approximated by calculating the distance after that the light intensity has decreased by the fraction of e , see Figure 5.1. The Rayleigh extinction coefficient at $\lambda=400$ nm, $\epsilon_R = 0.046 \text{ km}^{-1}$ (Roedel, 2000) yields, assuming only Rayleigh scattering, a characteristical distance of 22 km between the instrument and the point where the last scattering event occurred. This distance is reduced, if Mie scattering occurs additionally. A typical Mie scattering coefficient ϵ_{Mie} at $\lambda=400$ nm for continental aerosol type is $\epsilon_{Mie}=0.04$

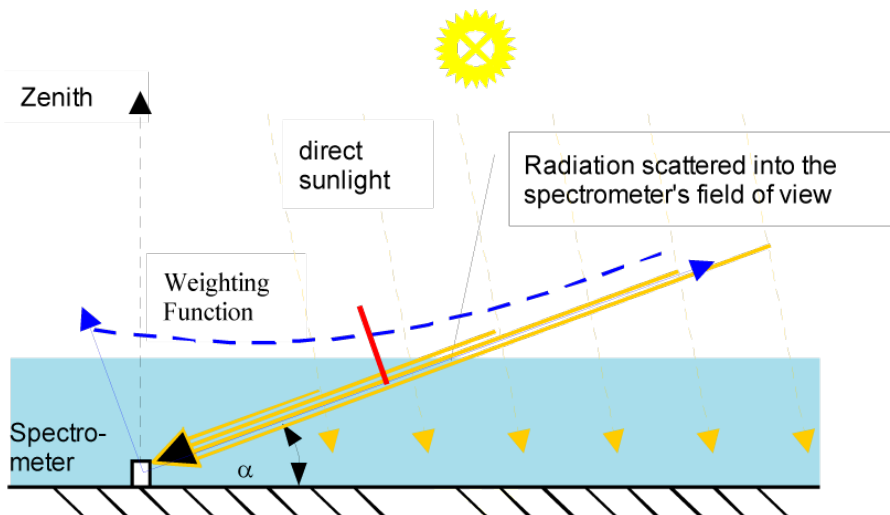


Figure 5.1: Sketch of radiative transfer in the vicinity of a MAX-DOAS instrument. A small fraction of sunlight is transported to the instrument from a range of distances indicated by the weighting function (dashed blue line). The weighting function has a characteristic (wavelength dependent) length of several kilometers (indicated by the red line), see text for details. The instrument is most sensitive for tracegases in its close vicinity, but also trace gas clouds in a distance of several kilometers can be detected.

km^{-1} (Roedel, 2000). This would further reduce the distance to 12 km. With a box layer height of 1 km the maximum telescope elevation angle at which the characteristic range of sensitivity is situated completely within the boundary layer is $\alpha=4.78^\circ$. This estimation may be adequate for visible light around $\lambda=400\text{ nm}$. Extinction coefficients for the UV are larger due to stronger Rayleigh scattering at smaller wavelengths. Applying equations (3.4) and (3.10) yields a characteristic length of $\sim 5\text{ km}$ at $\lambda=300\text{ nm}$.

As already mentioned, these approximations are only appropriate, as long as the according trace gases and aerosols are homogeneously distributed in a box-like shape. In general, however, the distribution of aerosols and trace gases diverts from a box-like shape due to transport processes, dilution or atmospheric life times, which are short compared to transport time scales, for example. Furthermore sufficient turbulent mixing is not always warranted within the 'mixed layer' due to local inversion layers, as will be seen in section 9.1. In the presence of clouds or high aerosol loads, also multiple scattering inside the layer of interest may occur, whereas the estimations above are only valid, when scattering occurs above the imagined trace gas layer. Also the surface albedo and the absorption by strong absorbers have an impact on the light path.

To account for these effects, the height dependent radiation field in the atmosphere has to be considered, including the vertical distribution of quantities having an impact on the light path. The necessary calculations are complex, so radiative transfer models are used to reproduce the light path by inversion methods. This will be discussed in the next section.

5.2 Inversion

In this work aerosol profiles and trace gas profiles of BrO and NO₂ were retrieved from differential slant column densities (see section 4.2) measured by MAX-DOAS at the Dead Sea, see sections 7.1.6 and 9.1. The information on the light path and thereby on atmospheric aerosols can be inferred from slant column densities ΔS of O₄, (e.g., Yilmaz, 2012a; Deutschmann, 2009; Sinreich et al., 2005; Friess et al., 2006). O₄ is a collision complex of oxygen. Its vertical profile is known, since it is proportional to the squared profile of oxygen, which is in turn given by the barometric height formula. The slant column density ΔS O₄ is mainly determined by the vertical distribution of O₄ and optical properties of aerosols, which are aerosol extinction, single scattering albedo, phase function and Ångström exponent, see section 3.2.4. These parameters are provided to the retrieval routine by the user or can be iteratively adjusted by the software package described in section 5.3. In this work the optimal estimation method (Rodgers, 2000), as described in literature (Yilmaz, 2012a, and references therein) is used for the retrieval of aerosol extinction profiles at 360 nm using the absorption band of O₄ at 360 nm. This yields aerosol profiles which are used for the retrieval of BrO and NO₂, also using the optimal estimation method. More information on the retrieval of atmospheric trace gas and aerosol profiles by inverse modeling in general can be found in Yilmaz (2012a). The notation in this chapter follows Rodgers (2000) and Yilmaz (2012a).

5.2.1 Basic Inversion Principle

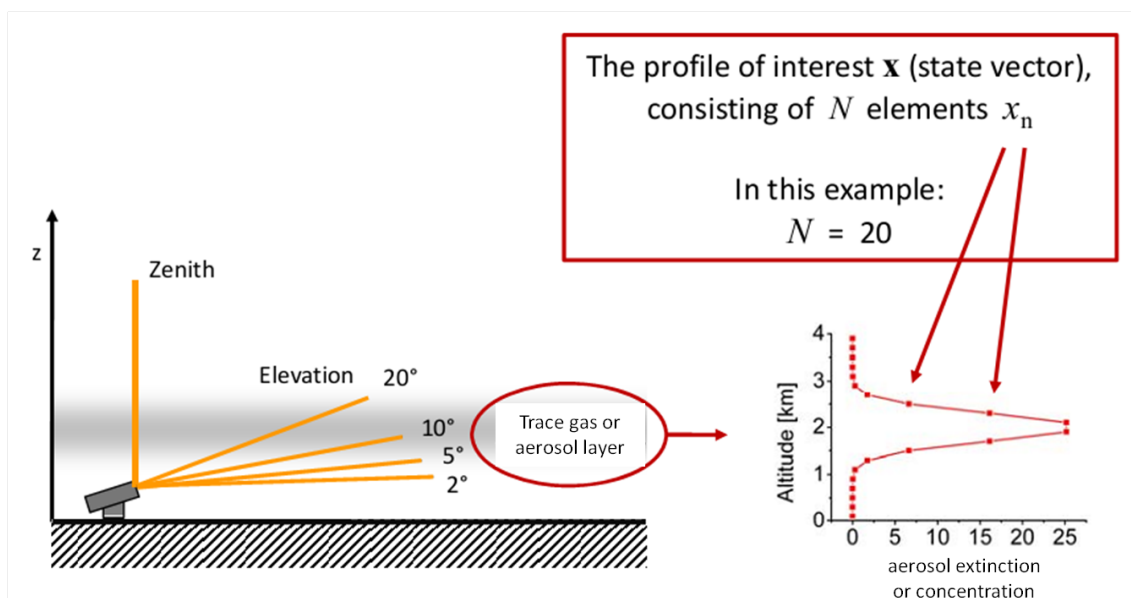


Figure 5.2: Example of an initial situation for the retrieval of a vertical profile of aerosol extinction or a trace gas, represented by the state vector \mathbf{x} . Adapted from Yilmaz (2012c).

Generally speaking, if a physical process is known and a result of that process is

found, it is, depending on the degree of ambiguity of the process, possible to gain information on the initial state.

An initial situation for the retrieval of vertical profiles out of MAX-DOAS measurements is sketched in Figure 5.2. In this case, the physical process is the radiative transfer in the atmosphere discussed in chapter 3, which is simulated by a forward radiative transfer model (RTM). The results of that process are the measured slant column densities of a trace gas at different telescope elevation angles. The initial state can be the vertical profile of aerosol extinction, or the volume mixing ratio or concentration of a trace gas species.

Formally, the RTM is represented by the model function \mathbf{F} . The initial state can be represented by a state vector \mathbf{x} and the results of M single measurements can be represented by M elements y_m forming the m -dimensional measurement vector \mathbf{y} . The basic aim is to find the most probable state vector $\hat{\mathbf{x}}$ by inversion.

The inversion is performed by using the method of optimal estimation (Rodgers, 2000). The principle of this method is to minimize the so called cost function $\chi^2(\mathbf{x})$, which consists of the squared, error weighted difference between measurement \mathbf{y} and modeled values $\mathbf{F}(x)$ from the model function as well as the squared, error weighted difference between the state and an a priori guess for the state, which can be derived, e.g., from climatological databases. An a priori profile is needed because of the underdetermination of the system: The number of independent measurements obtained from ground based MAX-DOAS is in general low compared to the elements of the state vector \mathbf{x} (cf. Figure 5.2). The a priori profile and its uncertainties are represented by x_a and σ_a , respectively. This yields:

$$\chi^2(\mathbf{x}) = \sum_{m=0}^M \left(\frac{F_m(\mathbf{x}) - y_m}{\sigma_{\epsilon,m}} \right)^2 + \sum_{n=0}^N \left(\frac{x_n - x_{a,n}}{\sigma_{a,n}} \right)^2, \quad (5.1)$$

with the error of the m -th measurement $\sigma_{\epsilon,m}$.

Using vector and matrix notation $\chi^2(\mathbf{x})$ can be described in a more general form:

$$\chi^2(\mathbf{x}) = [\mathbf{F}(\mathbf{x}) - \mathbf{y}]^T \mathbf{S}_{\epsilon}^{-1} [\mathbf{F}(\mathbf{x}) - \mathbf{y}] + [\mathbf{x} - \mathbf{x}_a]^T \mathbf{S}_a^{-1} [\mathbf{x} - \mathbf{x}_a], \quad (5.2)$$

with \mathbf{S}_{ϵ} being the diagonal measurement covariance matrix containing the square of the measurement errors $\sigma_{\epsilon,m}$. Equation (5.1) is a special case of equation (5.2) with \mathbf{S}_{ϵ} being a diagonal matrix. \mathbf{S}_a is the a priori covariance matrix consisting of the squared a priori state errors as the diagonal elements. It can also contain non-zero non-diagonal elements which constrain the smoothness of the state vector.

The linear case is given for:

$$\mathbf{F}(\mathbf{x}) = \mathbf{K}\mathbf{x} \longrightarrow \nabla_{\mathbf{x}}\mathbf{F}(\mathbf{x}) = \mathbf{K}, \quad (5.3)$$

The elements K_{ij} of the weighting function \mathbf{K} are the partial derivatives of the model function element $F_i(\mathbf{x})$ with respect to the state vector element x_j .

Then, the cost function is minimized by finding a solution for the equation:

$$\nabla_{\mathbf{x}}\chi^2(\hat{\mathbf{x}}) = 0 \longrightarrow \nabla_{\mathbf{x}}\mathbf{F}(\hat{\mathbf{x}})^T\mathbf{S}_\epsilon^{-1}[\mathbf{K}\hat{\mathbf{x}} - \mathbf{y}] + \mathbf{S}_a^{-1}[\hat{\mathbf{x}} - \mathbf{x}_a] = 0, \quad (5.4)$$

with the optimal state $\hat{\mathbf{x}}$. Depending on the state vector and the model function, the inversion and the solution of equation (5.4) is a linear or a non-linear problem. Inserting the gradient of \mathbf{F} in equation (5.3) into equation (5.4) yields the optimal state vector $\hat{\mathbf{x}}$:

$$\hat{\mathbf{x}} = (\mathbf{S}_a^{-1} + \mathbf{K}^T\mathbf{S}_\epsilon^{-1}\mathbf{K})^{-1} (\mathbf{K}^T\mathbf{S}_\epsilon^{-1}\mathbf{y} + \mathbf{S}_a^{-1}\mathbf{x}_a). \quad (5.5)$$

The inversion problem is non-linear, when the weighting function, represented by the matrix function \mathbf{K} , depends on the state vector \mathbf{x} . In principle profile inversions are a linear problem for weak absorbers, but the transition of \mathbf{x} into a "safe state" vector to avoid physically meaningless (i.e. negative values) results in a non-linear problem. For the treatment of the non-linear case iterative methods are necessary, such as the Gauss-Newton and Levenberg-Marquardt method (Levenberg, 1944; Marquardt, 1963). For more details on the retrieval methods see Yilmaz (2012a).

5.2.2 Retrieval Properties

A vertical profile retrieval is characterized by several properties which have to be regarded carefully for the interpretation of the retrieved state vector $\hat{\mathbf{x}}$. These properties are summarized in the following:

The retrieval gain function matrix \mathbf{G} , in the literature also called contribution function matrix, quantifies the sensitivity of the retrieval to the measurement and is calculated according to:

$$\mathbf{G} = \frac{\partial\hat{\mathbf{x}}}{\partial\mathbf{y}} = (\mathbf{S}_a^{-1} + \mathbf{K}^T\mathbf{S}_\epsilon^{-1}\mathbf{K})^{-1} \mathbf{K}^T\mathbf{S}_\epsilon^{-1}. \quad (5.6)$$

A useful quantity of the retrieval is the matrix product of the gain function matrix and the weighting function matrix \mathbf{GK} . It is called averaging kernel and relates the retrieved state $\hat{\mathbf{x}}$ to the true state \mathbf{x}_t indicating the sensitivity of $\hat{\mathbf{x}}$ towards \mathbf{x}_t :

$$\mathbf{A} = \frac{\partial\hat{\mathbf{x}}}{\partial\mathbf{x}_t} = \mathbf{GK} = (\mathbf{S}_a^{-1} + \mathbf{K}^T\mathbf{S}_\epsilon^{-1}\mathbf{K})^{-1} \mathbf{K}^T\mathbf{S}_\epsilon^{-1}\mathbf{K}. \quad (5.7)$$

For a noise free measurement, the retrieved state vector $\hat{\mathbf{x}}$ describes a smoothed version of the true state vector \mathbf{x}_t according to the vertical resolution and sensitivity of the retrieval at particular altitudes:

$$\hat{\mathbf{x}} = \mathbf{x}_a + \mathbf{A}(\mathbf{x}_t - \mathbf{x}_a), \quad (5.8)$$

with \mathbf{x}_a being the a priori state. Thus, the averaging kernel matrix \mathbf{A} of an ideal retrieval would be the identity matrix ($\mathbf{A} = \mathbf{I}$), yielding ($\hat{\mathbf{x}} = \mathbf{x}_t$).

The degrees of freedom for signal d_s are given by the trace of the averaging kernel matrix and quantify the number of independent pieces of information provided by

the measurement:

$$d_s = \text{tr}(\mathbf{A}) . \quad (5.9)$$

The width of the averaging kernel at altitude z yields the vertical resolution of the retrieval. It can be quantified by the so-called spread function. Rodgers (2000) follows the definition by Backus and Gilbert (1970):

$$s(z) = 12 \frac{\int (z - z')^2 A^2(z, z') dz'}{(\int A(z, z') dz')^2} . \quad (5.10)$$

In contrast to a Gaussian spread function, for example, this type avoids problems with negative values of the averaging kernel.

5.2.3 Retrieval Procedure

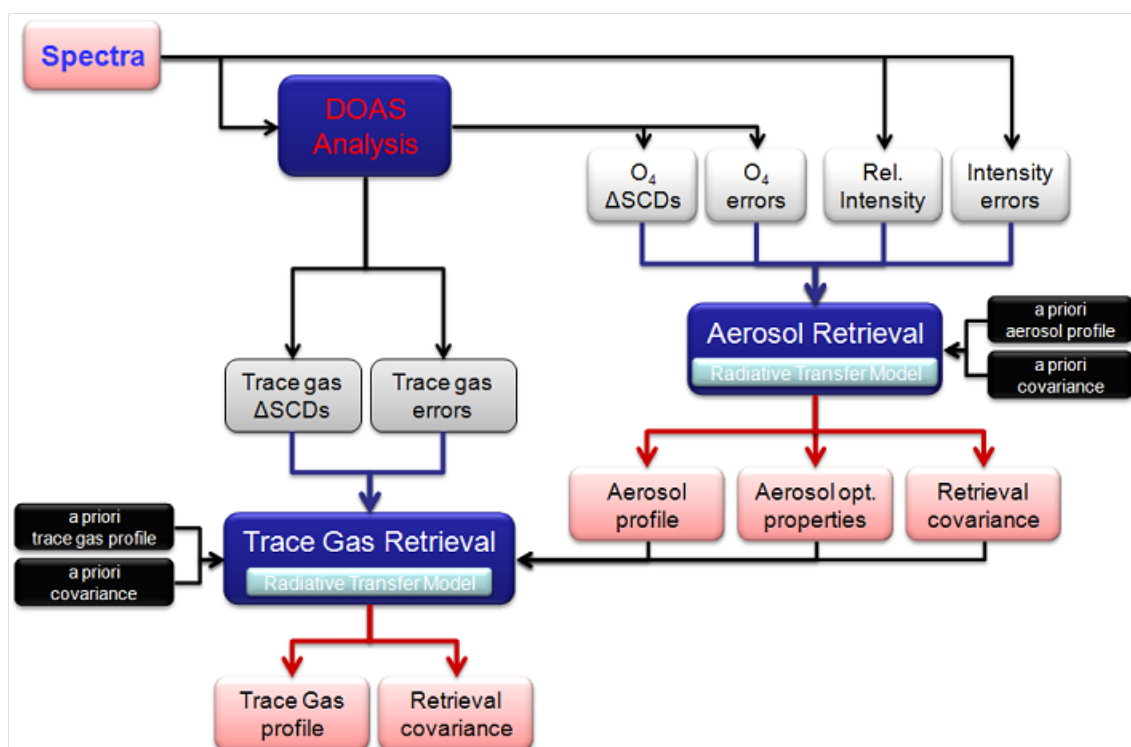


Figure 5.3: Flow chart of the aerosol and trace gas profile retrieval procedure applied on MAX-DOAS measurements. (Yilmaz, 2012a)

The sequence of the single retrieval procedures is depicted in Figure 5.3. MAX-DOAS spectra are analyzed to retrieve differential slant column densities of O_4 in a first step. Optionally, also the relative intensities and the relative intensity errors can be used as input for the aerosol retrieval and serve as measurement vector as described by Yilmaz (2012a). The optimal estimation is applied using the methods described above and the radiative transfer model SCIATRAN 2 (Rozanov et al., 2005) to obtain aerosol vertical profiles and optionally aerosol optical properties, see

section 3.2.4 and Yilmaz (2012b, chapter 6). In a second step, the retrieved aerosol profiles, along with slant column densities obtained from MAX-DOAS measurements serve as input for the optimal estimation of trace gas vertical profiles, along with an a priori trace gas profile. The individual wavelengths used for the profile retrievals are given by the user and should represent the range of the corresponding DOAS fitting wavelength window (see section 8.1). Apart from a vertical profile, also the set of retrieval properties, described in section 5.2.2, is provided by the retrieval.

5.2.4 Retrieval Errors

Following Yilmaz (2012a) the total retrieval error can be interpreted as the sum of the smoothing error covariance \mathbf{S}_s and the retrieval noise covariance \mathbf{S}_m :

$$\hat{\mathbf{S}} = \mathbf{S}_s + \mathbf{S}_m . \quad (5.11)$$

The smoothing error \mathbf{S}_s accounts for the fact, that not the true initial state \mathbf{x}_t is estimated by the retrieval, but a state smoothed by the averaging kernel. \mathbf{S}_m describes the error of the retrieved state vector due to the measurement error. The visualization of covariance matrices as a description of the error of a retrieved state is difficult to implement. Therefore, the diagonal elements of the covariance matrix, i.e. the variances, are used as the error of the retrieved quantities. For more details on the retrieval error see Yilmaz (2012a). The contributions of these errors to the retrieved profiles in this work will be discussed in section 8.3.2.

5.3 User Interface HEROE

The retrieval algorithms used in this work for the evaluation of MAX-DOAS slant column densities are described in more detail by Yilmaz (2012a). For the retrieval analysis of MAX-DOAS data, following the scheme in Figure 5.3, the user interface *HEROE: Heidelberg Retrieval using Optimal Estimation* was used provided by Yilmaz (2012b). HEROE is implemented using the program IDL from ITT Visual Information Solutions (former Research Systems, Inc.) and connects raw MAX-DOAS results (i.e. differential slant column densities) with methods of radiative transfer modelling to yield vertical profiles of aerosol extinction and trace gases. Its assignments are (Yilmaz, 2012a,d):

- Reading in the data retrieved from the MAX-DOAS measurements
- Case distinction for retrievals using dS or ΔS (see section 4.2)
- Creating of the necessary numerical quantities, namely the state and measurement vectors, the corresponding covariance matrices and so on
- Providing of predefined a priori profiles with linear, exponential or Boltzmann distribution shape which can be described by two parameters: a ground value and a characteristic height, cf. section 8.3.3

- Calling of the radiative transfer model, reading in the simulated quantities and creating the simulated measurement vector $\mathbf{F}(\mathbf{x})$ and the weighting function matrix \mathbf{K}
- Performing the matrix calculations for the iteration procedure and calculating of the relevant quantities and results
- Storing the retrieval results and properties

The application of HEROE will be presented in section 8.3.

Chapter 6

Instrumentation

In this chapter, a summary will be given on the MAX-DOAS instruments and the LP-DOAS instrument which were used for the measurements presented in chapter 7.

6.1 Spectrographs

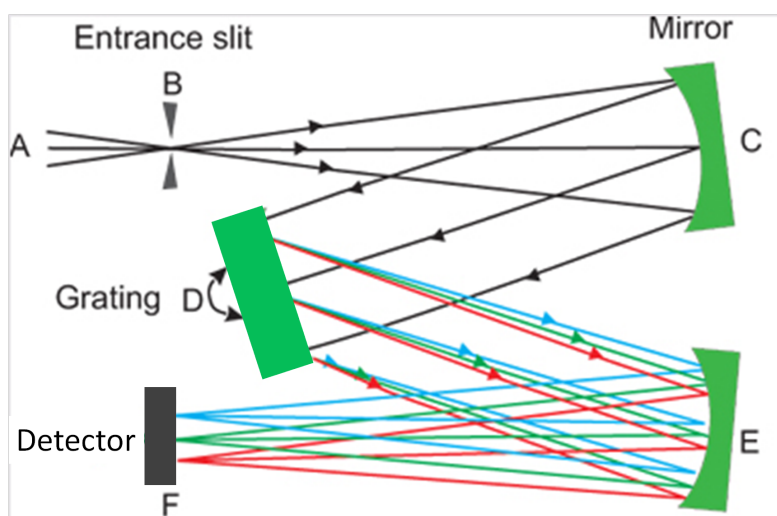


Figure 6.1: *Sketch of a spectrograph with Czerny-Turner configuration. Adapted from Zeiss.de*

All spectrographs used in this work are based on the Czerny-Turner principle (Czerny and Turner, 1930): The light passing the entrance slit (B) is collimated by an aspheric mirror (C) onto a grating (D) where it is dispersed. The light is focussed by a second aspheric mirror (E) and collected by a detector (F).

The specifications of the individual spectrographs are given in the corresponding sections below.

6.2 MAX-DOAS South Russia and Mauritania

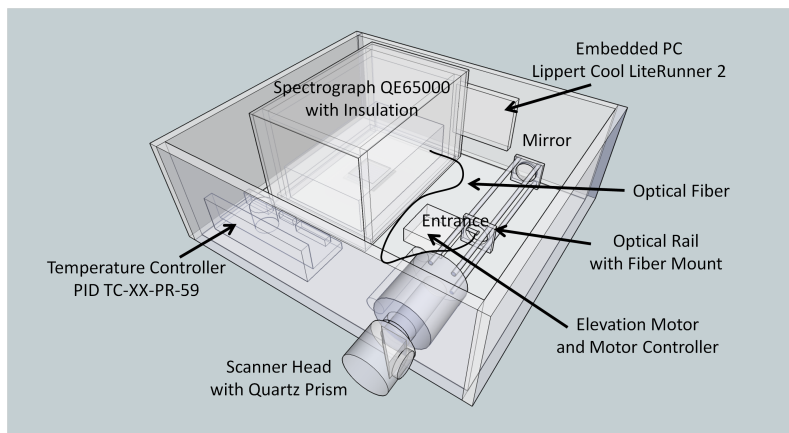


Figure 6.2: Sketch of the MAX-DOAS instrument used in South Russia and Mauritania.

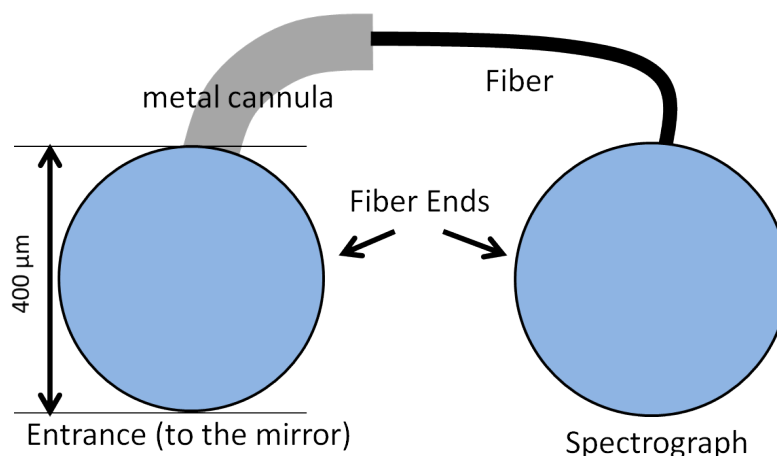


Figure 6.3: Sketch of the configuration of the fiber of the MAX-DOAS instrument (cf. Figure 6.5) used for the measurements in South Russia and Mauritania.

The MAX-DOAS instruments used in South Russia and Mauritania were designed by (Heue, 2008) for the use on an airship based on the concept developed by (Kern, 2009).

In contrast to the original design, an *Ocean OpticsTM QE65000* spectrograph with a UV-sensitive back-thinned detector (*HamamatsuTM S7031-1006*) was used instead of an *Ocean OpticsTM HR2000*.

Two identically constructed instruments were used in South Russia (section 7.1.2), one for measurements in the UV and one for the Vis. Both instruments were equipped with *QE65000* spectrographs, adjusted to wavelength ranges of 300-380 nm and 360-440 nm, respectively. The latter *QE65000* was equipped with a 100 μm entrance slit, whereas the UV spectrograph was equipped with a 50 μm entrance

slit. In Mauritania (section 7.1.3) only the UV instrument was used. The *QE65000* spectrograph has a focal length of 101.6 mm and is equipped with a 2400 lines/mm grating. Its spectral resolution is 0.62 nm (FWHM). Its detector is a CCD array consisting of 1044×64 individual pixels with a size of each $24 \mu\text{m} \times 24 \mu\text{m}$. To reduce stray light, the scanner head was equipped with optical filters. The UV instrument was equipped with a *SCHOTT™UG11* filter (2 mm thickness) and the Vis instrument with a combination of *SCHOTT™BG25* (1 mm) and *BG40* (1 mm).

The set up of the single components is shown in Figure 6.2. Scattered sun light is collected by a telescope rotatable around a horizontal axis allowing for measurements at different elevation angles α (see section 4.2). The entrance aperture has a diameter of 21 mm. Incoming light is deflected by 90° by a $25 \text{ mm} \times 25 \text{ mm}$ quartz glass prism. The telescope consists of a spherical mirror ($f = 100 \text{ mm}$) with a diameter of 25.4 mm focussing on a fiber (see Figure 6.3) with a core diameter of $400 \mu\text{m}$. The field of view was 0.2° (see Equation (6.1) below). The fiber's end is clad by a metal cannule which is attached to a 5 mm wide and 1.25 cm long aluminium plate in the optical axis at the focal plane of the mirror. The other end of the fiber is connected at the spectrograph's entrance slit via an FSMA connector.

The spectrograph was enclosed by an *Armaflex™* insulation with a recess for the spectrograph's fan. The air temperature inside the instrument housing was thermally stabilized by a thermoelectric system consisting of a heat exchanger with Peltier element and a *SuperCool™PR-59* temperature controller with constant voltage pulse-width modulation. For low and constant dark current, the detectors (*Hamamatsu™S7031-1006*) of the *QE65000s* were thermally stabilized at -10°C using their internal thermoelectric cooling systems. The optical bench of the spectrograph were thermally stabilized at $25\text{-}30^\circ\text{C}$ to avoid mechanical variations influencing the properties of the optical imaging.

The scanner head containing the quartz prism was moved by a brushless DC motor manufactured by *Faulhaber™*. The described components were controlled by an embedded personal computer of the type *Lippert™Cool LiteRunner 2* using the program *MS-DOAS* (Friess, 2008) allowing for autonomous measurements and simultaneous operation of several different instruments. The individual units are controlled and monitored by script-based commands. The instrument was supplied by a 12 V power source. The supply voltage of 5 V for the embedded PC and the *QE65000* was provided by an internal DC/DC converter (*Traco Power™TEN 60-2412*).

The instrument housing is a *Zarges™Alu-Case K 410* with the dimensions $360 \text{ mm} \times 300 \text{ mm} \times 140 \text{ mm}$.

6.3 MAX-DOAS Cape Verde and Australia

The MAX-DOAS instrument used for the measurements at Cape Verde and Australia consists of an external telescope unit and a thermally stabilized box containing the miniature spectrographs *QE6500* and *USB2000* for UV and Vis, respectively. Both are Czerny-Turner type spectrographs with an aperture ratio of $f/4$ and are manufactured by *Ocean Optics™*. For more details see e.g. OceanOptics.com.

The instrumental setup is sketched in Figure 6.4. An aluminium box ($560 \text{ mm} \times 430 \text{ mm} \times 305 \text{ mm}$) was used for the transport into and within the field and served

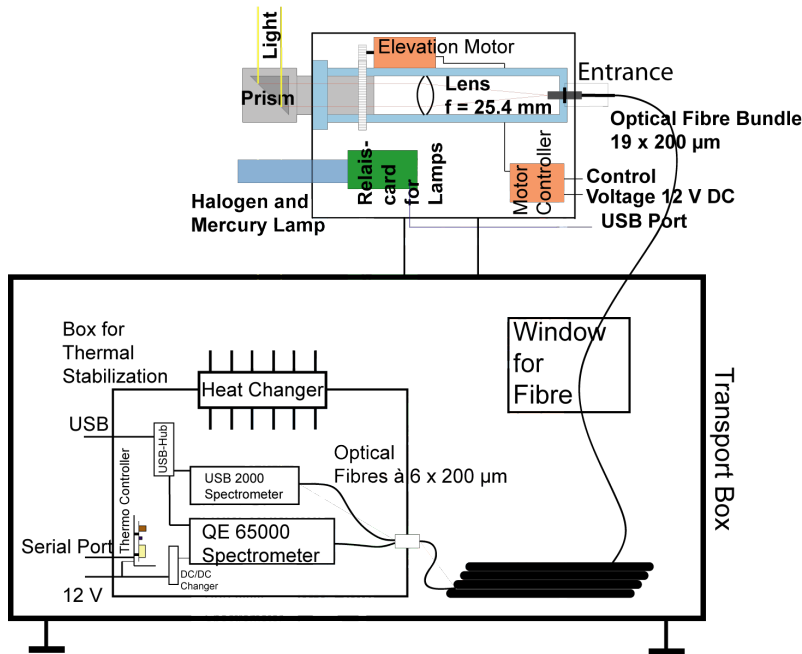


Figure 6.4: Sketch of the MAX-DOAS instrument used for the measurements in South West Australia, on the Cape Verdian island Sal, at the Kali dump and at the Bourtangier Moor.

as protection against direct sunlight, rain, and (in particular salty) dust, also for supplementary devices like the base console of a mobile weather station (*WMR 200 - Oregon Scientific™*) or the mobile ozone monitor (*Model 202 - 2B Technologies™*). At the same time, adequate air circulation for the inner box could be allowed for by small windows on each side of the transport box or a partially opened lid.

The telescope unit is similar to that described by Grossmann (2010), cf. section 6.6: The telescope consists of a fused silica lens with a diameter of 25.4 mm and a focal length of 100 mm yielding an f-number of $f/\# = f/d = f/3.9$.

Light is transmitted from the telescope to the spectrographs by an 8 m long fiber bundle. The entrance of the optical fibre bundle has a total diameter of 1.1 mm and consists of 19 single solarization stabilized fibers with a core diameter of 200 μm (+20 μm cladding) and a numerical aperture of 0.22 ($f/\# \approx 3$), from which 12 single fibers were used in the described set up. Directly in front of the entrance of the fiber a 3 mm *BG3* filter (*SCHOTT™*) was attached. Light was fed into each spectrograph by 6 fibers formed as a slit with a total height of 1.3 mm, see Figure 6.5. The resulting fields of view are according to Equation (6.1) 0.4° and 0.6° for the UV and Vis, respectively.

It should be noted that this slit exceeds the height of the *USB2000*'s detector by a factor of ~ 100 . This is only partly compensated by a collimator lens inside the *USB2000* and might cause unknown spectral structures by stray light.

Depending on environmental temperatures, the air inside the inner instrument box containing the spectrograph (30 cm \times 30 cm \times 15 cm) was stabilized at 20-25°C using the air-to-air heat exchanger *TE ASSEMBLY 12V DC* and thermal controller

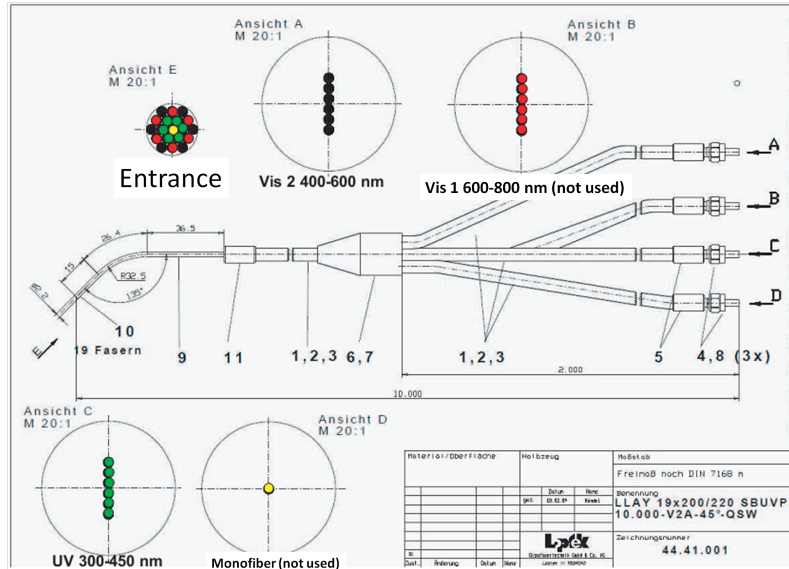


Figure 6.5: Sketch of the configuration of the fiber bundle of the MAX-DOAS instrument used for the measurements in South West Australia, on the Cape Verdian island Sal, at the Kali dump and at the Bourtangner Moor. Adapted from Tschritter (2012b).

unit *TC-XX-PR-59* by Laird TechnologiesTM (former *SupercoolTM*). The detector of the *QE65000* (HamamatsuTM *S7031-1006*) was thermally stabilized at -10°C using its internal thermoelectric cooling system.

The instrument was operated by a netbook (*ASUSTM Eee PC 1016P*) using the software *MS-DOAS* (Friess, 2008).

6.4 MAX-DOAS Masada 2002

The instrumental system used for the measurements at Masada in 2002 by Zingler (2002) is described by Hönninger (2002, p.100 ff.): The telescope consists of a fused silica lens with a focal length $f=100$ mm and a diameter $d=30$ mm and can be moved to different elevation angles by a linear stepper motor, see Figure 6.6. The light is fed into the spectrograph via a round bundle of 25 individual quartz fibers (core diameter $100\ \mu\text{m}$) with a total diameter of 0.8 mm. The entrance of the fiber is formed as a slit with a height of 2.5 mm. The field of view (FOV) of the instrument calculated by the diameter of the entrance opening and the focal length is 0.92° , see Equation (6.1). The Czerny-Turner spectrograph ACTON Spectra Pro 275 with a focal length of 275 mm (collimating mirror) and 310 mm (focussing mirror) and an aperture ratio of $f/3.8$ was used. The grating was 1200 grooves/mm and the linear dispersion $2.46\ \text{nm/mm}$ (or $0.062\ \text{nm/pixel}$). For recording the spectra, a 1024 pixel photodiode array detector (PDA) was mounted in the focal plane of the spectrograph. The spectra were recorded by a 1024 pixel photodiode array detector (PDA) mounted in the focal plane of the spectrograph.

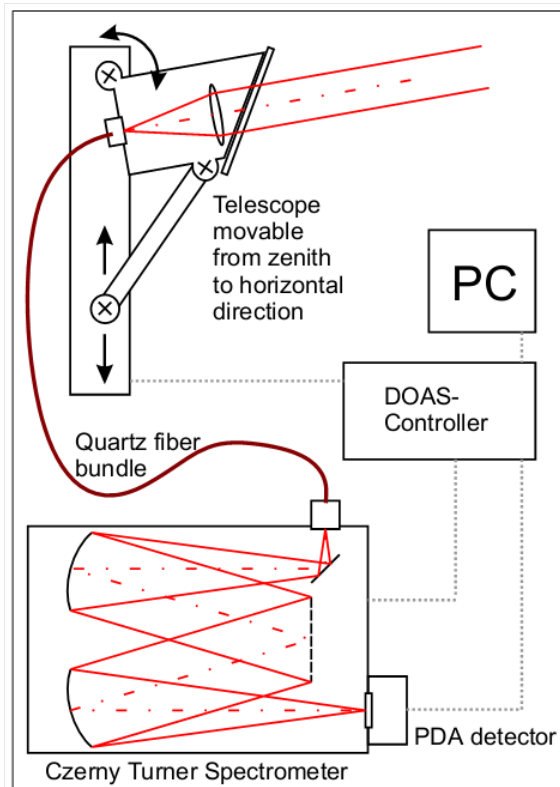


Figure 6.6: Simplified sketch of the MAX-DOAS instrument used for the measurements at Masada, Dead Sea in 2002. (Hönninger, 2002)

The instrument was operated by a personal computer using the software *MFC* (Gomer et al., 1993).

6.5 MAX-DOAS Masada 2012

The MAX-DOAS instrument used at Masada in 2012 is a modified version of the instruments described above in section 6.2.

The mirror optics were replaced by a lens system. The advantage of this system is that the entrance end of the fiber is readily positioned by a FSMA coupling on the optical axis, which is resistant to shocks and vibrations during the transport and, with regard to replacement or substitute issues, fibers with FSMA ends are more common than those with cannule ends.

On the other hand, using a lens system implies a wavelength dependent focal length due to dispersion and thus a wavelength dependent field of view. Therefore the distance between lens and fiber entrance should be chosen so that the average FOVs of different spectrographs resemble each other. The FOV of the instrument will be shown in section 6.5.3.

Furthermore the spectrograph *QE65000* was replaced by two *Avantes™ AvaBench-75* spectrographs for UV and Vis. The specifications are:

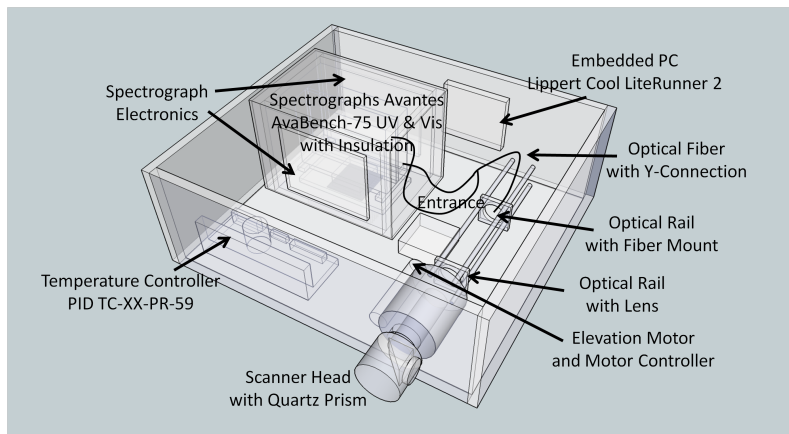


Figure 6.7: Sketch of the MAX-DOAS instrument used at Masada, Dead Sea in 2012.

UV and Vis

- optical bench with *ultra-low stray light design*
- 75 mm focal length
- 100 μm entrance slit
- Microprocessor Board, 16 Bit, AD, USB2.0, small design
- Connector cable ASM-5216 to USB2
- special demand *Uni Heidelberg Spezial*:
 - FWHM variation in nm smaller than 12.5%
 - FWHM not smaller than 5 pixels

ULS2048x64 (UV)

- *Hamamatsu*TM detector (2048 pixels, 14 μm \times 895 μm)
- UD grating 295 nm-450 nm
- optical filter *BG3* (7 mm \times 7 mm \times 1 mm) at entrance slit

ULS2048L-U2 (VIS)

- *Sony*TM 2048L detector (2048 pixels, 14 μm \times 200 μm)
- VD Grating 430 nm-565 nm
- UV/VIS collector lens for enhanced sensitivity for 200 nm-1100 nm

The *BG3* optical filter by *SCHOTT*TM is used to reduce stray light.

With respect to the instrument described in section 6.2 the heat removal from the spectrographs was improved by a grommet between the mounting of the spectrographs and the cooling radiator on the underside of the housing. In the former setup the heat was transferred less efficiently through the aluminium housing to the

cooling radiator. Another modification was made to the thermo electric system. By connecting a damping resonant circuit between thermo controller and Peltier element electric interferences are reduced and at the same time the Peltier element is operated more efficiently (Platt, 2009; DiSalvo, 1999).

Light collected by the telescope is conducted to the two spectrographs by a Y-shaped optical fiber bundle consisting of 7 single fibers with a core diameter of $200\ \mu\text{m}$ and a total diameter of $220\ \mu\text{m}$, see Figure 6.8. On the entrance end, the fibers are arranged alternating and circularly with an effective diameter of $550\ \mu\text{m}$ for each branch. The end connected to the spectrographs are arranged as slits with a total height of $660\ \mu\text{m}$.

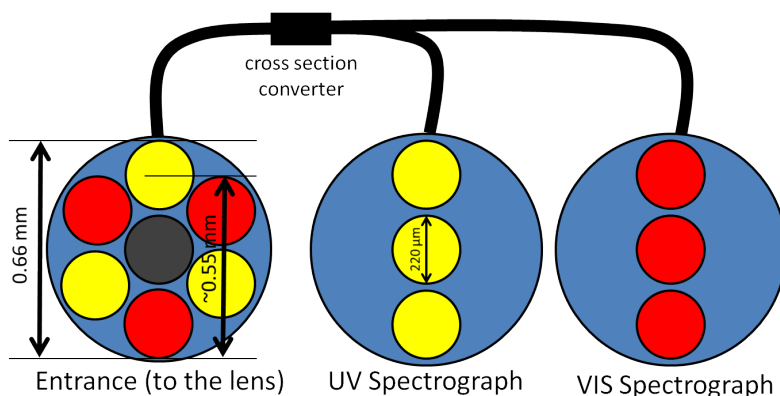


Figure 6.8: Sketch of the configuration of the fiber of the MAX-DOAS instrument used for the measurements at Masada, Dead Sea in 2012.

During the first days different ground potentials in front of and behind the DC/DC converter (12 V/5 V) in the MAX-DOAS caused communication problems at least between the embedded PC and the two *Avantes*TM spectrographs. This problem did not occur during test measurements at the Institute of Environmental Physics, probably because of an inadvertent short-circuit between USB ground and the grounded housing of the MAX-DOAS. Bypassing the ground potential at the DC/DC converter during the campaign stabilized the system.

6.5.1 Offset and Dark Current

Offset and dark current spectra are needed to account for signal contributions due to thermal electrons and artificial electrical offset signals in the recorded spectra. For more details on dark current and electrical offset see (e.g., Platt and Stutz, 2008; Friess, 2001).

Offset and dark current spectra of the described *Avantes*TM *AvaBench-75* spectrographs are shown in Figures 6.9 and 6.10. The shown dark current spectra are corrected for electrical offset.

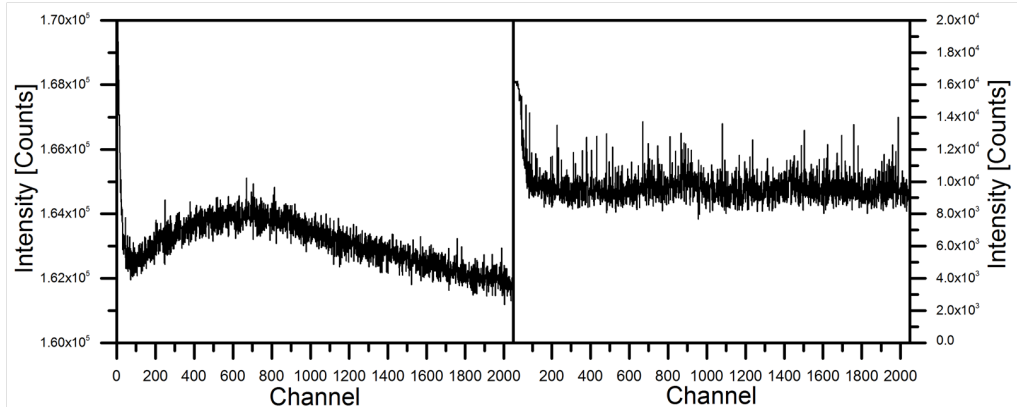


Figure 6.9: *Offset (left panel) and Dark Current (right panel) signal of the UV spectrograph for a detector temperature of 20°C (operating temperature). Offset was recorded with 1000 scans à 3 ms exposure time. Dark Current was recorded with 1 scan and an exposure time of 60000 ms.*

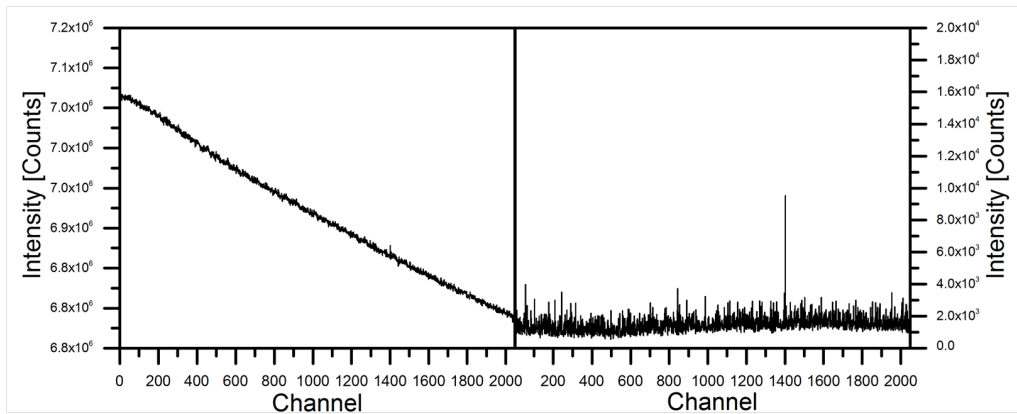


Figure 6.10: *Offset (left panel) and Dark Current (right panel) signal of the Vis spectrograph for a detector temperature of 20°C (operating temperature). Offset was recorded with 1000 scans à 3 ms exposure time. Dark Current was recorded with 1 scan and an exposure time of 60000 ms.*

6.5.2 Instrument Function

The knowledge of the instrument function is crucial for a DOAS analysis, since cross sections given by literature are in general recorded with a different, in most cases higher, spectral resolution than that of the instrument used for the DOAS measurement. Therefore literature cross sections need to be convolved by the instrument function for the spectral retrieval. The instrument function can be obtained by recording a spectral structure with a spectral width which is small compared to the spectral resolution of the spectrograph. The ideal spectral structure for this purpose would be a delta peak. A common method to obtain the instrument function is to spectra from elements with known emission lines, e.g. from mercury vapor lamps. Using atomic emission lines, the instrument function can be measured only at cer-

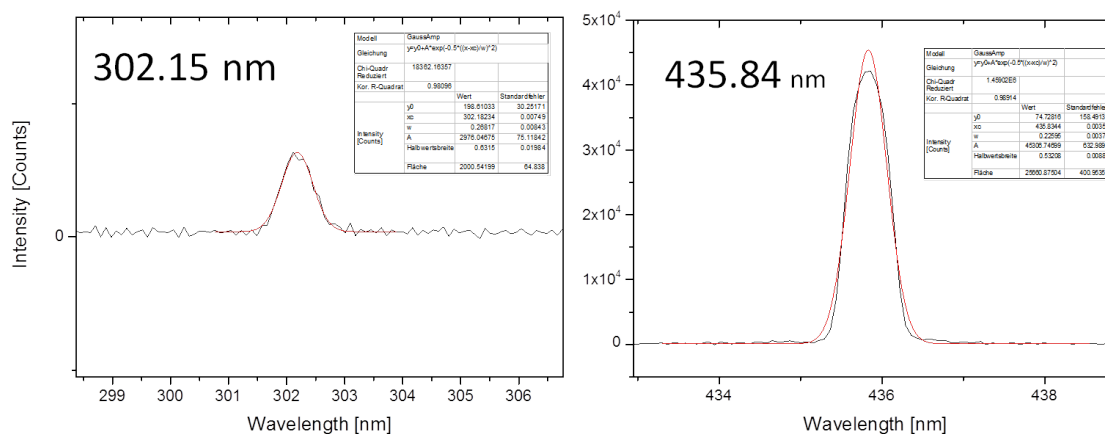


Figure 6.11: Mercury emission line spectra measured by the UV spectrograph at 20°C optical bench temperature with a fitted Gaussian distribution.

tain wavelengths. Therefore the shape and spectral width of the instrument function should not vary between the wavelength position of an emission line and the spectral wavelength interval used for the DOAS retrieval. For more details on the instrument function see (e.g., Platt and Stutz, 2008).

Different emission lines of mercury with FWHM recorded with *AvantesTM AvaBench-75* spectrographs for UV and Vis are shown in Figures 6.11 and 6.12, respectively and in Table 6.1.

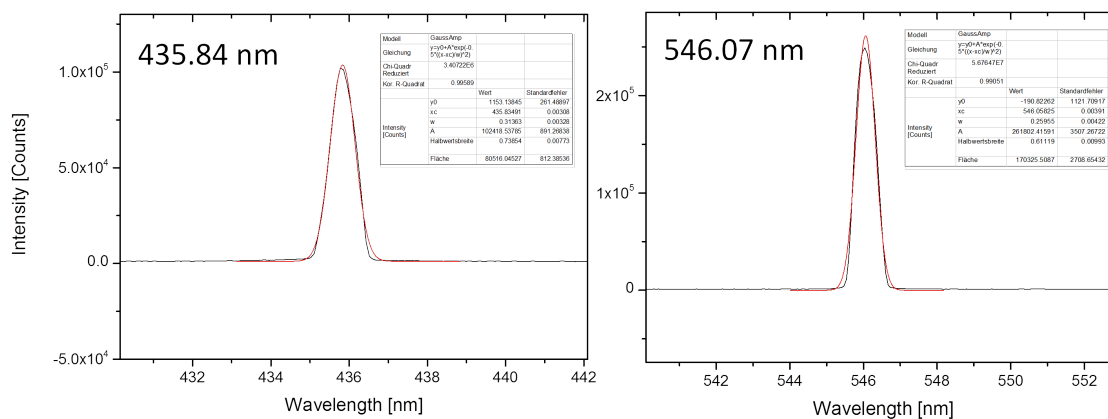


Figure 6.12: Mercury emission line spectra measured by the Vis spectrograph at 20°C optical bench temperature with a fitted Gaussian distribution.

6.5.3 Field of View

To determine the field of view of the instrument and to calibrate the viewing direction, a staff-shaped fluorescent lamp was set up in the laboratory at a distance

Table 6.1: FWHM of the mercury emission lines measured by the UV and Vis spectrograph, see Figures 6.11 and 6.12.

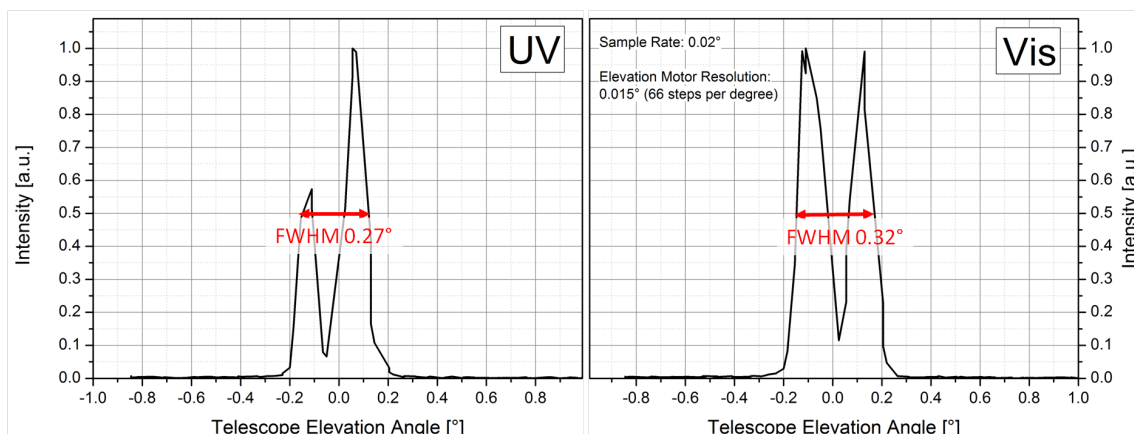
mercury line [nm]	FWHM [nm]	FWHM [channels]
UV		
302.15	0.63	7.1
435.84	0.53	7.5
Vis		
435.84	0.74	8.9
546.07	0.61	9.7

of 5 m from the telescope aperture. The lamp was orientated horizontally and equipped with an aperture, so that only a bright strip with a height of 3 mm ($\hat{=}$ 0.03°) remained. The lamp was aligned horizontally using a laser spirit level. To determine the vertical field of view (FOV) of the instrument the telescope elevation was changed iteratively in steps of 0.02° for $\alpha \in [-1^\circ, +1^\circ]$ crossing the lamp while recording spectra at short integration times. The normalized intensities averaged over the spectral range of the two spectrographs are shown in Figure 6.13.

The theoretical field of view α_{FOV} is given by:

$$\alpha_{FOV} = 2 \cdot \arctan\left(\frac{d/2}{f}\right), \quad (6.1)$$

with d being the vertical diameter of the entrance in the telescope and the focal length of the lens f . With $f = 125$ mm and $d = 550$ μm (see Figure 6.8) the resulting theoretical α_{FOV} for the telescope is 0.25° which is in good agreement with the measured value of approximately 0.3° indicated in Figure 6.13 for the two spectrometers. The reason for the two peaks is the fiber configuration depicted in Figure 6.8.

**Figure 6.13:** Vertical field of view for the spectrometers UV and Vis. The intensity is normalized to the maximum of the distribution.

6.6 MAX-DOAS Ein Bokek

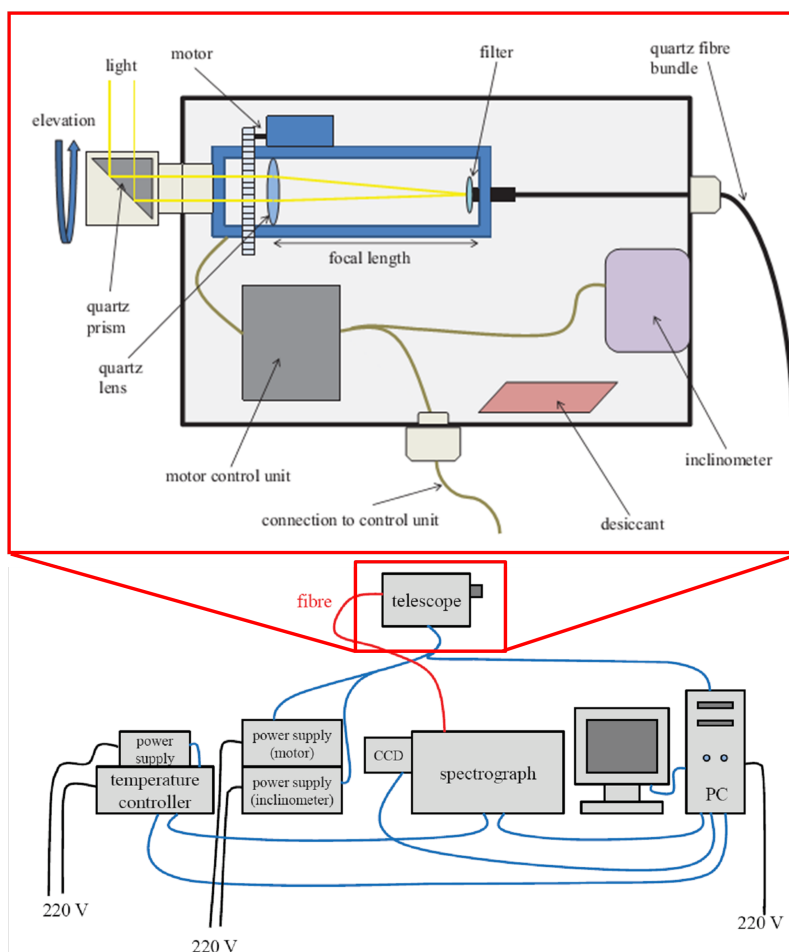


Figure 6.14: Sketch of the MAX-DOAS instrument used in Ein Bokek, Dead Sea in 2012. Adapted from Grossmann (2010).

The MAX-DOAS instrument used at Ein Bokek consists of a telescope unit, a spectrograph unit and a quartz fiber bundle transferring the light collected by the telescope to the spectrograph. The instrument is controlled by a personal computer using *MS-DOAS* (Friess, 2008).

The telescope unit consists of a rotatable quartz prism (25 mm × 25 mm) which is moved by a *Faulhaber*TM brushless DC motor to adjust the telescope elevation angle α . Light entering the telescope is focussed by a fused silica lens with the focal length $f = 100$ mm and a diameter of 21.4 mm on the entrance of the fiber bundle. The resulting f-number is $f/\# = f/4.67$.

The fiber bundle has a length of 13 m and consists of 37 single fibers with total diameters of 120 μm (core diameter is 100 μm). The entrance end is arranged as a circle with a total diameter of 840 μm and an effective diameter of 800 μm . The end connected to the spectrograph is arranged as a column with a total height of 4.44 mm serving as entrance slit of the spectrograph.

The spectrograph used in this work is an *ActonTM300i* with a focal length of 300 mm and an f-number of f/4. It covers the wavelength interval from 327 nm to 470 nm. A back-illuminated CCD is used as detector. The optical bench is thermally stabilized by a temperature control unit.

The CCD camera used in this MAX-DOAS setup is manufactured by *AndorTMTechnology* (model *DU 440-BU*). The CCD consists of 2048×512 pixels with a pixel size of $13.5 \times 13.5 \mu\text{m}$.

A sketch of the set up is shown in Figure 6.14. A more detailed description can be found in (Grossmann, 2010).

6.7 LP-DOAS Ein Bokek

A detailed description of the instrument type based on fiber optics is given in (Tschritter, 2007; Merten, 2008). The specifications for the presented measurements are the following: The used spectrograph type was an *ActonSpectra300i* with a *NTE-2* CCD and a *RoperScientificTM* camera. As light source a xenon arc lamp (*Osram XBO-75*) was used. Light was coupled out into the atmosphere propagating through a $800 \mu\text{m}$ mono fiber (mode mixing) and a $6 \times 200 \mu\text{m}$ multi fiber (Y-bundle, total length 10 m) and received again by the spectrograph through the multi fiber. The Newtonian telescope had a spherical mirror with a diameter of 300 mm and a focal length of 1500 mm. For measurements around 280 nm the filter *UG-5* (*SCHOTTTM*) was used, and for measurements around 430 nm the filter *B390* (*HOYATM*). The mirror was flushed with filtered air to avoid contamination. (Schmitt, 2012) A sketch of the set up is shown in Figure 6.15.

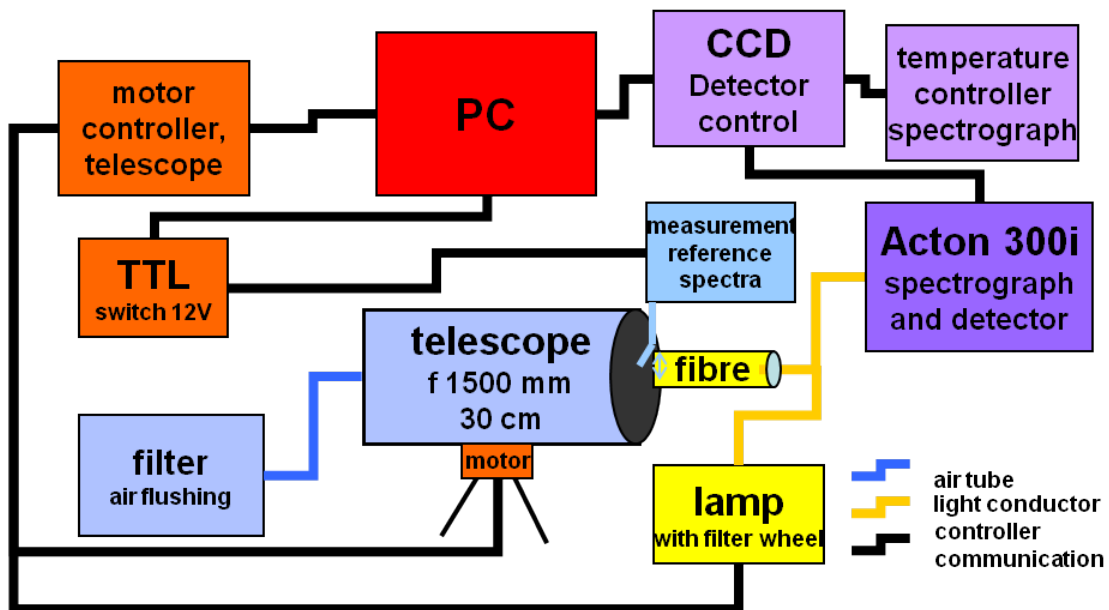


Figure 6.15: Sketch of the LP-DOAS measurement set up. Adapted from Tschritter (2012a).

The measurement sequence used for the LP-DOAS is depicted in Figure 6.16. The sequence is executed automatically by the program *COS*, described in (Pöhler, 2010). Short cut measurements are performed against an aluminium plate, which is moved by the measurement routine directly in front of the emitting and receiving optical fiber bundle, see Figure 6.15. The short cut measurements do not contain a significant contribution by atmospheric absorbers and are used as reference spectra. After a single short cut scan, four pairs of atmospheric scans and short cut scans are acquired, followed by background scans for atmospheric measurements and short cut measurements, for which the xenon arc lamp spectrum is shutted out. For more details on the set up and the application of the presented LP-DOAS instrument see (Pöhler, 2010).

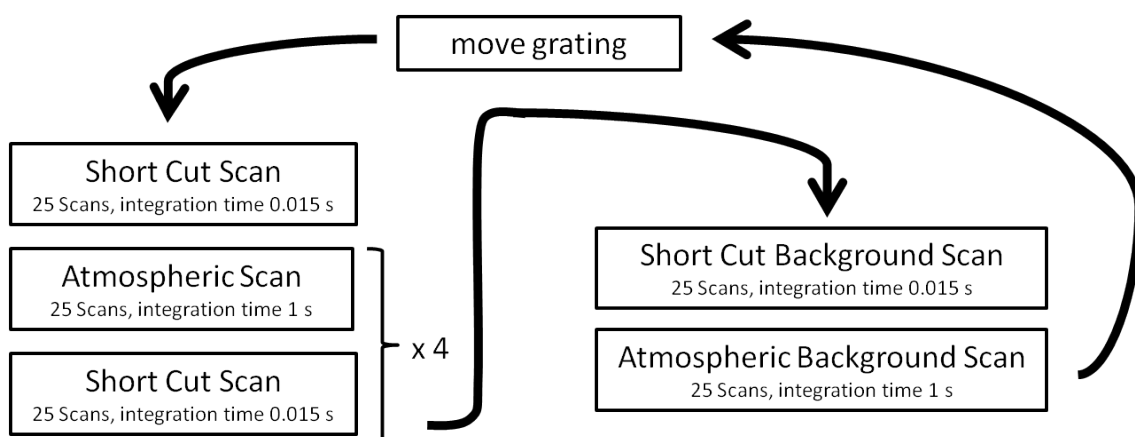


Figure 6.16: *Scheme of the LP-DOAS measurement sequence.*

6.8 IMK Weather Station

Meteorological parameters during the measurements at the Dead Sea in 2012 (section 7.1.6) presented and discussed in section 9.1 were acquired by the Karlsruhe Institute for Meteorology and Climate Research (IMK-TRO). IMK-TRO operates two weather stations at the measurement site, from which data during our campaign was kindly provided to us by Prof. Dr. Christoph Kottmeier and Dr. Ulrich Corsmeier. The position of the weather stations *Masada Top* and *P-88* are shown in 7.11). *Masada Top* is situated at an elevated position close to the top of the mesa Masada (see section 7.1.6). *P-88* is situated at the pumping station P-88 operated by the Dead Sea Works company (see section 7.1.6).

Characteristics and data of the stations are given in at http://imkbemu.physik.uni-karlsruhe.de/~ws_masada/ and http://imkbemu.physik.uni-karlsruhe.de/~ws_p88/index.html:

- weather station Masada Top, (N 31.319 E 35.348)
 - 3-component wind measurements (u,v,w) by propeller anemometer at 9 m height (Gill)

- temperature measurement at 2 m and 9 m height (HMP 35)
 - humidity measurement at 2 m and 9 m height (HMP 35)
 - total radiation from upper and lower half space (Schulze)
 - short wave radiation from upper and lower half space [Albedometer] (Kipp und Zonen)
 - air pressure (Setra)
 - soil heat flux (Rimco HP3)
 - Campbell data logger with multiplexer and GSM data link
 - precipitation measurements (Hellmann) [0.2 mm]
 - soil surface temperature sensor (KT 15)
 - dust measurements (mass concentration, Beta-meter)
- weather station at Dead Sea Works Pumping station P-88, (N 31.329 E 35.401)
 - 3-component wind measurements (u,v,w) by propeller anemometer at 3,5 m height (Gill)
 - temperature measurement at 2 m and 0.5 m height (HMP 35)
 - humidity measurement at 2 m and 0.5 m height (HMP 35)
 - total radiation from upper and lower half space (Schulze)
 - short wave radiation from upper and lower half space [Albedometer] (Kipp und Zonen)
 - air pressure (Setra)
 - soil heat flux (Rimco HP3)
 - Campbell data logger with multiplexer and GSM data link
 - precipitation measurements (Hellmann) [0.2 mm]
 - soil surface temperature sensor (KT 15)

Both stations are operated with a measuring interval of 10 min and data is transferred from Israel to Germany every 24 h (Corsmeier and Kottmeier).

Chapter 7

Field Studies

In this chapter, the eight field studies carried out during this work (within the scope of the DFG project Haloproc) will be described. The general objective of the field work was to study the tropospheric chemistry of halogen oxides in the vicinity of salt lakes, salt surfaces or saline soil. Both, traditional active long path DOAS and Multi-Axis-DOAS (see section 4) were applied in the field. Field campaigns were conducted at a variety of salt lakes, solar salt ponds and other areas with high halogen content. The locations were in Botswana, Southern Russia, Mauritania, Cape Verde, Australia and Israel (see Table 9.2) between June 2008 and May 2012. By these campaigns the existing data base on reactive halogen release from salt lakes previously encompassing three lakes (Great Salt Lake, USA (Stutz et al., 2002); Dead Sea, Israel (Hebestreit, 1999; Matveev, 2001; Tas, 2005; Zingler and Platt, 2005) and Salar de Uyuni, Bolivia (Hönninger et al., 2004)) was significantly expanded.

- In June 2008 the ground-level concentrations of BrO, IO, O₄ and NO₂ were measured above the Walfish Bay (Namibia) and Sua Pan (Botswana) (Buxmann, 2008).
- A measurement campaign in Southern Russia was performed in August 2009. The ground-level concentrations of BrO, IO, ozone and other trace gases above the salt lakes El'Ton, Baskuntschak and the surrounding steppe were measured.
- The third campaign was performed in Mauritania in November/December 2009 in cooperation with the BMBF project SOPRAN. In addition to MAX-DOAS measurements, a long-path DOAS instrument was employed in order to measure the ground-level concentrations at the salt pan Sebkha N'Dramcha and close to a sea weed field at Poste Iwik in a coastal area. The measurements at Sebkha N'Dramcha will be presented in this work.

These represent the first atmospheric measurements of RHS-relevant trace gases at the named salt lakes.

- In May 2012 a three-week campaign at the Dead Sea in Israel was conducted. The evaluation of data and the results from the field studies will be presented in chapter 9.

- Additionally two short campaigns in Germany were performed at sites with potential release of halogen species (7.2), a dump consisting of potash salts, called Kali dump, and at the peatland Bourtanger Moor.

7.1 Salt Lakes and Salt Pans

In this section, the measurement sites at the examined salt lakes will be presented. Short summaries will be given on the salt lakes' locations, sizes, origin of their salt and the meteorological conditions prevailing during the measurement periods. The Dead Sea will be discussed in more detail.

7.1.1 Botswana 2008

In June 2008 MAX-DOAS measurements were performed at Sua Pan in Botswana. Sua Pan is one of two salt pans being part of the Makgadikgadi salt pan complex. The complex is an ephemeral salt lake¹. With large inter-annual fluctuations Sua Pan can get covered with water during the wet season from November to April (Schulze, 1972). Sua Pan alone has a surface area of approximately 3400 km², the spare complex covers additional 10000 km². Beside the Salar de Uyuni and Etosha Pan in Namibia it is one of the largest salt pans in the world.

A MAX-DOAS instrument (Type MiniDOAS, for a detailed description see e.g. Hönninger et al. (2004)) was set up at Sua Pan on the afternoon of 23 June 2008 at S 20.4826 E 26.06 with viewing direction north, see Figure 7.1. The salt surface was reddish, indicating the presence of the halophile micro-algae *Dunaliella salina*.

Meteorological Conditions

The weather during the measurement period is described by Buxmann (2012b) as sunny and hot with wind coming from the north. Meteorological parameters derived from HYSPLIT (Draxler and Rolph, 2003) based on data by EMC: Data Assimilation Team show ranges of 8.1-9.3% relative humidity, solar irradiation declining from 815 W/m² at 13:00 UTC to 489 W/m² at 17:00 UTC and ambient temperatures between 48°C and 37°C.

7.1.2 South Russia 2009

A measurement campaign in Southern Russia (administrative districts Volgograd and Astrakhan) was conducted in August 2009. Measurements were performed at the salt lakes El'Ton, Baskuntschak and a smaller salt lake at Kasin using MAX-DOAS (see section 6.2). Also a background measurement in the surrounding was performed, which is classified as steppe or semi-desert. The area is part of the Botkul-Bulukhta Depression within the Caspian Lowland, which is a remnant of the prehistorical sea Parathetys. The salt deposits originate from the Caspian at its former higher stand (Grabau, 1920).

¹A lake which is filled with water only transitory due to seasonal or annual variations in precipitation.

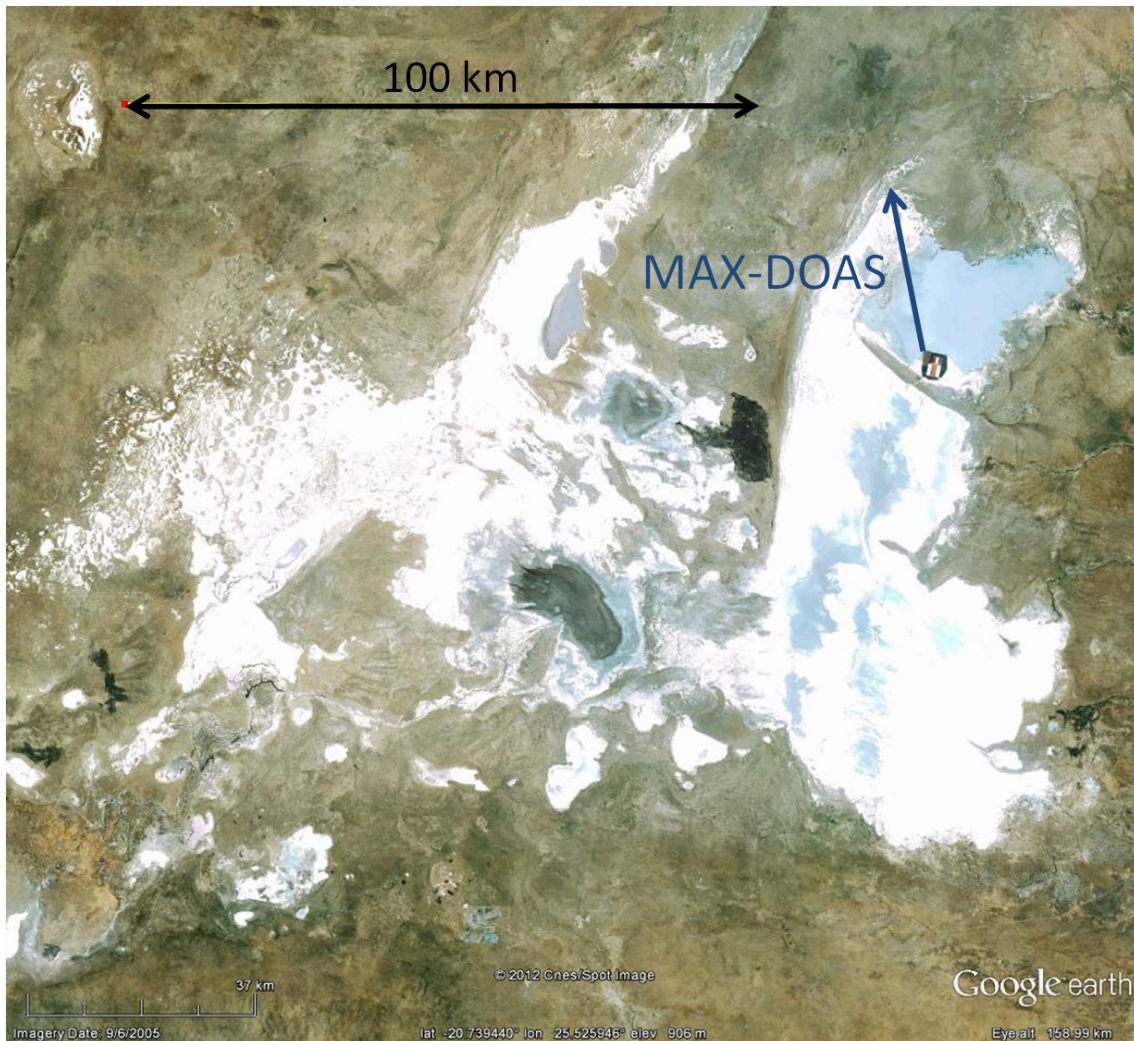


Figure 7.1: *Position of MAX-DOAS measurements performed at Sua Pan, Botswana.*

Measurement Sites

Lake El'Ton is situated 160 km in the northwest of Volgograd and has a surface area of around 185 km². The lake was used for salt production between the 18th and 20th century and is contemporarily still used for sanatorium purposes. Water added newly to the lake by numerous small streams dissolves salts from the bottom of the lake (Grabau, 1920) originating from salt-domes penetrating to the terrain's surface (Makarov and Matalin, 2009). Grabau (1920) states that on the whole its water surface remains stationary over the year with minor variations due to snow in the spring and rain in October indicating a balance between inflows and evaporation. During the presented measurement campaign approximately the half area of the lake was filled with a water body of several 10 centimeters. Its salinity is given by Grabau (1920) with values between 255 and 390 permille (corresponding to 255 and 390 g/kg, respectively). The MAX-DOAS measurements at Lake El'Ton were performed on 25 and 26 August 2009.

Lake Baskuntschak is situated 93 km in the south of Lake El'Ton at the foot of the hill Bobsoj-Bogdo and has an area of around 130 km². It is used for salt production and health issues. The purity of its salt in terms of NaCl excels that of Lake El'Ton due to a lower MgCl₂ content (Grabau, 1920). It is an ephemeral lake, during dry periods the lake is covered by a solid and extensive salt crust. The MAX-DOAS measurements at Lake Baskuntschak were performed on 22 and 23 August 2009. Background measurements and measurements at Kasin were performed on 18, 20 August 2009 and 21 August 2009. The positions and orientations of the MAX-DOAS measurements are demonstrated in Figure 7.2.

Table 7.1: Overview of the MAX-DOAS measurement sites in South Russia in Figure 7.2 with pH measured in soil samples by Huber et al. (2012).

measurement site	description	pH soil	coordinates	time periods (UTC)
Lake Baskuntschak	salt crust, partly water	6.9	N 48.240541° E 46.825259°	23 Mar 04:26- 23 Mar 09:52, 23 Mar 23:42-24 Mar 10:24
Lake El'Ton	salt crust, partly water	7.7	N 49.152627° E 46.804238°	25 March 23:22- 26 Mar 05:59
Kasin	sandy, no salt crust, partly water	7.5	N 47.600348° E 47.455398°	29 Mar 03:40-31 Mar 08:04
Background	sandy and dry	-	N 47.549790° E 47.305560°	27 Mar 08:34-28 Mar 07:58

Meteorological Conditions

Temperature and relative humidity were logged with a mobile weather station (*WMR 200* by *Oregon Scientific*TM). Average temperature and relative humidity between 12:00 LT(=UTC+3h) and 18:00 LT during the whole measurement period were 26°C and 38%, respectively. Strong winds developed around noon with wind speeds of up to 25 km/h, whereas in the morning and evening wind speeds were typically 5-10 km/h. On 18 and 20 August during the background measurements it was sunny, the other days were partly cloudy.

7.1.3 Mauritania 2009

The third campaign was performed in Mauritania in November/December 2009 in cooperation with the BMBF project SOPRAN. In addition to MAX-DOAS (section 6.2) measurements a Long Path-DOAS instrument (section 6.7) was employed in order to measure the ground-level concentrations of reactive halogen species at the

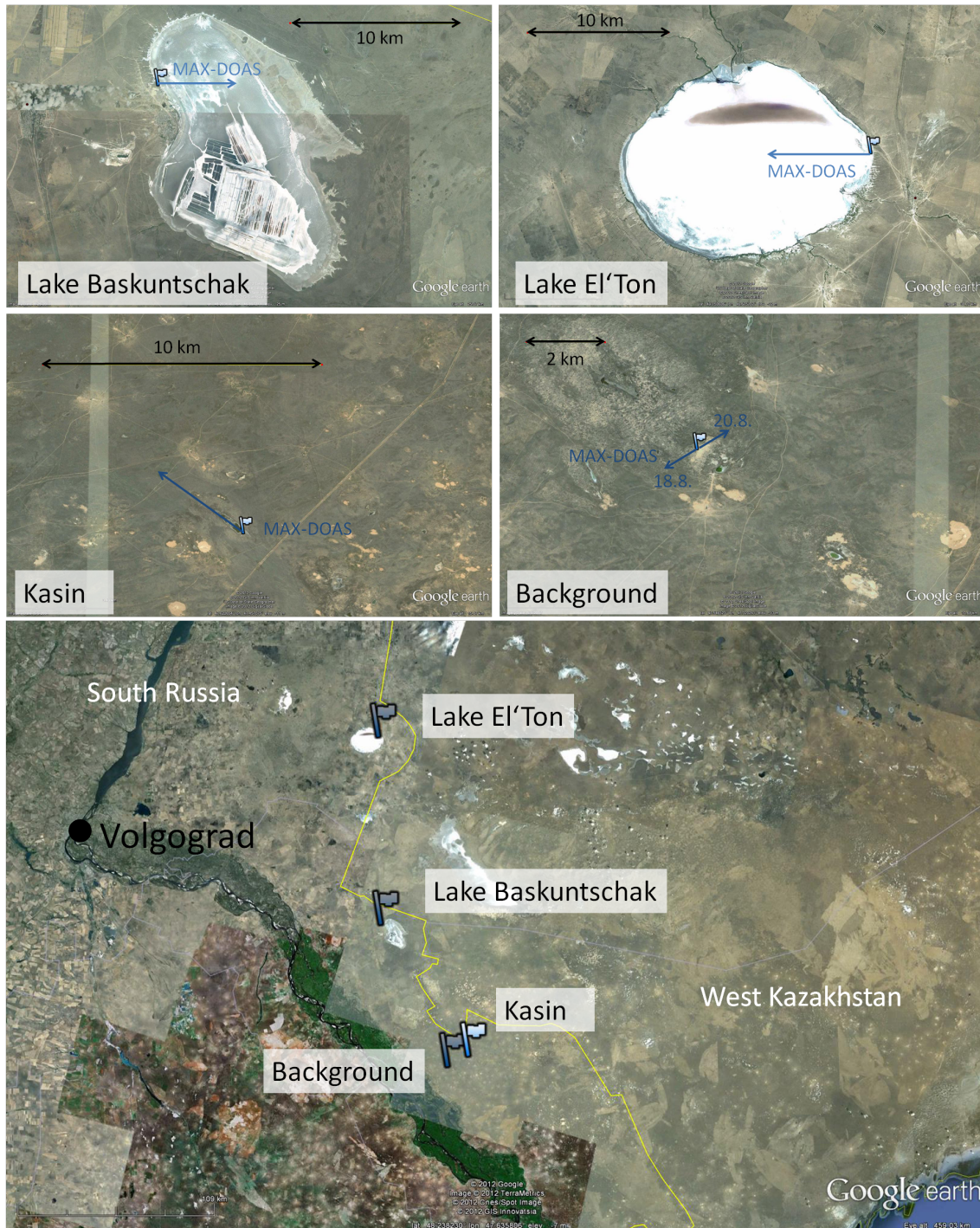


Figure 7.2: The sites where MAX-DOAS measurements were performed in South Russia.

salt pan Sebka² N'Dramcha and close to a sea weed field at Poste Iwik in a coastal

²A geologic feature in North Africa, which is a smooth, flat plain usually high in salt; after a rain the plain may become a marsh or a shallow lake until the water evaporates. Therefore sebka's belong to the ephemeral type of salt lakes and are also known as sabkha, sebcha, sebka or sibjet.

area. In the scope of this work only the conditions and results at the salt pan will be discussed.

Measurement Site

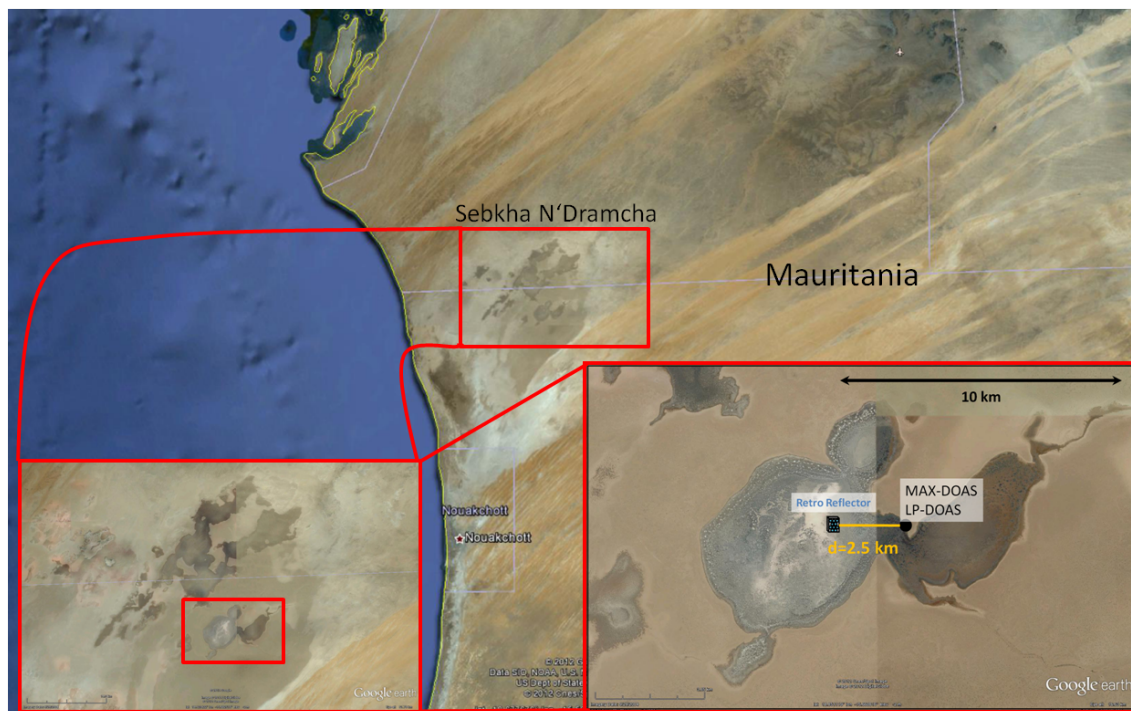


Figure 7.3: The measurement site with positions of MAX-DOAS and LP-DOAS + retro reflector at Sebkhia N'Dramcha in Mauritania. The light path of the LP-DOAS was 4 km.

Sebkhia N'Dramcha contains groups of ephemeral salt lakes and has an extent of up to 60 km and an area of around 200 km², the origin of its salt is the Atlantic ocean. It is situated around 50 km inland from the Mauritanian west coast and around 90 km in the north of the capital Nouakchott, see Figure 7.3. The whole sebkhia has an area of around 2300 km². For the presented measurements a sub-basin with an extent of 12 km and an area of 60 km² was chosen, because of its accessibility, size and patches with distinct salt crusts, see Figure 7.4. Measurements were performed between 25 November and 28 November. MAX-DOAS and LP-DOAS were set up inside the pan at N 18.858 E 15.656 orientated towards west. The distance between the retro reflector and LP-DOAS telescope was 2490 m and therefore the length of the light path was 4980 m.

Meteorological Conditions

During all three days of measurement easterly winds coming from the African continent prevailed. Temperatures were between 15°C in the night and 38°C peaking in the afternoon. Relative humidity was very low with maximum values of 25% in the early morning and 10-15% during the day.

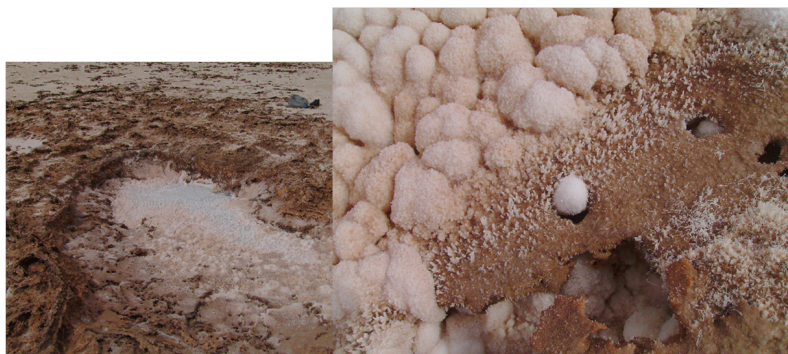


Figure 7.4: *Salt crystals at the surface of Sebkhya N'Dramcha. Exposed crystalline surfaces were constrained on patches with diameters of several meters distributed over the whole basin shown in the picture on the lower right.*

7.1.4 Cape Verde 2010

The Cape Verde Islands are repeatedly a subject to studies performed in the course of the international Surface Ocean Lower Atmosphere Study (SOLAS) project. In June 2010 the opportunity to join an intensive campaign executed by the German SOLAS subproject SOPRAN was used.

Since the 17th century salt is harvested on the Cape Verdian Island Sal. Today, there are still several solar salt ponds in operation. The origin of the salt is probably sea water intruding from below.

Measurement Sites

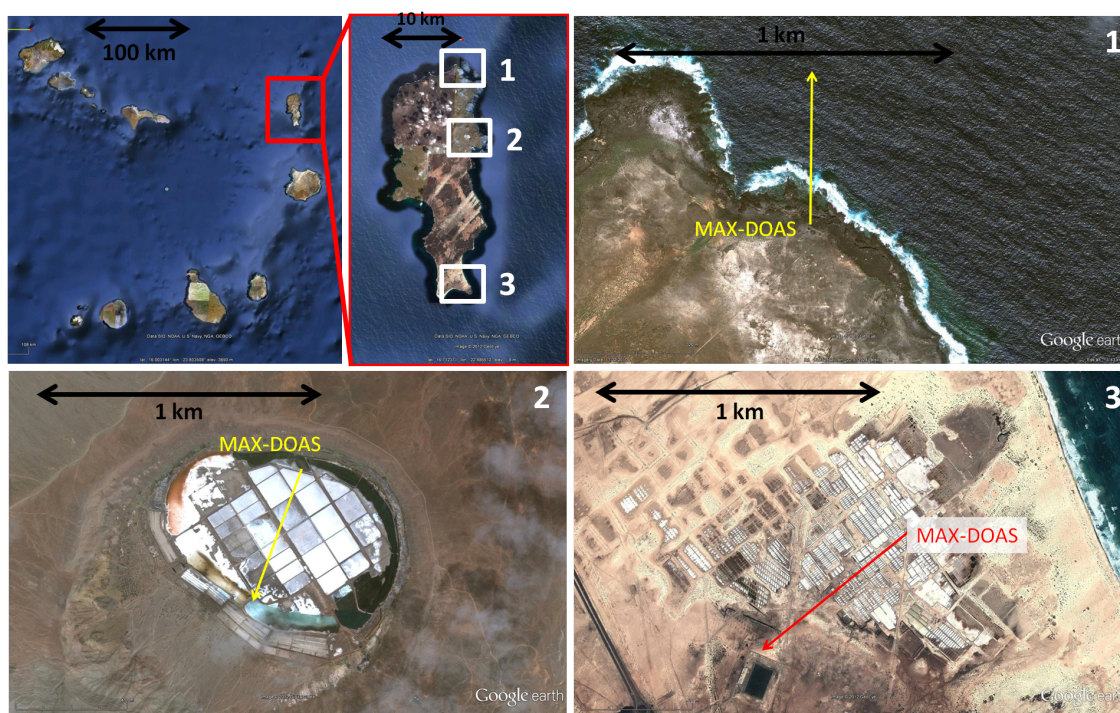
The measurement sites are shown in Figure 7.5. In particular, a salina inside a volcanic crater at Pedra Lume (2) was interesting with respect to the heterogeneous release of bromine species because of the possible acidification of brine or salt surfaces by volcanic emissions like it is proposed for the Salar de Uyuni in Bolivia (Hönninger et al., 2004) to fulfill the prerequisite of $\text{pH} < 6.5$ for the bromine explosion mechanism (see chapter 2). Furthermore we examined evaporation ponds close to Santa Maria (3). Background measurements were performed at Punte Norte (1). An overview of the measurement sites is given in Table 7.2.

Meteorological Conditions

Winds measured at Punte Norte, and Santa Maria were coming steadily from northerly to northeasterly directions with wind speeds of 8-12 km/h on 5 and 6 June 2012 and around 18 km/h on 7 June 2010. The wind direction at Pedra Lume was alternating around 90° , probably due to local turbulences. Wind speeds inside the caldera at Pedra Lume were 2-8 km/h with a distinct diurnal variation with its maximum around noon. Average daytime temperatures (12-18 LT=UTC-1h) during the whole period were 27°C . Relative humidity was 50-60% in the morning rising constantly over the day up to 80% in the evening. Trajectories calculated with HYSPLIT (Draxler and Rolph, 2003) show mesoscale winds coming constantly

Table 7.2: Overview of the MAX-DOAS measurement sites on Sal, Cape Verde.

measurement site	description	coordinates	time periods (UTC)
Punte Norte	northern coast	N 16.851621° W 22.915059°	5.6.2010 12:56-19:34, 6.6.2010 12:35-18:43
Santa Maria	solar salt ponds (in operation)	N 16.610335° W 22.902402°	7.6.2010 13:39-18:32
Pedra Lume	caldera filled with oceanic water	N 16.775758° W 22.900224°	8.6.2010 13:03-19:08, 9.6.2010 8:12-19:24, 10.6.2010 8:38-17:49

**Figure 7.5:** MAX-DOAS measurement sites on the Cape Verdian island Sal. Arrows indicate the orientation of the MAX-DOAS. (1) Punte Norte, (2) Caldera at Pedra Lume, (3) Evaporation ponds at Santa Maria.

from northeast crossing the Canarian Islands for all six days.

7.1.5 Australia 2011

As will be discussed in section 9.2 the measurements at the sites above did not reveal detectable abundances of RHS. The lakes had in common, that pH values reported from water or soil samples were alkaline. The bromine explosion mechanism (see chapter 2, reaction 2.27) needs $\text{pH} < 6.5$ to run effectively (Fickert et al., 1999). The salt lakes in South West Australia provided the opportunity to examine the pres-

ence of RHS in an area with a whole cluster of very acid lakes. Salt lakes are spread all over Australia, but in the southwest there is a particular frequent occurrence of smaller, shallow salt lakes with a wide spectrum of geochemical conditions. According to Bowen and Benison (2009) approximately 40% of the lakes and 84% of the measured groundwaters in WA are extremely acidic with $\text{pH} < 4$. The salt lakes in South West Australia are situated in a prehistoric lake and river system. Ionic ratios of the lakes seem to be related to oceanic water but the actual origin of the salt is debated (Deckker, 1983). Not long time before, Junkermann et al. (2009) discovered particle formation events above chains of smaller salt lakes, which might have been caused by the emission of reactive halogen species, in particular IO, cf. (O'Dowd and Hoffmann, 2005). In cooperation with Wolfgang Junkermann (KIT, Karlsruhe Institute of Technology) and Jorg Hacker (ARA, Flinders University), measurements were performed using a Compact LP-DOAS (Schmitt, 2012) and MAX-DOAS system (see section 6.3) at six salt lakes in the surrounding of Lake King in South West Australia, see Figure 7.6. Four of the examined lakes showed a cohesive and due to their hydrophilic properties very moist salt crust, see Table 7.3.

Table 7.3: Overview of the MAX-DOAS measurement sites in South West Australia shown in Figure 7.6.

measurement site	description	pH water	coordinates	time periods (UTC)
Lake Stubbs	moist salt crust	7.2	S 33.058612° E 118.99770°	23 Mar 04:26- 23 Mar 09:52, 23 Mar 23:42-24 Mar 10:24
Lake Orr	moist salt crust, very acid	3.1	S 33.146988° E 119.165623°	25 March 23:22- 26 Mar 05:59
Lake King	sandy and dry, no homogeneous salt crust	7.4	S 33.090258° E 119.591785°	29 Mar 03:40-31 Mar 08:04
Lake Tay	sandy and dry, no homogeneous salt crust	-	S 33.031719° E 120.740469°	27 Mar 08:34-28 Mar 07:58
Lake Chlorine	moist salt crust, "chlorine" smell	-	S 32.652212° E 119.425655°	1 Apr 02:59-2 Apr 03:39

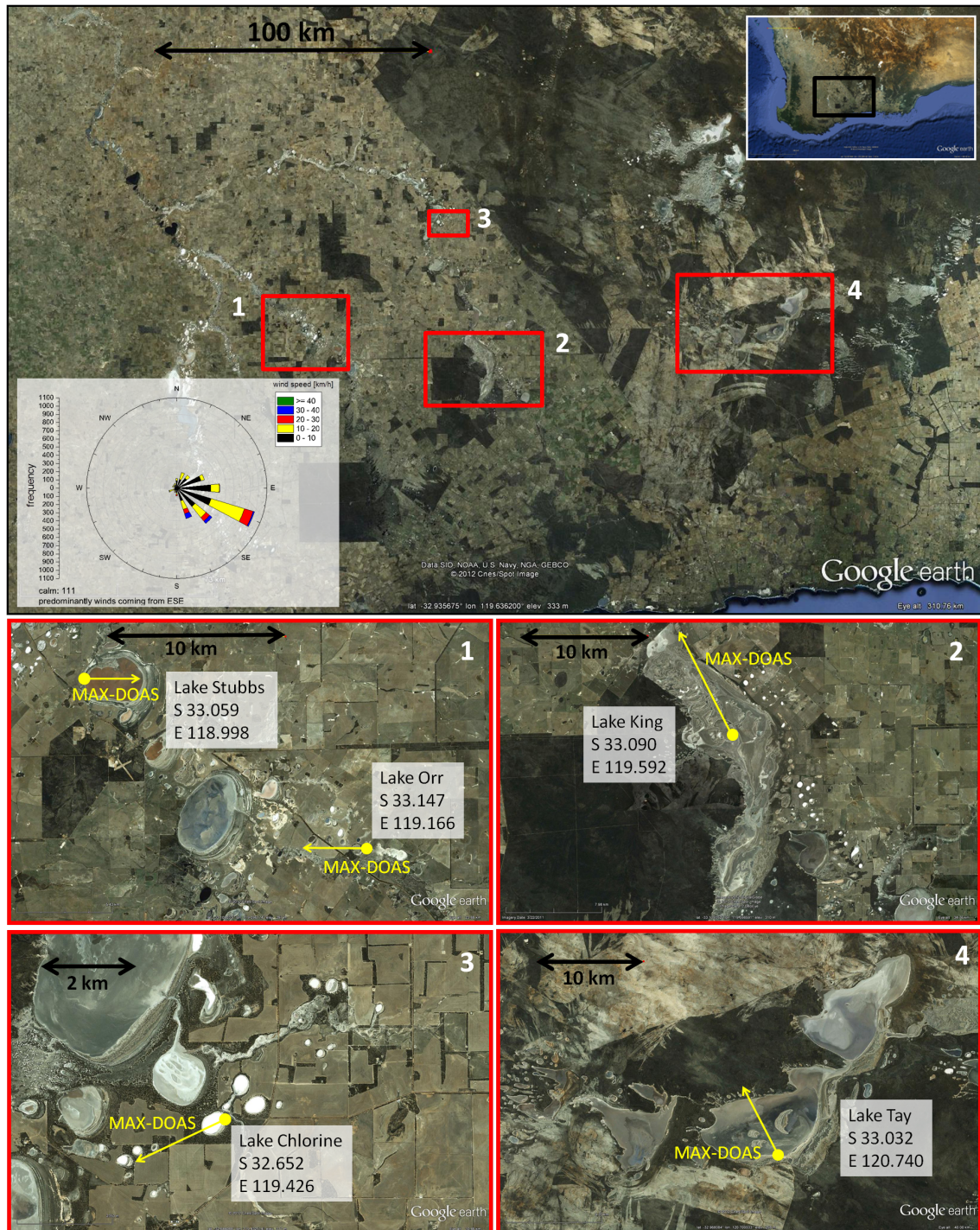


Figure 7.6: MAX-DOAS measurement sites in South West Australia with geo coordinates of the instruments position. Arrows indicate the orientation of the MAX-DOAS.

Measurement Sites

Meteorological Conditions

Meteorological parameters were measured with a mobile weatherstation (*Avantage Pro 2* by *Davis Instruments™*). Winds coming from ESE with wind speeds of up to

20 km/h prevailed, see wind rose in Figure 7.6. Daytime temperatures were between 25°C and 40°C. Relative humidity during daytime was below 50% in most cases, see Figure 7.7.

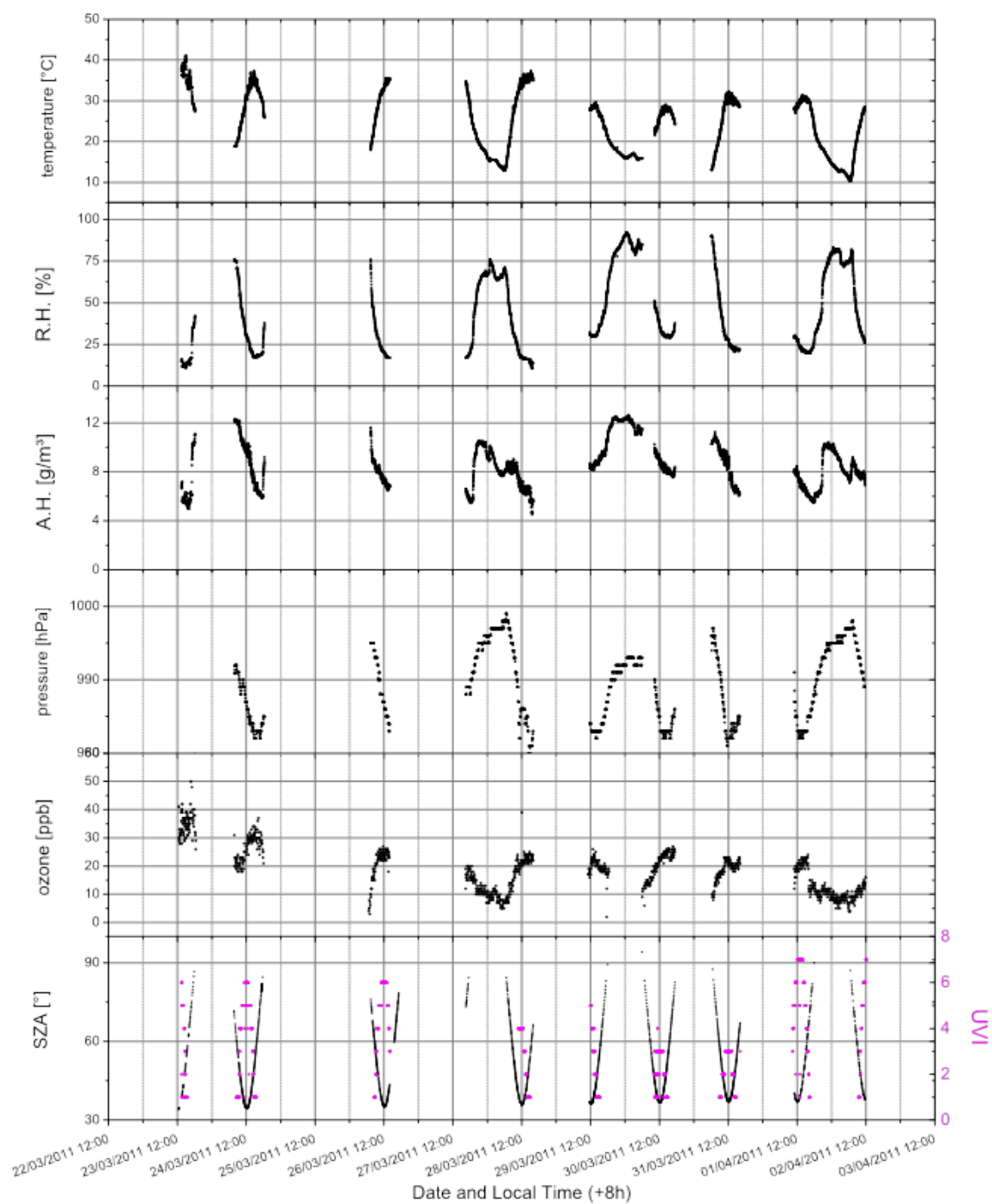


Figure 7.7: Weather and ozone data during the DOAS measurements in South West Australia between 23 March and 2 April 2011.

7.1.6 Israel 2002 and 2012

The Dead Sea - Background

The Dead Sea is a terminal lake situated within the northern end of the Great Rift Valley which divides the arabic and african plate and represents the lowest continental depression on earth (Niemi et al., 1997). The Dead Sea's surface ($810 \times 10^6 \text{ m}^2$ (ILEC, 1999)) is standing at 423 m below sea level (ISRAMAR), see Figure 7.8.

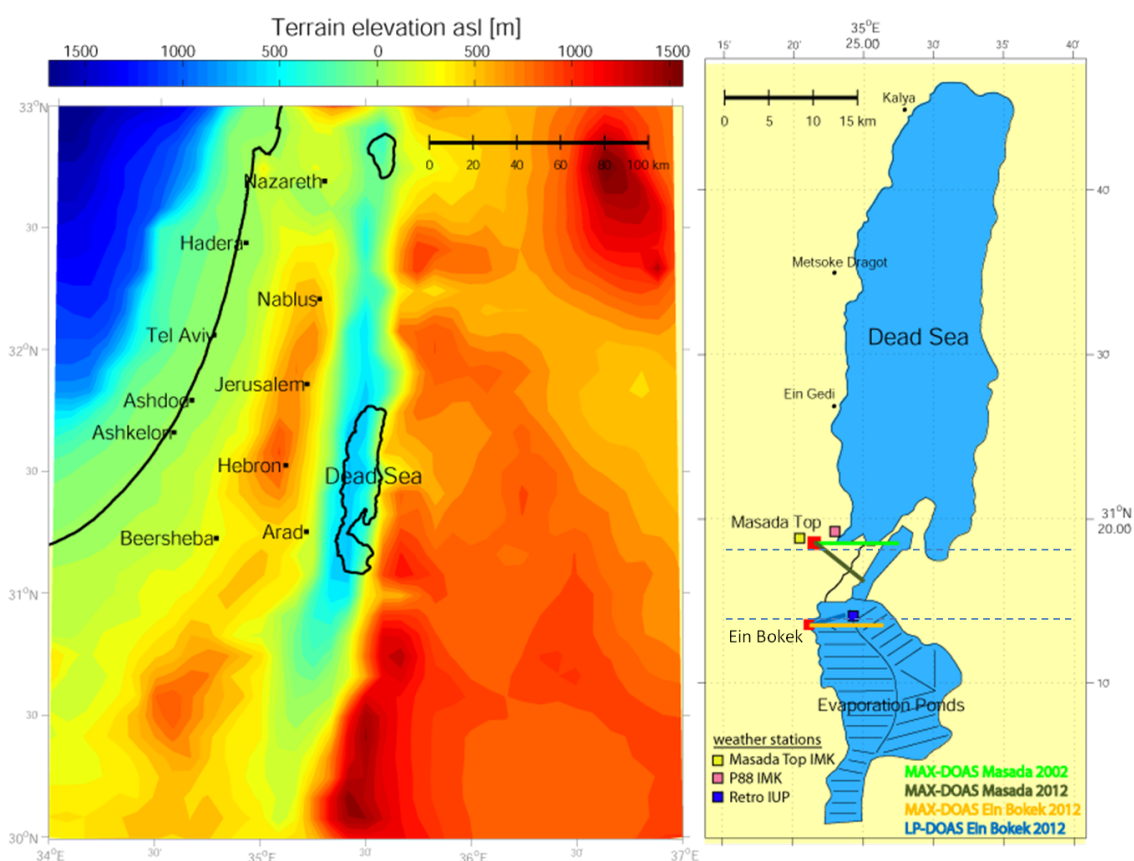
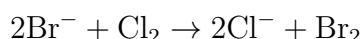


Figure 7.8: Left: Topography of the Dead Sea and its environment. The Dead Sea Valley is encompassed by the Judean Mountains in the west and the Amman Plateau in the east. Data from SRTM and NOAA (2011). Right: Outline of the Dead Sea with the location of the measurement sites Masada and Ein Bokek. The viewing directions of the MAX-DOAS and the lightpath of the LP-DOAS are indicated by the colored lines. The dashed lines indicate the position of zonal cross sections at Masada and Ein Bokek shown in Figures 7.12, 7.13, 9.23 and 9.24.

The Dead Sea brine is saturated with halite (NaCl), aragonite (CaCO_3) and gypsum (CaSO_4). With a high year-to-year variability the lake can receive fresh water in winter by inflows from flash floods and from the Jordan River runoff. Before 1979 the Dead Sea was a lake with a stable stratification (meromitic) and a permanent pycnocline at a depth of 40 m. A historical overturn in winter 1978/1979 mixed its water column due to the gradual weakening of its pycnocline by the diversion of the Jordan River (Niemi et al., 1997). The Dead Sea is assumed to be the largest reserve

of bromine in the world, with an estimated content of 1 billion tons of bromine (Lyday, 2003), and shows extraordinary bromine contents in its lake water, springs and underground waters, probably originating from fossil residual brines (Bentor, 1961).

The Dead Sea borders to Israel and the West Bank in the West and Jordan in the East. Since the 1980s (Klein and Flohn, 1987) it consists of two separated parts due to a lowering water level. Since the early 1930's the Dead Sea's water level has been lowering on average by 0.7 m per year (Al-weshah, 2000) and is predicted to lower further to 500 m below mean sea level assuming present climate conditions (Krumgalz, 2000). The border line between Israel and Jordan divides the southern part along a driveable dam. The southern part is divided into a cascade of evaporation ponds by Israeli and Jordan chemical companies to extract potash and other minerals. The water level of the southern part is artificially conserved and is even increasing due to the accumulating salt deposit. The western side is operated by the Israeli Dead Sea Works Company, an affiliate company of ICL fertilizers which makes Israel the second-largest producer of bromine compounds in the world, ranking after the USA (Kesner, 1999). The Dead Sea Works run bromine and chlorine plants directly at the southern part of the Dead Sea at Sdom where Cl_2 is obtained by electrolysis and Br_2 by the treatment of the bromide-rich brine with chlorine gas, flushing through with air. The process is based on the reaction of bromide ions with chlorine:



Most of the bromine produced in Israel is used for the manufacturing of bromine compounds at Ramat Hovav and other plants abroad. The Ramat Hovav plant is situated about 60 kilometers west from Sdom and about 10 kilometers south from Be'er Scheva. (Kesner, 1999)

Meteorological Conditions

Following Bendix (2004) the diurnal thermal dynamics in valleys in general are shown in Figure 7.9: After sunrise a convective boundary layer forms at the ground (t1) developing to strong transversal upslope winds lifting the inversion layer. Adiabatically backflowing air may mitigate the inversion (t2). In deep valleys there is a tendency to build two separated circulation cells with an inversion at middle valley elevations (Vergeiner and Dreiseitl, 1987; Kistemann and Lauer, 1990). The lower circulation compensates slope winds (transversely to valley axis) and the upper circulation compensates overall upward winds from the valley (valley and slope winds) by vertical fluxes (t3). Provided sufficient thermal-mechanical turbulence, by late afternoon the inversion may become completely dissolved resulting in unstable stratification (t4) in the entire valley. After sunset the valley slopes cool and relative cold air cells begin to flow into the valley and fill a 'pool' of cold air (t5). Displaced air can cause zones on the slopes, which are warm (t6). Until the end of the night the whole basin may be filled by the valley inversion (t7). In the Dead Sea Valley strong zonal (i.e. westerly) winds perturb this pattern regularly (tx).

Circulation at the Dead Sea Valley is dominated by a superposition of wind systems

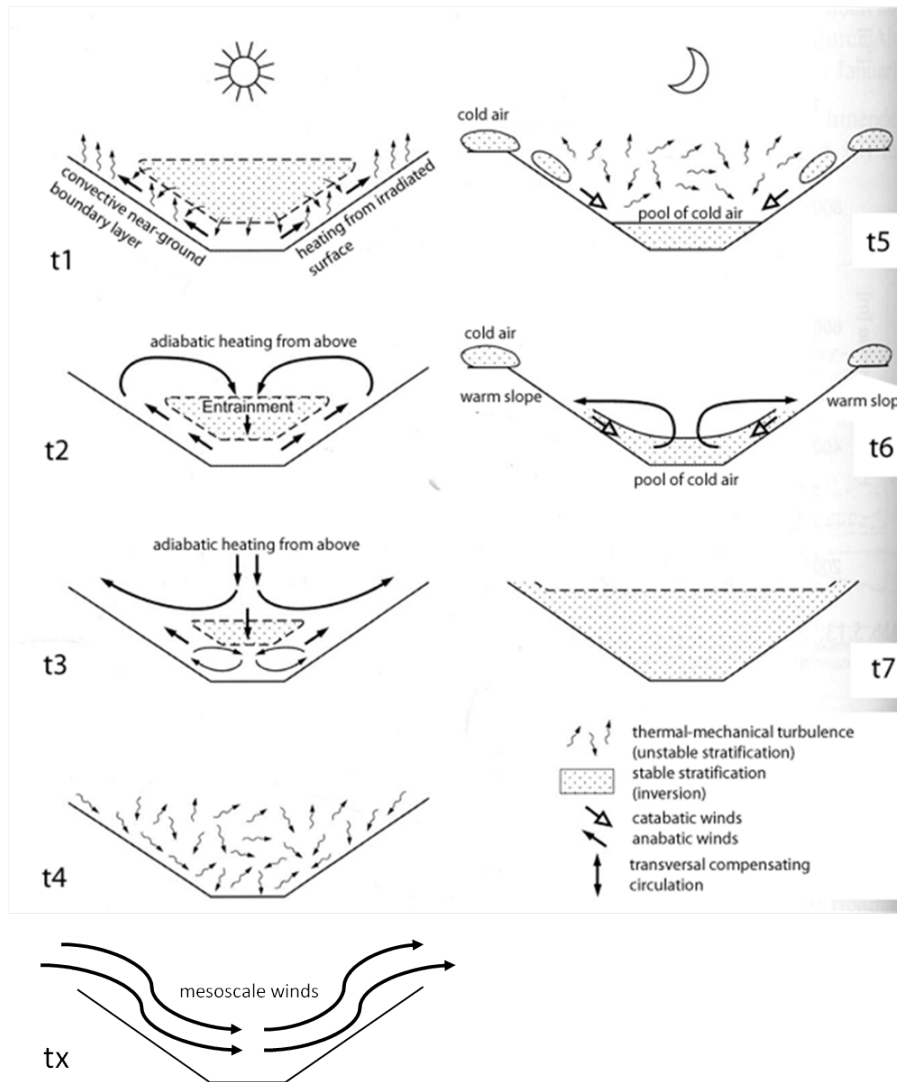


Figure 7.9: *The diurnal thermal dynamics in valleys and the generation of LMCs. Adapted from Bendix (2004).*

from synoptic to local scales.

Two synoptic situations are characteristic for summer (June to September) and winter (December to February), respectively: In summer a surface layer trough over the Arabian peninsula leads to northerly and westerly flows in the lower atmosphere. In upper layers the subtropical ridge originating from the Hadley cell leads to clear skies. Frequently in the afternoon the northerly and westerly winds are superimposed by the Mediterranean Sea breeze. This results in a sudden reversal of the slope winds in the Dead Sea Valley from upward to downward already at 16 UTC, instead of 19 UTC when catabatic winds would develop without external perturbation (Bitan, 1977; Schmitz, 2009; Segal et al., 1983). In winter the synoptic situation is less stable: Crossing pressure systems affect the Dead Sea region and as a consequence the Mediterranean Sea breeze penetrates the Dead Sea Valley less often. Frequently high pressure systems occur, resulting in clear skies and light synoptic

winds. Based on numerical model studies (Segal et al., 1983) states that in such conditions the flow patterns in the Dead Sea Valley are highly dominated by local lake-mountain thermally induced circulations (LMC). According to the explanations of dynamics of valleys in general above, LMCs are likely to be present at daytime recurrently at least in some parts of the Dead Sea Valley as a result of local (~ 1 km) and mesoscale (~ 10 km) thermal winds. Starting in the late afternoon most nights strong westerly catabatic winds (potentially enhanced by the Mediterranean Sea breeze and synoptic winds) blow into the valley throughout the year (see Figure 7.10).

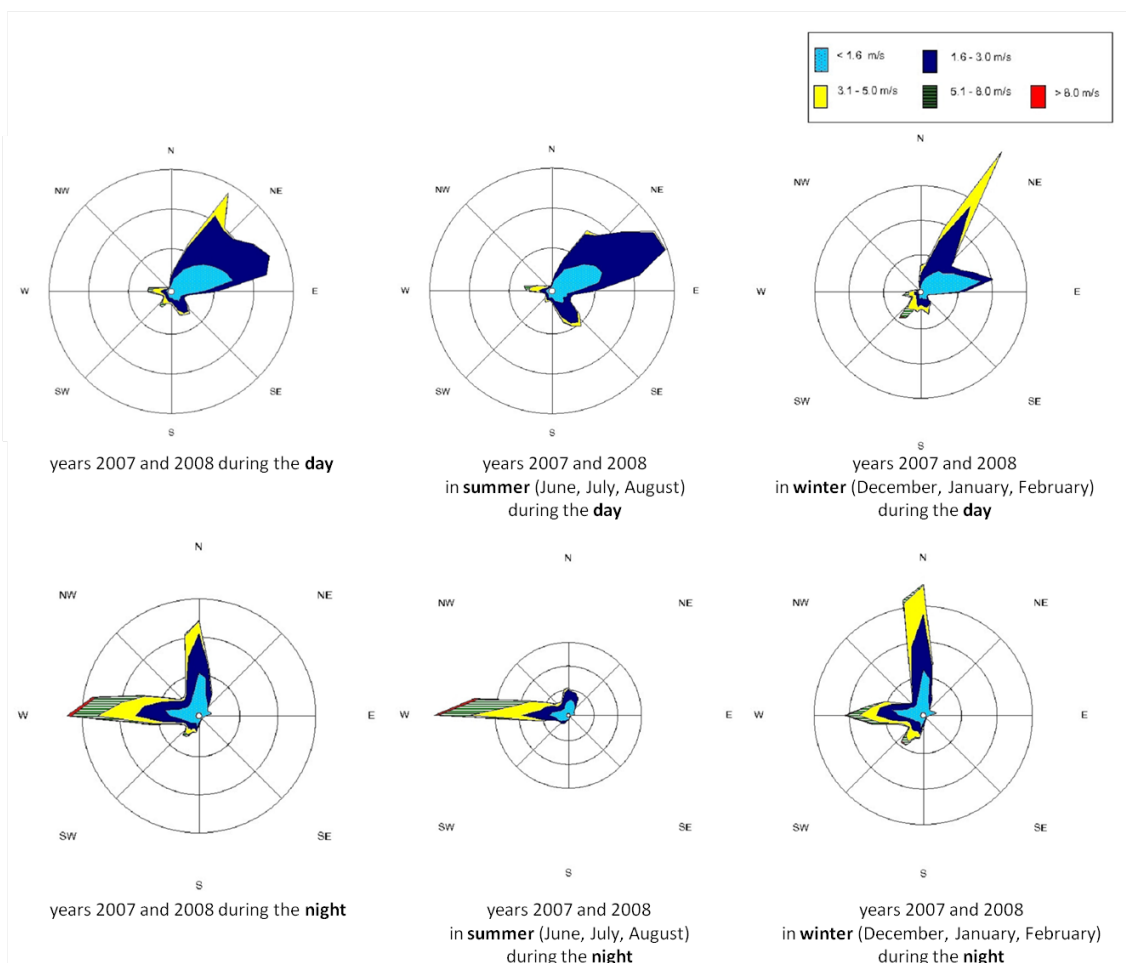


Figure 7.10: Wind roses of the years 2007 and 2008 at Masada Top (IMK) appor-
tioned by day/night and summer/winter. Adapted from Schmitz (2009).

Back trajectories derived with HYSPLIT (Draxler and Rolph, 2003) and local observations show that the meteorological conditions during the two periods of our DOAS measurements in 2012 (2 May to 15 May) and 2002 (25 June to 30 June) are consistent with the typical summer situation described above. A more detailed analysis of the air mass trajectories and their influence on local meteorology in the Dead Sea Valley will be given in section 9.1.

The solar radiation peaks at 9:30 UTC (11:30 IST (winter time) and 12:30 IDT

(summer time)) \pm 15 min with the largest monthly averaged diurnal insolation in June (964 W/m^2) and the least in December (471 W/m^2). Air pressure at the Dead Sea is about 53 mbar higher than at mean sea level with max. fluctuations of 20 mbar. Monthly averaged maximum air temperatures peak in the afternoon at 35.4°C in July and 19.6°C in January. Monthly average relative humidity at the sea (offshore) ranges from 60% (July) to 65 % (December). Overall 98% of the time relative humidity is between 50 and 70 %. The sea surface temperature (SST) in the northern basin peaks around 33°C in summer recurrently. In winter there is more year-to-year variability around 20°C than in summer due to fresh water inflows and consequently effects by the stratification of water. (Hecht and Gertman, 2003)

MAX-DOAS measurements at Masada 2002 and 2012

BrO was observed the first time at the Dead Sea using LP-DOAS already in summer 1997 (Hebestreit, 1999). The first MAX-DOAS measurements at the Dead Sea were performed at Masada by Jutta Zingler in 2002 using the MAX-DOAS described in (section 6.4). In 2012 these measurements were repeated similarly with a longer observation period using MAX-DOAS Z2 (section 6.5) allowing for better time resolution (15-30 min vs. 1h), an advanced wavelength range and higher sensitivity in the UV range.

Masada is the name of an isolated mesa on the rim of the Dead Sea Valley at the southern end of the northern basin, located at N 31.31° E 35.36° , see Figure 7.11. From the valley bottom it rises by around 400 m with an approximate slope of 50 %. Because of its importance in ancient history Masada is an UNESCO World Heritage Site. The MAX-DOAS instruments in 2002 was set up on the rail of the tramway and the one in 2012 on the balcony of a maintenance building, both on the western side of the mesa (see Figures 7.8 and 7.11) at 42 m and $\sim 32\text{m}$ above sea level (asl), respectively (see Figure 7.12). The telescope azimuth orientation in 2002 was East (90°), in 2012 it was shifted to 118.5° in order to have more overlap with the instruments at Ein Bokek.

Measurements 2002: Measurements were performed by Jutta Zingler from 25 June until 30 June 2002 and 3 May until 15 May 2002 (Zingler, 2002). The device was operated with the software MFC (Gomer et al., 1993). The automated measurement routine was continuously recording spectra of scattered sunlight in the wavelength range from 300 to 364 nm with a spectral resolution of 0.5 nm using the MAX-DOAS instrument described in section 6.4. The sequence of telescope elevation angles was 90° , -45° , -10° , (-5°), -2° , 0° , 2° , (5°), 10° (from 28 June 16:13 UTC on additionally the elevation angles -5° and $+5^\circ$ were used). Total exposure time per spectrum was fixed to 300 s with varying number of single scans per spectrum. Offset (60 ms exposure time, 5000 scans), Dark Current (500 s, 1 scan) and Hg emission line spectra were recorded in the dark manually. The Photo Diode Array (PDA) of the spectrograph was stabilized at -20°C , and the spectrograph at 30°C .

Measurements 2012: Measurements were performed from 3 May until 15 May, 2012. The software MS-DOAS developed by Udo Frieß allowed for fully automatic

measurements. The sequence of telescope elevation angles was 90° , 10° , 5° , 2° , 1° , 0° , -1° , -2° , -5° , -10° , -28° . The wavelength range of recorded spectra was 288 nm - 450 nm in UV range and 427 nm - 540 nm in VIS range. Spectra were recorded for solar zenith angles $\vartheta < 96^\circ$ in auto acquisition mode with a fixed total exposure time depending on ϑ : 40 s ($< 96^\circ$), 32 s ($< 90^\circ$), 24 s ($< 80^\circ$). Offset (10 ms exposure time, 1000 scans), Dark Current (30 s, 1 scan) and Hg emission line spectra were also recorded manually darkening the objective of the telescope. The spectrographs were thermally stabilized at 20°C .

Additionally a mobile Ozone Monitor (Model 202 - 2B Technologies) was set up at right next to the MAX-DOAS, measuring ozone mixing ratios every 10 s and logging 1 min averages.



Figure 7.11: Overview of the measurement sites and instruments used during the campaign in May 2012.

MAX-DOAS and LP-DOAS measurements at Ein Bokek 2012

The instruments were set up in a room on the eighth floor (~ 20 m above the ground) at the western side of Hotel Lot, located at $E 35.36^\circ N 31.20^\circ$, heading to 80° (LP-DOAS) and 88° (MAX-DOAS), see Figures 7.13 and 7.14. The measurements were performed between 3 May and 15 May, 2012.

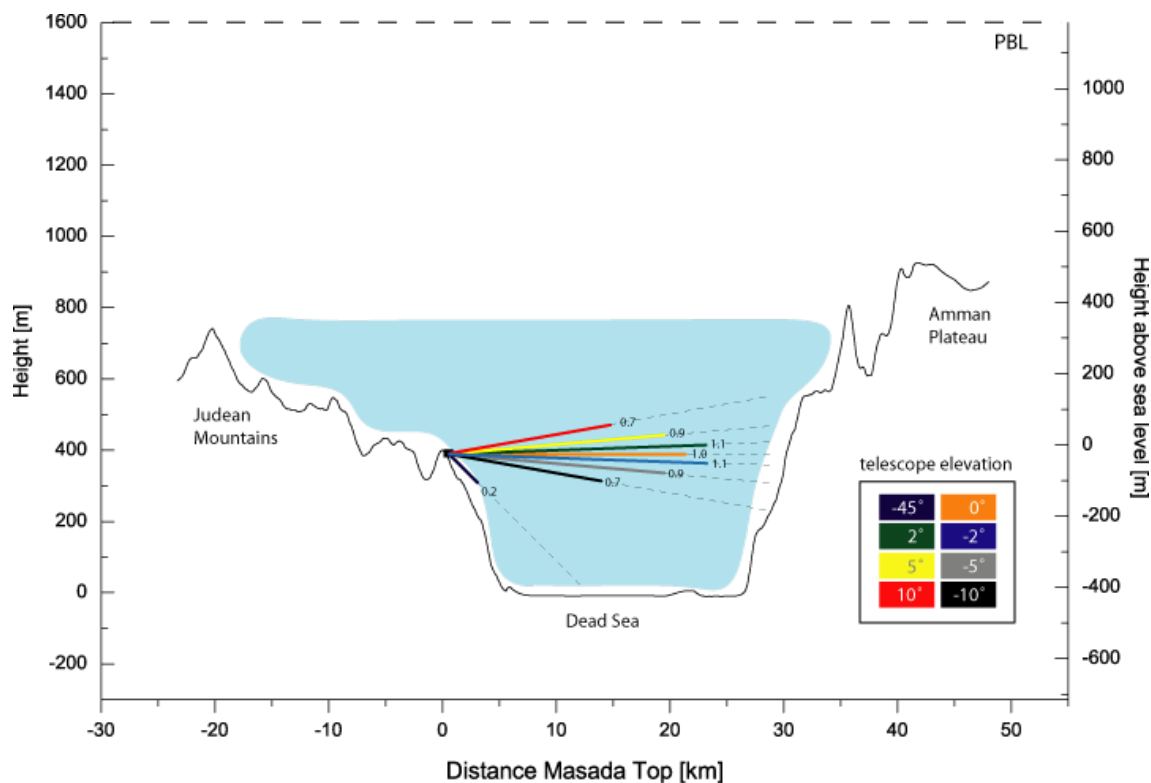


Figure 7.12: Zonal cross section of the terrain at Masada (cf. Figure 7.8) with viewing geometry of the MAX-DOAS measurements in 2002. The colored lines indicate average δS on 29 June, 2002. In 2012 additionally the telescope elevation angles $+1^\circ$ and -1° were used. Vertical axis is multiplied by 30 compared to horizontal axis, angles are true.

The MAX-DOAS described in chapter 6, section 6.6 was used. The scanner unit was mounted on the balustrade of the balcony (see Figure 7.11). Its azimuthal orientation was East (90°). It was also operated with the software MS-DOAS, scanning at the telescope elevation angles 80° , 20° , 10° , 5° , 2° , 1° , 0° , -5° . Reference spectra were recorded at 80° elevation angle, at 90° the telescope would have aimed at the balcony above. The optical bench of the spectrograph was stabilized at 38°C and the CCD was cooled down to -30°C . Several times the measurement routine hang up especially in the evening hours without displaying an error message and had to be restarted when we arrived at the hotel the next morning. The error could not be reproduced yet.

The LP-DOAS described in chapter 6, section 6.7 was used. The measurements were performed between 2 May and 15 May, 2012. The telescope was set up inside the room (see Figure 7.11) aiming at the retro reflector array on the dam at N31.207 E35.416 in a distance of 5 km, standing at an altitude of 5 m above water level. The retro reflector array consisted of 24 UV transmissive fused silica retro reflector prisms with a diameter of 7 cm.

Close to the position of the retro reflector a weather station (Avantage Pro 2 by

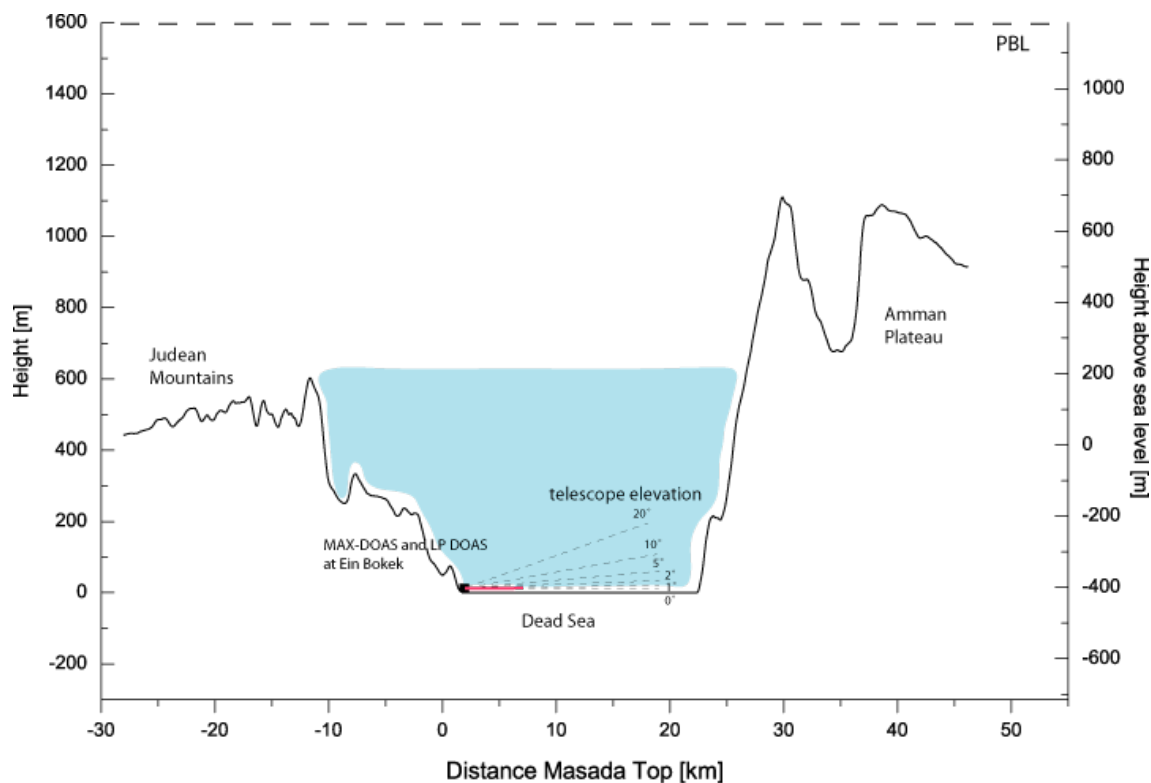


Figure 7.13: Zonal cross section of the terrain at Ein Bokek (cf. Figure 7.8) with viewing geometry of the LP-DOAS and MAX-DOAS measurements. The telescope elevation of 80° used for reference and -5° are not shown. Vertical axis is multiplied by 30 compared to horizontal axis, angles are true.

Davis Instruments) was set up. The parameters air pressure, temperature, relative humidity, wind direction, wind speed, solar irradiation and UV index were measured 3 m above ground and logged every minute.

Car-DOAS measurements along the Dead Sea

On six days between 9 May and 14 May 2012 DOAS measurements were performed along *Road 90* and *Road 31*, cf. Figures 9.21 and 9.22. For that we used the spectrograph and thermal stabilization unit from the instrument described in 6.3, but with a more simple telescope consisting of an aluminium tube and a lense with diameter $d = 2.54$ cm and focal length $f = 15$ cm. The telescope was mounted on a transport box inside the car heading towards the opened window with an elevation angle of 20° (see Figure 7.15). Depending on the direction of travel the telescope was heading to the right or to the left, so that it was aiming at the air masses above the Dead Sea as good as possible. The exploratory rides all took place between 9:00 LT and 19:40 LT. 9-11 May the route started at Masada or Ein Bokek going north to the first turning point close to Kalya and afterwards going south to the second turning point 2 km before Ein Tamar in the South and ended at Ein Bokek. 12-14 May start and end point was the same but turning point were vice versa. On 11 and 14 May an additional detour towards Arad (~ 600 m asl) was made in order to

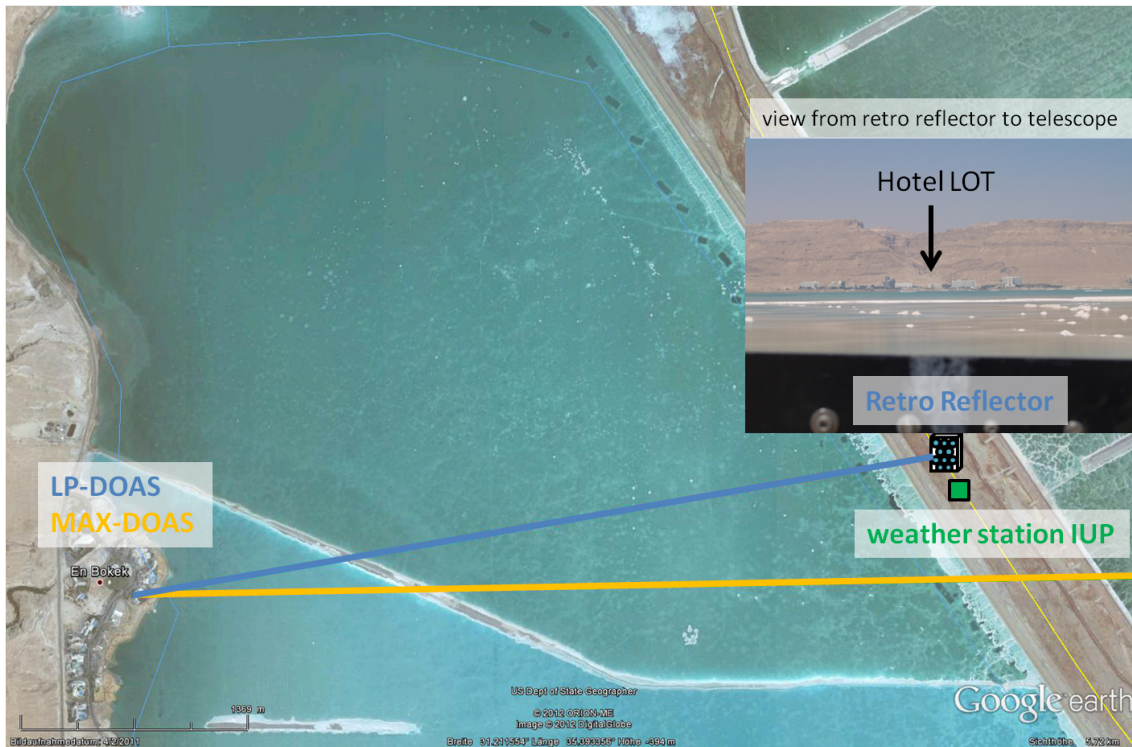


Figure 7.14: Light path of the LP-DOAS Amundsen (blue), retro position and viewing direction of the MAX-DOAS Ein Bokek (orange) across the evaporation ponds at Ein Bokek.

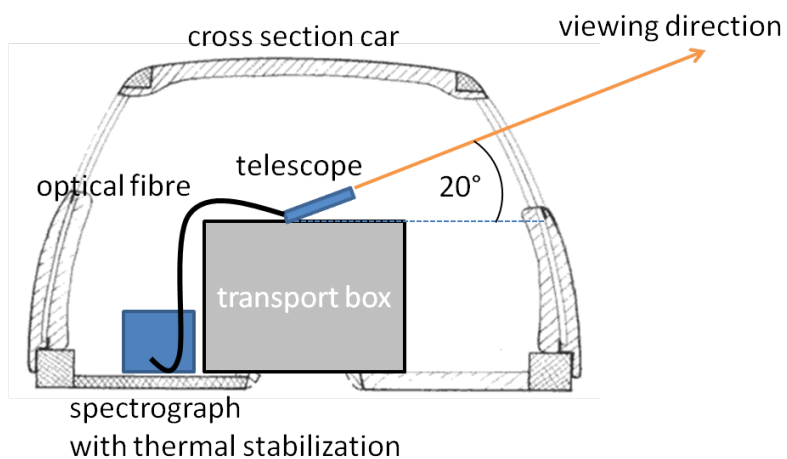


Figure 7.15: Instrumental setup of the Car-DOAS during the measurements along the Dead Sea on Route 90. The orientation of the telescope was turned at the end-points of the route so that it was facing the air over the Dead Sea.

measure at different altitudes.

7.2 Other Areas with High Salt Content

Within the terrestrial environment salt lakes are not the only reservoirs of halogens exposed to the atmosphere. For this reason two additional short campaigns were performed in Germany at sites with potential release of halogen species. RHS were measured using DOAS, supplemented by a mobile ozone monitor (2B) and a mobile weather station (*Avantage Pro 2* by *Davis Instruments*TM).

7.2.1 Bourtanger Moor 2011

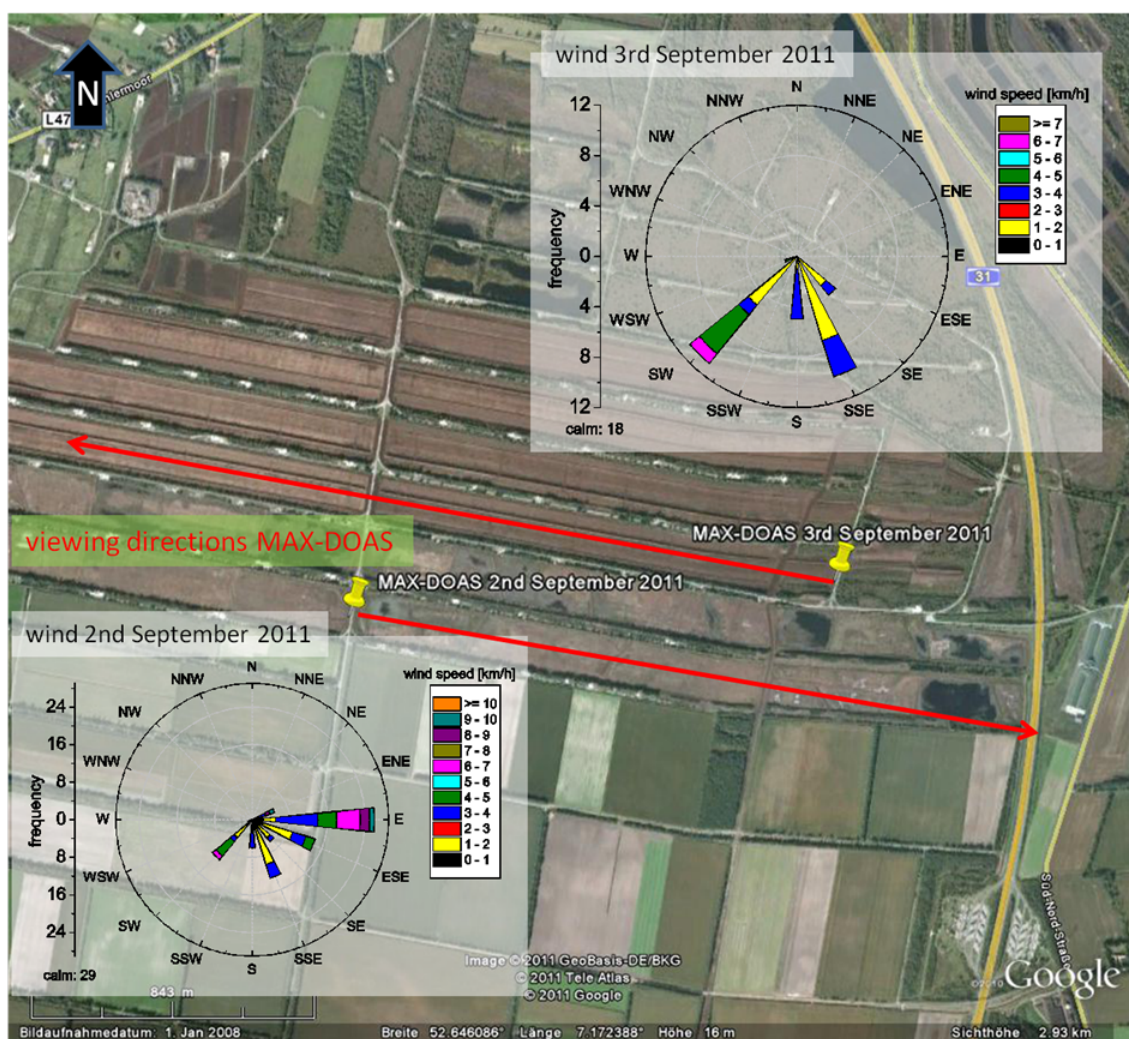


Figure 7.16: Geometry of the MAX-DOAS measurements and frequency of different wind speeds in dependence of wind direction during the measurements on 2 and 3 September 2011 in the Bourtanger Moor.

Peatlands contain about the half of the iodine bound in soil, but account only for 2% of the continental surface area. Besides leaching and surface runoff, volatilisation by formation of short chain alkyl iodides (e.g. CH_3I) is a possible loss process for

iodine in peatlands (Keppler et al., 2003). The Bourtanger Moor is one of Germany's largest peatland regions and is situated in the Emsland close to the Dutch border. This peatland was chosen for RHS measurements because of its relatively large area and preceding and continuous long-term measurements (soil studies, meteorology) performed there by the Johann Heinrich von Thünen-Institut, Braunschweig. On 2 and 3 September 2011 measurements were performed one day at a renaturalized part of the peat bog and half a day above a peat mining lane using a MAX-DOAS system (see section 6.3) for IO and BrO. The measurement set up is shown in Figure 7.16.

Meteorological Conditions

The wind was weak with wind speeds below 10 km/h and the sun was shining throughout the two days of measurement with solar irradiances peaking at 850 W/m² on the first day and 650 W/m² on the second day. Prevailing wind directions were 90° to 225° and 135° to 225° on 2 September and on 3 September, respectively (cf. Figure 7.16).

7.2.2 Kali Dump 2011

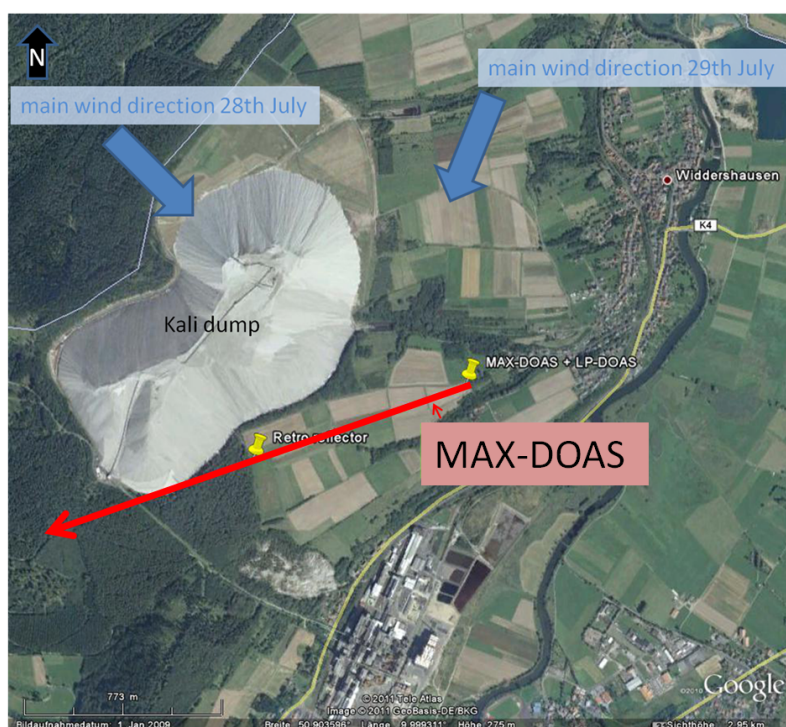


Figure 7.17: Geometry of the MAX-DOAS and LP-DOAS measurements and main wind directions at the Kali Dump close to Heringen. Results from LP-DOAS did not yield significant signals of BrO and IO and are not presented in this work.

Kali dumps originate from the mining of potassium salt and primarily consist of halite (BUND Region Hannover). Thus they pose a large surface of natural salt to

the environment and therefore are possible source regions of halogen compounds in the troposphere. On 28 and 29 July measurements were performed two half days (afternoon and morning) at the Kali dump close to Heringen (Werra) using both an active Compact LP-DOAS system (Schmitt, 2012) and a passive MAX-DOAS system (see section 6.3). The viewing direction of our instruments was 250° (WSW) (see Figure 7.17). Results from LP-DOAS did not yield significant signals of BrO and IO and are not presented in this work, as detection limits are higher than those from MAX-DOAS.

Meteorological Conditions

Wind was predominantly coming from north to north east during the 28 and from west to north during the 29 with average wind speeds of 3.8 km/h and 2.4 km/h, respectively. The UV index reached a maximum of 5 around noon. Average relative humidity was quite constant on 28 July 2011 at 31%, on 29 July humidity dropped from 72% in the morning down to 50% at noon.

Chapter 8

Data analysis

8.1 Spectral Evaluation

The retrievals of differential slant column densities $\Delta S = S(\vartheta, \alpha) - S(\vartheta_{ref}, \alpha_{ref})$ (cf. 4.2) of trace gases presented in this work were performed using a combination of the software DOASIS (Kraus, 2004) and Windoas (Fayt and Van Roozendael, 2001). DOASIS was used to execute a routine written in Jscript (Microsoft, 2000) adapted from (Hönninger and Filsinger). This routine searches for spectra recorded at a certain telescope elevation, which is specified by the user (usually $\alpha = 90^\circ$), to use them as reference spectra for the DOAS analysis. To account for variations of the channel-to-wavelength mapping, the individual selected spectra are fitted against a solar spectrum (Kurucz et al., 1984), which is convolved with the instrument function of the corresponding spectrograph. This yields a wavelength shift for the reference spectrum within the wavelength interval where the actual DOAS fit is applied. The channel-to-wavelength mappings of the reference spectra are shifted linearly by this values for each elevation sequence accordingly.

Each spectrum is corrected for electronic offset and dark current (cf. chapter 6). The initial channel-to-wavelength mapping is retrieved by the Windoas calibration tool allowing to subdivide spectra (pre-calibrated with recorded mercury lines) into a given number of windows in which the calibration via a high resolved solar spectrum (Kurucz et al., 1984) are performed. In contrast to the JScript routine described above, also non-linear channel-to-wavelength mappings can be retrieved. The initial channel-to-wavelength mapping is gained from spectra selected for each measurement period individually and is shifted by the JScript routine by a constant for each reference to account for smaller spectral shifts caused by temperature variations of the instrument.

From the reference spectra pre-processed in this way, Ring spectra are calculated using the software DOASIS, which approximates the Ring spectrum following the method proposed by Bussemer (1993). In principle the Ring spectrum can be calculated from an arbitrary solar spectrum. As the convolutions caused by inelastic Raman scattering and the instrument function can be exchanged, calculating it from measured spectra ensures to use the appropriate spectral resolution and spectral sampling (Wagner et al., 2009).

After each selection of a reference spectrum, Windoas is executed to perform the

spectral evaluation using the fitting scenarios listed in Table 8.2. Each spectrum is evaluated against the preceding reference spectrum. The general settings of the different fitting scenarios are listed in Table 8.2. For the retrieval of O_4 a 2nd order polynomial is fitted and a 3rd order polynomial for the retrieval of BrO , IO and NO_2 , respectively. This accounts for broadband spectral structures caused by atmospheric Rayleigh and Mie scattering. Additive polynomials are fitted non-linearly to account for intensity offsets, which are usually caused by additional light with wrong or no wavelength information (straylight) reaching the detector of the spectrograph.

Table 8.1: *Cross sections of trace gas absorption and inelastic scattering used in this work.*

#	cross section (Temperature)	Reference
1	BrO (298 K)	(Fleischmann et al., 2004)
2	CHOCHO (296 K)	(Volkamer et al., 2005)
3	H ₂ O (294 K)	(Rothman et al., 2009)
4	HCHO (298 K)	(Meller and Moortgat, 2000)
5	IO (298 K)	(Spietz et al., 2005)
6	O ₃ (223 K)	(Bogumil et al., 2003)
7	O ₃ (293 K)	(Bogumil et al., 2003)
8	O ₄ (298 K)	(Hermans et al., 2003)
9	O ₄ (296 K)	(Greenblatt et al., 1990)
10	NO ₂ (223 K)	(Voigt et al., 2002)
11	NO ₂ (293 K)	(Voigt et al., 2002)
12	Ring Spectrum RRS*	(Bussemer, 1993)
13	Ring $\times\lambda^4$ + Ring _{norm}	(Wagner et al., 2009)
14	VRS [†]	(Vountas et al., 2003)

*Rotational Raman Scattering

[†]Vibrational Raman Scattering on liquid water

The spectral analysis of O_4 was performed in the wavelength interval between 350 nm and 375 nm, which was demonstrated to be stable against small variations of the wavelength range used for the fit (Yilmaz, 2012a). For the spectral analysis of BrO , the wavelength interval 331-357 nm was chosen encompassing five BrO absorption bands. This is in agreement with the intervals recommended by Vogel (2011).

Windoas was also used for the convolution of all literature molecular absorption cross sections. The absorption cross sections are convolved with an instrument function gained from a mercury emission line at 334.15 nm for DOAS retrievals in the UV and 435.84 nm for retrievals in the VIS range.

If not denoted otherwise presented results of BrO and IO refer to the "standard" scenarios $BrO_{331-357_std}$ and $IO_{414-438_std}$. Scenario "BrO_331-357_2ndRing" contains two Ring spectra (calculated from literature solar spectrum (Kurucz et al., 1984) using DOASIS) normalized by the method proposed by Wagner et al. (2009). In contrast to the other scenarios, the Ring spectrum is not calculated for each reference individually.

Following findings by Grossmann et al. (2012) for possible inelastic vibrational Raman scattering (VRS) by liquid water, a VRS compensation spectrum, provided by Dinter (2011), is implemented in scenario "IO_414_438_VRS". This is in particular relevant for the measurements on Punte Norte, Cape Verde, where the measurement site is located directly at the coast and the telescope is pointing to the ocean, see Figure 7.5.

To account for the absorption structure of glyoxal, which might have been present in particular on Sal, Cape Verde, cf. (Sinreich et al., 2010), the absorption cross section by Volkamer et al. (2005) is included in the spectral retrieval. The inclusion of glyoxal in the spectral retrieval of IO tends to reduce ΔS_{IO} and increases the fitting error by 20-25%, see histograms in the appendix A. Significant signals of glyoxal were, however, not found.

Table 8.2: *Applied fit scenarios used for the spectral retrieval of O₄, NO₂, BrO and IO from MAX-DOAS spectra.*

fit scenario	wavelength interval	cross sections # (see Table 8.1)	polynomial order	additive polynomial order	shift and stretch
O4	350-375 nm	(4), (6), (7), (8), (10), (11), (12)	2	-	Spectrum: shift, stretch 1st order
NO2 (uv)	354-380 nm	(6), (7), (8), (11), (12)	3	0	Spectrum: shift, stretch 1st order
BrO_331_357_std	331-357 nm	(1), (4), (7), (9), (11), (12)	3	0	Spectrum: shift, stretch 1st order Ring: shift, stretch 2nd order
BrO_331_357_2ndring	331-357 nm	(1), (4), (7), (9), (11), (13)	3	0	Spectrum: shift, stretch 1st order Ring: shift, stretch 2nd order
BrO_331_357_offs2	331-357 nm	(1), (4), (7), (9), (11), (12)	3	2	Spectrum: shift, stretch 1st order Ring: shift, stretch 2nd order
BrO_331_357_nooffs	331-357 nm	(1), (4), (7), (9), (11), (12)	3	-	Spectrum: shift, stretch 1st order Ring: shift, stretch 2nd order
NO2 (vis)	398.5-420 nm	(6), (7), (9), (11), (12)	3	0	Spectrum: shift, stretch 1st order Ring: shift, stretch 2nd order
IO_414_438_std	414-438 nm	(6), (7), (9), (11), (12)	3	0	Spectrum: shift, stretch 1st order Ring: shift, stretch 2nd order
IO_417_438_std	417-438 nm	(6), (7), (9), (11), (12)	3	0	Spectrum: shift, stretch 1st order Ring: shift, stretch 2nd order
IO_414_438_VRS	414-438 nm	(6), (7), (9), (11), (13)	3	0	Spectrum: shift, stretch 1st order Ring: shift, stretch 2nd order
IO_414_438_offs1	414-438 nm	(6), (7), (9), (11), (12)	3	1	Spectrum: shift, stretch 1st order Ring: shift, stretch 2nd order
IO_414_438_glyo	414-438 nm	(6), (7), (9), (11), (12), (2)	3	0	Spectrum: shift, stretch 1st order Ring: shift, stretch 2nd order

8.2 Measurement Error and Detection Limit

The given detection limits in this work refer to a 2σ measurement error. In other words, an ensemble of retrieved slant column densities is considered to be significant, when its 2σ range is located above zero entirely. In this case a single data point has a probability of more than 95.4% to be above zero.

The error of the DOAS measurements is estimated using the method proposed by (Stutz and Platt, 1996): The width τ of the absorption structures and the characteristic frequency of the fit residual, represented by the parameter W , has to be determined. A parameter W greater than 1 represents residual structures other than noise, e.g. caused by the instrument itself or unknown absorbers. Based on numerical studies this yields a correction factor C (see Figure 8.1), which has to be applied to the fit error in order to obtain the measurement error. Typical values for the presented measurements are 1-2 nm for the FWHM of the absorption structures τ and a parameter W of 10. This yields a correction factor of 2 and thus a detection limit being the four-fold DOAS fit error. Yet this is only true for Gaussian distributed measurements. Stable residual structures lead to systematical errors, for example caused by unknown absorbers, inaccurate cross sections or the instrument itself. It should be noted that the correction factor given by (Stutz and Platt, 1996) is only valid for randomly generated non-Gaussian residuals. The actual measurement error can be larger, but also smaller than indicated by this correction factor, depending on the actual shape of an unknown residual structure. For example, the latter might be the case if a set of residual structures can be described by a large parameter W , but the spectral structures themselves do not overlap with absorption bands. In that case, the correction factor might be overestimated by the method described above.

To get a realistic estimate of the error and detection limit of the DOAS measurements under environmental and operational conditions, BrO was retrieved from spectra recorded on the roof of the IUP (Institute of Environmental Physics, Heidelberg, Germany), where significant amounts of tropospheric BrO are not expected. 399 single spectra were recorded with the MAX-DOAS instrument described in section 6.5 using the same measurement procedure as described in section 7.1.6, but only recording spectra at elevation angles 10° , 5° , 2° and 1° are considered, since measurements at lower angles are obstructed. Figure 8.2 shows the histograms of the measured absolute $\Delta S BrO$ minus different multiples of the DOAS fit error. On a 2σ confidence interval only 4.6% of the measurements should remain above zero. Therefore the detection limit for BrO is estimated with the five-fold DOAS fit error, see Figure 8.2. The same analysis was done for the retrieval of $\Delta S IO$ yielding a detection limit of the 6-fold fit error. The higher detection limit in the visible wavelength range is probably due to systematical structures caused by straylight reaching the spectrograph's detector. In general for MAX-DOAS measurements, using a telescope lens shade reduced systematical errors in the fit of IO. Residuals of the other instruments from which data is presented in this work are generally similar, for this reason and with regard to the fact that the correction factor is nearly constant for $W \gtrsim 10$ the same detection limits are assumed in that cases.

Fitting errors of the spectral retrievals presented in this work are distributed non-

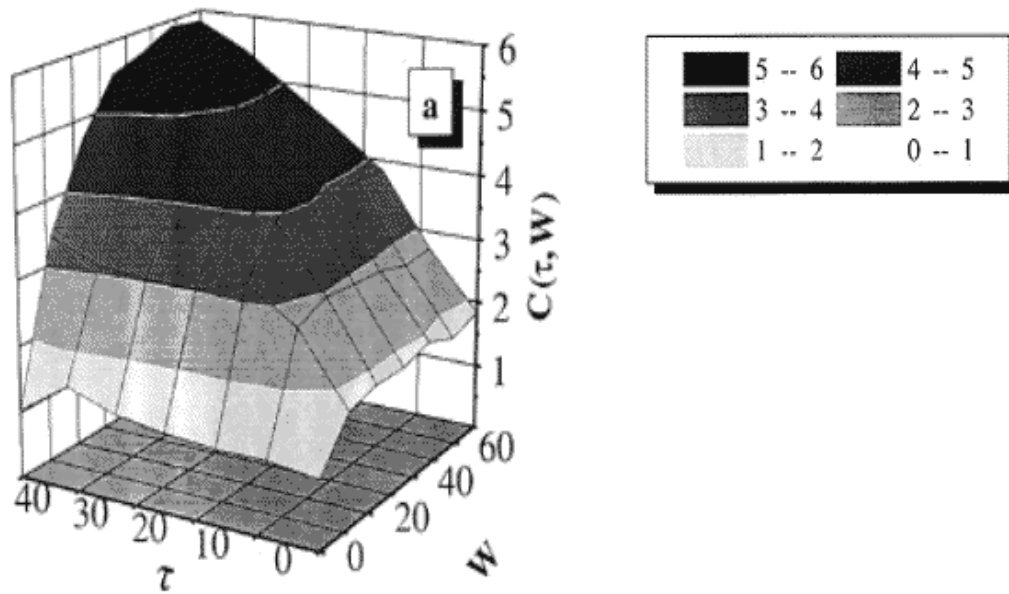


Figure 8.1: The diagram yields the correction factor $C(\tau, W)$ for a linear least-squares fit error depending on the width of absorption structures τ and the width of residual structures other than noise represented by W (Stutz and Platt, 1996).

symmetrically, which is mainly because of two reasons:

1. As described in section 8.1 the spectral retrieval routine automatically evaluates each single spectrum against the preceding FRS, which has been corrected for shifts of 0th order in the channel-to-wavelength mapping. This procedure is also applied to the FRS themselves. The resulting fitting errors are attributed to numerical noise only and are several orders of magnitude lower than the fitting errors of the "actual" spectral retrievals. These are not excluded from the Histograms shown in Chapter A.
2. In some cases systematic structures in the residual of the DOAS fit can cause enormous fitting errors. These "bad spectra" can be due to passing obstacles in the light path of the instrument generating unknown spectral structures or oversaturation, or interferences in the instrument itself, for example. For the final evaluation of trace gases (chapter 9) and data charts (chapter A), DOAS retrievals with residual structures with a root mean square $\text{RMS} > 1\%$ were sorted out.

For these reasons median values are considered to be more representative than mean values for "average" fitting errors (cf. Histograms in A). The detection limits specified in Table 9.2 in Section 9.2 refer to median values, too.

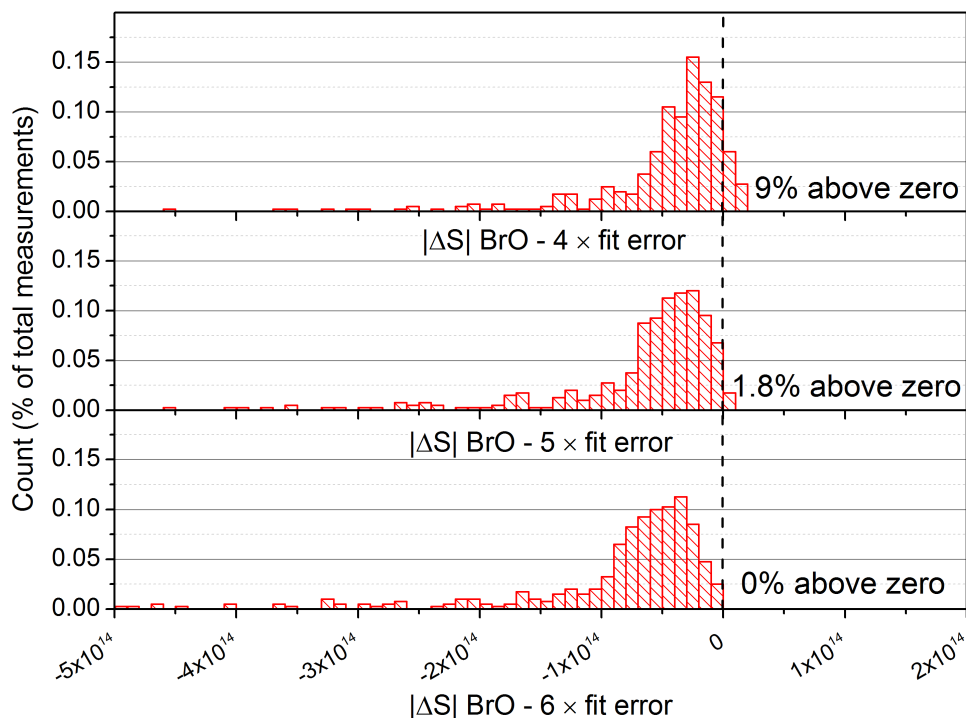


Figure 8.2: Histograms of the measured absolute ΔS of BrO subtracted by their fit error weighted with correction factors C of 4, 5 and 6. A factor of $C=5$ agrees best with a confidence interval of 2σ .

8.3 Retrieval of Vertical Profiles

The retrieval of vertical profiles of aerosol extinction, NO_2 and BrO were performed following the sequence described in section 5.2.3. For the retrievals presented in this work, relative intensities were not used due to a complication by using negative telescope elevation angles: The surface albedo and thus the relative intensity strongly depends on the (negative) telescope elevation angle and the corresponding surface albedo, which is not known. Also clouds are a huge problem for relative intensity retrievals. For this reason retrievals performed with the use of relative intensity did not yield unambiguous results.

8.3.1 Profile Retrieval Parameters

The properties and parameters used for the retrievals of vertical profiles of aerosol extinction, BrO and NO_2 presented in section 9.1 were the following, unless stated otherwise:

- Time resolutions Δt of 75 min and 30 min were chosen for the 2002 and 2012 data, respectively, to ensure that complete elevation sequences (see Table 8.3) are used for the retrievals.

- Retrievals were performed at the wavelengths 360 nm, 344 nm and 346.5 nm for aerosol extinction (O_4), BrO and NO_2 , respectively.
- An Ångström exponent (see section 3.2.4) of $\alpha_M = 1.36$ was used to account for the different wavelengths of the retrievals.
- The weighting function \mathbf{K} (see section 5.2.2) was calculated for each profile retrieval individually.
- The telescope elevation angles used for the retrievals are shown in Table 8.3. Measurements at 90° and 80° , respectively, are used as references. The telescope elevation angles α of the measurements at Masada in 2002 had to be corrected by $+1^\circ$ because of a misalignment of the telescope. For the trace gas retrievals at Masada in 2012 the measurement at $\alpha = 0^\circ$ was not used due to an unknown problem of SCIATRAN 2 concerning trace gas retrievals, yielding unrealistic, extraordinarily high air mass factors at angles of 0° , this was also found by (Yilmaz, 2012d). Due to the correction mentioned above, this problem did not occur in the trace gas retrievals of data from Masada in 2002.
- For aerosol extinction retrievals in SCIATRAN 2 the O_4 cross section provided by (Hermans et al., 2003) was used. According to findings by (Clémer et al., 2010), the absorption cross section of O_4 was previously underestimated by as much as 25% and hence, the O_4 cross section is multiplied by 1.25.
- A surface albedo of 0.06 was chosen which is compliant with the albedo of sandy loam in the UV. As mentioned above, the actual surface albedo depends on the telescope elevation angle. Therefore retrievals were performed using different albedo values (0.01, 0.05, 0.06, 0.08 and 0.1). Best agreement between model and measurements was found using an albedo of 0.06.
- A model grid with a height of 4 km and a grid resolution of 0.05 km was used.
- A priori profiles with exponentially decreasing aerosol extinction and trace gas volume mixing ratio were used. Initial values on the ground were 0.2 km^{-1} , 20 ppt and 0.2 ppb for aerosol extinction, BrO and NO_2 , respectively. At 2 km the a priori profiles have decreased to zero. The error of the a priori profile was set to 100%.
- The correlation length for covariance constrains the strength of the smoothness of the retrieved profiles. It was set to 0.5 km, for details see (Yilmaz, 2012a, p. 85).
- A single scattering albedo (SSA) of 0.93 and an asymmetry parameter of 0.69 were assumed. These are average daytime values found in (AERONET, 2012) data sets from the Dead Sea in 1999 and 2000.
- A linearly decreasing temperature height profile (10°C per km) with 35°C ground temperature and a barometric height profile of pressure with $p(h=0 \text{ km})=1062 \text{ hPa}$ was used.

The elevation angle sequences used for the retrievals and the resulting average degrees of freedom d_s of the signal (see section 5.2.2) are listed in Table 8.3. Elevations used as reference spectra of ΔS are in brackets. As described in section 5.2.2, d_s is a measure for the information content of the measurements. The measurements at Masada at an altitude of ~ 400 m agl in 2012 using 9 telescope elevation angles contain the highest degree of information, whereas the measurements at Masada in 2002 and those close to the ground at Ein Bokek have comparable contents of information, cf. the averaging kernels in Figure 8.3.

Table 8.3: *Telescope elevation angles α and diurnal average of degrees of freedom d_s of signal (see section 5.2.2) with 1σ at the different measurement sites at the Dead Sea for aerosol, BrO and NO_2 retrievals (see text).*

retrieval	sequence of elevation angles [°]	degrees of freedom d_s		
		Aerosol	BrO	NO_2
Masada 2002	(91), -9, -1, 1, 3, 11	3.7 ± 0.4	3.3 ± 0.8	3.2 ± 0.7
Masada 2012	(90), 10, 5, 2, 1, 0, -1, -2, -5, -10	4.6 ± 0.7	3.7 ± 0.6	3.6 ± 0.6
Ein Bokek 2012	(80), 20, 10, 5, 2, 1	3.8 ± 0.6	3 ± 0.5	2.9 ± 0.5

8.3.2 Profile Retrieval Errors

As described in section 5.2.2, the sensitivity of the retrieved profiles towards true abundances at given altitudes is described by the corresponding averaging kernels. In Figure 8.3 averaging kernels of aerosol extinction and BrO profiles are shown.

At Masada the maximum sensitivity is found at altitudes between 200 m and 600 m agl, whereas at Ein Bokek the maximum sensitivity is in the lowest 500 m agl. This affects on the total error of the vertical profiles. Typical examples of aerosol extinction and BrO vertical profiles with total retrieval error and the contribution of smoothing and noise error are shown in Figure 8.4: The major contribution to the total retrieval error is due to the smoothing error, which originates from the finite vertical resolution of the retrieval, see section 5.2.4. Corresponding to the averaging kernels (Figure 8.3) described above, at Masada retrieval errors are lowest at instrument height around 400 m agl.

Due to the difference in sensitivity for different altitudes, the measurements at ground level (Ein Bokek) can not be directly compared to the measurements at 420 m altitude agl (Masada) without considering the averaging kernels.

8.3.3 Sensitivity Studies of Profile Retrievals

To test the sensitivity of the profile retrievals to the choice of a priori profiles, different types of profiles were used. Aerosol and BrO profile retrievals were performed with linear, exponential and Boltzmann shaped (smooth-box-shaped) a priori profiles with three different characteristic heights, see Figure 8.5. The χ^2 values of these retrievals are compared. The use of different a priori profiles is discussed in more detail in (Yilmaz, 2012a).

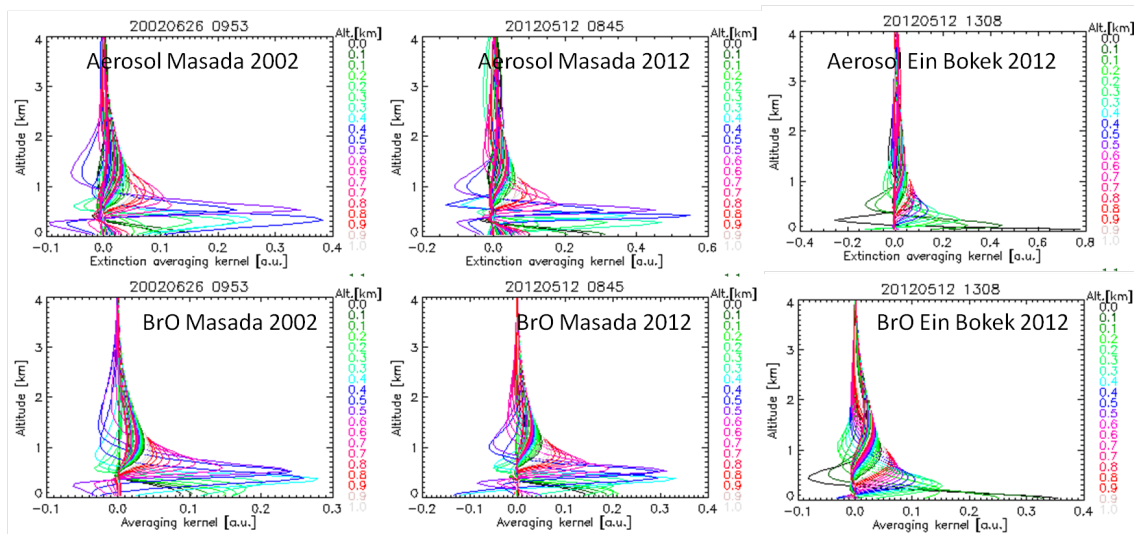


Figure 8.3: Typical averaging kernels of the aerosol extinction and BrO profile retrievals shown in Figures 9.6, 9.8 and 9.9. Colors refer to the altitudes of aerosol or BrO layers, indicated on the right.

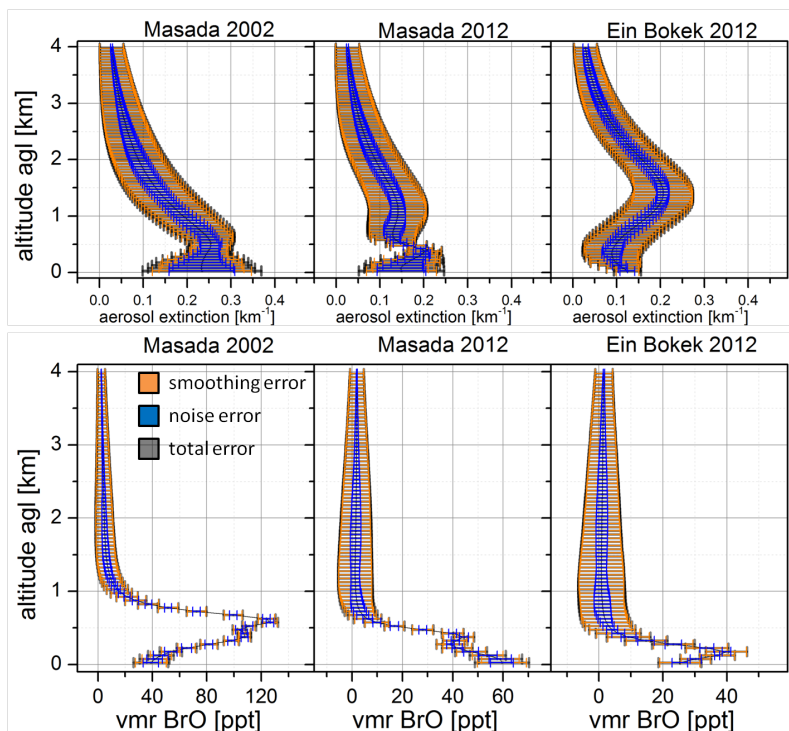


Figure 8.4: Profiles of aerosol extinction and BrO volume mixing ratio both retrieved with exponential shape a priori profiles with characteristic heights of 2 km. Total retrieval errors are black, noise error blue and smoothing error orange (cf. section 5.2.4). Examples are from 26 July 2002 9:53 UTC, 12 May 2012 8:45 UTC, 12 May 13:08 UTC, respectively.

The linear and exponential distributions are characterized by a value at ground (altitude agl $z = 0$ km) and the altitudes, where the distribution has dropped to zero and $1/e$, respectively. The Boltzmann distribution can be used to avoid large gradients in the profile shape, since aerosol and trace gas distributions in the atmosphere are rather smooth than constrained by sharp edges. Thus, the aerosol profile can be described by two parameters using the relationship:

$$\epsilon(z) = \frac{\epsilon(0)}{1 + \exp\left(\frac{z - \frac{\tau}{0.3}}{\frac{\tau}{0.3}}\right)}, \quad (8.1)$$

whith $\epsilon(0)$ being the extinction coefficient at the surface and τ is the optical depth.

For the retrieval of aerosol extinction at Masada the best fits are found with exponential and Boltzmann shape a priori, where extinction is $1/e$ and 50% at 2 km and 3 km, respectively. The choice of the a priori constraints has a very small influence on the retrieved BrO profiles, confirming that the trace gas retrieval is very robust. In contrast, the altitude of upper aerosol layers reveals to be quite unstable against changes of the a priori for Boltzmann shaped profiles, because of the relatively large gradient. Modelled values of differential slant optical density tend to reproduce the measured values better for a priori profiles with larger characteristical heights. The retrieval of BrO profiles shows only minor dependence on the a priori shape, both at Masada and Ein Bokek, see Table 8.4 and Figure 8.5.

However, the planetary boundary layer height in Israel and at the Dead Sea was studied by (DAYAN et al., 1988) in detail and is reported not to exceed altitudes of 1.3 km asl (≈ 1.7 km agl) with only insignificant changes in the thickness of the mixed layer for different synoptic situations. Thus, a priori profiles with characteristical heights of 3 km are regarded as less likely and exponential shape a priori profiles will be used for aerosol and BrO retrievals, where extinction and volume mixing ratios are $1/e$ at 2 km altitude.

Table 8.4: χ^2 of the retrievals shown in Figure 8.5.

a priori shape	χ^2								
	Masada 2002			Masada 2012			Ein Bokek 2012		
	Aer	BrO	d_s BrO	Aer	BrO	d_s BrO	Aer	BrO	d_s BrO
linear 1 km	70	83	2.1	367	48	3.3	830	56	2.6
linear 2 km	20	80	2.9	103	50	4.0	411	56	3.1
linear 3 km	8	78	3.3	77	51	4.4	290	57	3.5
exponential 1 km	22	80	2.8	104	51	4.0	387	57	3.1
exponential 2 km	7	79	3.2	81	52	4.4	254	60	3.5
exponential 3 km	4	78	3.4	81	53	4.6	221	61	3.7
Boltzmann 1 km	23	80	2.9	116	50	4.0	462	55	3.1
Boltzmann 2 km	4	78	3.5	71	52	4.6	277	58	3.7
Boltzmann 3 km	3	77	3.7	76	54	4.9	207	61	3.9

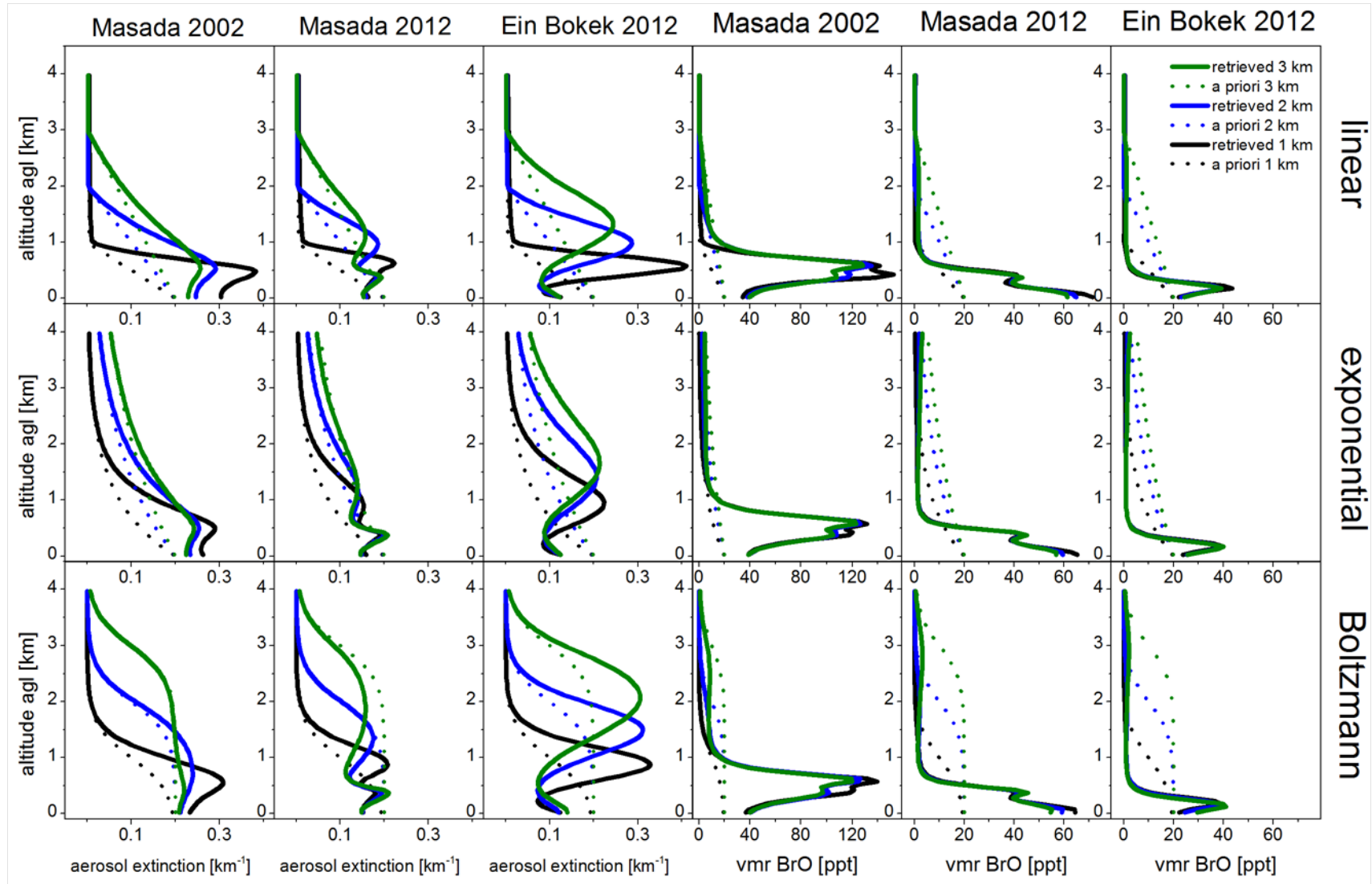


Figure 8.5: Profiles of aerosol extinction (left side) and BrO volume mixing ratio (right side) retrieved with different types of a priori profiles (rows) with characteristic heights of 1 km, 2 km and 3 km (columns), see text.

8.3.4 Intercomparison of measurements at Masada and Ein Bokek

As will be seen in section 9.1, profile retrievals regularly show vertical distributions of aerosol and BrO with maxima elevated above ground. The measurements at Masada are most sensitive for absorber signals at altitudes between around 200 m and 600 m, which corresponds to the approximate altitude where the instrument is located (420 m agl). The sensitivity of the measurements at Ein Bokek has its maximum directly above the ground decreasing by the half in the lowest 200 m (see above). In this respect, it might be interesting to compare how vertical profiles of BrO retrieved from measurements at Masada, assumed that they represent true state vectors, would compare to those retrieved from measurements at Ein Bokek and vice versa. Yet, differing BrO levels in measurements at Masada and Ein Bokek, which might be due to transport phenomena (see section 9.1.2 on the discussion of 12 May 2012) and/or the different viewing geometries of the MAX-DOAS instruments, reduce the comparability of coincident measurements at the two sites. Rather than comparing coincident measurements, it will be tested, how absorber layers situated in elevated layers at Masada or very close to the ground at Ein Bokek would be detected with the sensitivity of the other MAX-DOAS instrument.

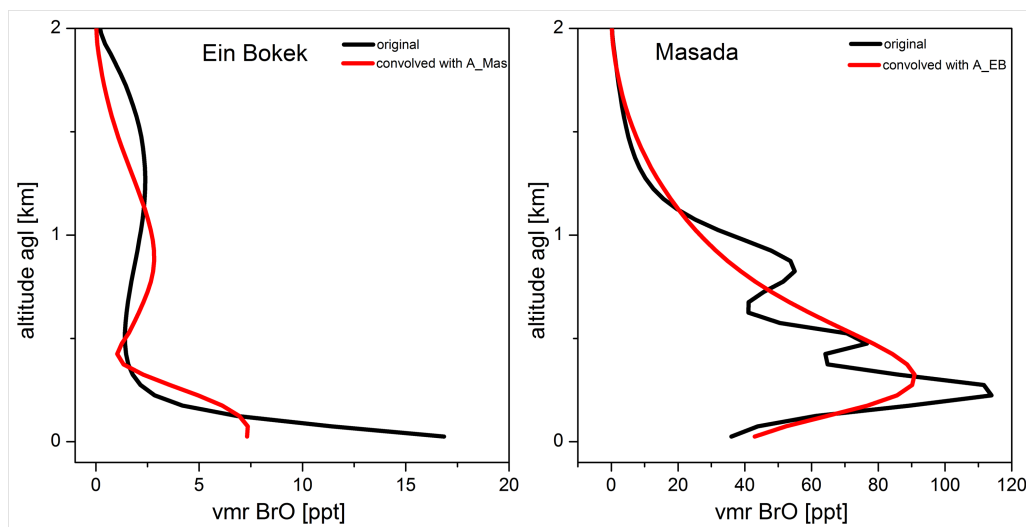


Figure 8.6: Typical profiles of the volume mixing ratio of BrO found at Masada and Ein Bokek convolved with the averaging kernel of the contrary instrument.

Therefore, two retrieved vertical profiles of BrO, one of each site, containing the mentioned characteristics are selected and compared using the method proposed by (Rodgers, 2003): The corresponding vertical profiles $\hat{\mathbf{x}}_{Mas}$ and $\hat{\mathbf{x}}_{EB}$ are regarded as true state vectors \mathbf{x}_t and convolved by the averaging kernels of the other instrument \mathbf{A}_{EB} and \mathbf{A}_{Mas} , respectively. The resulting state vectors $\tilde{\mathbf{x}}_{Mas}$ and $\tilde{\mathbf{x}}_{EB}$ are given by (cf. Equation 5.8):

$$\tilde{\mathbf{x}}_{Mas} = \mathbf{x}_a + \mathbf{A}_{EB}(\hat{\mathbf{x}}_{Mas} - \mathbf{x}_a) \quad (8.2)$$

and

$$\tilde{\mathbf{x}}_{EB} = \mathbf{x}_a + \mathbf{A}_{Mas}(\hat{\mathbf{x}}_{EB} - \mathbf{x}_a), \quad (8.3)$$

and are shown in Figure 8.6.

Obviously the instrument at Ein Bokek cannot resolve elevated layers with thicknesses of several hundred meters, whereas the instrument at Masada underestimates abundances close to the ground.

Chapter 9

Results and Discussion

In this chapter, the results from DOAS measurements at salt lakes and two other sites with high halogen content described in chapter 7 will be presented and discussed.

9.1 Results from Israel 2002 and 2012

For the first time vertical profiles of *BrO* at the Dead Sea were determined based on data from three MAX-DOAS measurements. Measurements were performed at Masada Top (upper station of an aerial tramway) by Zingler (2002) in 2002 and in the scope of this work at Masada and Ein Bokek in 2012. Additionally qualitative DOAS measurements were made from the car along the Dead Sea on *Road 90* in 2012. The aim of the measurements was to identify the vertical and horizontal distribution of BrO at the Dead Sea to get a better understanding of responsible release processes of reactive halogen species from salt lakes and their surrounding. The spectral evaluation and the retrieval of vertical profiles of aerosol, BrO and NO₂ will be presented in sections 8.1 and 8.3. Results of BrO and NO₂ measured by LP-DOAS and MAX-DOAS at Ein Bokek are compared. In the following times will correspond to Local Time, which was Israel Daylight Time (IDT = UTC+3) during all of the presented measurements. Altitudes above ground level (agl) refer to the water level of the Dead Sea and the bottom of the valley, respectively. Altitudes above sea level (asl) will refer to the mean ocean level.

For a description of the measurement sites see section 7.1.6.

9.1.1 MAX-DOAS measurements in 2002

Differential Slant Column Densities ΔS of BrO and O₄ retrieved from MAX-DOAS spectra (Zingler (2002), cf. chapter 8) are shown in Figure 9.2. BrO ΔS are highest at flat angles (-2°, 0°, 2°). The maximum BrO ΔS during the period is on 26 June 2002 with 1.1×10^{15} molecules/cm². Using the routines by (Yilmaz, 2012b) vertical profiles were retrieved for aerosol, BrO and NO₂ as presented in 8.3, see Figure 9.6. Significant amounts of aerosols and BrO are found every day at daytime during the measurement period for several hours. Aerosol extinction shows distinct maxima between 11:00 and 14:00 LT with aerosol extinctions up to 0.4 and one stronger

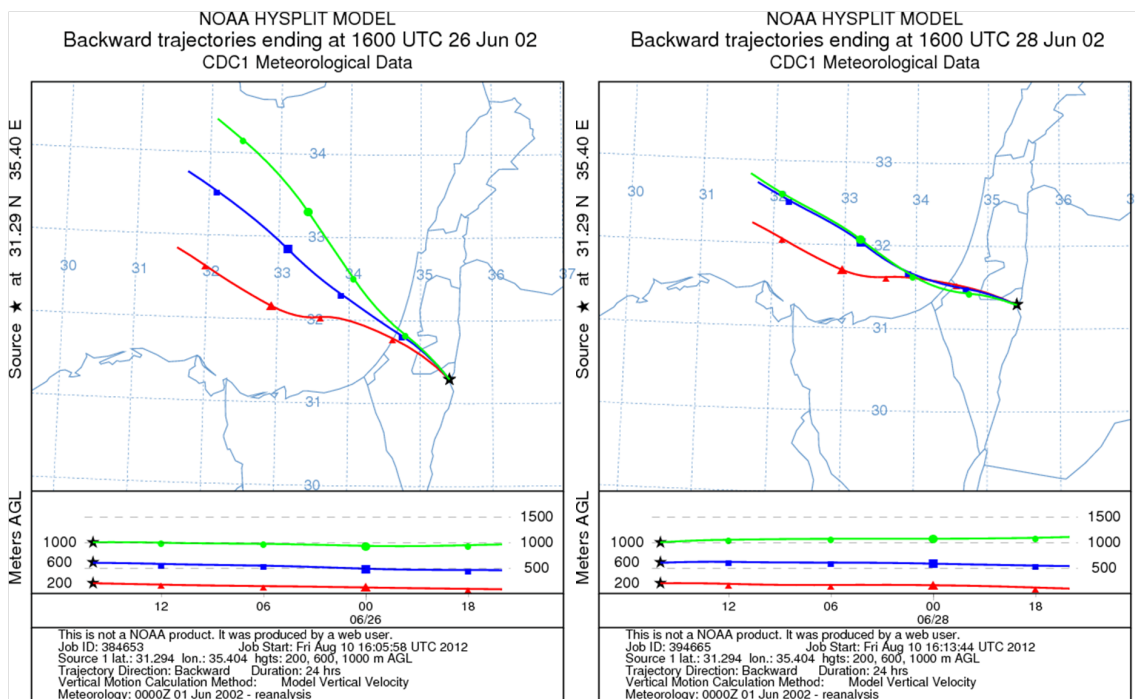


Figure 9.1: Back trajectories ending in the mid of the Dead Sea Valley in the evening on 26 June and 28 June 2002. Height levels above ground of 200 m, 600 m and 1000 m are indicated in different colors.

event on 28 June with 0.7. The aerosol event in the evening coincides with high NO_2 mixing ratios. Trajectories calculated with HYSPLIT (Draxler and Rolph, 2003) reveal westerly wind crossing the Mediterranean coast around Gaza, see Figure 9.1 (right panel), so aerosols and NO_2 probably originate from polluted air penetrating the Dead Sea Valley (cf. 7.1.6). Most aerosol is abundant in elevated layers above 300 m agl. Often the upper aerosol layer is accompanied by a lower layer at ground level (cf. Figure 9.3) with a minimum around 400 - 500 m agl (corresponds to around 0 - 100 m asl).

A similar pattern was found by Levin et al. (2005) during three airborne measurements of aerosols above the Dead Sea on 31 July 1998 (11:00 and 13:00 LT) and 29 April 1999 (09:45 - 10:15 LT) using a condensation nuclei counter mounted near the nose of the plane. The measurements were performed during "hazy conditions", which are typical for the Dead Sea. The airplane flew back and forth between the north of the Dead Sea and Sodom in the south. Two main layers were found on 31 July 1998 11:00 LT and 29 April 1999. The vertical profile on 31 July 13:00 is explained by Levin et al. (2005) with mixing and dilution of the two layers. The positions of the layers is in between the temperature inversions at 0 m and 600 m asl, see Figure 9.4.

Aerosol profiles obtained with MAX-DOAS also show transitions from two layers to one upper layer between 11:00 and 14:00 LT on four out of six days, but sometimes also a re-formation of the second layer in combination with a decreasing upper layer in the late afternoon.

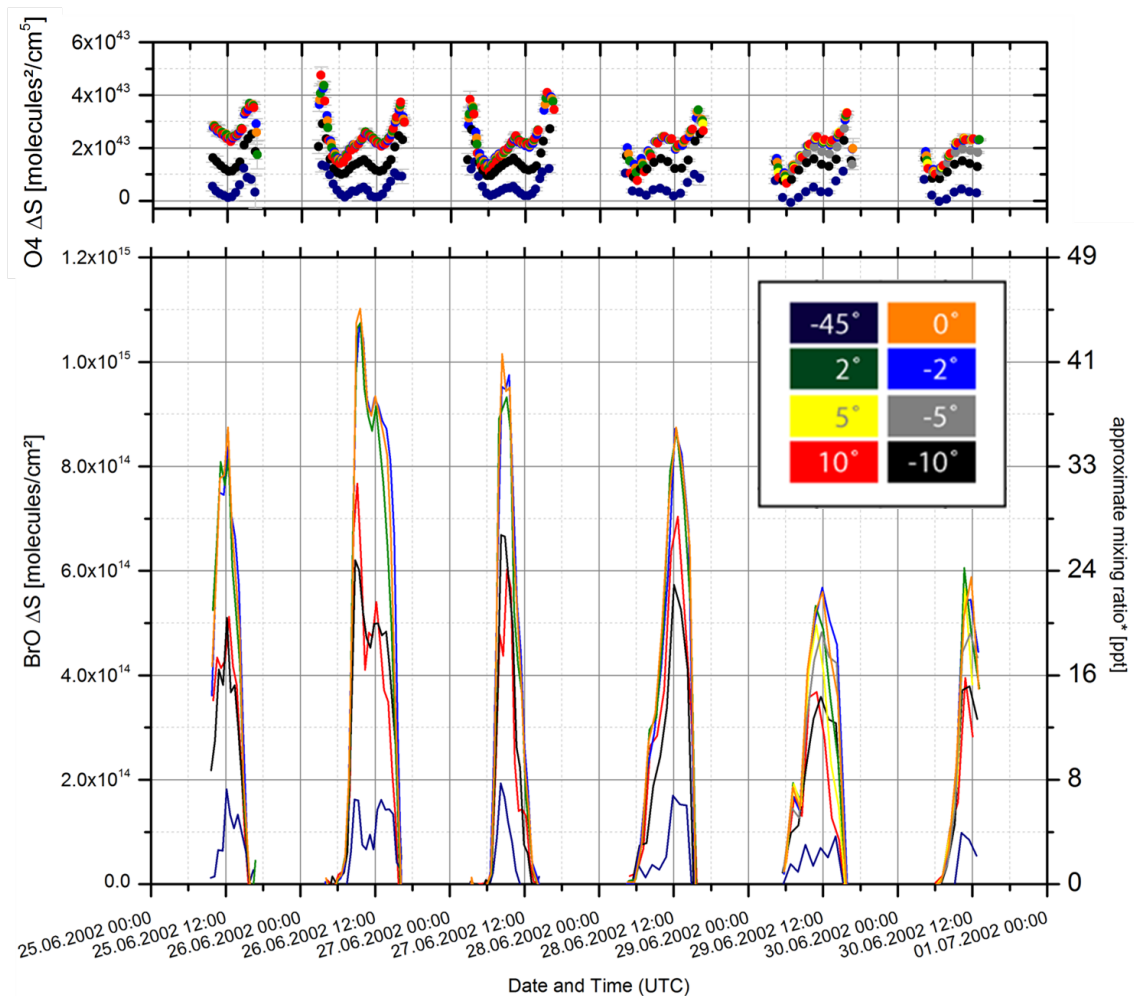


Figure 9.2: Differential slant column densities ΔS of BrO for a series of telescope elevation angles (color coded) between 25 June 2002, 9:03 UTC and 1 July, 12:45 UTC at Masada Top. Data provided by Zingler (2002). (*mixing ratios on the right y-axis are a rough estimate for a homogeneous distribution of the absorber along a characteristic light path of 10 km.)

BrO shows one to three maxima between 9:00 and 18:00 LT with mixing ratios up to 135 ppt (see Figure 9.6). Often the highest mixing ratios are found in elevated layers up to 1400 m agl with an extent of several hundred meters. It should be noted, that several hundred meters correspond to the order of magnitude of the vertical resolution of the profile retrievals and that the actual thickness of the layers might even be thinner. The diurnal variation of the profiles indicates that BrO is probably formed in elevated layers apparently independently from direct surface emissions of BrO.

A striking temporally as well as spatially complementary behavior between BrO and NO_2 is visible on each day. The mixing ratios of BrO plotted against the mixing ratios of NO_2 during the six days (Figure 9.5) reveal that BrO is observed only when NO_2 is below a threshold of 2-3 ppbv. Possible explanations for this will be given

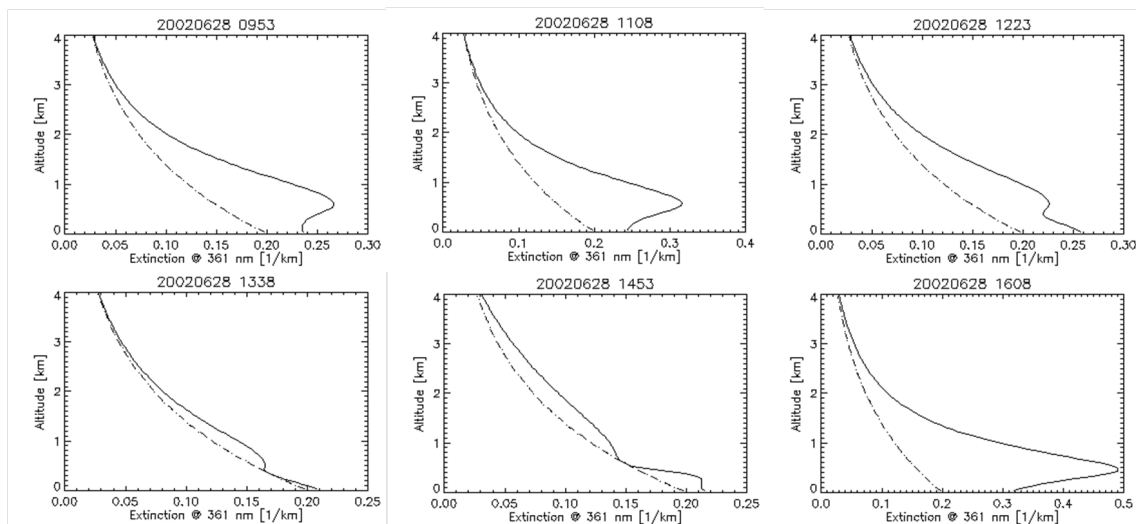


Figure 9.3: Example of aerosol extinction vertical profiles retrieved from MAX-DOAS ΔS of O_4 in the course of the day on 28 June 2002. Times are given in UTC. The profiles were retrieved with a exponential a priori vertical profile (dashed line). Grid resolution is 50 m. Altitudes refer to ground (agl). (cf. Figure 9.6)

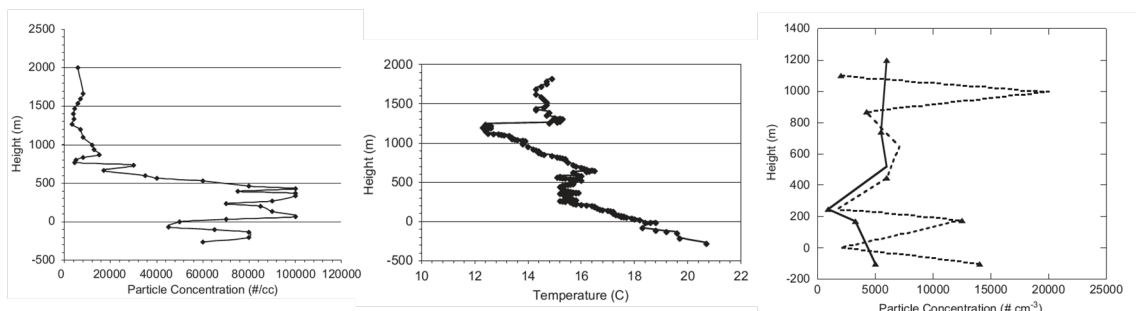


Figure 9.4: Left panel: The vertical profile of particle concentrations as measured by the CN counter during a flight above the Dead Sea valley on 29 April 1999, (starting at 09:45 and ending at 10:15LT); central panel: The vertical profile of temperature measured during a flight above the Dead Sea on 29 April 1999 (starting at 09:45 and ending at 10:15LT); right panel: Vertical profiles of average particle concentrations, measured on 31 July 1998. The dashed and solid curves represent the particle concentrations at 11:00LT and at 13:00LT, respectively. Altitudes refer to sea level (asl) with 0 m asl = 423 m agl. (Levin et al., 2005)

in the discussion in the end of the section.

History of Air Masses: Trajectories calculated with HYSPLIT (Draxler and Rolph, 2003) based on data by the NCEP/NCAR Reanalysis Project show three different mesoscale scenarios at the Dead Sea during the measurement period with only minor variations during daytime. Backward trajectories (24 hours run time each) are calculated with end points at 200 m, 600 m and 1000 m height above

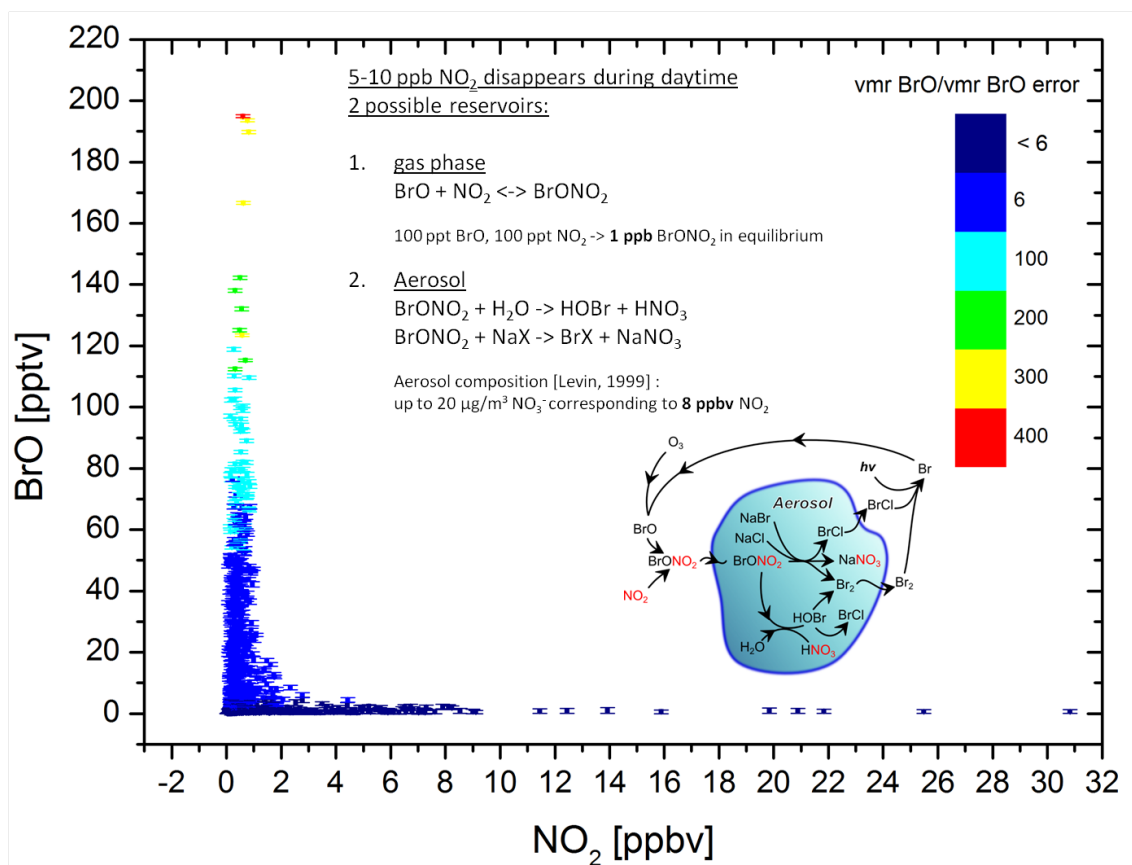


Figure 9.5: *BrO versus simultaneous NO_2 mixing ratios retrieved from MAX-DOAS during the measurement period in 2002. The colorbar indicates the ratio between signal and retrieval error. BrO is observed only when NO_2 is below a threshold of 2-3 ppbv.*

ground at 31.294°N , 35.404°E which is situated between the northern and the southern part of the Dead Sea, east of the measurement site at Masada. On all days the trajectories indicate air masses coming from the Mediterranean sea from northwestern directions. On 25 and 26 June air masses arrive at the coast between Gaza and Tel Aviv and propagate to the Dead Sea crossing Hebron. On 27 and 28 June the trajectories coming from the sea over the Gaza Strip divert from the vicinity of Hebron and go past West Bank more southerly. Finally on 29 and 30 June air masses reach the coast between Tel Aviv and Haifa, pass Jerusalem and the southern part of West Bank before they arrive at the Dead Sea. A dependency of *BrO* on the origin of the air masses can not be recognized. Example trajectories from 26 and 28 June 2002 16:00 are shown in Figure 9.1.

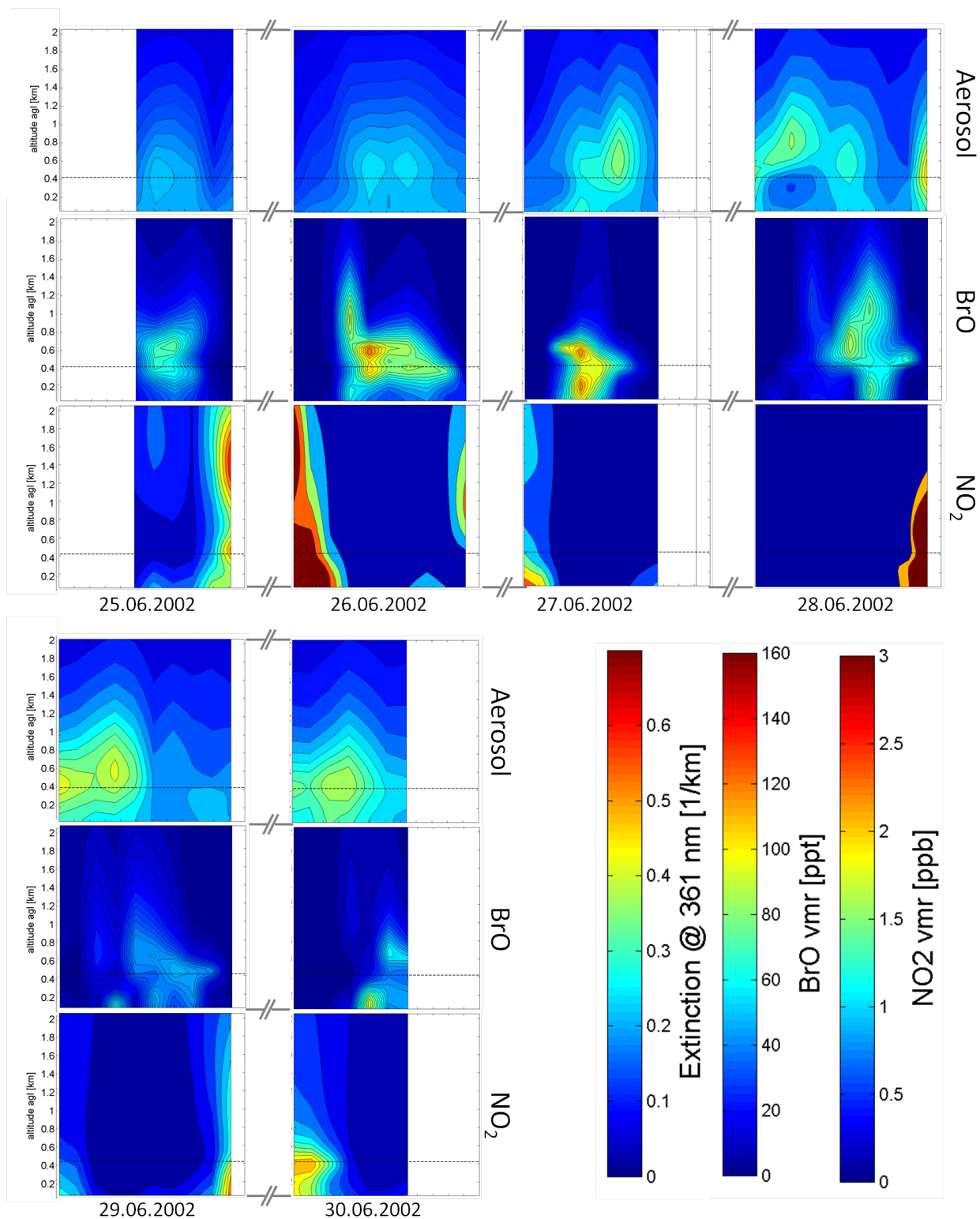


Figure 9.6: Diurnal profiles between 8:00 and 20:00 LT of aerosol extinction and mixing ratios of BrO and NO₂ retrieved from MAX-DOAS slant column densities, measured between 25 June and 30 June 2002 at Masada Top. The dashed line indicates the altitude of the instrument at Masada above the water level of the Dead Sea.

9.1.2 MAX-DOAS and LP-DOAS measurements in 2012

Vertical Profiles of aerosol extinction, BrO and NO₂ at Masada and Ein Bokek are shown in Figures 9.8 and 9.9, respectively.

Some of the characteristics described in 9.1.1 can be found again at both measurement sites: Aerosol abundance is highest in the upper half of the valley. Below 200 m - 500 m a second layer can be seen; in most cases BrO is constrained to layers with a thickness of 200 m - 300 m and high BrO and NO₂ mixing ratios are mutually exclusive. At Masada occasionally the lower aerosol layer splits into two, see Figure 9.7 and the lower layers tend to apparently merge with the upper one until 14:00 LT.

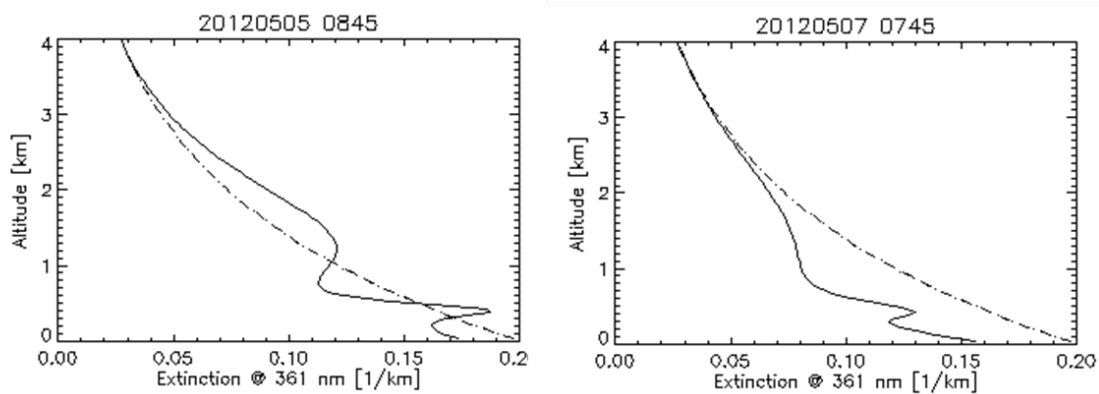


Figure 9.7: *Aerosol extinction vertical profiles on 5 May 2012 and 7 May 2012. Times are given in UTC. The profiles were retrieved with a exponential a priori vertical profile (dashed line). Grid resolution is 50 m. (cf. Figure 9.8)*

Two of thirteen days (13 and 14 May 2012) show unique meteorological conditions and will be compared with a "typical" day (12 May 2012), which is dominated below. Figures 9.10 (whole measurement period), 9.11 and 9.12 show a comparison between the well-defined mixing ratios measured by LP-DOAS at Ein Bokek, provided by Schmitt (2012), and MAX-DOAS measurements from Masada and Ein Bokek. The MAX-DOAS values shown represent the lowest 50 m of the height grid (cf. chapter 5 and section 8.3). MAX-DOAS and LP-DOAS at Ein Bokek show generally very good agreement, in particular for surface NO₂ volume mixing ratios, although the measurements at Masada have smaller sensitivity for the ground. On the comparison of MAX-DOAS and LP-DOAS measurements also see Friess et al. (2011). Differences in BrO with time shifts of around 30 minutes between the two devices as can be seen in the left panel of Figure 9.12 may be due to the slightly different measurement geometries. On 3 May between 9 and 11 UTC MAX-DOAS seems to detect the signal BrO 20-30 min before the LP-DOAS. At that time wind came from East with 10-5 km/h. Due to the longer lightpath and the orientation of the MAX-DOAS it probably detects BrO-rich air masses before they arrive the lightpath of the LP-DOAS. This indicates a heterogeneous horizontal distribution of BrO. At Masada overall higher mixing ratios of BrO are observed than at Ein Bokek, also ground values are higher. Ground values at Masada are afflicted with higher errors

due to the lower sensitivity at low altitudes, see Figure 8.3.

At Ein Bokek BrO from MAX-DOAS is frequently lower than from LP-DOAS. a possible reason for this finding is that BrO is located in a very shallow layer above the ground that cannot be resolved by MAX-DOAS, which yields over the lowermost ≈ 200 -300 m (see averaging kernels discussed in section 8.3.2). Also IO was detected by the LP-DOAS measurements showing distinct peaks around 15:00 LT with mixing ratios up to 4 ± 0.6 ppt and an anticorrelation with BrO (not shown). This is consistent with findings by Zingler and Platt (2005). However, this work focusses on BrO at the Dead Sea.

History of Air Masses: On 10 out of 14 days (2 May - 15 May) daytime air masses from the north-west arrive at the Dead Sea after entering the Mediterranean coast between Gaza and the northern border of Israel and crossing West Bank. The other days Mediterranean air masses curve over Egypt and arrive at the Dead Sea more southwesterly. The influence of trajectories on the local meteorology at the Dead Sea will be regarded in the next paragraph.

Meteorological parameters during the measurement campaign are given in Figures A.3 and A.4, courtesy of IMK (Corsmeier and Kottmeier). Solar radiation, air pressure and air temperature are consistent with the findings by Hecht and Gertman (2003). Relative humidity during daytime is 20-30 % lower than reported by Hecht and Gertman (2003) from weather stations offshore and close to the shore (cf. section 7.1.6).

Except for 5 days (2, 3, 10, 13 and 14 May), rather constant northerly to easterly winds predominate during daytime in the Dead Sea Valley. Most deviations from northerly/easterly daytime winds are combined with high wind speeds. Excluding 10 May, these days with variable wind directions coincide with synoptic winds from southwest to west, which tend to be stronger than northeasterly synoptic winds. This agrees with the finding by Segal et al. (1983) that strong zonal winds perturb local circulation patterns. From our data it can be assumed that the formation of thermally induced flow patterns has a stabilizing character inside the valley, whereas strong external zonal winds (windspeed > 3 -4 m/s) penetrate the valley resulting in alternating winds. This will be examined in more detail in the following on the days 12, 13 and 14 May 2012.

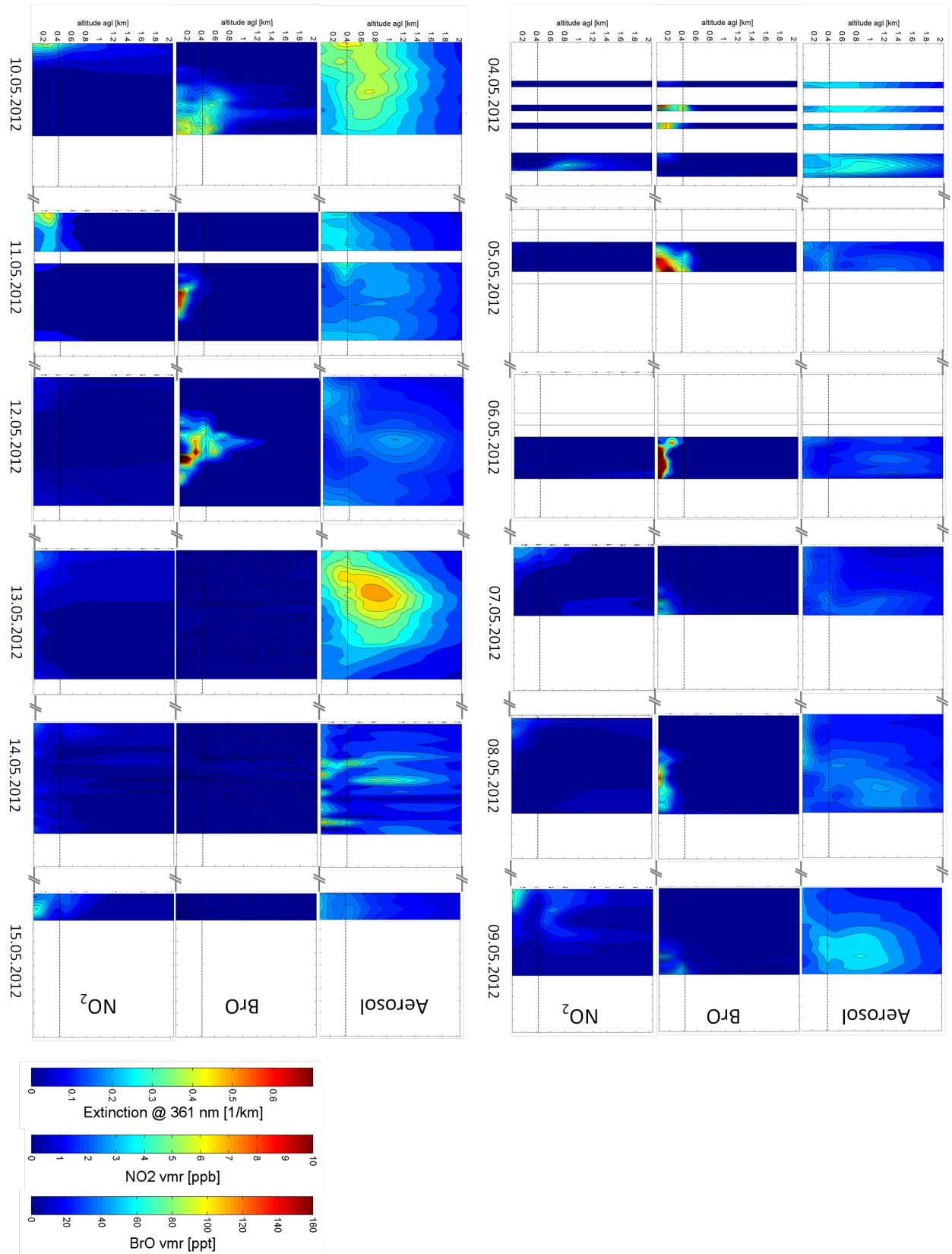


Figure 9.8: Diurnal profiles between 8:00 and 20:00 LT of aerosol extinction and mixing ratios of BrO and NO₂ retrieved from MAX-DOAS slant column densities, measured between 4 May and 15 May 2012 at Masada Top. The dashed line indicates the altitude of the instrument at Masada above the water level of the Dead Sea. Date on the x-axis refers to local time.

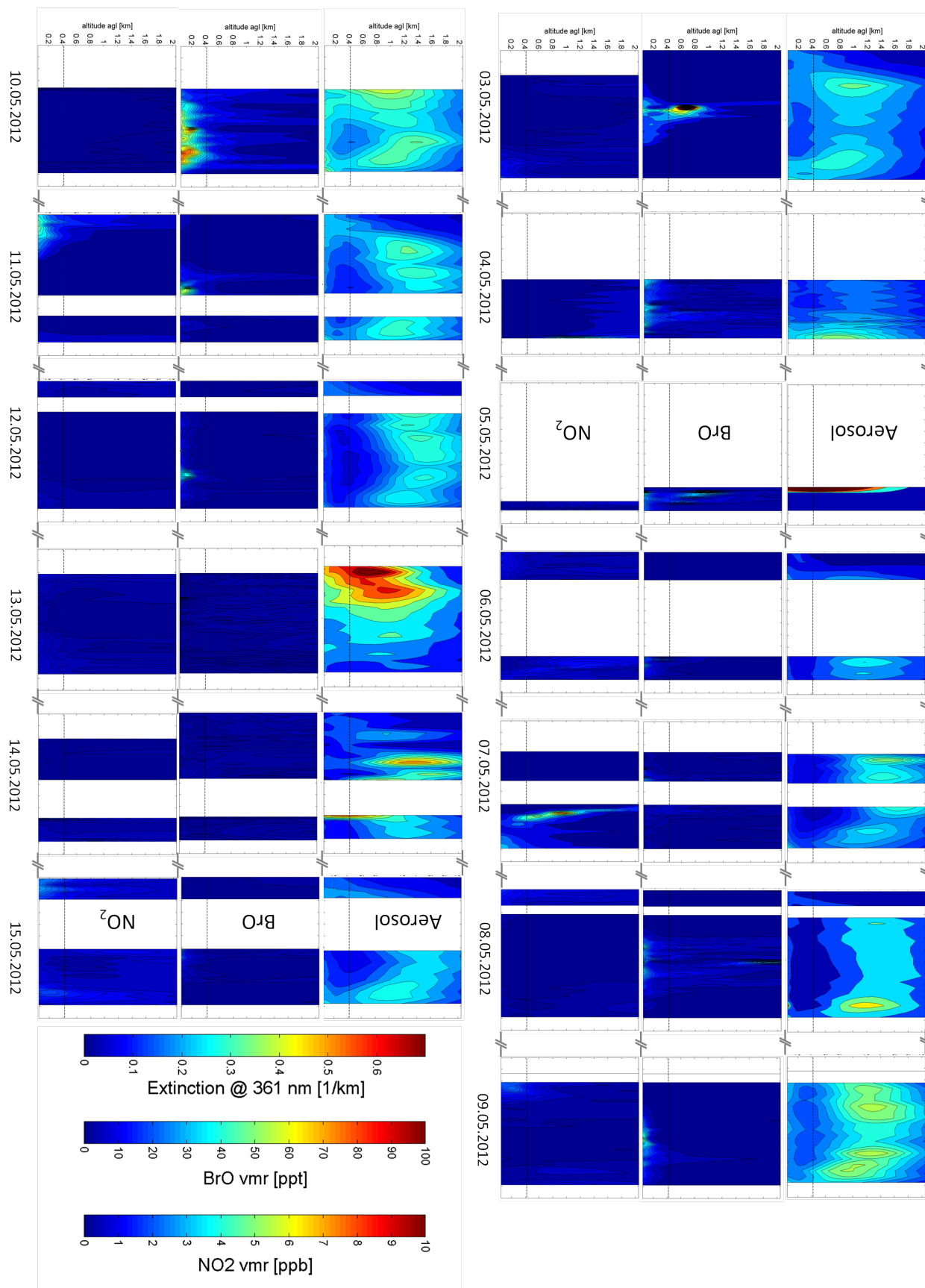


Figure 9.9: Diurnal profiles between 8:00 and 20:00 LT of aerosol extinction and mixing ratios of BrO and NO₂ retrieved from MAX-DOAS slant column densities, measured between 3 May and 15 May 2012 at Ein Bokek. The dashed line indicates the altitude of the instrument at Masada above the water level of the Dead Sea. Date on the x-axis refers to local time.

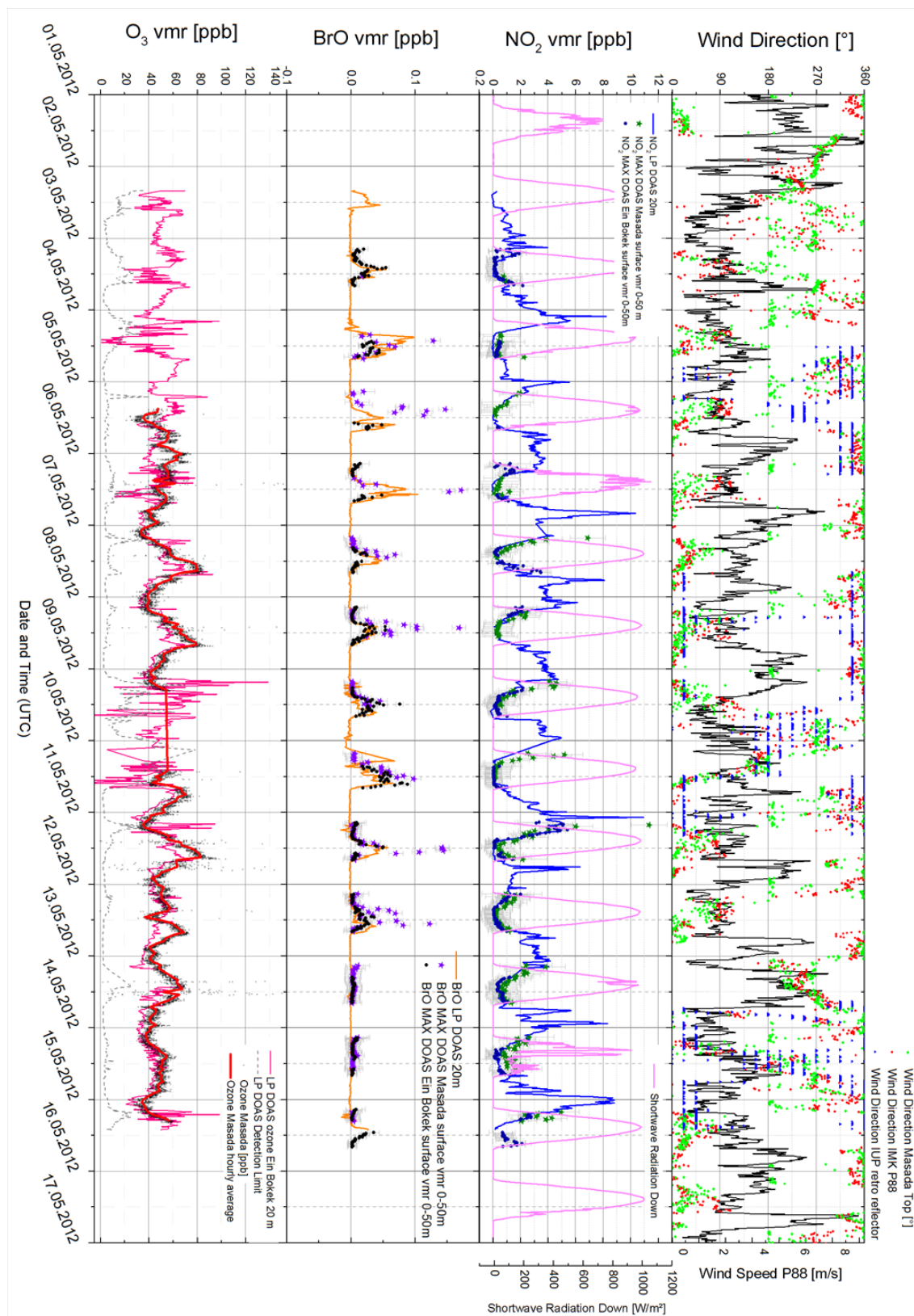


Figure 9.10: Mixing ratios of BrO and NO₂ measured with MAX-DOAS and LP-DOAS (Schmitt, 2012) between 2 May and 15 May 2012 at Ein Bokek and Masada. Wind data was kindly provided by IMK (Corsmeier and Kottmeier). Ozone was measured with LP-DOAS at Ein Bokek and with a mobile ozone monitor at Masada.

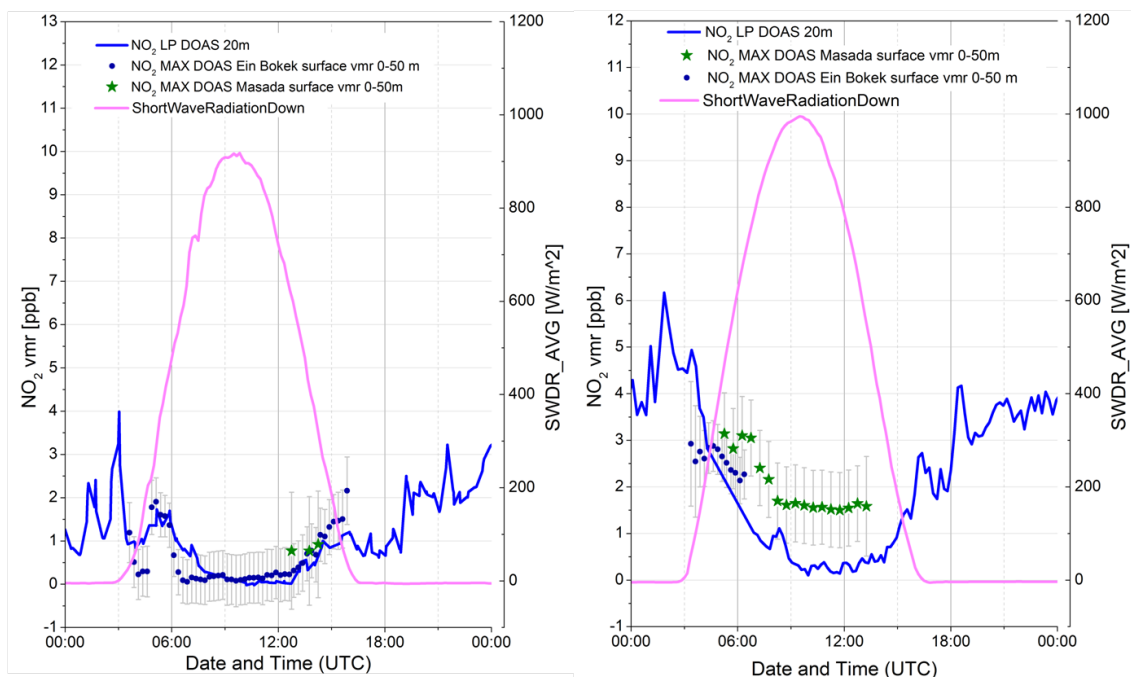


Figure 9.11: *Mixing ratio of NO₂ measured with MAX-DOAS and LP-DOAS (Schmitt, 2012) on 3 May and 8 May 2012 at Ein Bokek and Masada.*

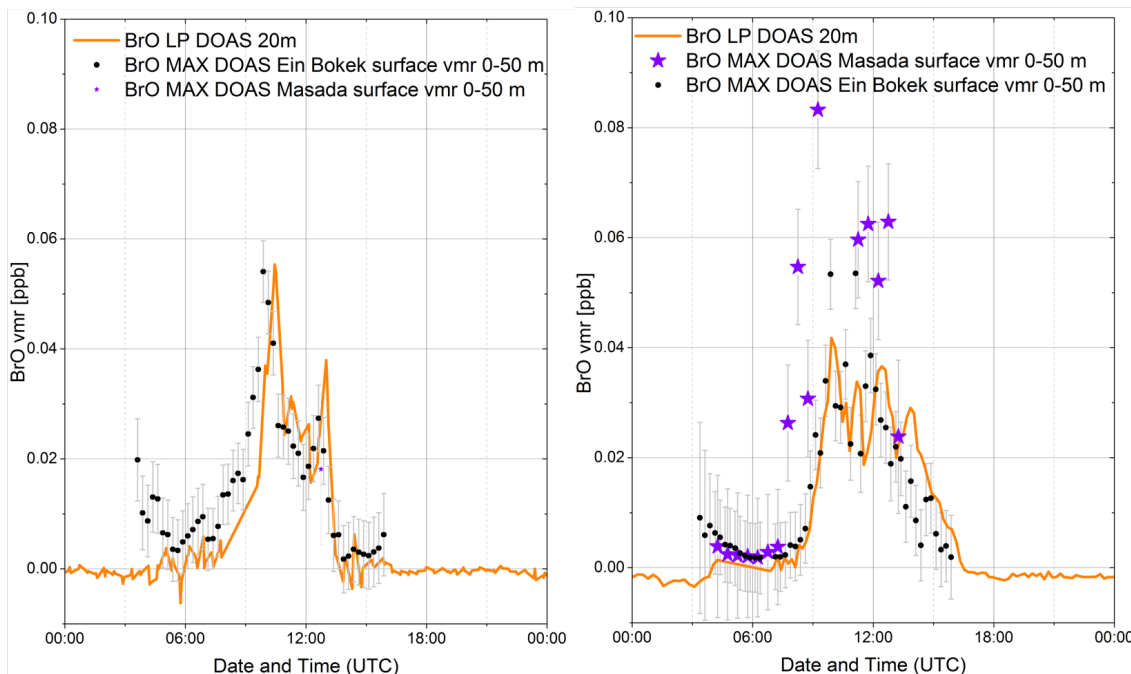


Figure 9.12: *Mixing ratios of BrO and NO₂ measured with MAX-DOAS and LP-DOAS (Schmitt, 2012) on 3 May and 8 May 2012 at Ein Bokek and Masada.*

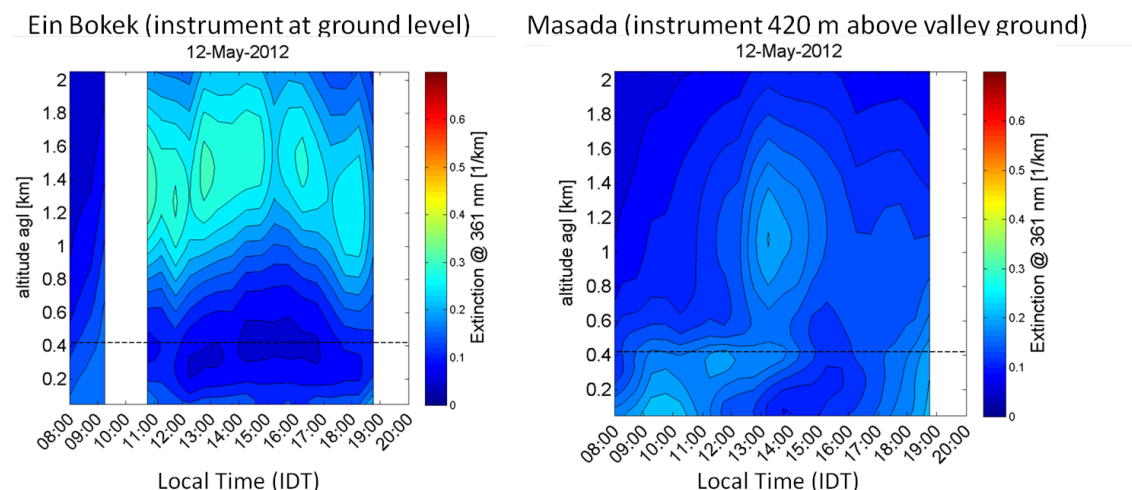


Figure 9.13: Diurnal profiles of aerosol extinction on 12 May, 2012 at Ein Bokek and Masada. The dashed line indicates the altitude of the instrument at Masada above the water level of the Dead Sea.

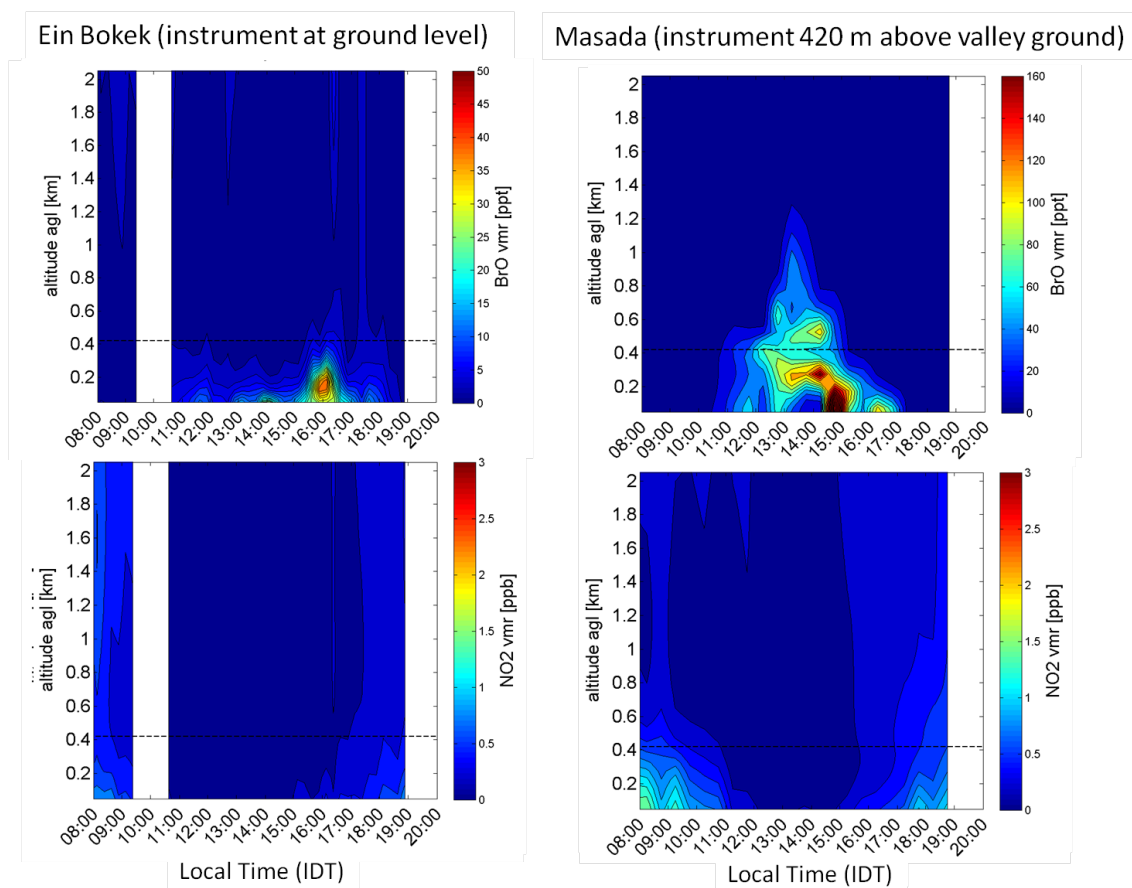


Figure 9.14: Diurnal profiles of the mixing ratios of BrO and NO₂ on 12 May, 2012 at Ein Bokek and Masada. The dashed line indicates the altitude of the instrument at Masada above the water level of the Dead Sea.

12 May 2012: The 12 May 2012 is a day with meteorological conditions, which can generally be described as "typical" referring to literature and local sources. A white haze reduces the visibility of the opposing Jordan mountains, see Figure 9.20. In the night northwesterly winds with windspeed > 3 m/s prevail. At the bottom station P88 around 1:00 LT wind becomes weaker (< 3 m/s) and begins to turn over south to east until 9:00 LT, resulting in constant easterly wind until the afternoon. Around 11:00 LT the wind speed decreases from ~ 2.3 to ~ 1.5 . This is when NO_2 falls below 1 ppb and first BrO becomes visible, see Figure 9.15. It should be noted that total retrieval errors (including both noise error and smoothing error) are max. 10 ppt for BrO and 0.7 ppb for NO_2 , respectively. BrO appears first at ground and at instrument height Masada 25 min later, probably due to vertical transport (0.3 m/s). At both sites there is a maximum at 11:45 (12 ppt at Ein Bokek, 60 ppt at Masada). Until 15:00 LT BrO at Ein Bokek is only present in shallow layers, whereas at Masada elevated layers form while ground values even decrease below detection limit between 13:30 and 14:15 LT. A reason for this might be a short period of increased wind speed of up to 2.2 m/s between 13:00 and 13:50. A similar event can be seen at Masada at 15:45 LT with maximum wind speed 2.6 m/s. Only around 15:00 LT wind shifts to northerly directions and increases from 1.8 to 2.6 m/s. Between 15:20 and 17:00 LT at P88 the vertical wind speed is negative down to -0.1 m/s. This coincides with the BrO peak around 16:00 LT at Ein Bokek (~ 30 ppt). At Masada the corresponding peak occurs around 1 hour earlier. This is in good agreement with the transport time of northern wind from Masada to Ein Bokek with a wind speed of 2.5 m/s and a distance of 10 km between the two lightpaths. The shift of wind direction, the negative vertical wind speeds and the decreasing upper BrO at Masada indicate that the upper layers destabilize and BrO-rich air masses fall down and are advected to Ein Bokek. At Masada from 17:15 LT and at Ein Bokek from 18:40 LT on BrO is below detection limit, which is assumed to be the six-fold DOAS fit error (see chapter 4). At that times solar radiation has dropped from 1368 W/m^2 at peak (12:50 LT) to 770 W/m^2 and 510 W/m^2 , respectively.

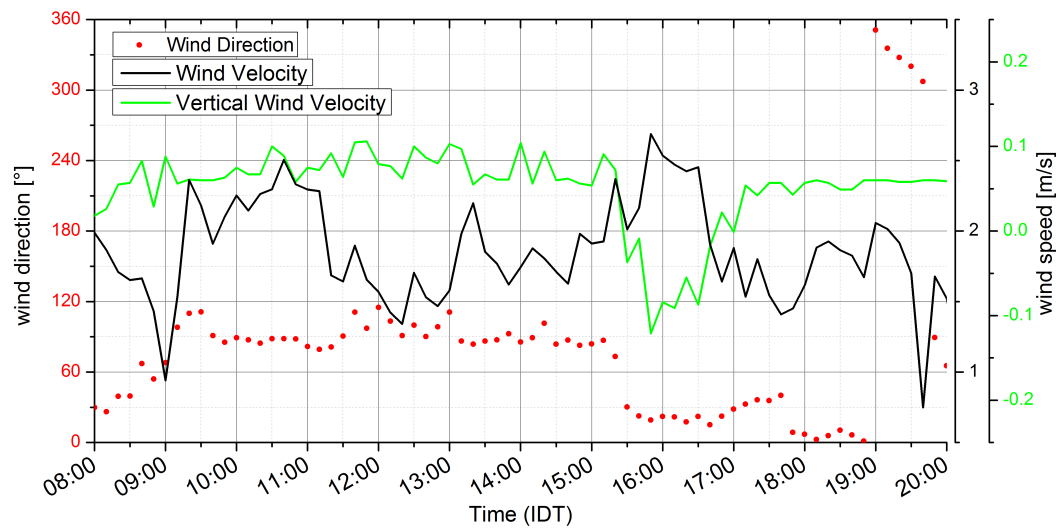


Figure 9.15: Horizontal and vertical wind speed and wind direction measured at weather station P88 (cf. Figure 7.11) on 12 May 2012 (Local Time).

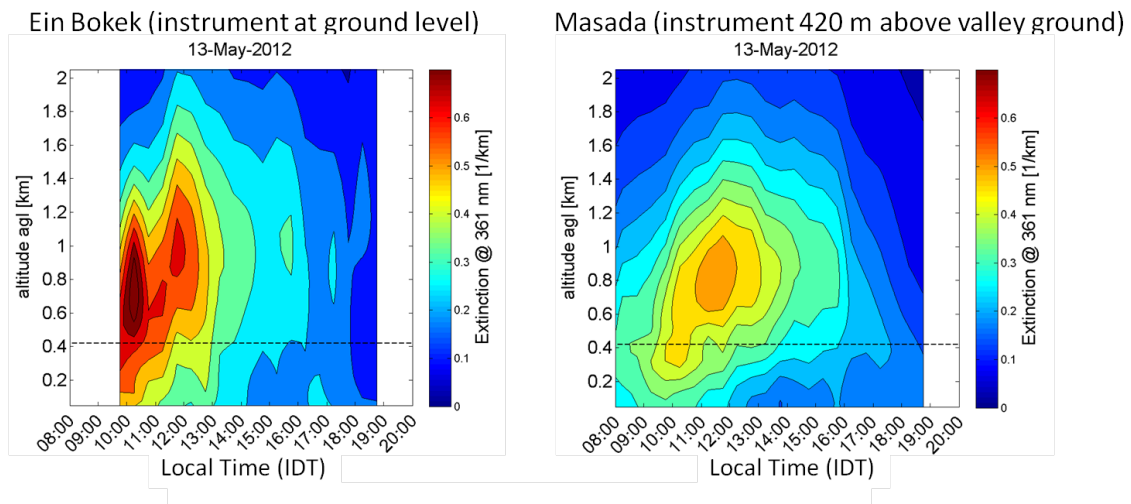


Figure 9.16: Diurnal profiles of aerosol extinction on 13 May, 2012 at Ein Bokek and Masada. The dashed line indicates the altitude of the instrument at Masada above the water level of the Dead Sea.

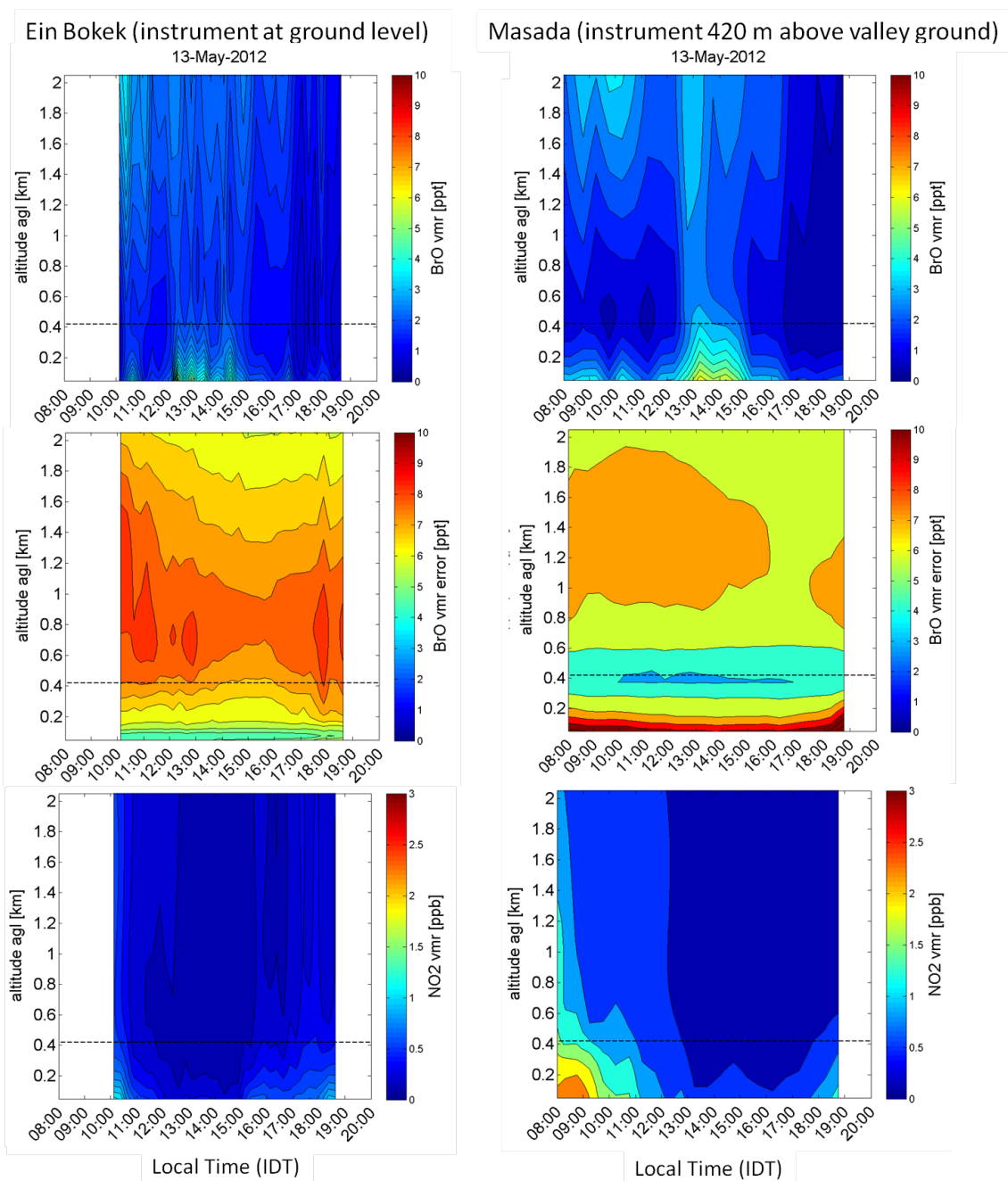


Figure 9.17: Diurnal profiles of the mixing ratios of BrO and NO₂ on 13 May, 2012 and retrieval error of BrO at Ein Bokek and Masada. The dashed line indicates the altitude of the instrument at Masada above the water level of the Dead Sea.

13 May 2012: This day is characterized by continuous and strong (> 3 m/s) westerly wind starting at 7:30 and ending at 20:20 LT. At both measurement sites the highest aerosol extinction during the measurement period is observed with extinctions of up to 0.7 km^{-1} . The aerosol load in the forenoon is closer to the valley ground than on other days, see Figure 9.16. Strong westerly winds were observed bringing dust into the Dead Sea Valley, which was deposited on surfaces. Instead of the typical whitish haze prevailing in the Dead Sea Valley, a more dense, reddish one could be observed. From Ein Bokek the opposite shore could not be seen until $\sim 18:00$ LT (cf. Figure 9.20). Mixing ratios of *BrO* are scarcely above detection limit, see Figure 9.17. NO_2 is slightly higher after 11:00 LT than at the preceding days. From 12:00-13:00 LT the bulk of aerosol is constrained on heights above 400 m (Figure 9.16) coinciding with increasing *BrO* below.

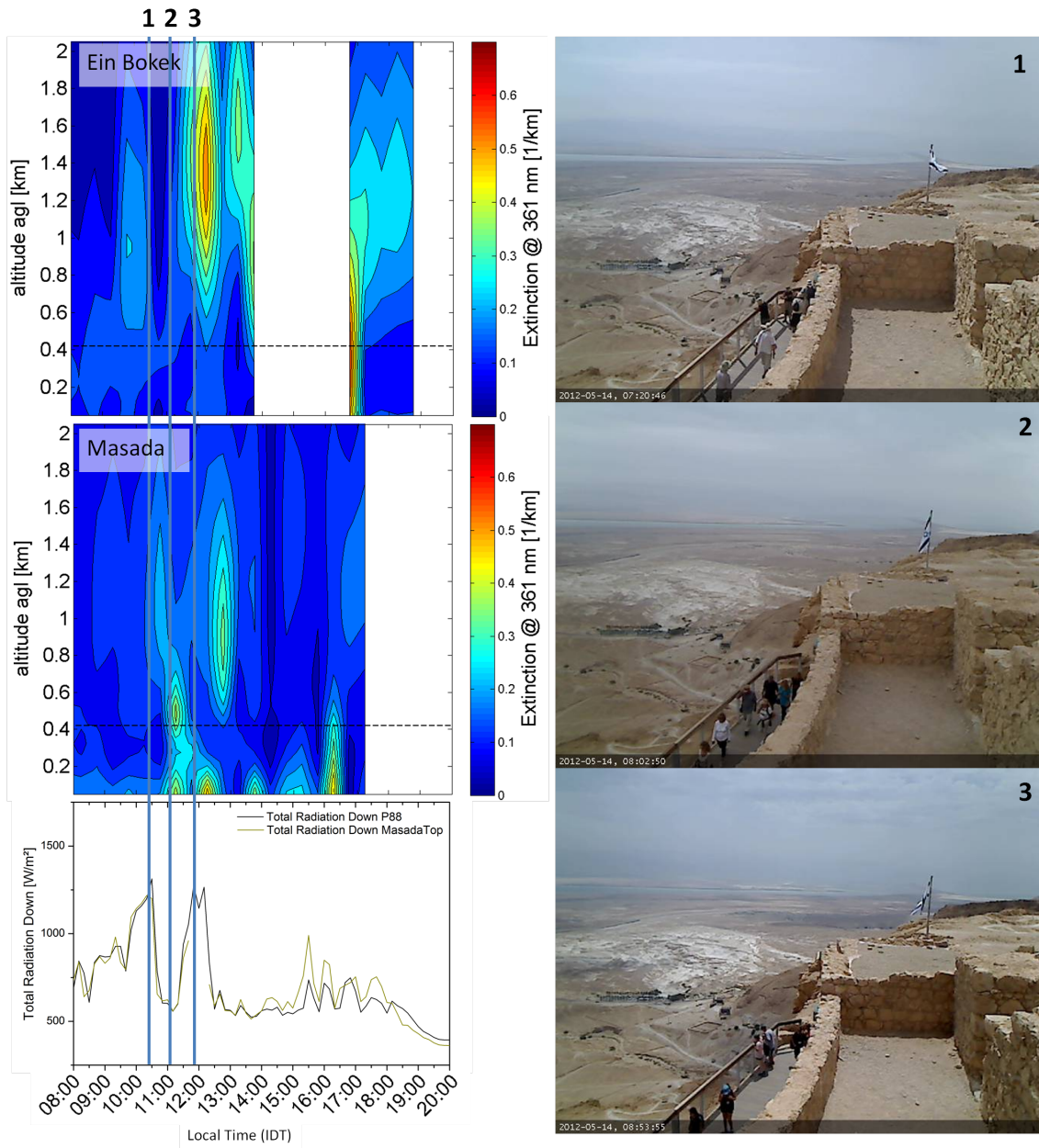


Figure 9.18: Diurnal profiles of aerosol extinction at Ein Bokek and Masada on 14 May 2012. Below on the left the course of the total solar radiation (Corsmeier and Kottmeier) is shown. On the right hand side automatically recorded pictures at the measurement site Masada show the lighting conditions recognizable by the shadow of the walls. The vertical lines on the left hand side indicate the recording times of the photos.

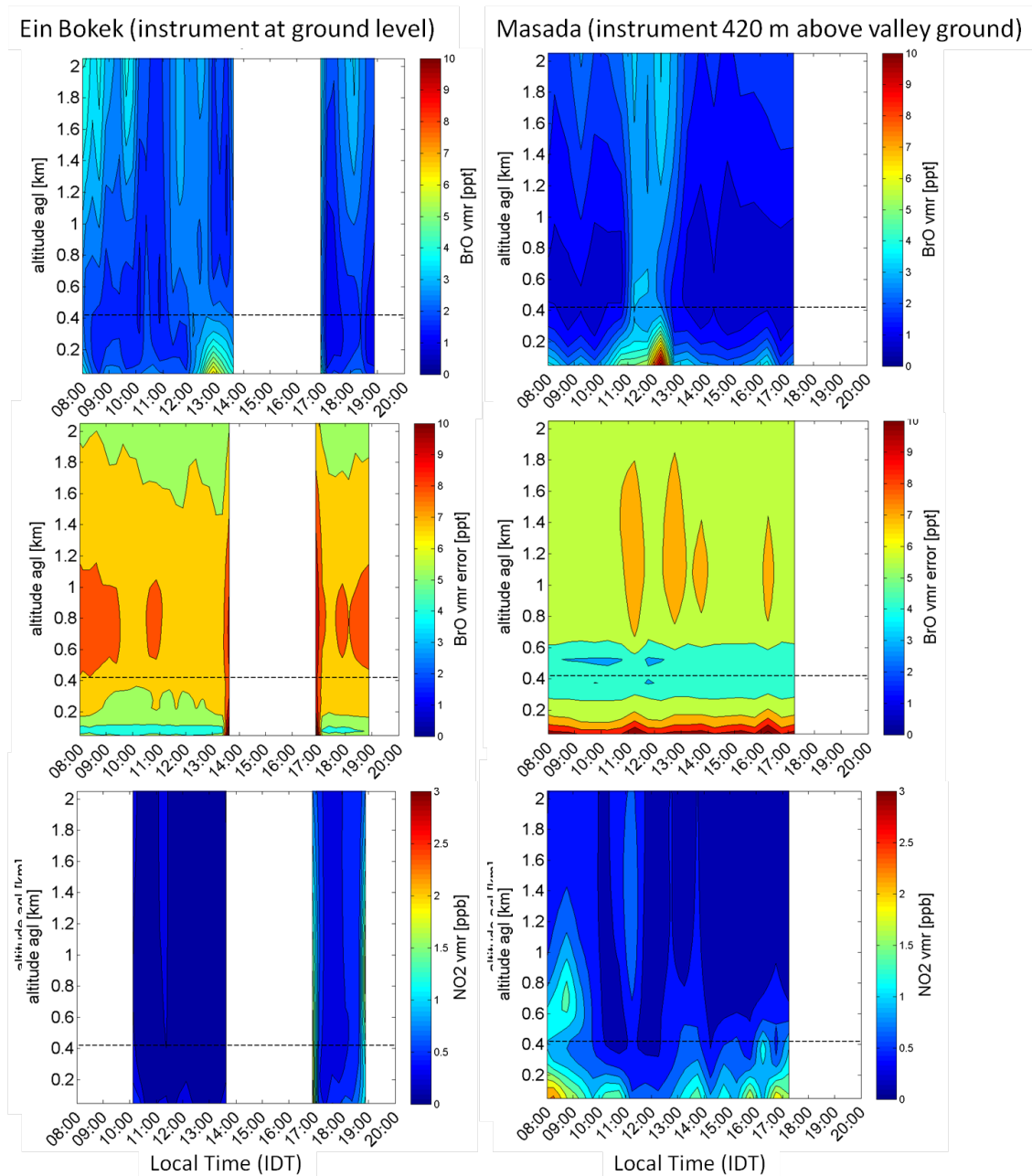


Figure 9.19: Diurnal profiles of the mixing ratios of BrO and NO₂ on 14 May, 2012 and retrieval error of BrO at Ein Bokek and Masada. The dashed line indicates the altitude of the instrument at Masada above the water level of the Dead Sea.

14 May 2012: Aerosol layers disappear and redevelop at hourly intervals, see Figure 9.18). In contrary to "typical" days on both days mixing ratios of BrO are mostly below and sporadically very close above the detection limit at both measurement sites for all three DOAS instruments (cf. Figure 9.10 (third panel) and 9.19). NO_2 appears in single peaks at Masada with an approximate duration of 1 hour, partly coinciding with aerosols indicating polluted air.



Figure 9.20: View from Ein Bokek measurement site towards the retro reflector on three consecutive days (12, 13 and 14 May 2012). Left picture: On 12 May, like eleven days before, a whitish haze was present throughout the day. On some days only the ridge of the opposite Jordan mountains is recognizable. Central picture: Strong westerly winds bring dust into the valley resulting in reddish haze. The Jordan mountains are not visible until the evening. Right picture: Variable cloudy conditions alternate with short periods of sunshine. Structures of the opposite Jordan mountains can be seen clearly.

9.1.3 Car-DOAS measurements in 2012

Six exploratory cruises were performed for Car-DOAS measuring slant column densities dS of BrO. The measurement periods are shown in Figure 9.21. It should be noted that this data has to be regarded just qualitatively, for the following reasons: Reported wind directions were read from a magnetic compass and waving flags or trees. Also compare A.4 and A.4.

The shown dS are relative to an arbitrary reference spectrum during the cruise and thus, they indicate lower limits, since they contain an unknown offset. dS correspond to integrated concentrations along the lightpaths entering the telescope, which are not known exactly due to missing information on radiative transfer. Especially during hazy conditions the characteristic length of light path is shorter than 10 km, therefore the presented dS have to be regarded as integrated along several kilometers perpendicular to the street. Further uncertainties are caused by the unknown lateral and longitudinal angles of the street and the car. Nevertheless, from 10 to 12 May a consistent trend of highest dS close and slightly south of Masada is recognizable and patterns of BrO along the route could be reproduced while driving in the opposite direction a few hours later on all of those three days (cf. Figure 9.22, 14:45-15:50 LT). On 9 May overall BrO levels are relatively low (especially at Masada) and at the starting time of the car measurement 17:30 LT the main peak might have already been over. On 13 and 14 May dS are scarcely above detection limit (median detection limit is 2×10^{13} molecules/cm²).

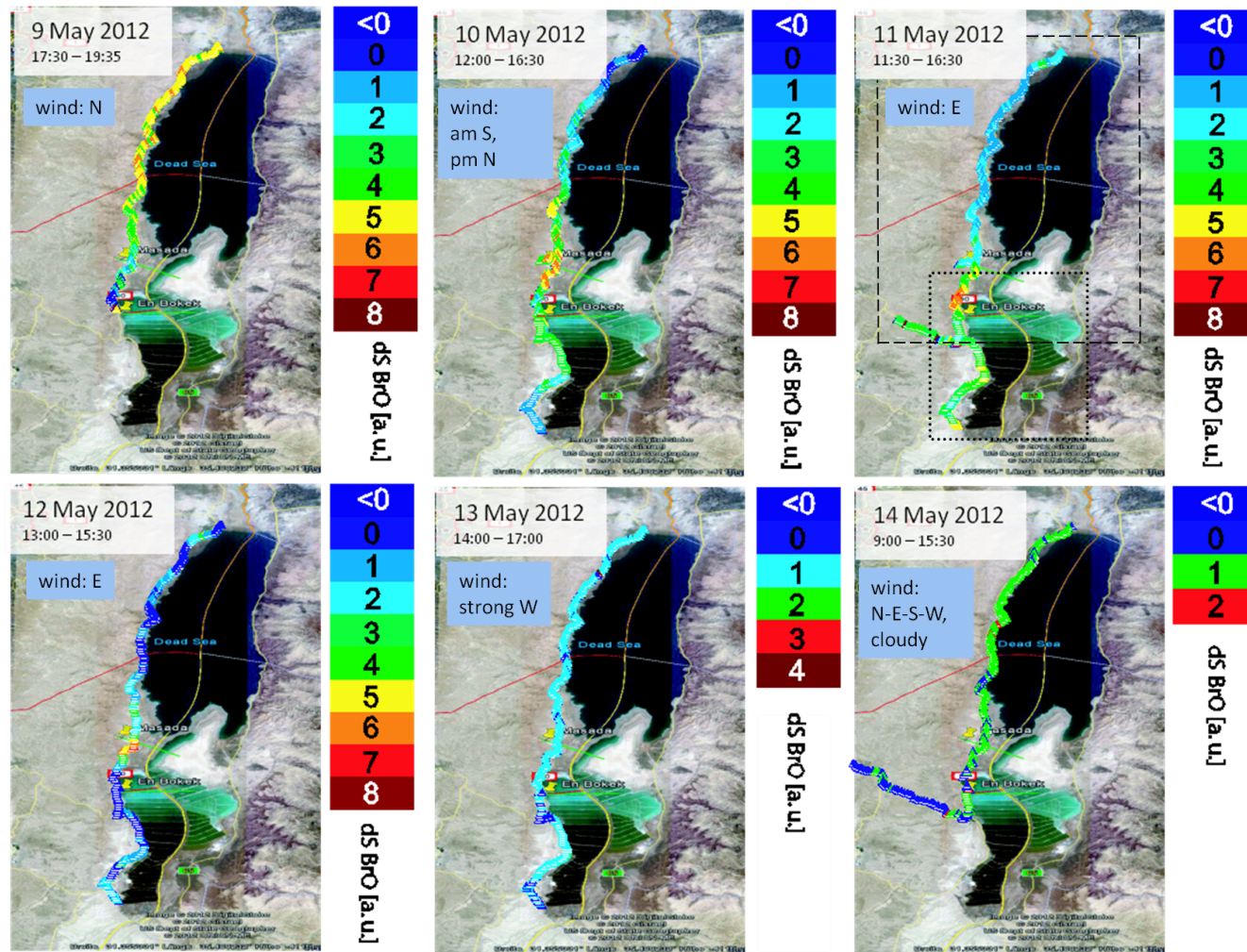


Figure 9.21: Differential slant column densities dS of BrO measured along Route 90 (north to south) during the indicated times with cruise periods and main wind directions. Unit intervals correspond to 1×10^{14} molecules/cm². The telescope was orientated towards the Dead Sea with an elevation angle of 20° relative to the car. Highest relative levels were found from 10 May to 12 May in the south of Masada (cf. Figure 9.22). The dashed and dotted lines indicate the northern and southern map areas displayed in Figure 9.22, respectively.

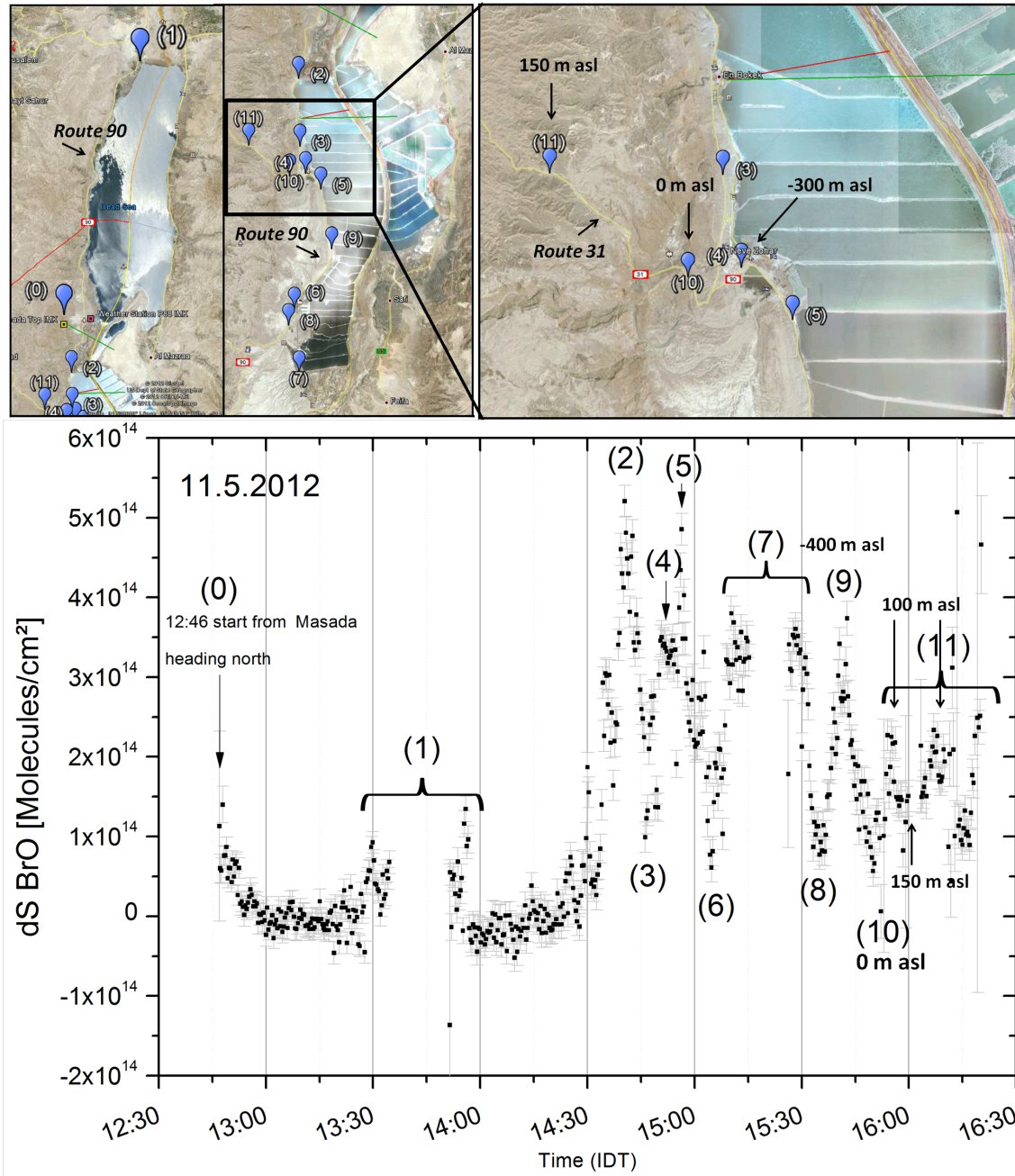


Figure 9.22: Differential slant column densities dS of BrO in the course of Route 90 on 11 May 2012. Numbers in brackets mark special events described in the text in chronological order.

As an example, more detailed information on the data obtained from the cruise on 11 May 2012 is shown in Figure 9.22. *Route 90* follows the north-south axis of the Dead Sea, whereas *Route 31* leaves the Dead Sea Valley in the central southern part, crossing the mean sea level (0 m asl) and leading to the city Arad in the West. The measurement started at Masada from where we went north to the turning point at (1), parking there from 13:30 to 14:00 LT. During that time we observed easterly wind to still air and significant BrO levels were detected dropping below detection

limit again while driving south around 13:56 LT. Between (1) and (2) there are two minor peaks at 14:14, coinciding with an elevated street level (up to -270 m asl = 145 m above lake level), and at 14:30 in the plain in front of Masada where first northeasterly winds were observed. At (2) we passed the Dead Sea Works pumping station P5 and the first evaporation pond on Israeli side accompanied by northerly to northeasterly winds, the water surface was smooth. *BrO* levels decrease clearly passing the Hotel area at Ein Bokek at (3), possibly due to the larger horizontal (~ 400 m) and vertical (~ 70 m) distance between street and ponds, but increase again passing Neve Zohar, interrupted by a curve where viewing direction was northwest at 14:49 LT. After the curve levels remain quite stable until the street gets closer (< 100 m) to the evaporation ponds again at (5). Moreover the evaporation ponds in the center of the southern part are those with the highest salt concentration. The next distinct minimum at (6) coincides with comparatively very high *dS* of NO_2 ($\sim 3 \times 10^{16}$ molecules/cm², not shown) attributed to the Dead Sea Works premises, wind came from northeast. At (7) we parked at the southern end of the basin with wind coming from north, where *BrO* levels are higher again, probably due to the smaller distance to the evaporation ponds. Afterwards we returned to the north finding again the local minimum at (8), a local maximum at (9) corresponding to (5), where the street is close to the ponds and NO_2 is low again. On the way back north we turned to the left leaving *Route 90* at Neve Zohar going towards Arad on *Route 31* (10) and leaving the Dead Sea Valley. We followed the road up to an altitude of approximately 220 m asl, where we turned the vehicle and returned to Ein Bokek (11). After the first local maximum at approximately 100 m asl *BrO* levels found at northeasterly viewing directions dropped down until the turning point and increased again the way back at around 100 m asl peaking at similar values.

9.1.4 Discussion

Almost every day, the vertical profiles of aerosol extinction and *BrO* presented in 9.1.1 and 9.1.2 show local minima between 10:00 LT and 19:00 LT at altitudes between 300 m and 500 m agl and sometimes also between 700 m and 900 m agl. This suggests the existence of recurrently forming barriers for vertical transport during daytime, see section 7.1.6. The presence of elevated layers is confirmed by ozone levels at Masada Top, which decrease down to around 40 ppb in the presence of elevated *BrO* layers on 10 and 12 May, but peak around 75 ppb on days where no elevated layer of *BrO* is observed at Masada, e.g. on 7, 8 and 11 May 2012 (cf. Figures 9.8 and 9.10).

Also the results from Car-DOAS measurements on 11 May 2012 support the thesis of elevated *BrO* layers showing local maxima at 100 m asl \approx 500 m agl. However, as already mentioned above, this data has to be regarded carefully.

A probable explanation for this phenomenon is already given in 7.1.6 considering the dynamics in valleys in general: thermal winds on local scales and mesoscales create convective inversions and/or wind shears limiting vertical transport. An imaginable pattern for the specific case is sketched in Figure 9.23. The illustrated pattern has to be regarded as one plausible solution, but also other patterns with another number of circulation cells are possible. Especially the circulation cells on the eastern side

might be less pronounced than the ones in the west according to Segal et al. (1983). Of course this is a two-dimensional simplification neglecting superposed meridional components along the valley. The heights mentioned above (300-500 m agl and 700-900 m agl, respectively) conspicuously correspond to the edge of the valley and the terracing in the mid valley. Furthermore the existence of elevated layers seems to be strongly dependent on the locality, as can be seen by the comparison of BrO profiles at Masada and Ein Bokek (cf. the described example day 12 May 2012) and also the Car-DOAS measurements on 11 May 2012. Probably this is due to the complex, spatially highly variable patterns of dynamics in the Dead Sea Valley. The courses of 13 and 14 May 2012 obviously are clear examples of days not dominated by local circulations: On 13 May strong westerly winds penetrate the valley and suppress the formation of circulation systems, see Figure 9.24. On 14 May repeatedly decrease in solar radiation seem to disturb the perpetuation of vertical transport barriers, as can be seen by dissolving and subsiding aerosol layers, see Figure 9.18. Yet, it must be noted that this might also be an artifact caused by fractured clouds.

The explanation, that elevated layers of BrO and aerosols are caused by vertical transport barriers, is corroborated by observations reported by Bitan (1977), Segal et al. (1983), Niemi et al. (1997), Hecht and Gertman (2003) and Levin et al. (2005): As already mentioned, based on model studies (Segal et al., 1983) thermally induced circulations are predicted under suitable synoptic conditions. (Niemi et al., 1997), (Hecht and Gertman, 2003) and (Bitan, 1977) report about high spatial variability of wind directions along the Dead Sea. (Hecht and Gertman, 2003) summarize that there are significant differences in wind direction and wind speed measured at different positions around the Dead Sea with a prominent diurnal variation, indicating pronounced thermal turbulence. (Bitan, 1977) discusses the wind patterns between Kalya at the north of the Dead Sea and Sodom in the south in more detail. He also presents measurements of wind speed and wind direction at different heights over the bottom of the valley close to Mitspe Shalem in the northern part of the Dead Sea. Between 10:00 LT and 17:00 LT the author observes a "clear easterly flow" at a height of 200 - 400 m above the lake, whereas southeasterly to southwesterly winds are observed close to water level. Also the measurements of vertical particle concentration and vertical temperature profiles by (Levin et al., 2005) presented in 9.1.1 are consistent with the thesis of periodically developing transport barriers at the named heights. They state that haze layers regularly appear in the early morning and disappear in the late afternoon, when the thermal convection and the Mediterranean sea breeze destabilize the stratification within the Dead Sea Valley. Finally model studies by (Smoydzin and von Glasow, 2009) demand a limited vertical transport in order to simulate the observed strength and speed of BrO events. Frequently occurring BrO events with in-/decreases of the order of magnitude of 100 ppt within few hours could only be reproduced in model runs with general limited transport between 10:00 and 12:00 LT or with a flux of halogen species out of the Dead Sea water enhanced by a factor of 30. (Smoydzin and von Glasow, 2009) state that "relative humidity along the Dead Sea valley is often very low (...), aerosol phase chemistry is likely to be of minor importance." referring to (Alpert et al., 1997) and they assume that relative humidity is about 40-50 % during summer. As the data of Alpert et al. (1997) is based on shore sta-

tions, in their model calculations relative humidity above the water surface might be underestimated. (Hecht and Gertman, 2003) state that relative humidity offshore measured on bouys is significantly larger and give levels of 50-70 % in 98 % of cases. Furthermore relative humidity is likely additionally increased by possible inversion layers as mentioned above, where moisture from the sea accumulates. Also lower inversions directly above the water surface are possible. (Segal et al., 1983, p.~555) finds the effect that colder sea surface temperatures lead to larger relative humidity above the lake than warmer sea surface temperatures, inspite of the lower evaporation rate. The assumption of dry conditions and thus of minor importance of aerosol also contradicts the observations during the campaigns presented in this work with regard to the typical white haze already mentioned above.

Vertical transport barriers likely favor the formation of BrO in two ways: First BrO emitted by the sea surface is accumulated directly below the transport barrier, and second, enhanced relative humidity might increase the total aerosol surface resulting in both faster bromine explosion reactions, (cf. Buxmann, 2012a, chapter 3), and faster recycling of BrONO₂ as described in 2.2. According to the presented data it is also imaginable that BrO emitted by the lake rises convectively and gets capped afterwards from above and below. Dilution would be reduced even more and increasing BrO concentration would amplify the release of Br₂ from aerosol and therefore the concentration of BrO even further until the bromide within the aerosol is consumed completely. Occasionally BrO appears to develop independently of fluxes from the surface (e.g. 3 May 2012 Ein Bokek, 27 June 2002 Masada). This raises the question, if release from the aerosol alone would be fast enough and if the total bromide content inside the aerosol would be sufficient to explain the observed events. The relevance of the release of bromine species from aerosol is discussed controversially (see Smoydzin, 2008; Smoydzin and von Glasow, 2009; Tas, 2008, 2009), but, as already mentioned above, the presented data supports the idea that aerosol and therefore relative humidity plays an important key role. Singer et al. (2003) finds that the ratios of soluble cations and anions are all related to Dead Sea water (ratios are given in (Krumgalz and Millero, 1982), (Niemi et al., 1997)), unfortunately they could not determine absolute concentrations. However (Levin et al., 2005) finds 12 $\frac{\mu\text{g}}{\text{m}^3}$ sodium in the lower aerosol layer at -150 m asl at noon. With the ratios $\text{Na}^+/\text{Cl}^- = 0.28$ and $\text{Br}^-/\text{Cl}^- = 0.8\%$ (Singer et al., 2003, number ratios) this yields a gas phase equivalent of 370 pptv bromide inside the aerosol at 1050 mbar and 35°C. Thus, disregarding the rates of release processes, the total amount of bromide contained in aerosol might be enough to account for the observed peaks. Besides bromide already contained inside the aerosol also the abundance of BrONO₂ within the gas phase has to be regarded, as there are known processes recycling BrONO₂ on aerosol back to reactive species (reactions 2.30 to 2.35).

Frequently, increases in BrO are coincident with low NO₂ abundances (cf. Figure 9.5), demonstrated more clearly in Figure 9.25. Also compare section 2.2.2 and Figure 2.2. Similar findings are presented by Tas et al. (2006) and Platt and Zingler (2004). A low NO₂ mixing ratio ($\lesssim 2$ ppb) seems to be a prerequisite for high BrO production. During the night several ppb of NO₂ are present (see Figure 9.10). NO₂ is Most likely advected into the Dead Sea Valley by polluted air coming from urban areas in the surroundings, especially in the west and in the north (cf.

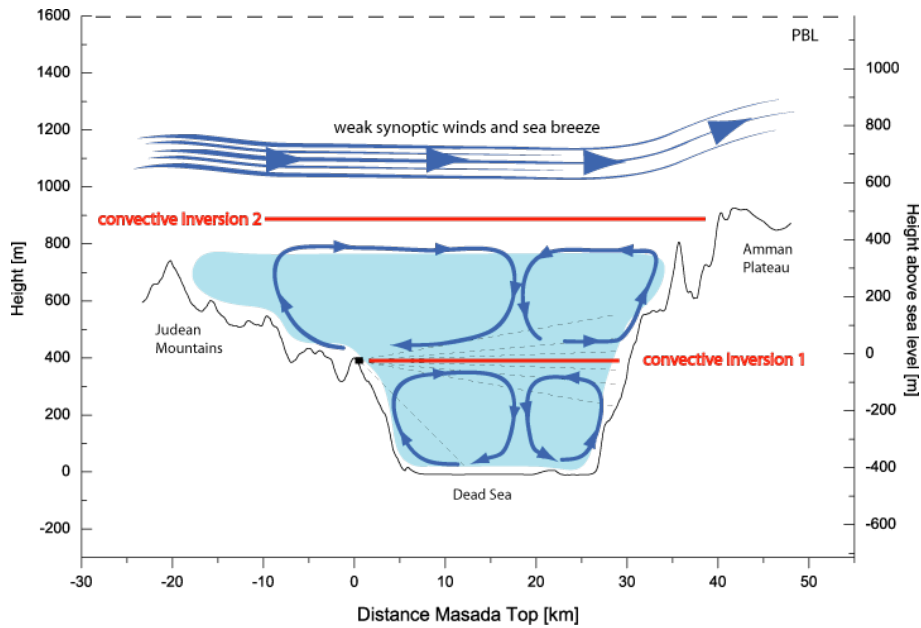


Figure 9.23: A possible pattern of mountain induced thermal circulations in the Dead Sea Valley on days with elevated layers found with MAX-DOAS: Lower circulations compensate local slope winds, while upper circulations compensate the whole air mass transfer out of the valley by mesoscale valley winds. Thermal updraft winds can form convective inversion layers and opposed streams prevent vertical transport.

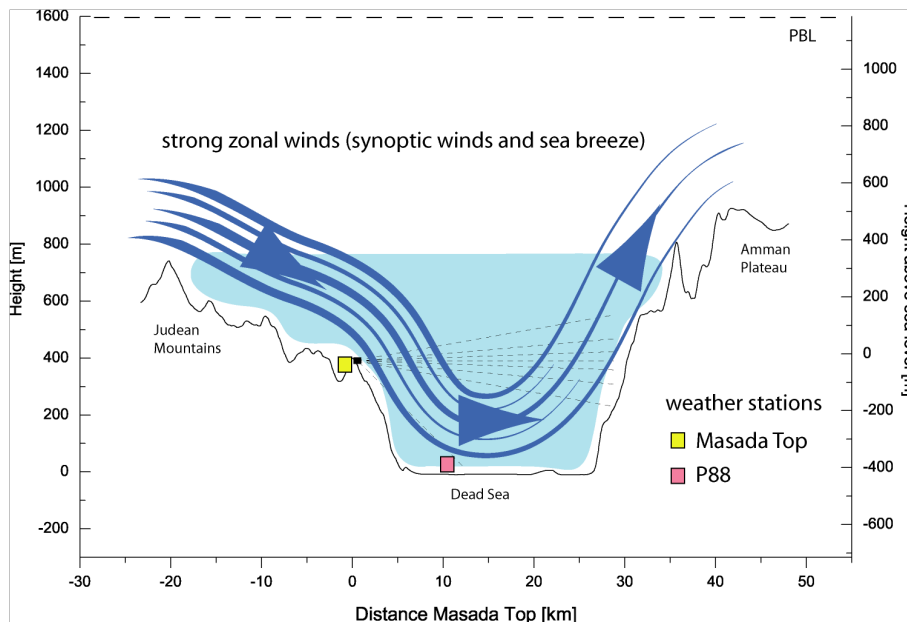


Figure 9.24: Possible dynamics in the Dead Sea Valley under the influence of strong westerly winds, which dissolve circulations and/or inversion layers or prevent their formation.

section 7.1.6). Starting at dawn, NO_2 drops below the detection limit of around 50 ppt until the afternoon while BrO increases up to several 10 ppt or even 100 ppt. BrO reacts with NO_2 rapidly ($\tau_{\text{BrO}+\text{NO}_2} = 300$ s with $[\text{BrO}] = 10$ ppt, $k_{\text{NO}_2+\text{BrO}} = 1 \times 10^{-11} \text{ cm}^3/\text{molecules}$ at 308 K (Atkinson et al., 2007)) to form BrONO_2 (reaction 2.29). BrONO_2 remains within the gas phase until it photolyzes ($\tau_{\text{hv}} \approx 6 \text{ min}$ (Deters et al., 1998), reaction 2.30), decomposes thermally ($\tau_{\text{therm}} \approx 5 \text{ h}$ at 30°C (Orlando and Tyndall, 1996), reaction 2.31) or is taken up by the liquid phase of the aerosol ($\tau_{\text{uptake}} \approx 25 \text{ min}$). The uptake rate of BrONO_2 can be approximated using the formula presented by Buxmann (2012a, and references therein), see next section. Disregarding the uptake by aerosol and thermal decay, approximately 500 ppt BrONO_2 and 5 ppt BrNO_2 should be present during daytime when photolysis (reactions 2.30, 2.33) and re-formation (reactions 2.29, 2.32) are in equilibrium at the measured levels of BrO and NO_2 . During previously campaigns, described in (Platt and Zingler, 2004), levels of NO_x measured by LP-DOAS and total photolysable NO_y measured by an NO chemiluminescence monitor with a photolytical converter were compared. The differences $[\text{NO}_y] - [\text{NO}_2] - [\text{NO}]$ indicated up to ~ 6 ppb nighttime BrONO_2 and several 100 ppt daytime BrONO_2 in the gas phase. However, it should be noted that the comparison of in-situ-measurements and LP-DOAS measurements, which integrate over several kilometers, has to be treated with caution. Furthermore, other compounds containing nitrogen, for example HONO, may be responsible for differences between total NO_y and NO_2 .

Two potential pathways exist which recycle BrONO_2 to reactive species: The reaction via NaBr or NaCl and hydrolysis. The recycling via reactions 2.28 and 2.27 (section 2.2) is discussed in (Tas et al., 2008), but the relevance of the recycling is still controversial, cf. (Smoydzin and von Glasow, 2009) and references therein. Nitrate (NO_3^-) was found in the aerosol sampled at the Dead Sea by (Singer et al., 2003) and (Levin et al., 2005) not related to the Dead Sea water. Levin et al. (2005) attributes NO_3^- to pollution coming from the Israeli Mediterranean coast (upper layer 100-500 m asl) and local sources (-150 m asl). Up to $20 \mu\text{g}/\text{m}^3$ NO_3^- was found in the aerosol. This would correspond to up to 8 ppbv NO_2 spanning a range which is consistent with the concentration of NO_2 disappearing during our measurements during several hours, see Figure 9.25. Consistent with measurements presented in (Platt and Zingler, 2004), this indicates that NO_2 is likely converted to BrONO_2 and the bulk of NO_3^- is stored in the aerosol, whereas less than 0.5-1 ppb BrONO_2 is present within the gas phase, see section 9.1.6. With regard to the data presented in this work and the considerations above, it is plausible to assume that the combination of salt aerosols from the Dead Sea and high humidity accumulating below or in between transport barriers is a crucial prerequisite for the high BrO levels measured at the Dead Sea, especially within elevated layers. Subsiding or advected BrO-rich air masses also might ignite further bromine explosions at other places above the water surface.

It can be assumed that the formation of BrO starts close to the water or salt surface, where Br_2 degases from the water, gets photolysed and reacts with O_3 (reactions 2.19 and 2.21). It may be helpful for understanding to roughly estimate the orders of magnitudes of bromine emissions from the Dead Sea water: Smoydzin (2008) uses a flux F_{Br_2} of Br_2 out of the water of $1.1 \times 10^{10} \text{ molecules cm}^{-2} \text{ s}^{-1}$ and states that it

is nearly constant for all scenarios, even for those with the lowest boundary layer of 500 m (fluxes of bromine species out of the aerosol prove to be negligible under the assumed conditions in the model studies). The southern part of the Dead Sea has an area of $\sim 100 \text{ km}^2$. From the vertical profiles discussed above one can assume a layer height of 400 m. With a resulting volume of $4 \times 10^{10} \text{ m}^3$, and when neglecting advection, the flux leads to an increase of 40 ppt Br_2 , or $\Delta[\text{BrO}]/\Delta t = 80 \text{ ppt BrO}$ per hour (at 30°C and 1050 mbar). Without any loss processes, the volume would contain 320 ppt BrO after 4 hours. The timescales for the reaction of BrO with NO_2 (reaction 2.29) is seconds to minutes at the observed NO_2 concentrations. The timescale of uptake of BrONO_2 at the aerosol is estimated to 25 min (cf. section 9.1.5), thus after around 30 min the BrO molecule has transferred one NO_2 molecule to the aerosol, so one individual BrO molecule is able to transfer up to 8 NO_2 molecules to the aerosol within 4 hours. For example, the BrO molecules formed within the first hour could transfer an average of 560 ppt NO_2 to the aerosol, though obviously the real flux of BrO precursors at the Dead Sea is much larger than assumed in the model studies by (Smoydzin, 2008) and thereby much larger amounts of NO_2 are transferred to the aerosol. Fluxes out of the water need to be enhanced by factors of up to 30-50 compared to F_{Br_2} in order to reproduce the observed BrO events at the Dead Sea in model studies and, therefore in reality the amount of BrO at the Dead Sea is supposed to be sufficient to transfer 5-8 ppb NO_2 to the aerosol within several hours and to account for loss processes at the same time. The recycling of BrONO_2 is most efficient, where the total aerosol surface per volume is the largest, this is expected to be directly below an inversion layer and may be the cause for the observed elevated layers of BrO.

Furthermore, a production rate of $\Delta[\text{BrO}]/\Delta t = 80 \text{ ppt BrO}$ per hour is in good agreement with results from Buxmann (2012a, p. 121). This results from the given area and flux, which, is used in the model studies of Smoydzin (2008), as mentioned above. Buxmann (2012a) conducted smog chamber experiments in a simulated atmosphere with an artificial salt surface and sun light in a Teflon chamber with a boundary layer height equivalent of 7 m (inverse surface-to-volume ratio). Measurements of BrO using a White-type Multi Reflection System showed production rates of 30 ppt/s at 60% and 68% relative humidity. Converting this to the assumed volume at the Dead Sea with a height of 400 m yields $30 \text{ ppt/s} \cdot 3600 \cdot 7 \text{ m}/400 \text{ m} = 1890 \text{ ppt/h}$. This corresponds to a factor of 24, thus being in the same order of magnitude as the mentioned factor of 30-50 between the standard and the enhanced flux, which is needed to reproduce the observed BrO events at the Dead Sea in the model. Buxmann (2012a) states that the bromine explosions observed in the chamber are faster than expected from theory. This seems to be valid also at the Dead Sea. One possible reason for this might be a more efficient recycling of BrONO_2 . NO_2 was below the detection limit of 2 ppb during the smog chamber experiments (Buxmann, 2012b). Nota bene: Only differences of NO_2 absorption can be detected with DOAS during the experiments, therefore possible background concentrations of NO_2 might have remained undetected. Another reason for the fast bromine oxide production mentioned by Buxmann (2012a) could be the formation of Br_2 as a precursor in the dark. Also additional release from crystallized salt deposits is discussed, see (Smoydzin, 2008, p. 125) and references therein. Yet, additional salt

surfaces cannot explain the fast bromine explosion in the smog chamber. Car-DOAS and MAX-DOAS measurements might give the impression that the central evaporation ponds with the highest salt concentrations on Israeli side and the most northern basin on Jordan side are the strongest sources of BrO. The Dead Sea Works pump water out of the Dead Sea into the most northern ponds, where it is gradually pre-concentrated. Consequently the water is pumped from a pond in the mid to the elevated southern end, from where it flows back to the north, ending in a middle pool. Unfortunately the purpose of the Jordan basins could not be identified, but satellite imagery and the inclination of the terrain (southern basins are elevated) suggest that it is filled with highly enriched brine. The concentration of Br⁻ in the Dead Sea water is given by Kesner (1999) and Niemi et al. (1997) as 4.6 g/l (annual average, upper 40 m). Within the evaporation ponds bromine concentrations reach 10-12 g/l and after bromine extraction brine with 1-2 g/l is carried back to the Dead Sea (Kesner, 1999). During the presented measurement campaign in 2012 6.8 g/l and 7.9 g/l were found in water samples from Ein Gedi and Ein Bokek, respectively. In the most southern pond 10.9 g/l Br⁻ were found (errors are 1%) (Huber et al., 2012). Along with the higher salinity and acidity the Br⁻/Cl⁻ ratio is assumed to be responsible for stronger and more frequent ozone depletion events over the southern part compared to the northern part, but the presented results demonstrate that also local atmospheric circulation patterns and thus also the local topography are likely to play a key role in the BrO chemistry of the Dead Sea. Bitan (1977) states that the formation of local sea breeze is favored, where the valley slope does not steeply end close to the water surface, as there is no "run up distance" for ascending air masses and air fluxes get more canalized in north-south direction instead. However, in the central area of the Dead Sea around Masada a broad (5 km) strip of land is present, which slightly inclines from the lake towards quite steep valley slopes. This may favor the formation of circulations as illustrated in Figure 9.23 in that area. Additionally the southern evaporation ponds containing high concentrated brine are still comparatively close, so this is supposed to be the reason for the extraordinary high mixing ratios of BrO in the central area.

9.1.5 Approximation of the Uptake of BrONO₂ on Aerosol

To approximate the order of magnitude of the uptake rate of BrONO₂ onto the aerosol in the Dead Sea valley the formula e.g. given in (Buxmann, 2012a, p.41), (Finlayson-Pitts, 2000, p.158 ff., and references therein) is used, yielding the life time $\tau_X = \frac{1}{f_{upt,X}}$ of a constituent X towards the collision with aerosol and a subsequent heterogeneous reaction H . $f_{upt,X}$ denotes the frequency of uptake of species X due to diffusion and gas kinetic uptake:

$$\tau_{upt,X} = \frac{1}{f_{upt,X}} = \left(\frac{r}{D_X} + \frac{4}{\gamma_{upt,X} \cdot v_X} \right) \cdot \frac{V}{A} [s], \quad (9.1)$$

with volume V and surface area A of the aerosol, radius r of the aerosol, diffusion constant D_X of constituent X , uptake coefficient γ_{uptake} and average molecular velocity v_X of species X , which is given by the Maxwell-Boltzmann distribution by

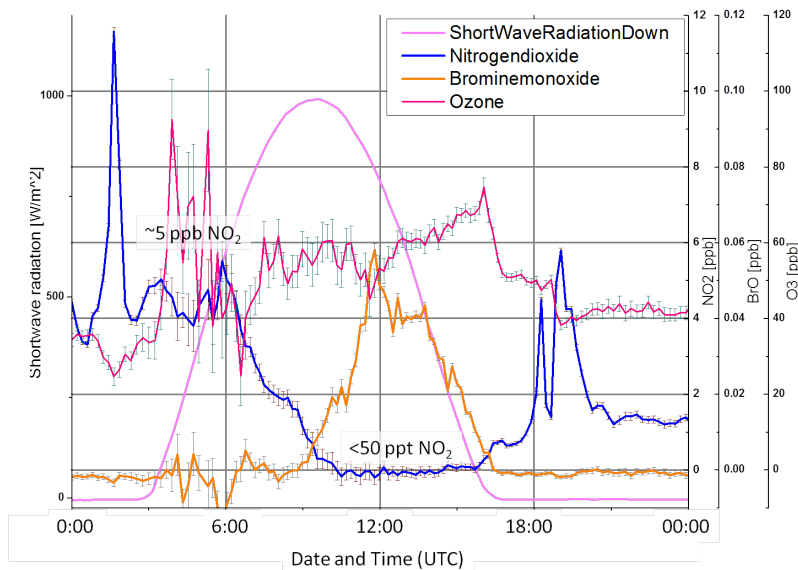
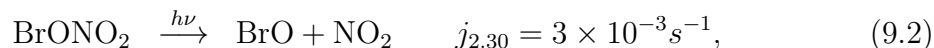


Figure 9.25: Diurnal behavior of BrO, NO₂ and O₃ on 11 May 2012 measured with LP-DOAS at Ein Bokek.

$v_X = \sqrt{\frac{8k_B T}{\pi m_X}}$. With $k_B = 1.38 \cdot 10^{-23}$ J/K, $T = 303$ K and $m_{BrONO_2} = 2.4 \cdot 10^{-25}$ kg this yields $v_{BrONO_2} = 210$ m/s. The diffusion constant D_{BrONO_2} in N₂ was calculated by Hanson et al. (1996) to be $75 \text{ torr cm}^2 \text{ s}^{-1}$ thus being approximated with $D \approx 10^{-5} \text{ m}^2/\text{s}$ at $760 \text{ torr} = 1 \text{ atm}$. An uptake coefficient of $\gamma = 0.75$ was chosen by Tas et al. (2006) referring to Hanson et al. (1996) and Atkinson et al. (2002). Smoydzin (2008, p.128) states that this may be too large and assumes a value for dry aerosol particles of 0.3 referring to Aguzzi and Rossi (1999). According to Levin et al. (2005) aerosol in the two lowest haze layers at the Dead Sea, see Figure 9.4, is bimodal with local maxima at $0.4 \mu\text{m}$ and $1 \mu\text{m}$, with the smaller particles being double as abundant. Therefore a radius of $r \approx 0.4 \mu\text{m}$ is chosen. The volume to area ratio V/A can be assumed from the range of sight L , which is estimated to be around 5 km under hazy conditions. The effective optical area of the particles is assumed to be twice the physical cross section. This yields a ratio of $\frac{V}{A} = 2 \cdot L = 10 \text{ km}$. Equation 9.1 yields $\tau_{upt,BrONO_2}(\gamma = 0.8) \approx 11 \text{ min}$ and $\tau_{upt,BrONO_2}(\gamma = 0.3) \approx 17 \text{ min}$. In both cases the life time towards uptake is in the same order of magnitude as photolysis of BrONO₂. Choosing a large particle size of $r \approx 1 \mu\text{m}$ and a low uptake coefficient $\gamma_{upt,BrONO_2} = 0.3$ results in $\tau_{upt,BrONO_2} \approx 27 \text{ min}$.

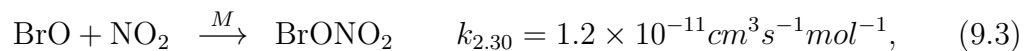
9.1.6 Gas Phase Mixing Ratio of BrONO₂ in Equilibrium

As discussed above, photolysis (reaction 2.30 in section 2.2) is the dominating decomposition process of BrONO₂ in the gas phase:



with the photolysis rate $j_{2.30}$ (Deters et al., 1998).

The formation of BrONO_2 occurs via reaction 2.29



In equilibrium $d[\text{BrONO}_2]/dt = 0$ it is

$$[\text{BrONO}_2] = \frac{k_{2.30} \cdot [\text{BrO}] \cdot [\text{NO}_2]}{j_{2.30}}. \quad (9.4)$$

With typical daytime mixing ratios $[\text{BrO}] = 100$ ppt and $[\text{NO}_2] = 100$ ppt this yields:

$$[\text{BrONO}_2] = 2.5 \times 10^{10} \text{ molecules/cm}^3 \hat{=} 1 \text{ ppb}. \quad (9.5)$$

Typically $[\text{Br}]$ is in the order of 1% of $[\text{BrO}]$, therefore BrNO_2 is supposed to play a minor role.

9.2 Results from other measurement sites

Slant column densities ΔS of BrO and IO at the locations described in section 7.1.1 other than the Dead Sea are all below or very close above the detection limits (cf. section 8.2) of the MAX-DOAS instruments, see Figures A.6 to A.28 in the appendix A.

Due to unknown spectral structures, weak absorber signals can be affected by the choice of fitting parameters particularly. To test the sensitivity of the spectral retrievals of BrO and IO from MAX-DOAS data to different fitting parameters and to account for the possible presence of glyoxal and water (cf. section 8.1), several different fitting scenarios were used to retrieve slant column densities listed in Table 8.2 in section 8.1. The complete time series of retrieved slant column densities of BrO and IO at these locations, except of Mauritania, are presented from sections A.2 to A.7.

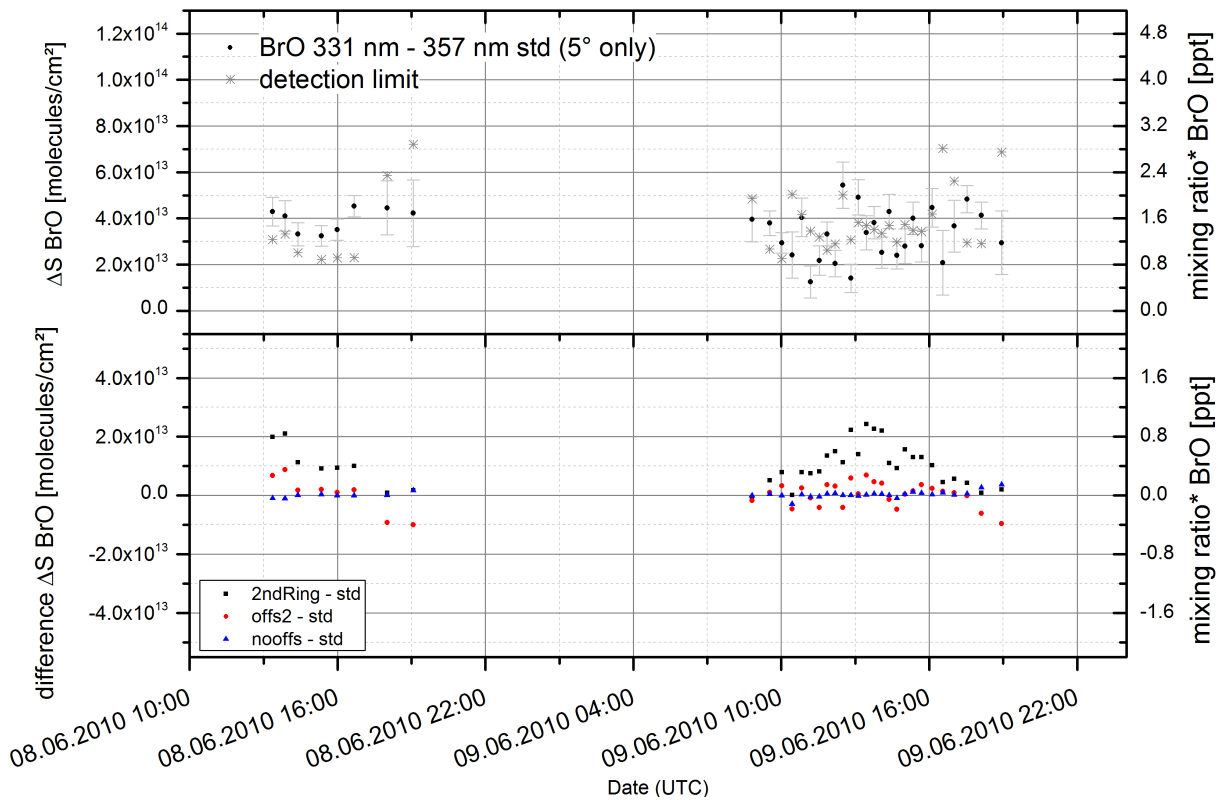


Figure 9.26: BrO differential slant column density $\Delta S(\alpha = 5^\circ)$ retrieved from MAX-DOAS with fit scenario "BrO_331_357_std" (upper panel) and differences of $\Delta S(\alpha = 5^\circ)$ retrieved with other fit scenarios (see Table 8.2) to the standard fit scenario (lower panel) on Sal, Cape Verde. Significant levels are found on 8 and 9 June 2010.

In South West Australia single data points of BrO and IO exceed the detection limit, but whether the points exceed the five-fold fit error or not randomly depends

on the used fitting scenario. Therefore the signals remain ambiguous. On the Cape Verdian island Sal significant signals of BrO can be seen on 8 and 9 June, 2010, see Figure 9.26 for all scenarios except of "BrO_331_357_2ndRing", which shows higher fit errors in general (see Figure A.13), probably due to the fact that the two Ring spectra used for that fit are fixed and do not account for variations in the spectral instrument function sufficiently (cf. section 8.1). Repeating the DOAS fit with two normalized Ring spectra generated from the proximate FRS measured at $\alpha = 90^\circ$ reduces the residual's RMS of scenario "BrO_331_357_2ndRing" to similar values like in the other fitting scenarios. Example fits of scenarios "BrO_331_357_std" and "BrO_331_357_2ndRing" with significant levels of BrO are shown in Figures 9.27 and 9.28. On both days measurements were performed inside the caldera at Pedra Lume (see section 7.1.4). The pH values found in the water inside the caldera at Pedra Lume ranged between 7.5 and 7.8 (Huber et al., 2012).

South Russia 2009

The presented measurements in South Russia (Figure A.10) show upper limits for the mixing ratios of BrO and IO in the range of several ppt and 1 ppt, respectively. By summing up spectra the upper limits of ΔS could be reduced to average values of 5×10^{13} molecules/cm² and 2.75×10^{13} molecules/cm² (five-fold fit error, cf. section 8.2, resulting time resolutions are 72 min). Assuming a length of light path of 10 km through the absorbers this would correspond to upper limits of 2 ppt for BrO and 1.1 ppt for IO.

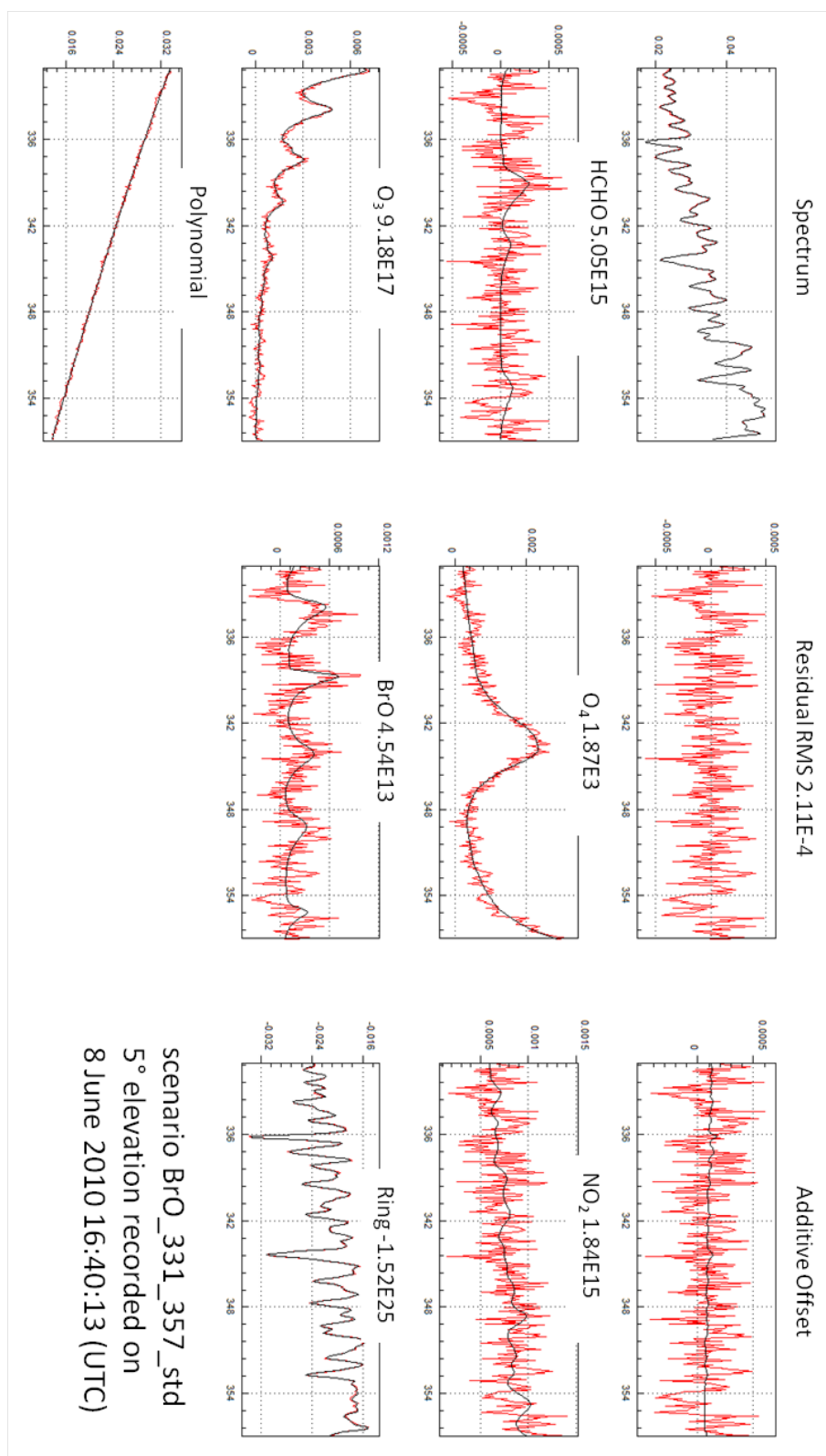


Figure 9.27: Example of a DOAS fit using scenario "BrO_331_357_std" on Sal, Cape Verde, on 8 June 2010 16:40 (UTC) (=15:40 LT). The slant column density of BrO exceeds the detection limit (cf. Figure 9.26).

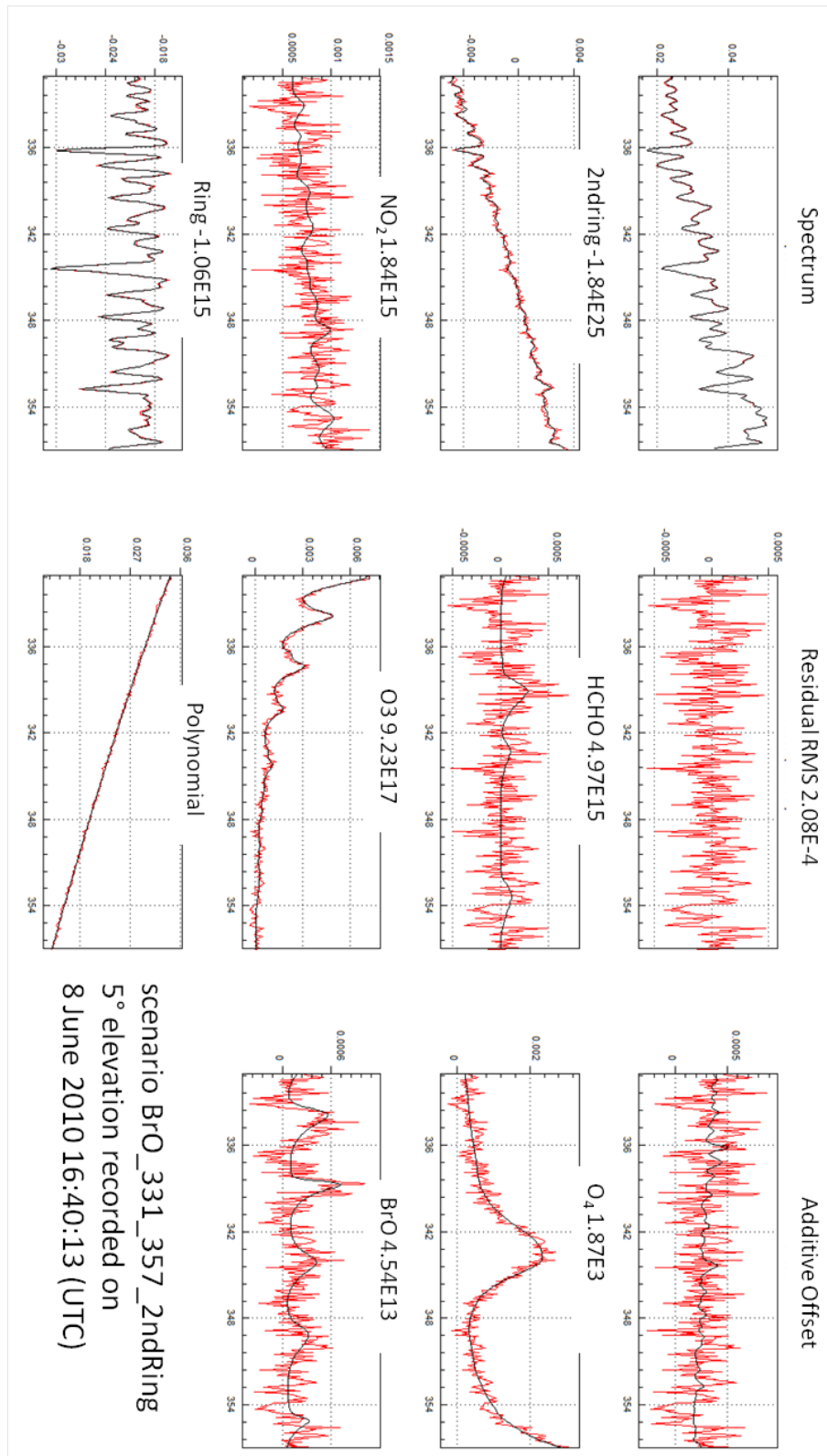


Figure 9.28: Example of a DOAS fit using scenario "BrO_331_357_std" on Sal, Cape Verde, on 8 June 2010 16:40 (UTC) (=15:40 LT) using two normalized Ring spectra generated from the proximate FRS. The slant column density of BrO exceeds the detection limit.

Mauritania 2009

High environmental temperatures of up to 38°C and winds between 20 and 30 km/h during daytime aggravated the measurements at Sebkhya N'Dramcha seriously and caused several technical problems with regard to thermal and mechanical stabilization of the MAX-DOAS and LP-DOAS systems. Therefore only BrO could be evaluated with a high level of uncertainty. The measurement periods and average detection limits of LP-DOAS and MAX-DOAS are shown in Table 9.1. BrO did not exceed the detection limit during these times.

Table 9.1: *Measurement periods during the campaign in Mauritania in 2009 (times are UTC) with average detection limits. For the detection limit of MAX-DOAS a light path with a length of 10 km through the absorbing layer is assumed.*

device	measurement period	average detection limit <i>BrO</i>
LP-DOAS	26 Nov 20:18-22:10, 27 Nov 3:24-3:53, 7:22-13:49, 18:35- 20:42, 28 Nov 7:06-7:31	12.5 ppt
MAX-DOAS	25 Nov 15:37, 26 Nov 9:11-14:14, 27 Nov 8:54-16:46	34 ppt

9.2.1 Discussion

Among the presented locations only on Sal significant levels of RHS were observed. The slant column densities of BrO on Sal found at the evaporation ponds on 8 and 9 June 2012 ($3.2\text{-}5.4 \times 10^{13}$ molecules/cm²) are not significantly higher than the upper limits found at the northern coast of Sal (Punte Norte) on 5 and 6 June 2010 (cf. Figures 9.26 and A.14, 9.28, 9.27) with air masses coming from the ocean in the northeast in both cases. Subsequent MAX-DOAS measurements at the Cape Verde Atmospheric Observatory Humberto Duarte Fonseca (CVAO) on the island Sao Vicente between 15 and 20 June using the same instrument show significant slant column densities of BrO (up to 5.4×10^{13} molecules/cm²) in the afternoon (Tschritter, 2012b; Buxmann and Holla, 2011) on two out of six days (18 and 19 June). Distinct increases of BrO in the late afternoon on 18 and 19 of June are also indicated by contemporary LP-DOAS measurements conducted by (Poehler and Tschritter, 2010) within the scope of the BMBF joint research project SOPRAN. The analysis of back trajectories generated with HYSPLIT (Draxler and Rolph, 2003) did not reveal any dependencies of BrO on the source regions of the air masses during the measurements on Sal and Sao Vicente. The detected BrO signals were not associated with trajectories crossing the upwelling region off the West African coast, which is discussed as a source for precursors of RHS (e.g., Quack et al., 2007; Grossmann et al., 2012). The ΔS of BrO observed at the solar salt ponds at Pedra

Lume are within the range of daily variations observed on Sao Vicente, therefore a possible signal from the evaporation ponds could not be separated from the local ocean background.

Table 9.2 gives an overview of the measurements performed within the scope of Haloproc at salt lakes and salt pans in the context of previous RHS measurements at the Great Salt Lake in Utah, the Salar de Uyuni in Bolivia and the Dead Sea in Israel.

Table 9.2: Results from field campaigns performed in the scope of HaloProc at salt lakes (yellow) and other areas with high salt content (orange) in the context of previous RHS measurements at salt lakes (green).

site	detection limit BrO [molecules/cm ²]	detection limit IO [molecules/cm ²]	approximate RHS mixing ratios	instrument	Br/Cl ⁻ [number ratio]	pH	salinity
Sua Pan (Botswana)	2.2x10 ¹³	1.2x10 ¹³	<4.4 ppt BrO <2.8 ppt IO	MAX-DOAS	0.6%*	10.1	8-17%*
Elton, Baskuntschak (South Russia)	2.9x10 ¹³	5.2x10 ¹²	<2 ppt BrO <1.1 ppt IO	MAX-DOAS	0.3-0.6%, 1.3-1.9%*	6.9, 7.7	~5%*
Sebkha N'Dramcha (Mauritania)	3x10 ¹⁴	/	<60 ppt BrO	LP-DOAS	0.05%*	8.6	~20%*
Pedra Lume (Sal, CV)	8x10 ¹²	4.6x10 ¹²	~1.8 ppt BrO <1.1 ppt IO	MAX-DOAS	not determined	7.6	~17%
South Western Australia	7.7x10 ¹²	6.2x10 ¹²	<1.5 ppt BrO <1.5 ppt IO	MAX-DOAS	0.5 – 1%*	3.1, 7.4, 7.2 [†]	13-25%*
Kali dump Heringen	7.5x10 ¹²	6.1x10 ¹²	<1.5 ppt BrO <1.5 ppt IO	MAX-DOAS	not determined	n.d.	-
Bourtanger Moor	7.2x10 ¹²	6.7x10 ¹²	<1.4 ppt BrO <1.6 ppt IO	MAX-DOAS	not determined	n.d.	n.d.
Great Salt Lake (USA)	-	-	15 ppt ClO 6 ppt BrO*	LP-DOAS	0.03% [⊙]	8*	10-30%*
Dead Sea (Israel)	-	-	~100 ppt, up to 200 ppt 10 ppt IO*	MAX-DOAS LP-DOAS	1% [†]	~6.5	33.7%
Salar de Uyuni (Bolivia)	-	-	up to 20 ppt [□]	MAX-DOAS	2 ppm -0.01%#,*	5- 7.5 [⊙]	8.5% [⊕]
open ocean (Atlantic)	-	-	2.5 ppt BrO 1.4 ppt IO	LP-DOAS	0.34%	~8	~3.5%

* [Huber, S., Tubbesing, C., Krause, T., Rheinberger, S., & Kotte, K. (2012). pers. comm. Heidelberg.],

[†] [Kesner, 1999]; [⊕] [Risacher, 1991]; [#] [Risacher, 2000]; [⊙] [Rettig1980]; [•] [Lynn1980]; [•] [Stutz2002];

^{*} [Matveev2001]; [Tas2005]; [□] Hönninger2004; [⊙] [Sturm1980], ~ Lake Orr, Lake King, Lake Stubbs (in that order)

In general, the measured column densities and upper limits of the reactive halogen species BrO and IO found at the sites described in section 7.1.1 other than the Dead Sea were at least one order of magnitude lower than one could have expected from the existing data from the Dead Sea and, concerning BrO, from Salar de Uyuni. Also the levels of BrO of up to 6 ppt at the Great Salt Lake in Utah reported by (Hönninger et al., 2004) were higher than the detection limits during the field studies presented in this work, with the exception of Sebkha N'Dramcha in Mauritania. From Walfish Bay in Namibia ΔS of BrO were reported to be below the detection limit of 6.5×10^{13} molecules/cm² (Buxmann, 2008).

This raises the question of the differences between the salt lakes and possible influences by different environmental conditions during the measurements. Parameters that are considered to favor the heterogeneous emission of RHS (see section 2.2) are high salinity, low pH and for halogens other than chlorine a high quantity ratio (e.g., Br^-/Cl^- for reactive bromine species). This release mechanism may occur on saline water surfaces or in liquid microlayers directly on the saline surfaces, i.e. salt crusts or saline soil (cf. Buxmann, 2012a). It should be noted, that salt surfaces can get moist by air humidity, when the relative humidity in ambient air is higher than the deliquescence point of the corresponding type of salt. For pure NaCl the deliquescence point is at 76% relative humidity, but can be as low as 33% for MgCl_2 , for example. The actual deliquescence point depends on the exact composition of the salt.

In some cases the pH at the lakes might have been too large. The autocatalytic release mechanism of BrO (reaction 2.27) consumes H^+ ions and therefore needs acid environments, but generally salt lakes tend to be alkaline (cf. Table 9.2). According to Tas et al. (2006) this reaction is the rate determining step of the heterogeneous reaction cycle. Also Kali dumps are generally alkaline. Yet, it should be noted that a pH within microlayers, where heterogeneous reactions occur, cannot be measured using conventional methods and the pH values reported from the salt lakes are average values gained from water or soil samples. Also possible acidification by advected polluted air or, in the case of Salar de Uyuni, volcanic emissions need to be taken into account. Some of the salt lakes in South West Australia belong to the most acid salt lakes in the world, among them is Lake Orr, which was examined in this work. No significant levels of RHS were found at Lake Orr, either, but this may be due to several other reasons discussed below.

In the environment there are also many additional possible influences complicating the separation of the contributions by the different possible release processes described in Chapter 2:

- As it has become clear at least since the discussion in Section 9.1 dynamics can play a key role for the mixing ratios of RHS found in the field for several reasons: Obviously transport and dilution effects have to be considered, but also possible secondary effects having an impact on release or production processes might be triggered by transport phenomena.
- Buxmann (2012a) demonstrated that BrO formation was strongly humidity dependent during the experiments, possibly controlled by the liquid layer on salt crystals. Maximum BrO concentrations were observed at 60% relative humidity in the laboratory. This might also be the reason why at the Great Salt Lake in Utah, during one month of measurements Stutz et al. (2002) detected BrO and ClO only on one day of October 2000 after a period with light rain falls and relative humidity of 60%.
- Besides liquid microlayers on crystalline surfaces, the heterogeneous release mechanism explained in chapter 2 also occurs on water surfaces, as far as a water plane exists (cf. Table 9.3). A water plane can also be a source of salt aerosols, which again pose surfaces for the heterogeneous release mechanism.

- Unknown sinks in the vicinity of the salt lakes have to be considered. Halogens might have been present in other forms than oxides. Potential sinks for the oxides could be the reaction with background NO_2 (cf. Table 9.3) or with hydrocarbons, for example emitted by the surrounding vegetation. The latter is particularly valid for the lakes in South West Australia, where most of the lakes are surrounded by eucalyptus trees, which are known to emit large amounts of hydrocarbons. Also in the Russian steppe a clear smell originating from the abundant vegetation indicated the presence of hydrocarbons, cf. e.g. Finlayson-Pitts (2003); Buxmann (2012a) on the interaction of RHO with organics. Aldehydes are degradation products of the reaction $\text{RH} + \text{OH}$ (RH may be isoprenes emitted by vegetation or other hydrocarbons) and can also be a relevant sink for reactive bromine species. The reaction competes with the reaction of Br and O_3 (reaction 2.25) and gets relevant for HCHO mixing ratios of ~ 10 ppb. Approximate average mixing ratios of formaldehyde (HCHO) inferred from MAX-DOAS measurements are below 1.2 ppb ($= 2.8 \times 10^{16}$ molecules/cm²) for all measurements on salt lakes presented in this work. LP-DOAS measurements at the Dead Sea show a mean HCHO mixing ratio of 1.6 ± 1.1 ppb (1σ deviation from mean).
- A further crucial factor might be the exposure time of air masses above a lake or saline surface. The heterogeneous release mechanism of Br_2 contains the autocatalytic reaction 2.27. Therefore air masses crossing the saline surface may accumulate bromine species, consequently the increasing concentrations enhance the further release of bromine. As soon as air parcels leave the saline surface the concentrations of bromine species are supposed to decrease due to dilution or sink reactions. An estimation of the orders of magnitude of exposure times is given in Table 9.3.

Certainly these issues are valid for any other site with high halogen content, too, like the Bourtanger Moor and the Kali dump in Heringen:

Bourtanger Moor At the Bourtanger Moor ozone levels exceeded 50 ppb until the afternoon on both days. Column densities of HCHO and NO_2 , which can both act as sinks for reactive halogen species (cf. section 9.1), indicate an abundance of several ppb, probably originating from the nearby motorway A 31. With regard to this, smaller amounts of reactive halogen species would probably have been depleted rapidly.

Kali dump At the Kali dump ozone levels were mostly between 40 and 50 ppb with single peaks of up to 80 ppb. Results from LP-DOAS did not yield significant signals of BrO and IO, showing a higher detection limit and are not presented in this work. HCHO and NO_2 were found in amounts of several ppb and several hundreds of ppt, respectively.

At the Salar de Uyuni (Hönninger et al., 2004) found several ppt of BrO on each day of a four days measurement period. At first sight, this is surprising, as the Br^-/Cl^- ratio at the Salar de Uyuni has been reported to be one of the lowest in the world in the range of several ppm (Risacher, 2000) to 0.01% (Kotte, 2011).

However, discussing the emission of BrO out of the Dead Sea water Tas et al. (2006) states:

”According to a laboratory study (Fickert et al., 1999) the efficiency of Br₂ release by activation of HOBr, is not expected to increase once Br⁻ exceeds a value of ~0.8 mol/m³ (for pH=5.5 and T=274K). The Br⁻ at the Dead Sea exceeds this value by about two orders of magnitudes, while the Br⁻ of normal ocean water is about equal to this value. However, a previous study (Tas, 2005) has shown high frequency and high concentrations of BrO towards the more concentrated salt ponds, indicating that the high Br⁻ concentrations at the Dead Sea contribute to the BrO formation. Even so, the very high Br⁻ content may not be solely responsible for the high BrO levels observed at the Dead Sea.”

In brine saturated with NaCl (salinity 35.9%) the Br⁻/Cl⁻ = 0.01% quantity ratio in surface water reported from the Salar de Uyuni would correspond to 0.5 mol/m³, which is only 37% lower than the critical value above mentioned by Tas (2005). Consequently the efficiency of Br₂ release by activation of HOBr at the Salar de Uyuni and the Dead Sea might be similar, although the bromide content (relative to chloride) at the Dead Sea is two orders of magnitude larger than at the Salar de Uyuni.

Table 9.3: Comparison of different properties and trace gas abundances found at salt lakes where RHS were measured potentially affecting the presence of BrO and IO.

	lake area [km ²] (without saline soil)	typical wind speed [km/h]	approximate air parcel exposure time over lake surface	NO ₂ [ppb]	O ₃ [ppb]	water plane in general/during measurements
Dead Sea	630 km ² northern part, 270 km ² southern part	7-14 ^[1]	up to 14 h	several ppb ^[1]	50-80 ^[1]	stationary
Great Salt Lake	9550 lake and salt crust	7-11 ^[2]	up to 15 h	< 1 ppb ^[2]	30-40 ^[2]	stationary
Salar de Uyuni	10000 ^[4]	~ 20 #	up to 5 h	-	up to 70 ^[3]	seasonal/no water
Sua Pan	10000 (whole Makgadikgadi)	~ 20 #	up to 5 h	up to 400 ppt (Sua Pan)*	-	seasonal/no water
El'Ton; Baskuntschak	180, 130	~ 10-20**	up to 40 - 90 min	⊙ 310 ppt*	⊙ 30 ppb♦	stationary; seasonal/water
Sebkha N'Dramcha	60	10-30 ⁺	up to 12 - 36 min	<160 ppt*	32 ppb♦	probably seasonal/no water
South West Australia	max. 160 but silty, most several km ²	10-20	up to 3 - 6 min	< 210 ppt*	20-40 ppb♦	seasonal/sparse water surface, but moist salt crusts

[1] Matveev et al., 2001

[2] Stutz et al., 2002

[3] Hönninger et al., 2004

[4] Risacher and Fritz, 1999

* approx. from MAX-DOAS slant columns

** from hourly averages

+ from log book

♦ measurements with mobile ozone monitor (2B Technologies)

estimations from current weather <http://www.uyuni-bolivia.travel/salar-de-uyuni-weather> and <http://www.wunderground.com/global/stations/68038.html>

Chapter 10

Conclusion and Outlook

The field studies presented in this work showed that the presence of RHS at salt lakes, salt pans and saline soils is less widespread than previously assumed from earlier measurements.

Halogen compounds are known to be produced naturally by biogeochemical processes (see section 2.1.1). There is also evidence for abiotic formation of organohalogenes in soils and sediments (Schöler, 2003; Huber et al., 2009). One task of this work was to evaluate the relevance of saline soil for the emission of RHS and their precursors. Saline soils cover 2.5% of the land surface of the earth (von Glasow, 2007, and references therein), thus potentially being important for global halogen emissions and atmospheric chemistry. In the context of exacerbated desertification by global climate change (Yohe et al., 2007) saline soils might gain even more importance.

The salt lakes examined in this work (see Table 9.2) in Mauritania, South Russia and South West Australia are surrounded by several hundred square kilometers of saline soil. As mentioned in section 9.2 the upper limits (12.5 - 34 ppt) of BrO at Sebkhia N'Dramcha in Mauritania are large and measurement periods are incoherent. Thereby the conclusions that can be drawn from that are not very meaningful and the region cannot be ruled out completely to be an important source for tropospheric halogen compounds. However, from the presented measurements in South Russia upper limits of 2 ppt BrO and 1.1 ppt IO could be approximated. Also in South West Australia BrO and IO did not exceed average detection limits of 1.5 ppt. Thus it can be stated that, at least under the meteorological conditions described in 7.1.2, mixing ratios of BrO and IO in those extensive saline areas do not exceed the order of magnitude reported from the marine background (Read et al., 2008). Of course, during the measurements halogens might have been present in the troposphere in other forms.

As discussed in section 9.2.1, under the conditions prevailing during the examinations, the salt lakes themselves did not show mixing ratios of RHS as high as at the Dead Sea or the Salar de Uyuni. It was also tried to retrieve concentrations of ClO from the active DOAS measurements in South West Australia, at the Kali dump and the Dead Sea, but results were not unambiguous.

For the first time the vertical as well as the horizontal distribution of BrO at the Dead Sea was measured at the same time. The results from this work reaffirm the outstanding position of the Dead Sea among the salt lakes studied to date in

terms of RHS production: It appears that the special patterns of its dynamics and topography in combination with its high salt, and especially bromide, content lead to the particular large (> 100 ppt) abundances of *BrO*. Also the attenuation of UV radiation (probably mainly due to aerosols; up to 15% in UVB and 5% in UVA, respectively, Kudish (2009)), might cause specific effects in photochemical processes at the Dead Sea. For example a lower photolysis frequency of BrONO_2 would favor the uptake by aerosol, see section 9.1, 116. The factories in the south have been ruled out as sources of the observed bromine in several studies before (e.g., Hebestreit, 1999; Zingler and Platt, 2002). This agrees with the results of this work. Uncertainties remain concerning the actual abundances of BrONO_2 and its uptake and recycling to active species on aerosol. Some other open questions that remain to date are the importance of cross and competing reactions of the whole bundle of RHS (particularly BrO , IO , ClO), the deeper understanding of the role of NO_x and OH in RHS chemistry, as well as the influence of aerosols and radiation. In future studies the observed anticorrelation of BrO and IO mentioned in section 9.1 and the presence of IO in existing data from this work should be examined in more detail. It may shed a light on cross reactions of bromine and iodine species. Further it should be noted, that the presence of such high levels of iodine oxide itself outside of the marine boundary layer is striking, because of the fact that 70% of the earths iodine is located in the oceanic crust (including seawater) (Muramatsu, 1998).

The comparatively high levels of BrO found at the Salar de Uyuni (see Tables 9.2 and 9.3) remain puzzling with respect to the absent cohesive water and probably lower (humid) aerosol load compared to the Dead Sea. The crystalline surface seems to be sufficient to emit the observed amounts of BrO (up to 20 ppt). However, the Br^-/Cl^- ratio is reported to be varying from the ppm range (Risacher, 2000) to $\sim 0.01\%$ (Kotte, 2011) in the salt crust. With respect to the discussion in section 9.2.1, the heterogeneous release process of BrO might be efficient inspite of the low bromine content in areas with $\text{Br}^-/\text{Cl}^- \approx 0.01\%$.

For future field studies of RHS two main approaches are imaginable:

1. Repeated and, as far as possible, long-term measurements at a salt lake that is known to emit significant amounts of RHS, like the Dead Sea or Salar de Uyuni, in order to investigate a wider range of different meteorological and air chemical conditions which might have an influence on natural RHS release. For example at the Dead Sea ascents of radio sonde balloons or measurements from an air plane accompanying the DOAS measurements would be a good opportunity to test the hypothesis of this work. Concerning logistic and organisational aspects the Dead Sea is clearly to be preferred because of the good infrastructure provided by the region. Nevertheless at the Salar de Uyuni a recently built airport and other developments due to the rising local lithium industry offer new possibilities.
2. Adaptation of the methods to low concentrations and stronger dilutions of RHS. This would be necessary to evaluate the relevance of saline soils and smaller salt lakes for tropospheric RHS on a global scale. This could be

achieved with cavity enhanced DOAS measurements (Hoch, 2010; Horbanski, 2010) directly in or on saline soils or salt crusts. The device would be set up within a pit or a box where it could be covered with a Teflon sheet, so that emitted RHS could accumulate.

In peat lands or at Kali dumps, long-term measurements of RHS would be interesting in order to assess their potential role as a source for atmospheric halogen radicals. The emissions of RHS from Kali dumps or peat lands cannot be excluded in general on the basis of our preliminary short-term measurements. Concerning peat lands, an alternative to the Bourtanger Moor should be considered because of its proximity to the motorway with high emissions of NO_x and HCHO. The use of compact Cavity DOAS systems would reduce or even exclude the influence of dynamics on the measurements and an accumulation of detectable amounts of trace gases might be achieved where concentrations are below the detection limit of MAX-DOAS or LP-DOAS instruments. Of course, also the development of instruments with lower detection limits would allow for further studies at areas with low levels of RHS. Furthermore at the moment a feasibility study for the construction of a Cavity system for measurements of BrONO_2 is carried out at the Institute of Environmental Physics, Heidelberg.

Appendix A

Data Charts

This chapter contains the whole data sets of DOAS measurements performed at the locations presented in chapter 7 in the scope of the DFG research group Haloproc (Schöler and Zetzsch, 2008), if not already shown in chapter 9. For the discussion on the distribution of the Histograms presented below see Section 8.2.

A.1 Israel 2012

The following figures show histograms of the DOAS slant column density errors and RMS of the spectral retrieval of BrO , and the whole data set of meteorological parameters during the campaign in Israel 2012.

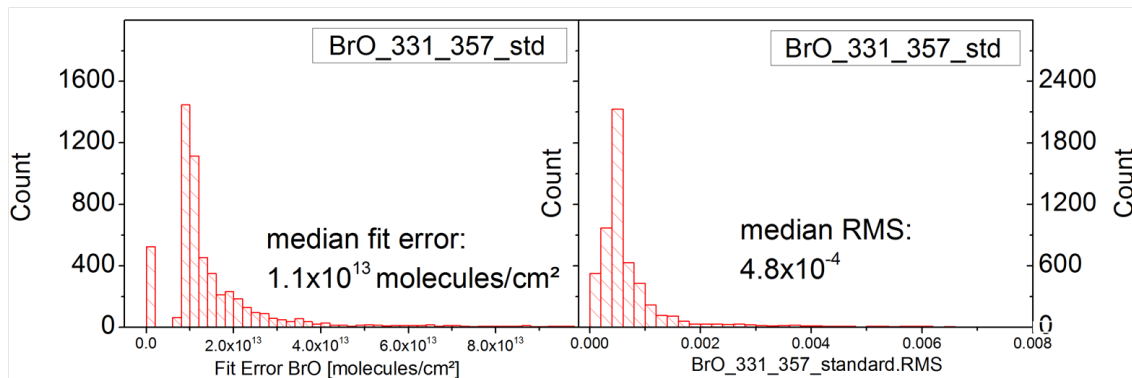


Figure A.1: Histograms of the fit errors of the BrO retrieval and RMS from fitting scenario "BrO_331_357_std" (see Table 8.2) at Masada, Dead Sea in 2012.

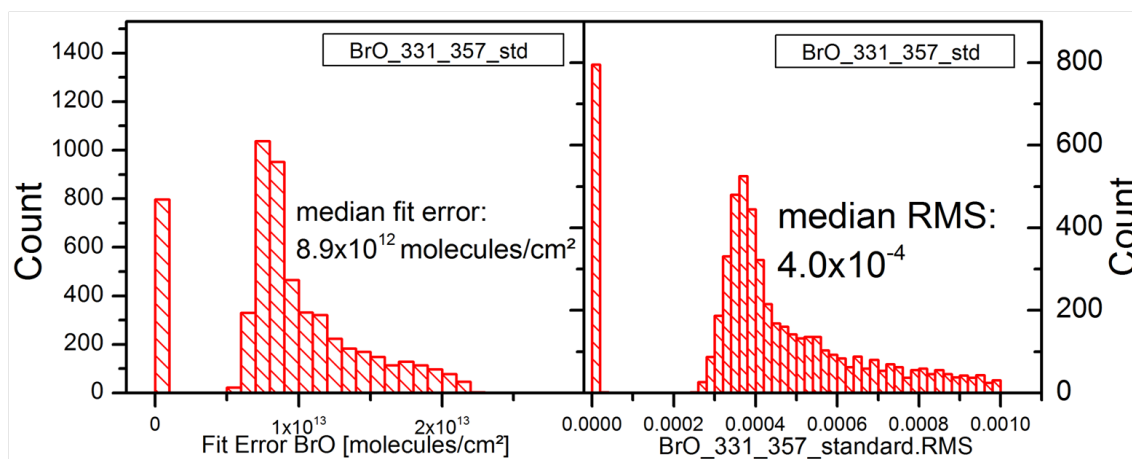


Figure A.2: Histograms of the fit errors of the BrO retrieval and RMS from fitting scenario "BrO_331_357_std" (see Table 8.2) at Ein Bokek, Dead Sea in 2012.

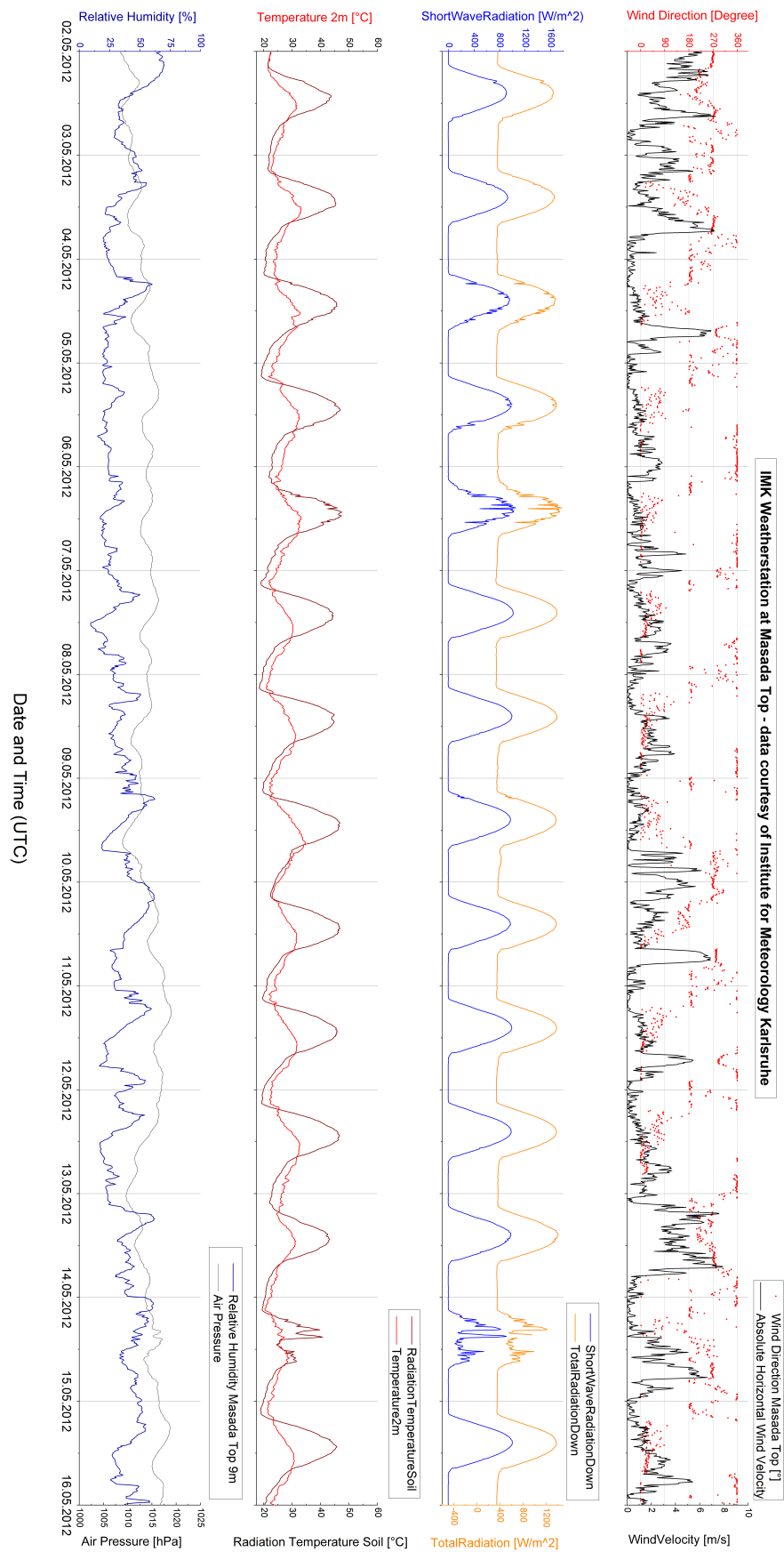


Figure A.3: Meteorological parameters from IMK weather station (Corsmeier and Kottmeier) at Masada Top (see 7.11) during the DOAS measurements 2012.

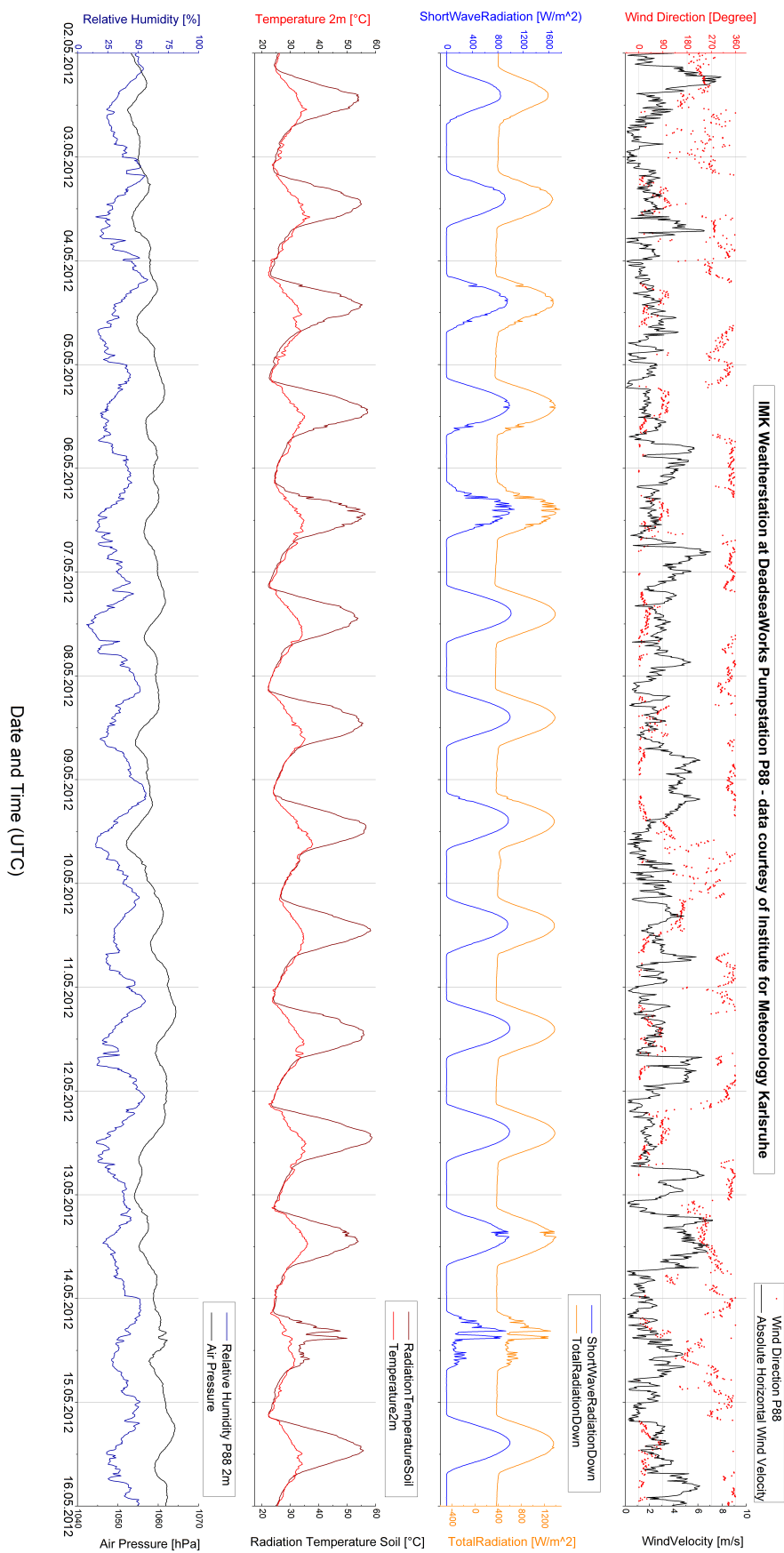


Figure A.4: Meteorological parameters from IMK weather station (Corsmeier and Kottmeier) at the Dead Sea Works pumping station P88 (see 7.11) during the DOAS measurements 2012.

A.2 Botswana 2008

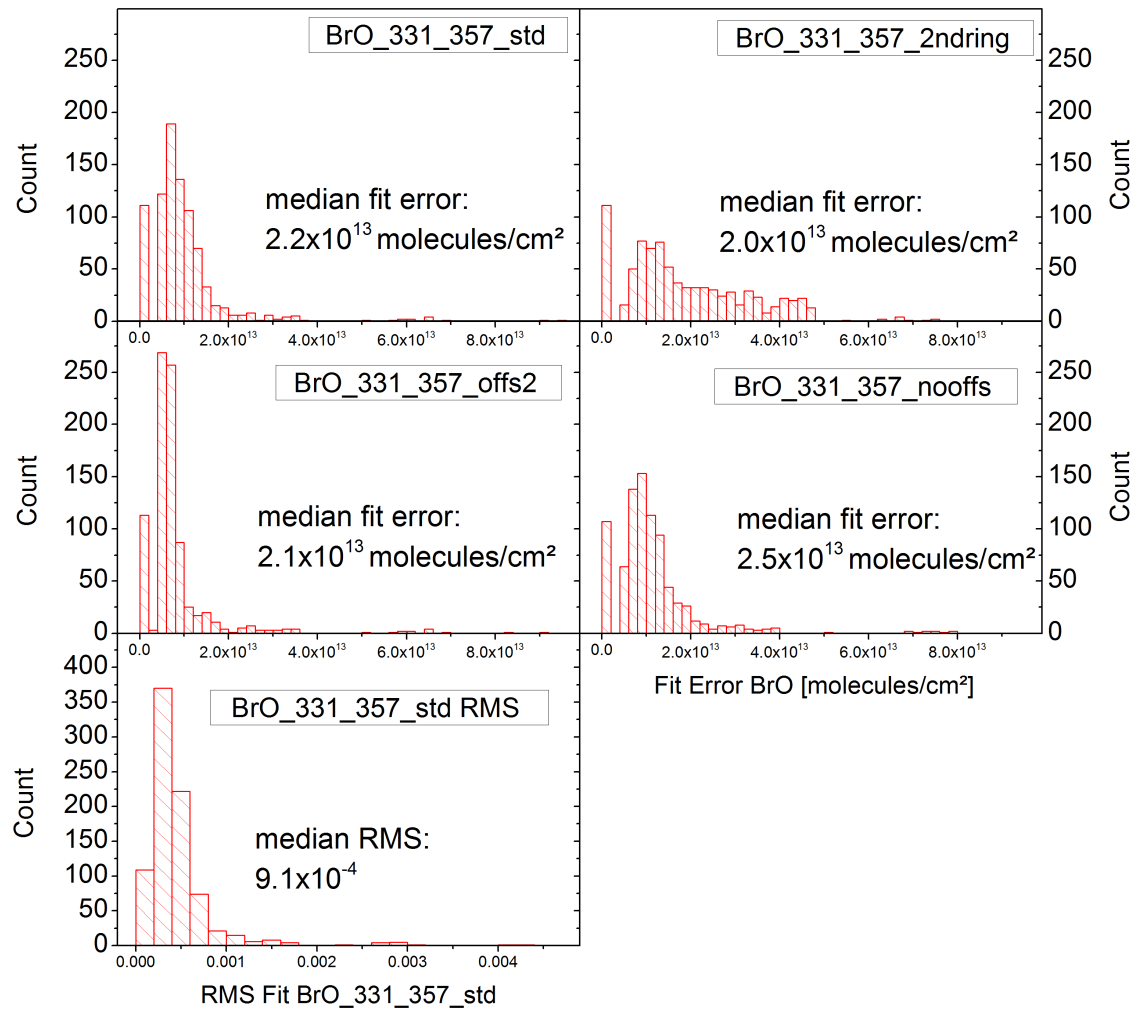


Figure A.5: Histograms of the fit errors (1-4) of different BrO retrievals (see Table 8.2) and RMS from fitting scenario "BrO_331_357_std" (5) at Sua Pan.

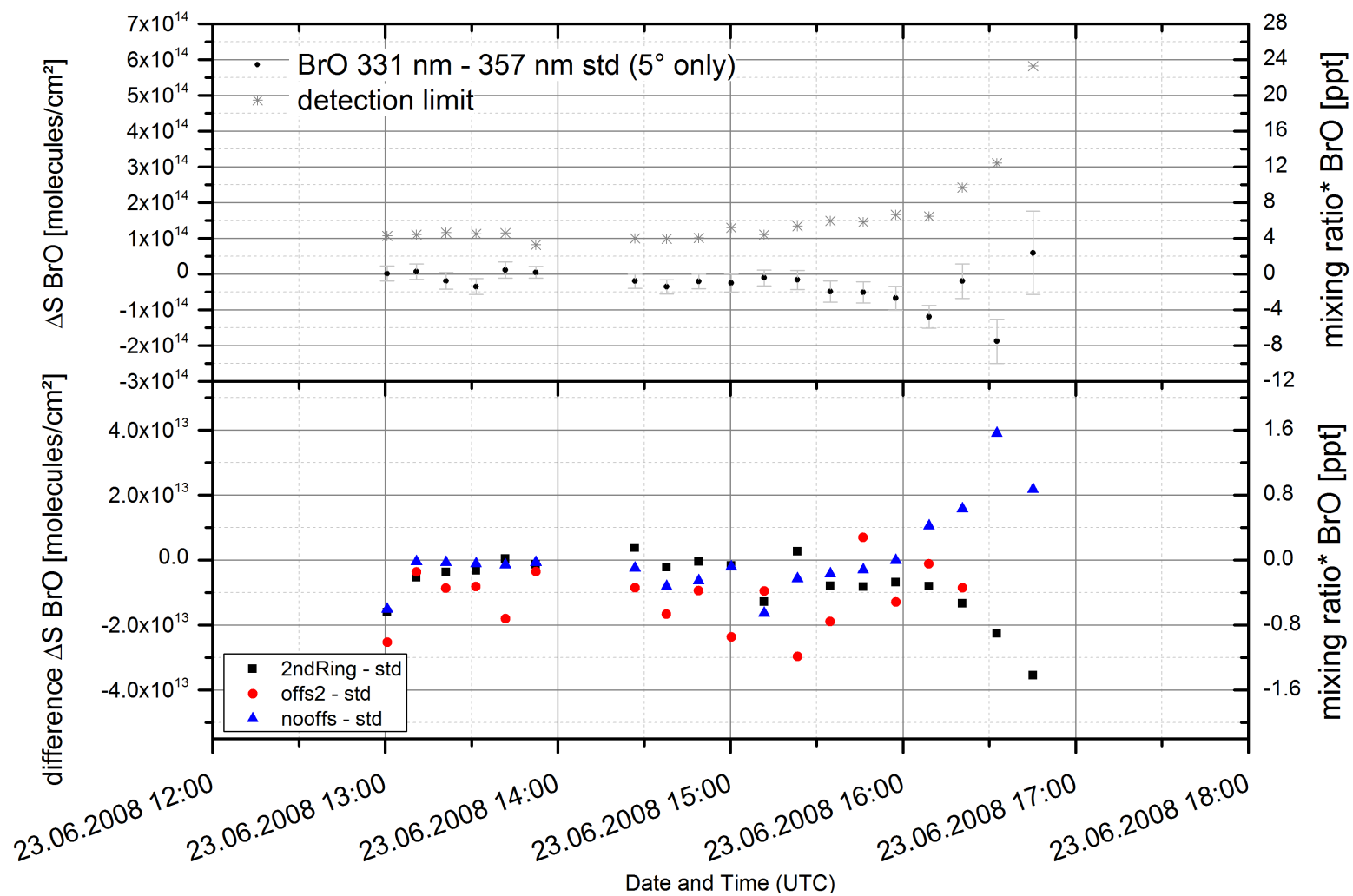


Figure A.6: *BrO differential slant column density $\Delta S(\alpha = 5^\circ)$ retrieved from MAX-DOAS with fit scenario "BrO_331-357_std" (upper panel) and differences of $\Delta S(\alpha = 5^\circ)$ retrieved with other fit scenarios (see Table 8.2) to the standard fit scenario (lower panel) at Sua Pan.*

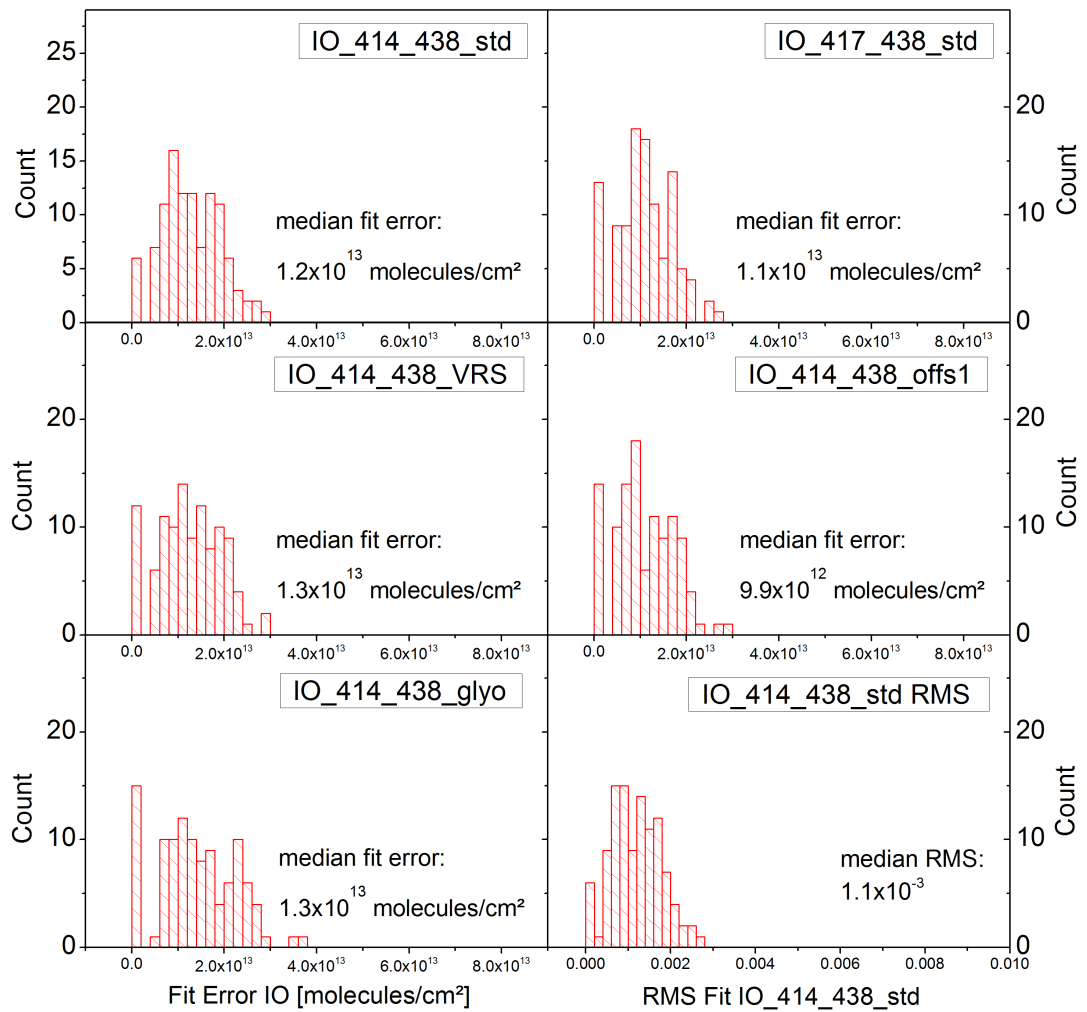


Figure A.7: Histograms of the fit errors (1-5) of different IO retrievals (see Table 8.2) and RMS from fitting scenario "IO_414_438_std" (6) at Sua Pan.

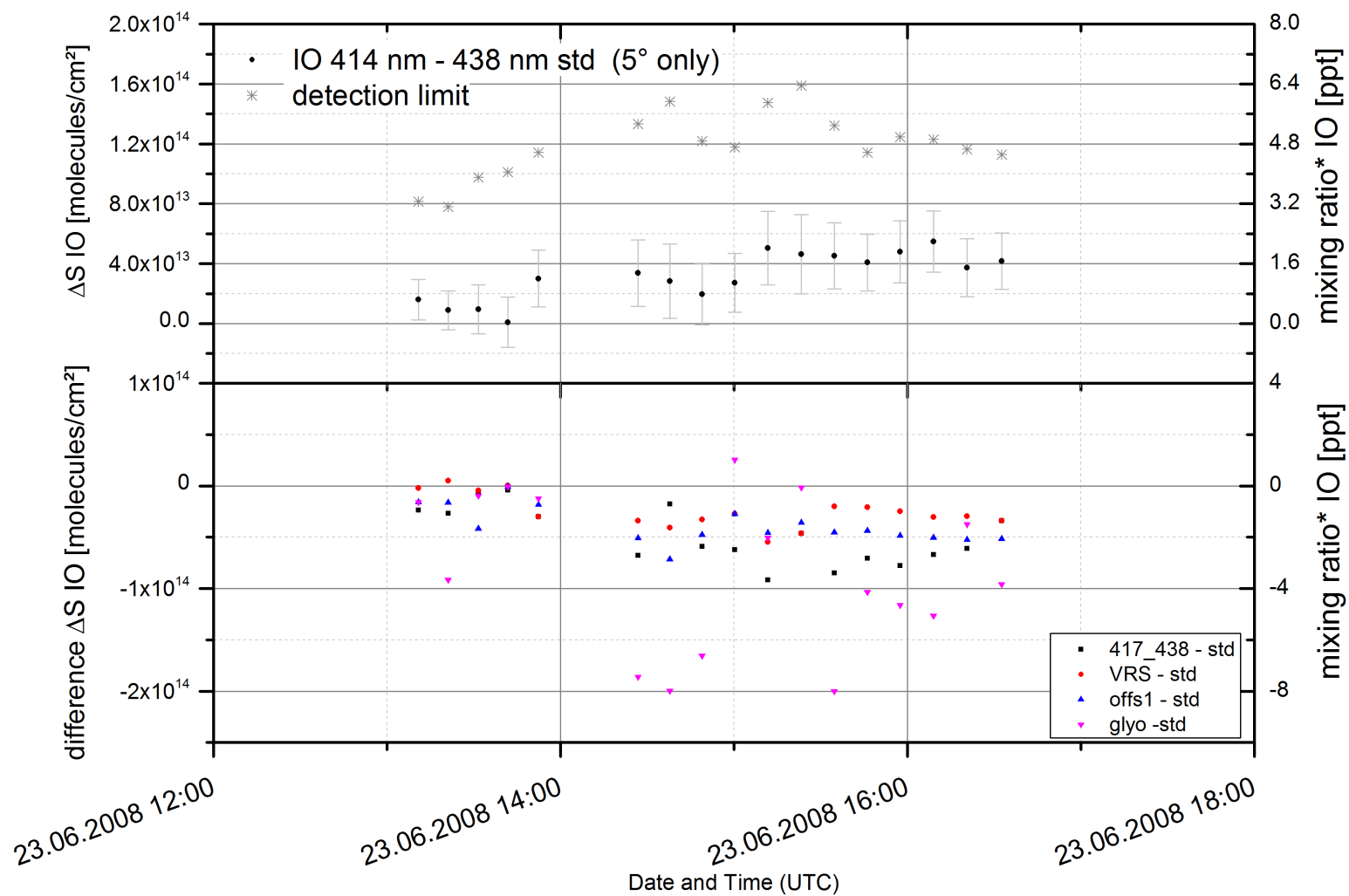


Figure A.8: IO differential slant column density $\Delta S(\alpha = 5^\circ)$ retrieved from MAX-DOAS with fit scenario "IO_414_438_std" (upper panel) and differences of $\Delta S(\alpha = 5^\circ)$ retrieved with other fit scenarios (see Table 8.2) to the standard fit scenario (lower panel) at Sua Pan.

A.3 South Russia 2009

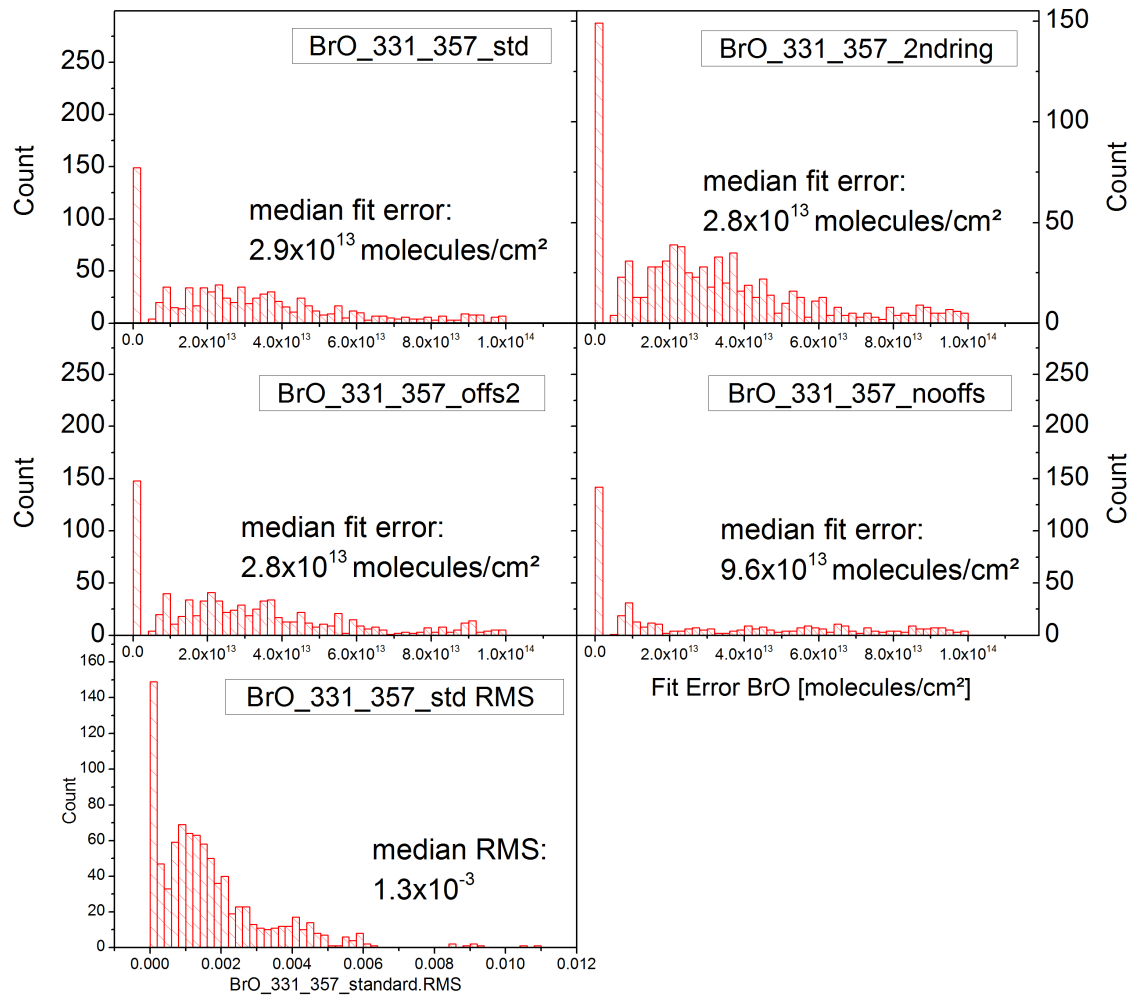


Figure A.9: Histograms of the fit errors (1-4) of different BrO retrievals (see Table 8.2) and RMS from fitting scenario "BrO_331_357_std" (5) at locations in South Russia.

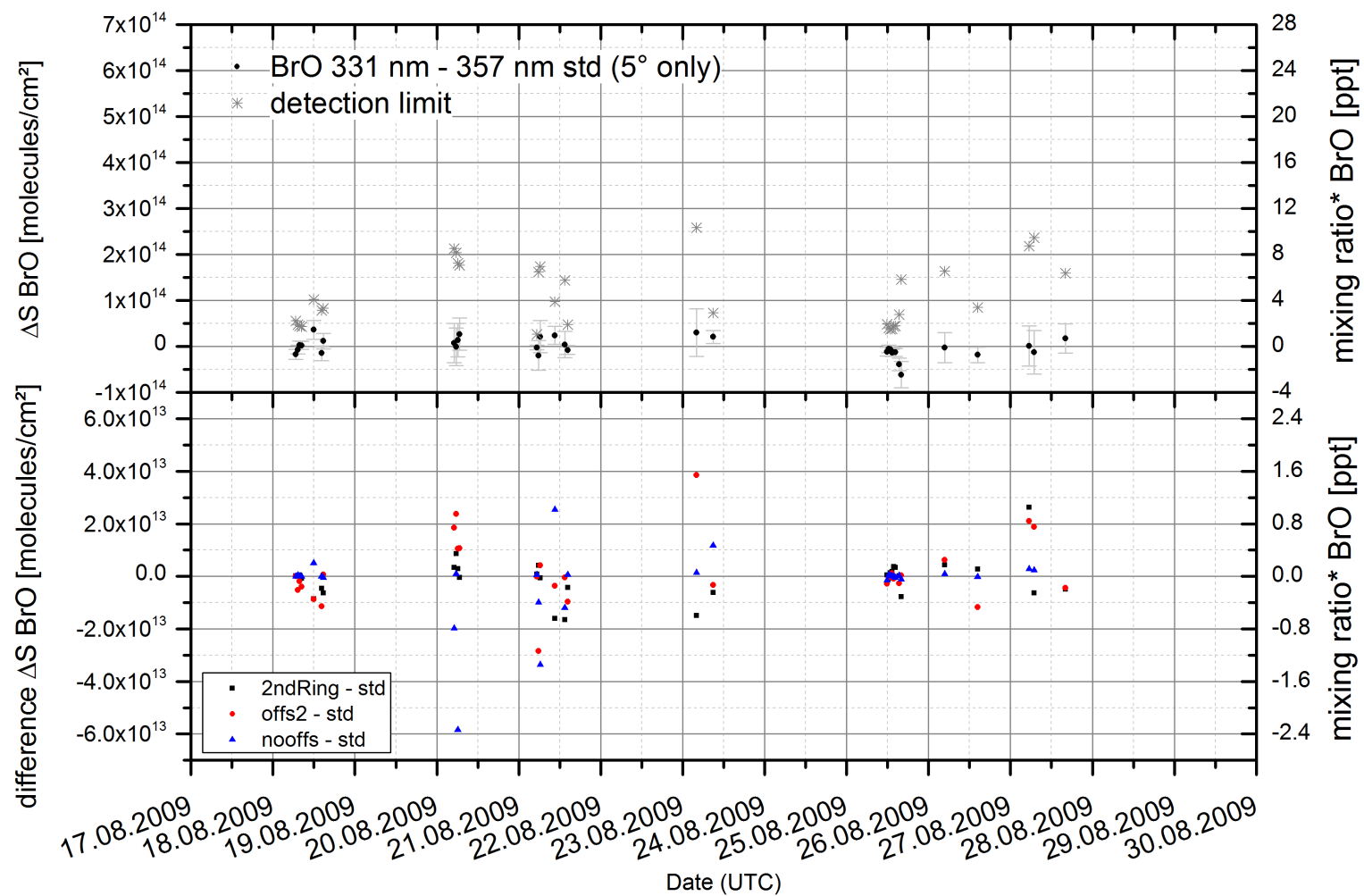


Figure A.10: BrO differential slant column density $\Delta S(\alpha = 5^\circ)$ retrieved from MAX-DOAS with fit scenario "BrO_331-357_std" (upper panel) and differences of $\Delta S(\alpha = 5^\circ)$ retrieved with other fit scenarios (see Table 8.2) to the standard fit scenario (lower panel) at locations in South Russia.

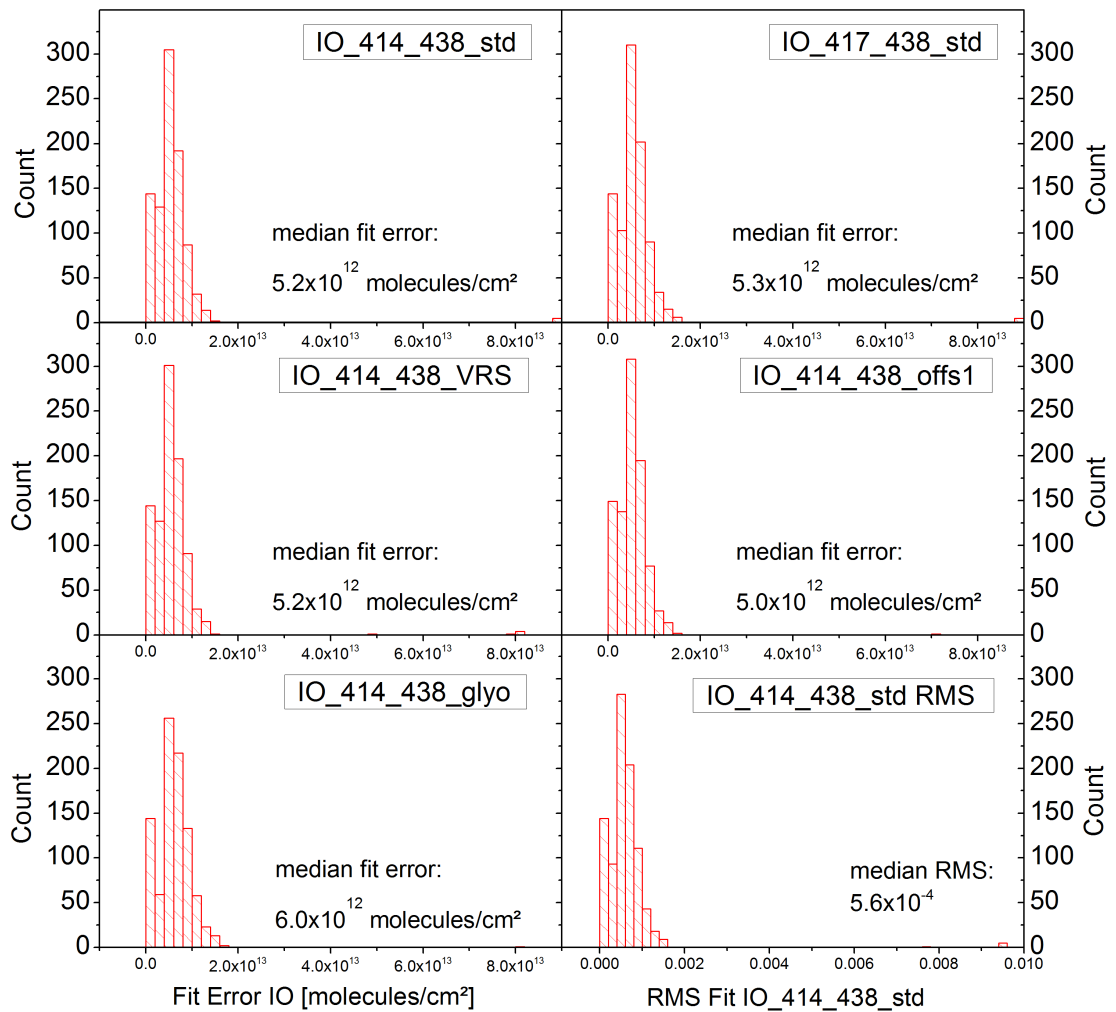


Figure A.11: Histograms of the fit errors (1-5) of different IO retrievals (see Table 8.2) and RMS from fitting scenario "IO_414_438_std" (6) at locations in South Russia at locations in South Russia.

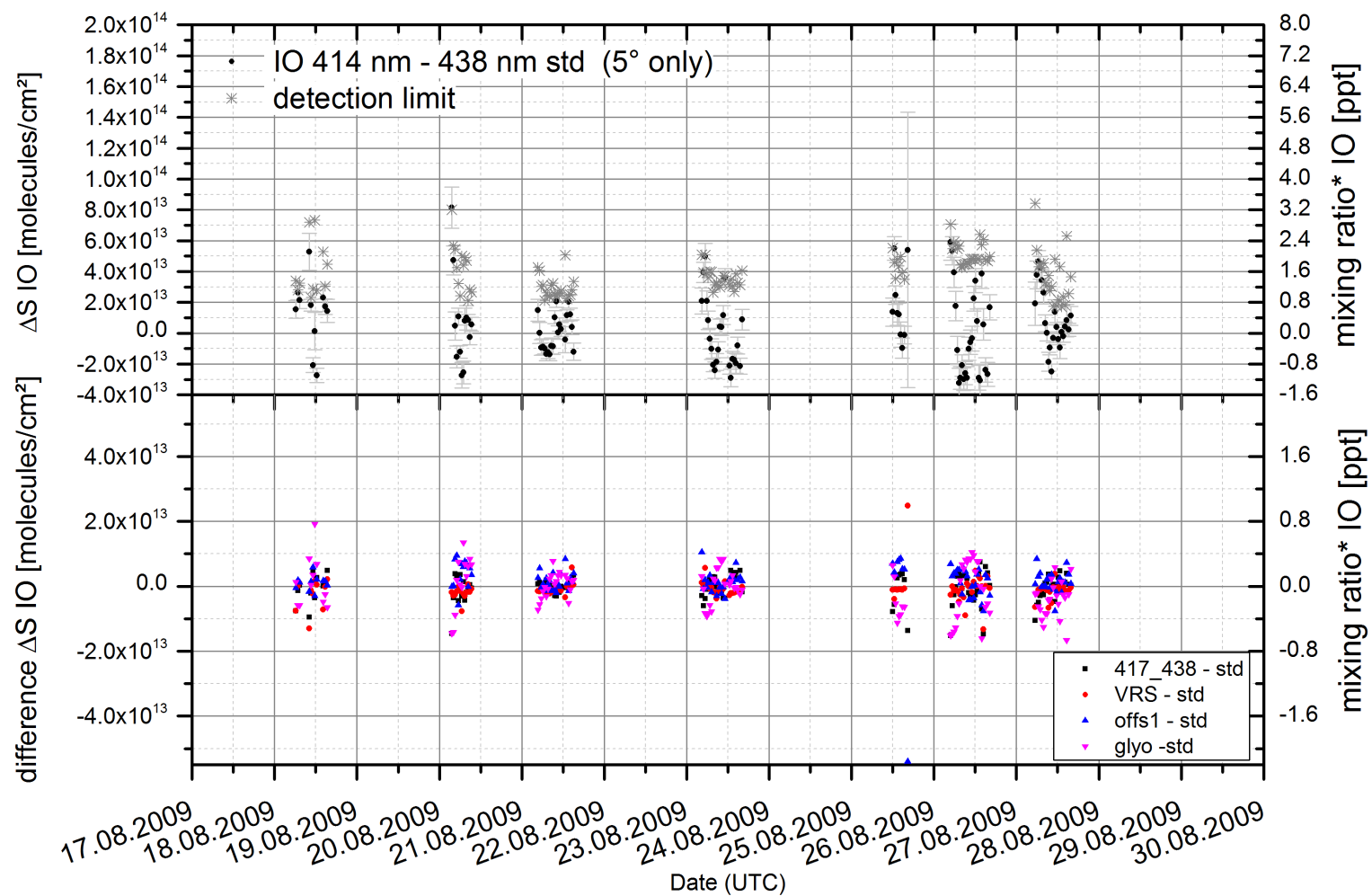


Figure A.12: IO differential slant column density $\Delta S(\alpha = 5^\circ)$ retrieved from MAX-DOAS with fit scenario "IO_414_438_std" (upper panel) and differences of $\Delta S(\alpha = 5^\circ)$ retrieved with other fit scenarios (see Table 8.2) to the standard fit scenario (lower panel) at locations in South Russia.

A.4 Cape Verde 2010

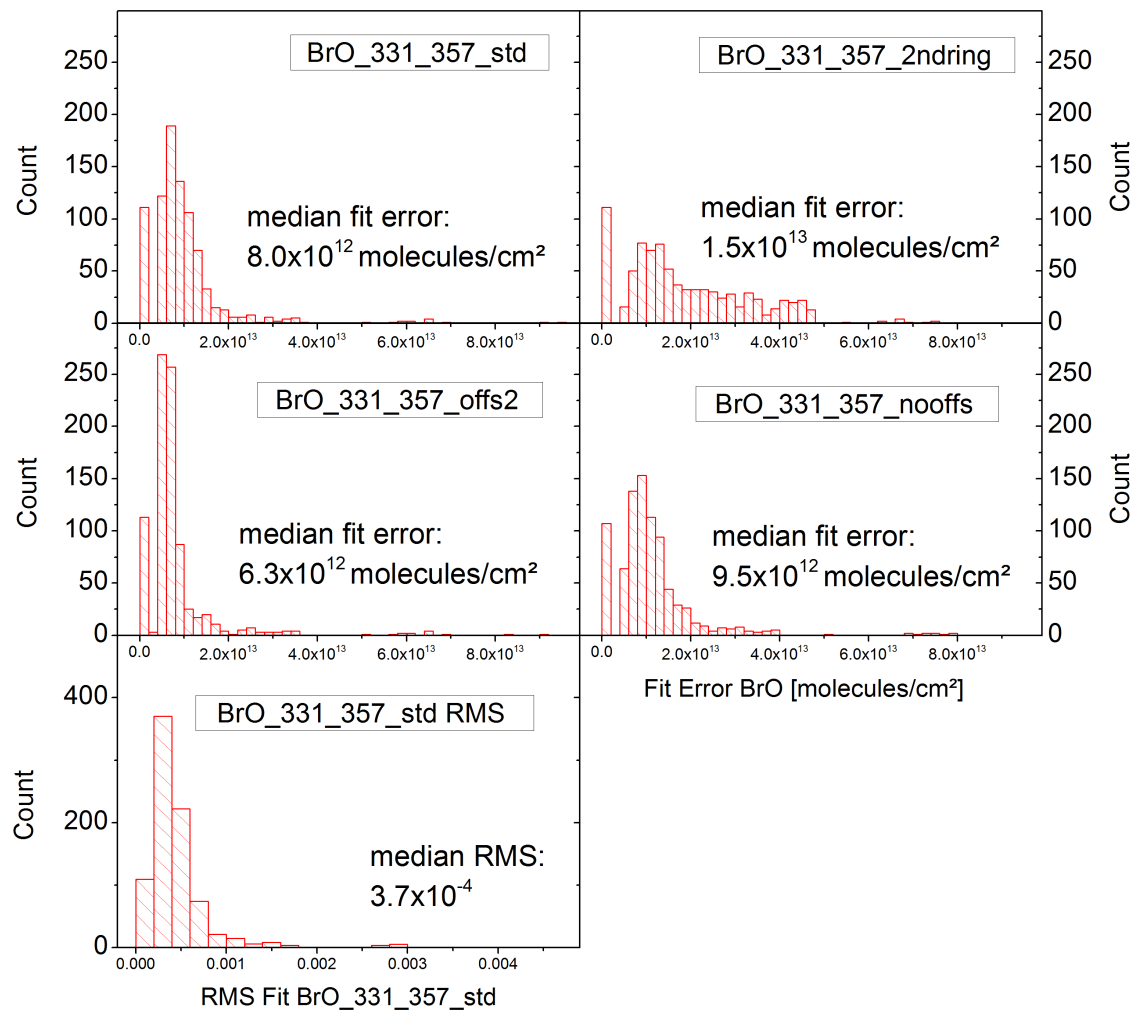


Figure A.13: Histograms of the fit errors (1-4) of different BrO retrievals (see Table 8.2) and RMS from fitting scenario "BrO_331_357_std" (5) on Sal, Cape Verde.

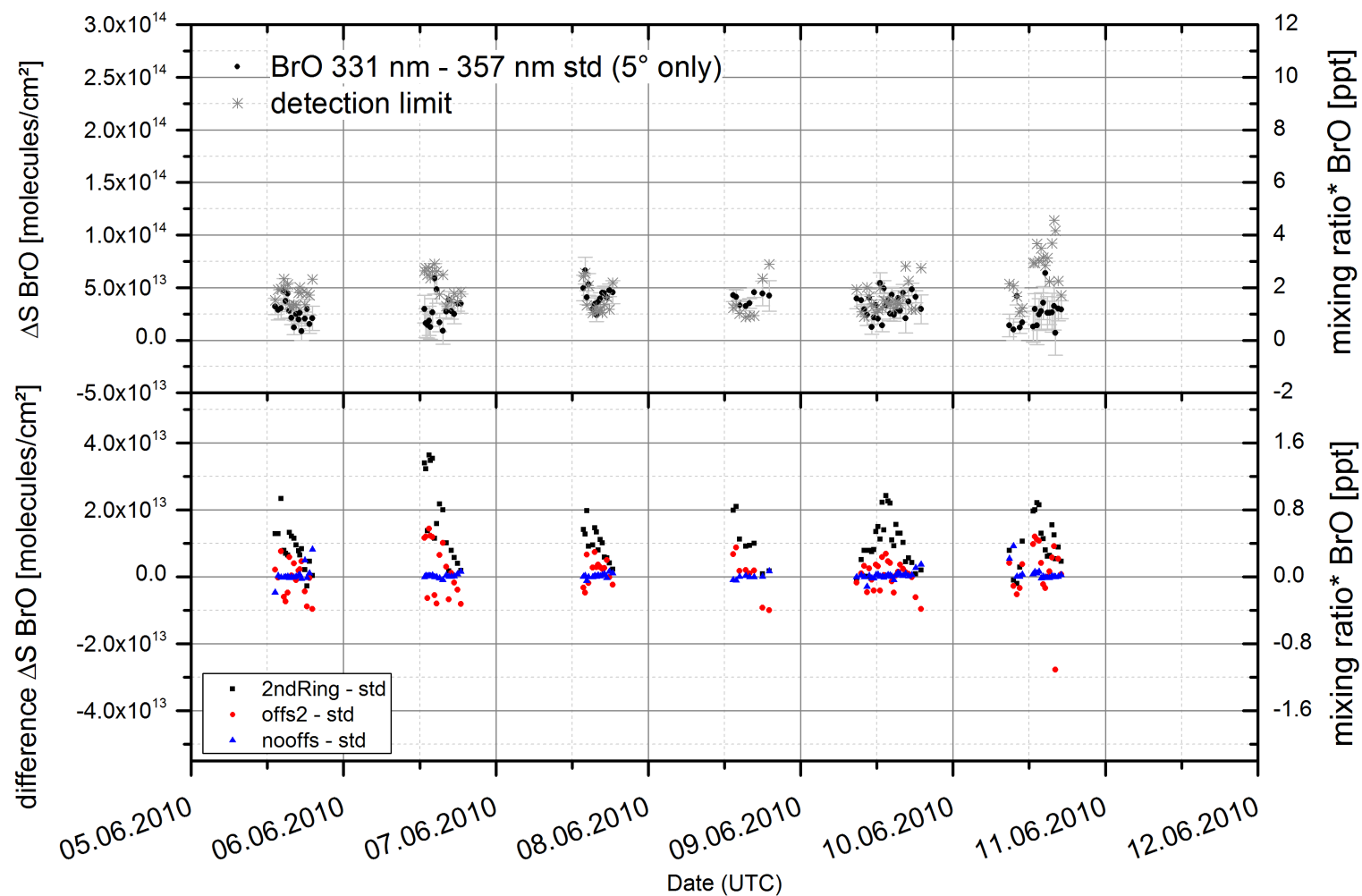


Figure A.14: BrO differential slant column density $\Delta S(\alpha = 5^\circ)$ retrieved from MAX-DOAS with fit scenario "BrO_331-357_std" (upper panel) and differences of $\Delta S(\alpha = 5^\circ)$ retrieved with other fit scenarios (see Table 8.2) to the standard fit scenario (lower panel) on Sal, Cape Verde.

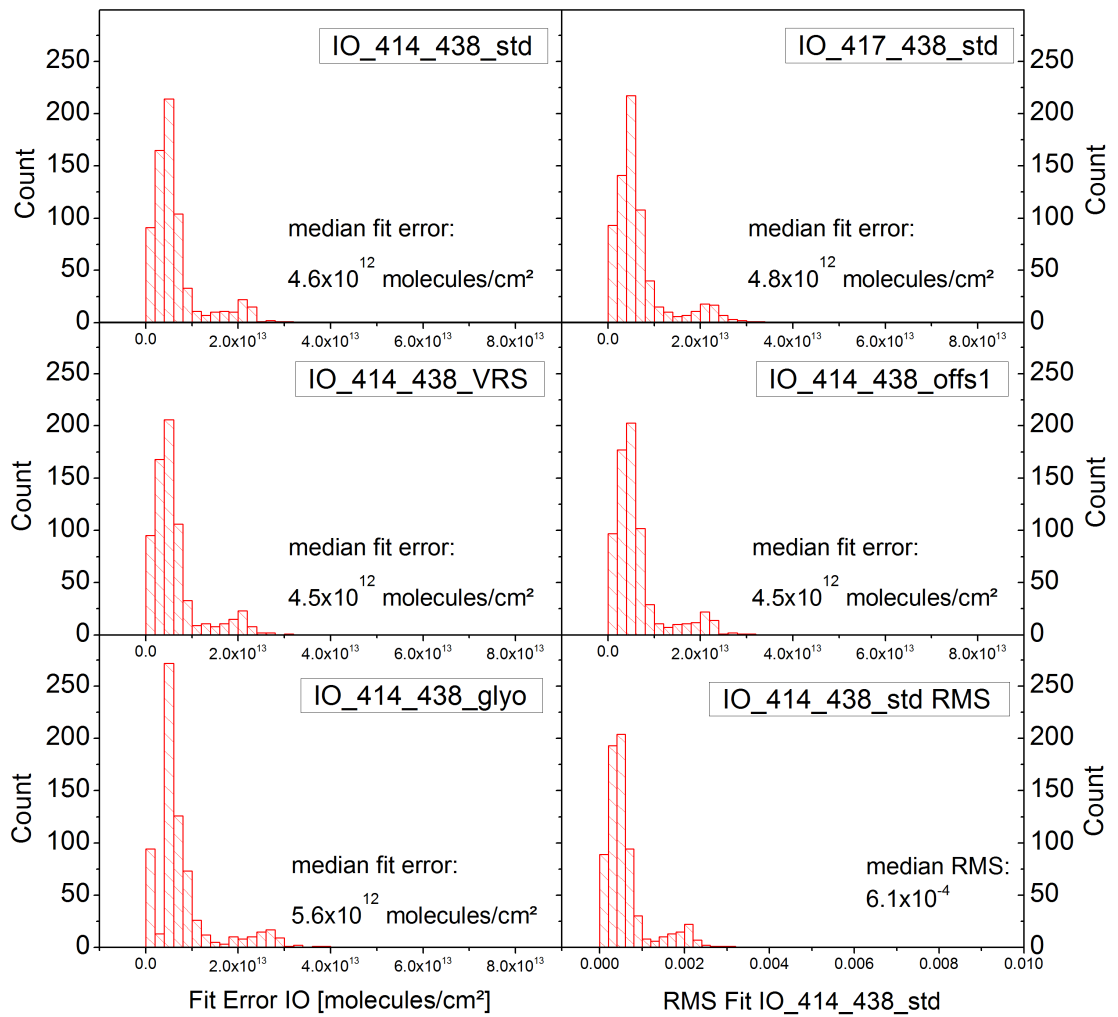


Figure A.15: Histograms of the fit errors (1-5) of different IO retrievals (see Table 8.2) and RMS from fitting scenario "IO_414_438_std" (6) on Sal, Cape Verde.

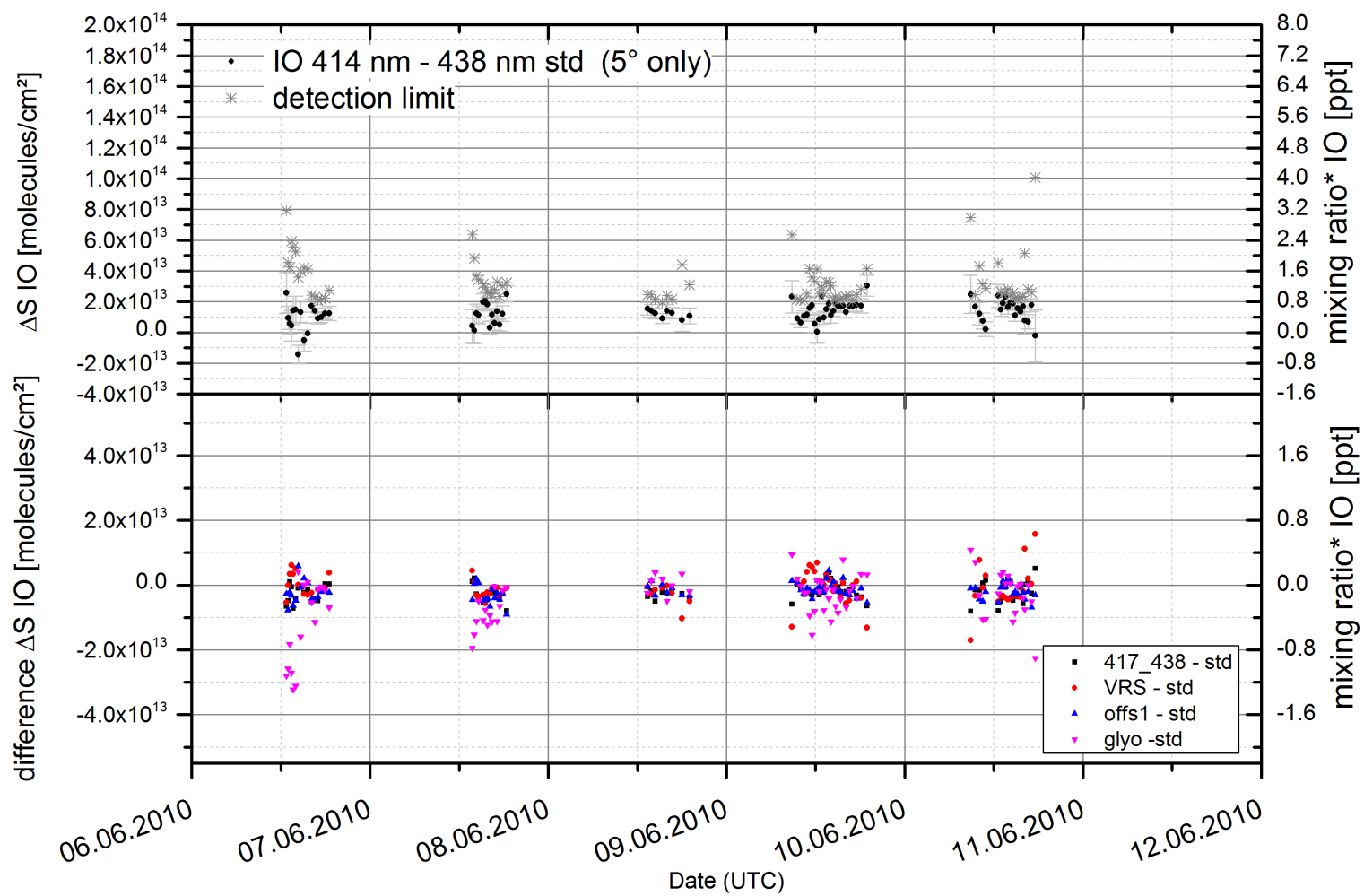


Figure A.16: IO differential slant column density $\Delta S(\alpha = 5^\circ)$ retrieved from MAX-DOAS with fit scenario "IO_414_438_std" (upper panel) and differences of $\Delta S(\alpha = 5^\circ)$ retrieved with other fit scenarios (see Table 8.2) to the standard fit scenario (lower panel) on Sal, Cape Verde.

A.5 South West Australia 2011

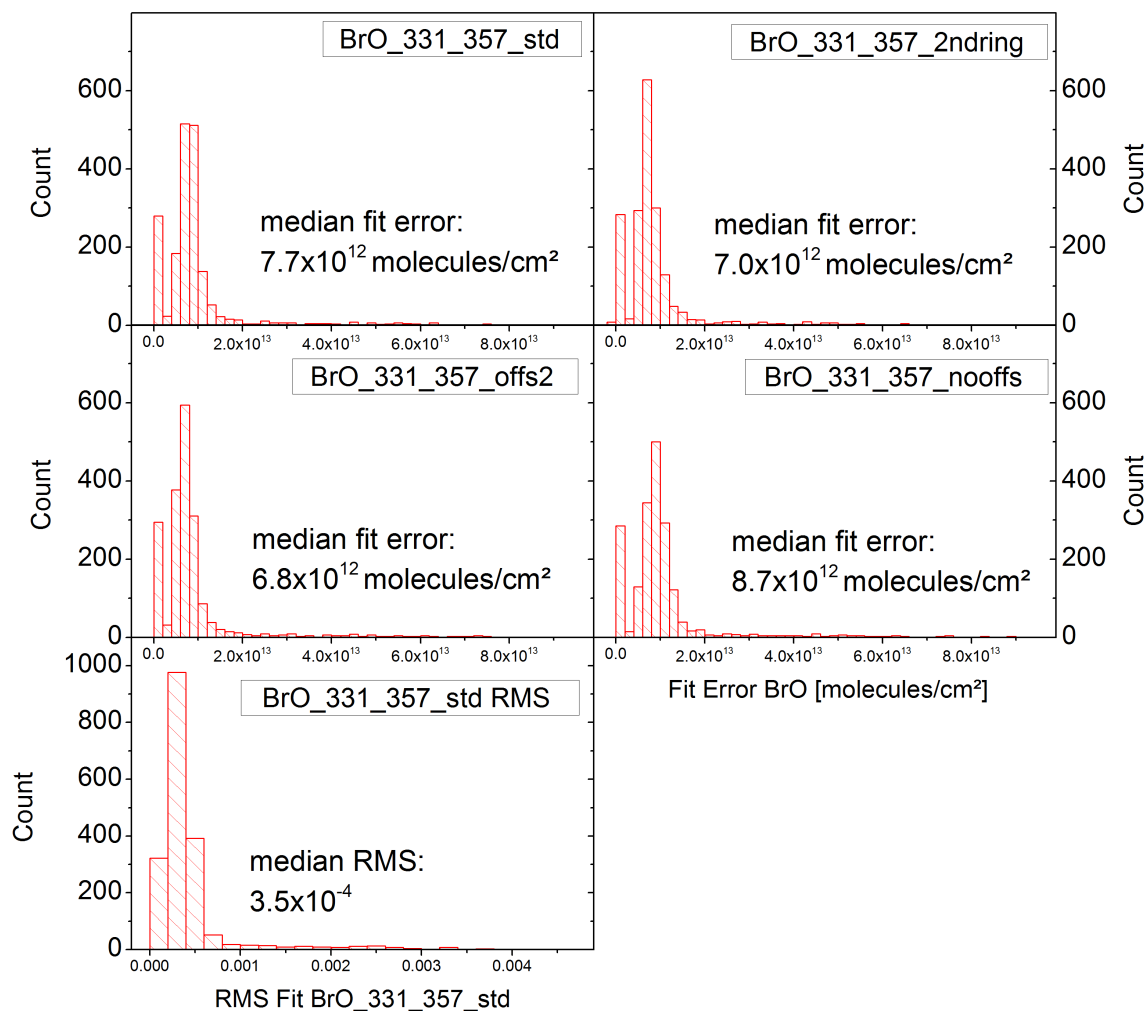


Figure A.17: Histograms of the fit errors (1-4) of different BrO retrievals (see Table 8.2) and RMS from fitting scenario "BrO_331_357_std" (5) at locations in South West Australia.

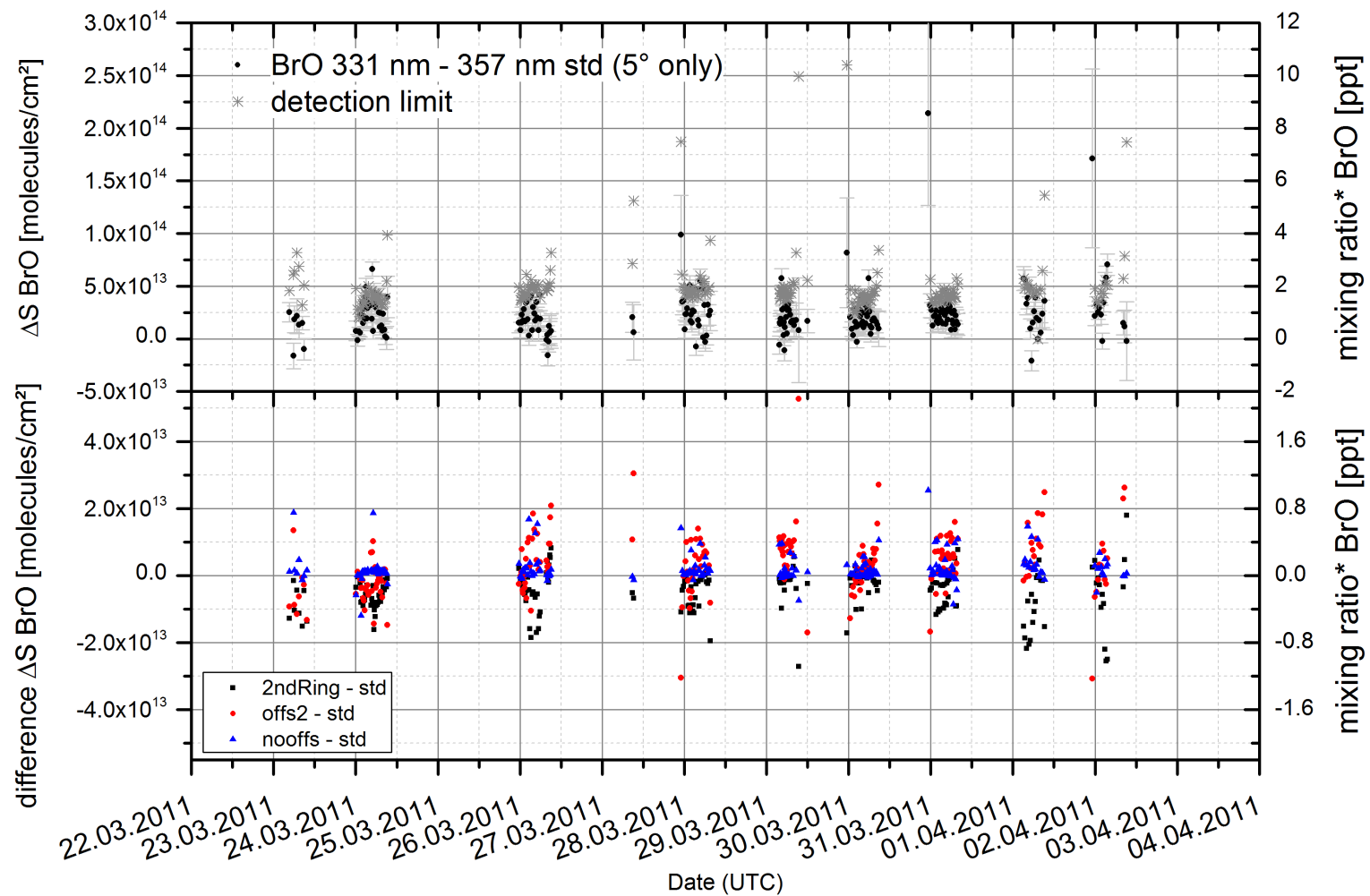


Figure A.18: BrO differential slant column density $\Delta S(\alpha = 5^\circ)$ retrieved from MAX-DOAS with fit scenario "BrO_331-357_std" (upper panel) and differences of $\Delta S(\alpha = 5^\circ)$ retrieved with other fit scenarios (see Table 8.2) to the standard fit scenario (lower panel) at locations in South West Australia.

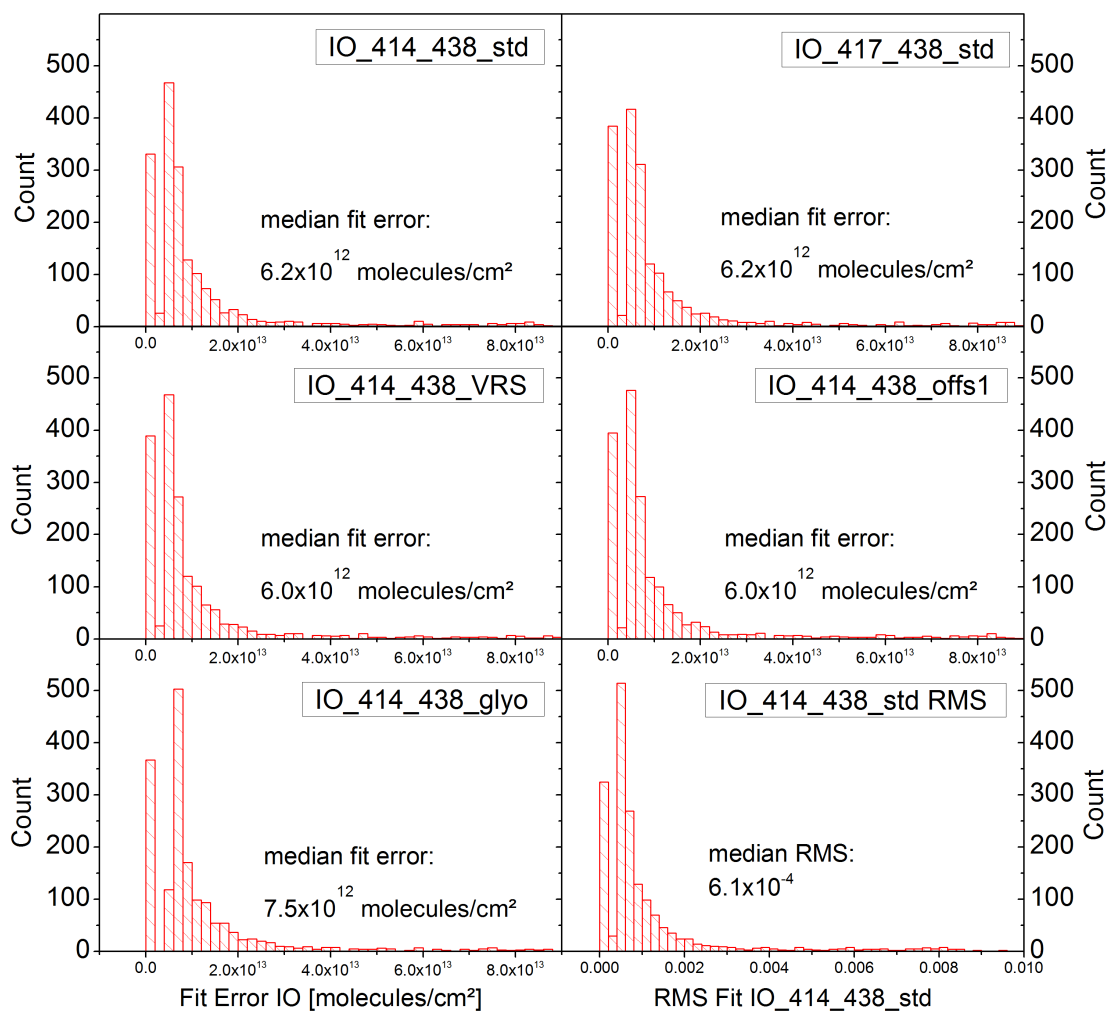


Figure A.19: Histograms of the fit errors (1-5) of different IO retrievals (see Table 8.2) and RMS from fitting scenario "IO_414_438_std" (6) at locations in South West Australia.

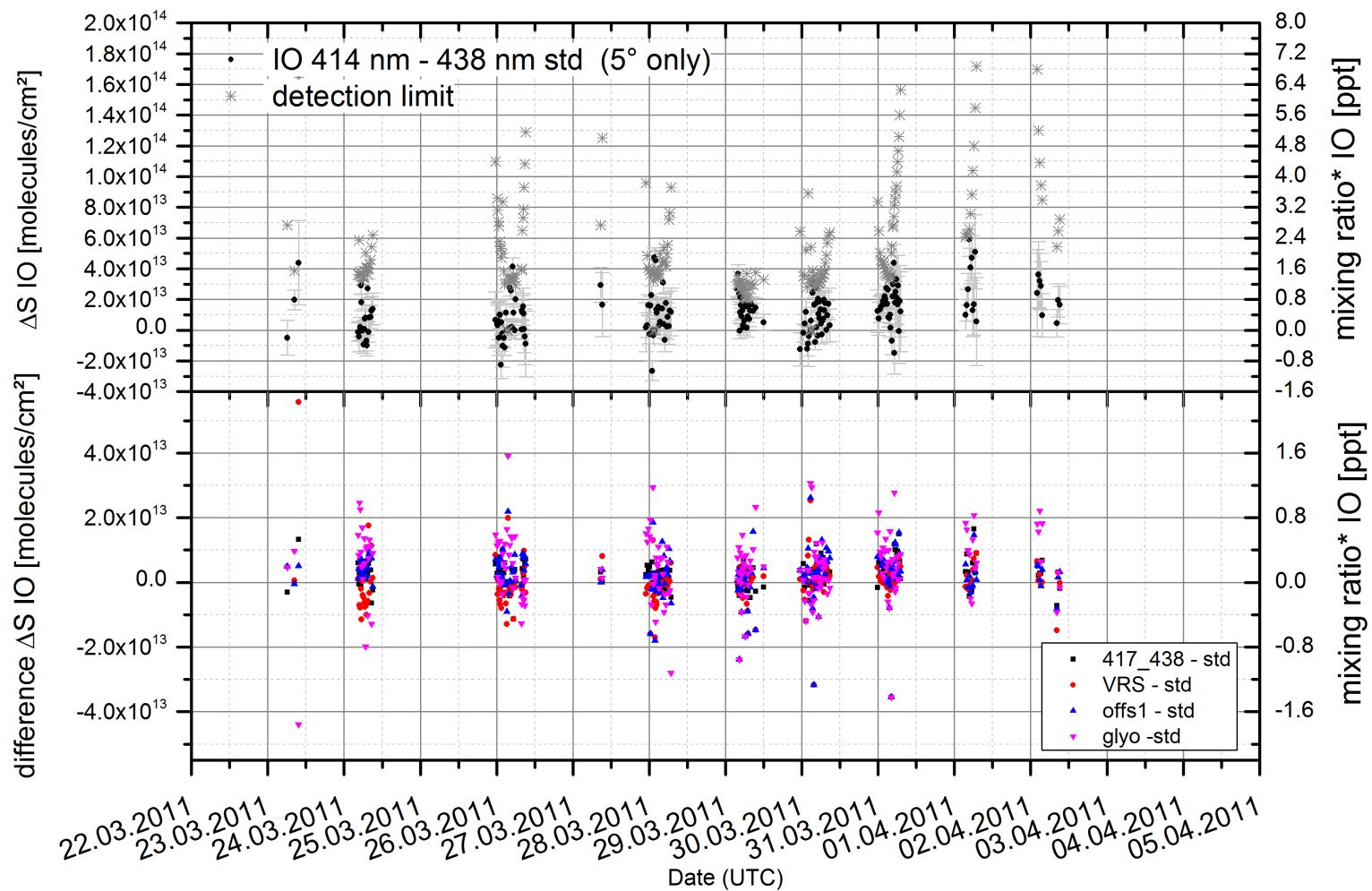


Figure A.20: IO differential slant column density $\Delta S(\alpha = 5^\circ)$ retrieved from MAX-DOAS with fit scenario "IO_414_438_std" (upper panel) and differences of $\Delta S(\alpha = 5^\circ)$ retrieved with other fit scenarios (see Table 8.2) to the standard fit scenario (lower panel) at locations in South West Australia.

A.6 Kali Dump Heringen 2011

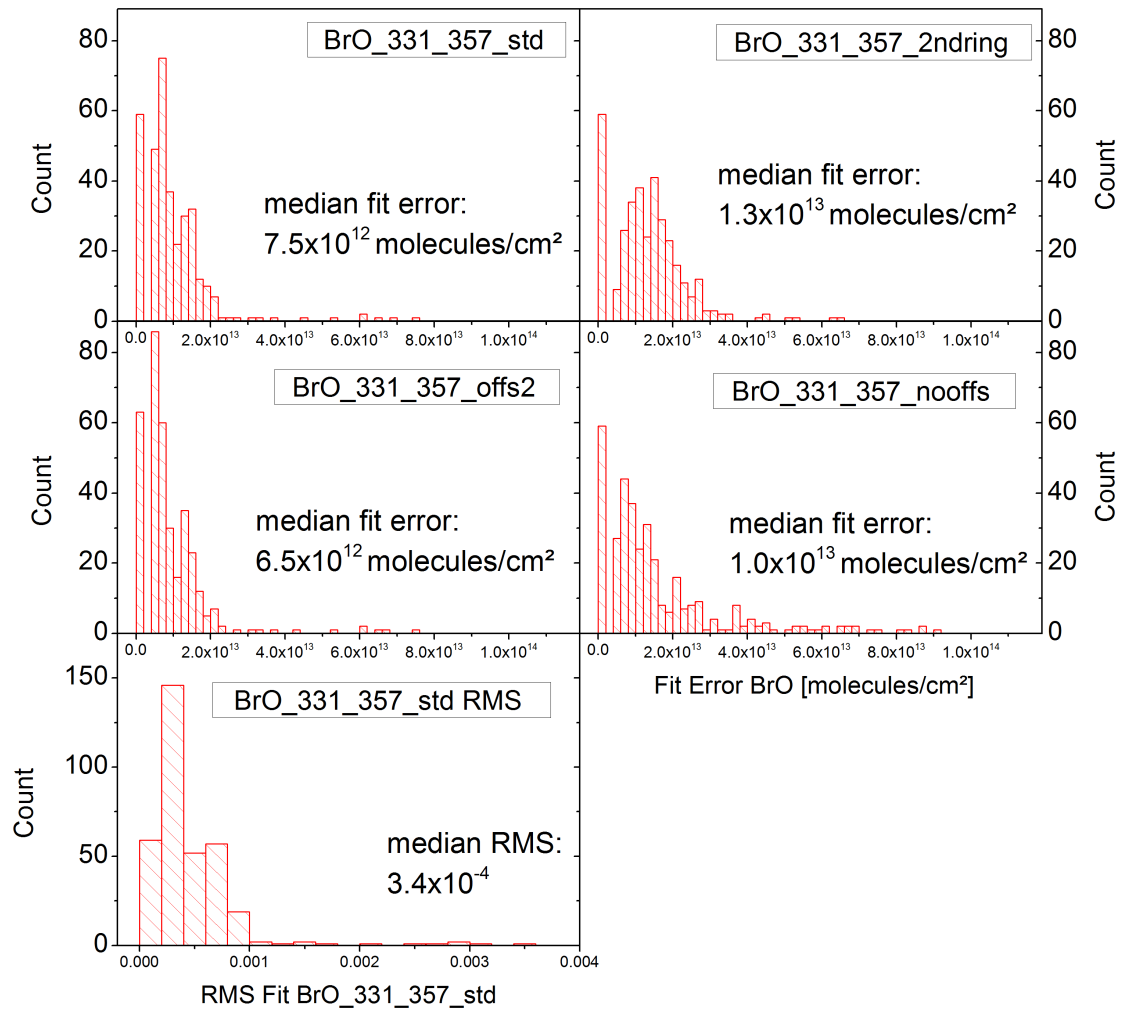


Figure A.21: Histograms of the fit errors (1-4) of different BrO retrievals (see Table 8.2) and RMS from fitting scenario "BrO_331_357_std" (5) at the Kali dump in Heringen, Germany.

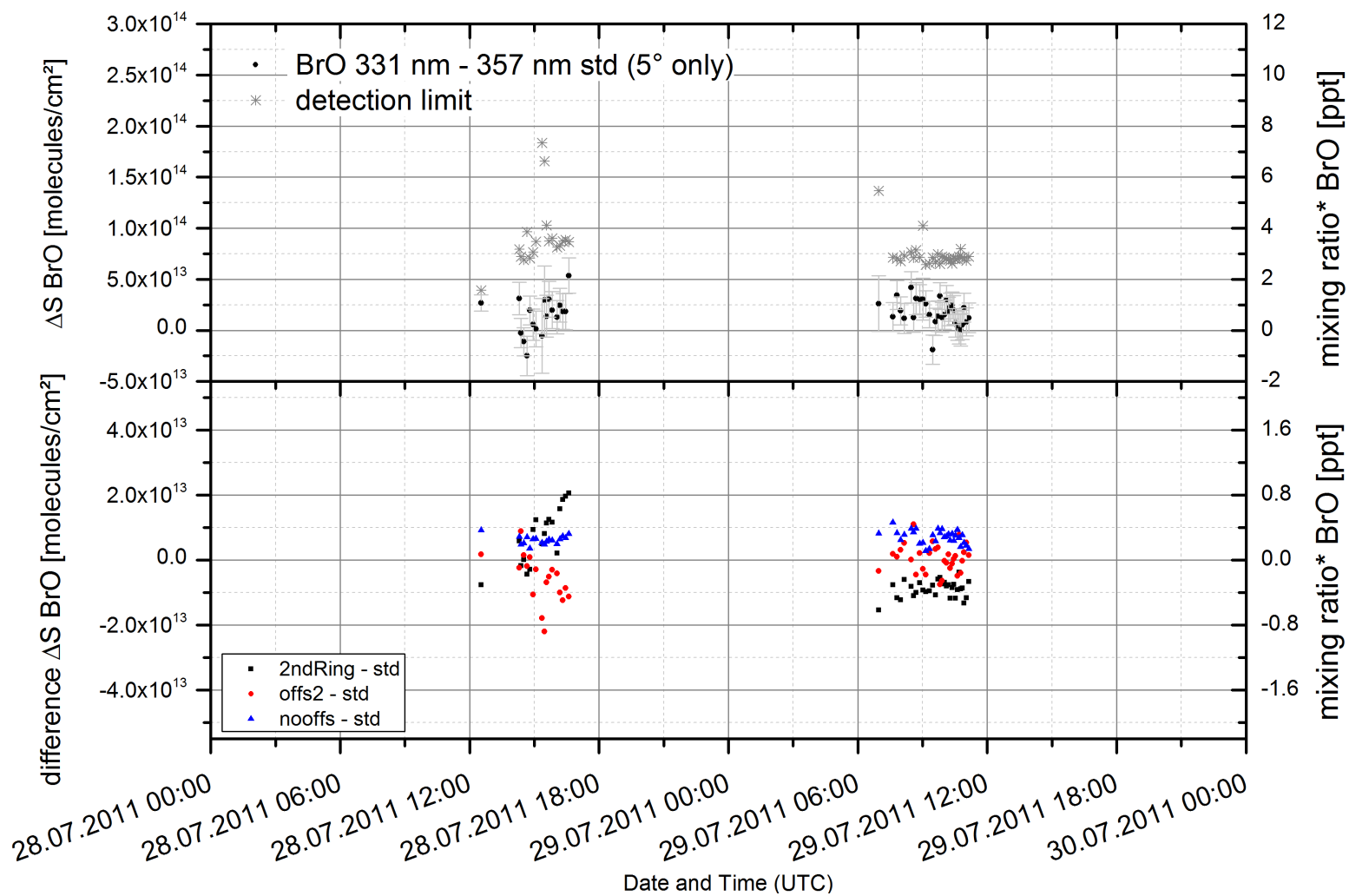


Figure A.22: BrO differential slant column density $\Delta S(\alpha = 5^\circ)$ retrieved from MAX-DOAS with fit scenario "BrO_331-357_std" (upper panel) and differences of $\Delta S(\alpha = 5^\circ)$ retrieved with other fit scenarios (see Table 8.2) to the standard fit scenario (lower panel) at the Kali dump in Heringen, Germany.

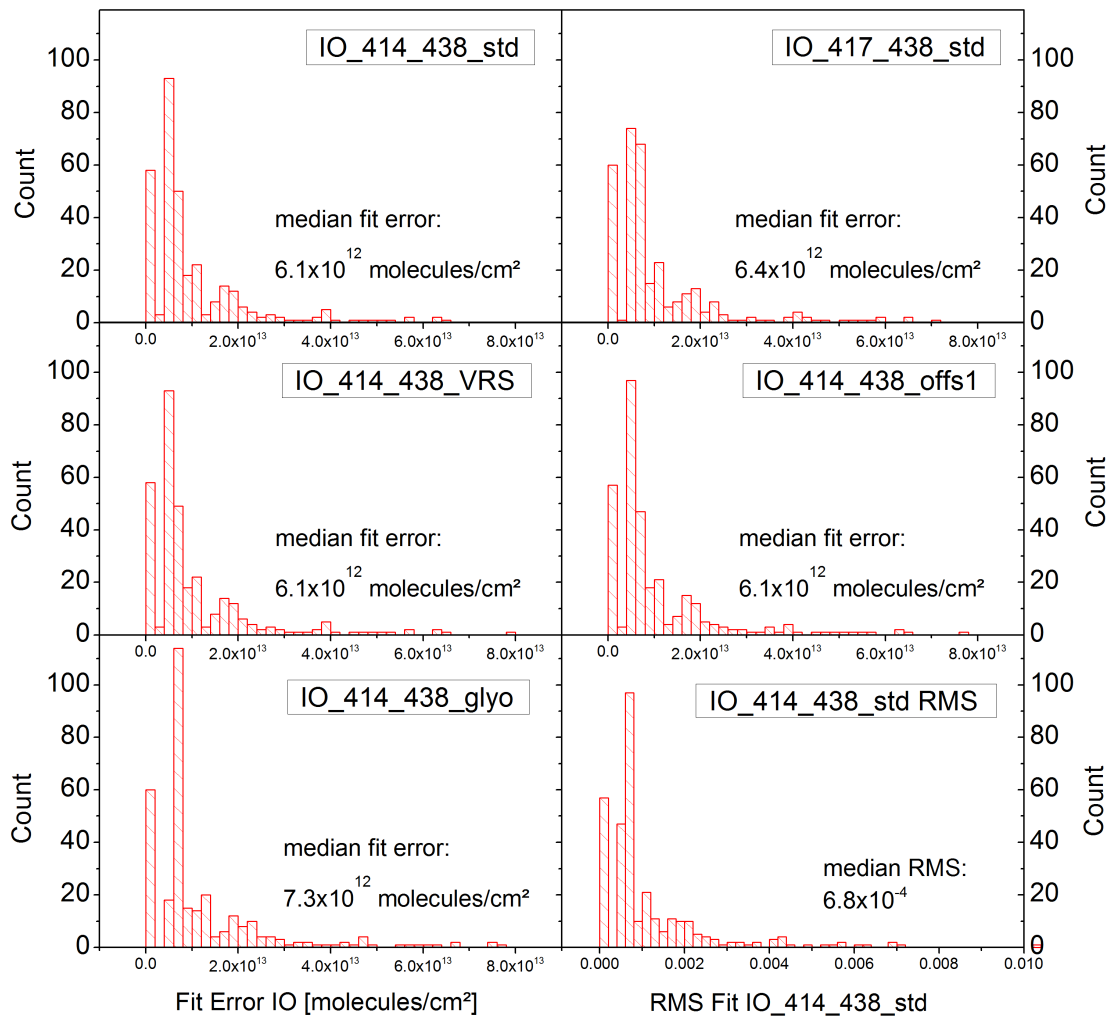


Figure A.23: Histograms of the fit errors (1-5) of different IO retrievals (see Table 8.2) and RMS from fitting scenario "IO_414_438_std" (6) at the Kali dump in Heringen, Germany.

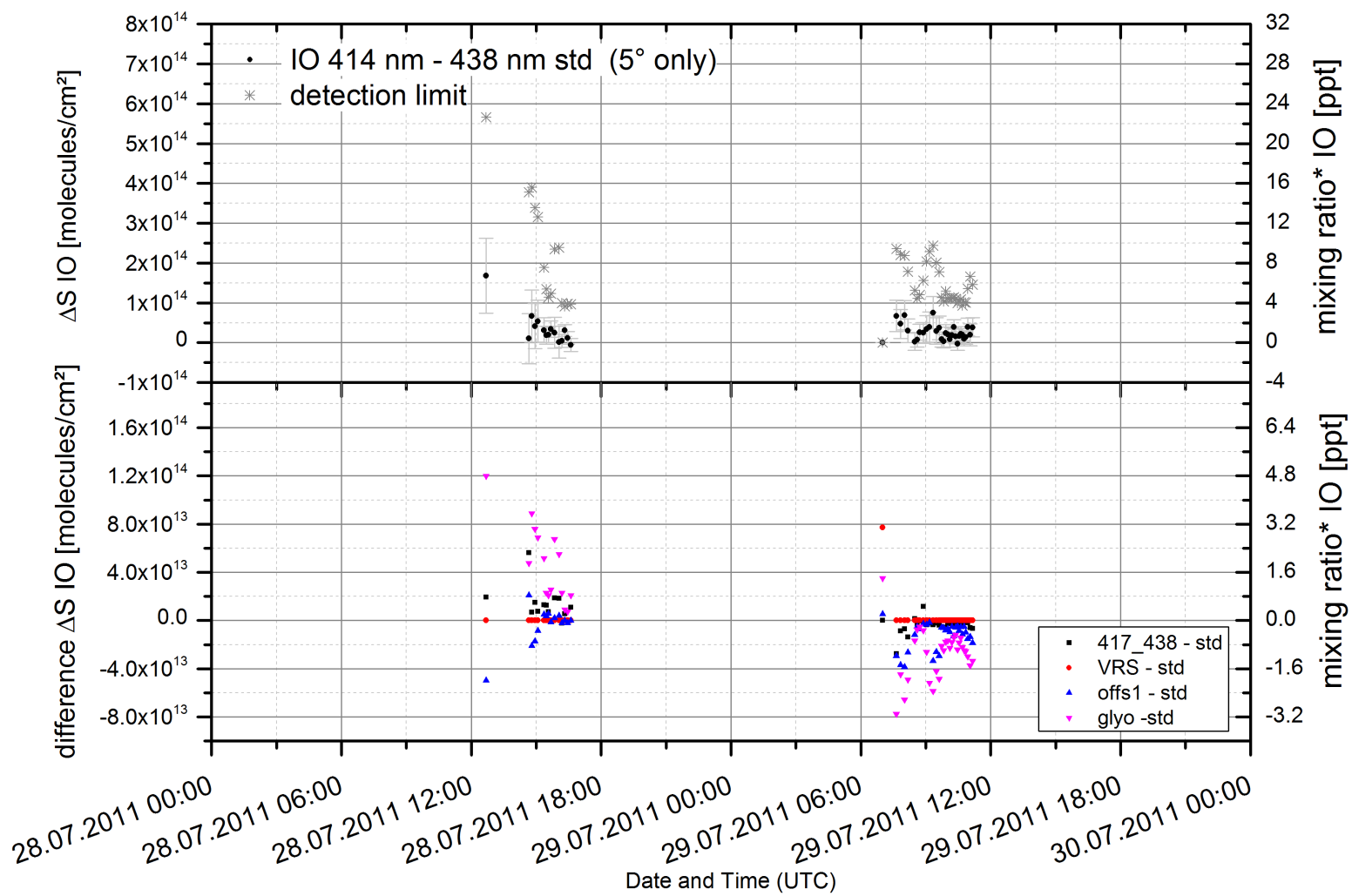


Figure A.24: IO differential slant column density $\Delta S(\alpha = 5^\circ)$ retrieved from MAX-DOAS with fit scenario "IO_414_438_std" (upper panel) and differences of $\Delta S(\alpha = 5^\circ)$ retrieved with other fit scenarios (see Table 8.2) to the standard fit scenario (lower panel) at the Kali dump in Heringen, Germany.

A.7 Bourtanger Moor 2011

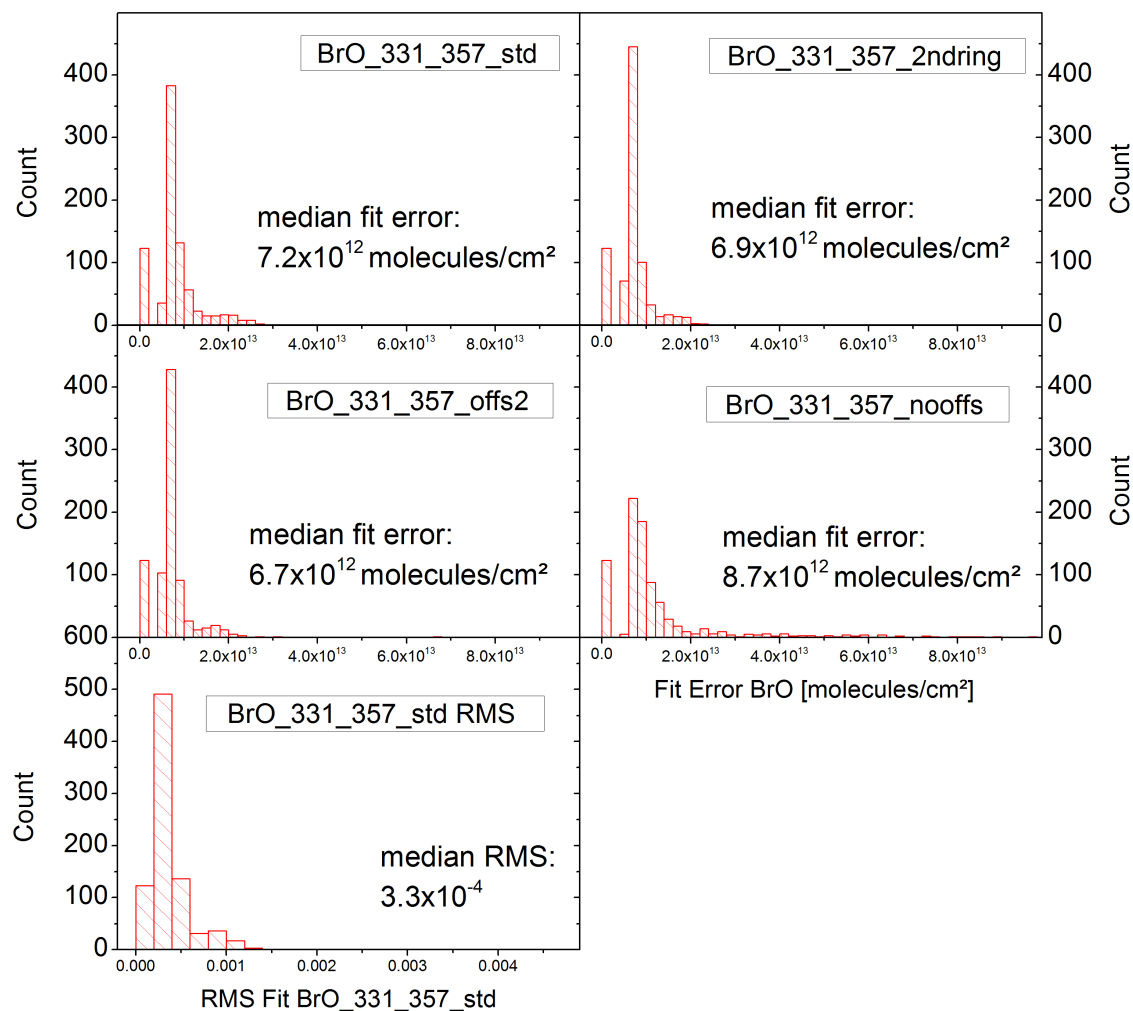


Figure A.25: Histograms of the fit errors (1-4) of different BrO retrievals (see Table 8.2) and RMS from fitting scenario "BrO_331_357_std" (5) at the Bourtanger Moor, Germany.

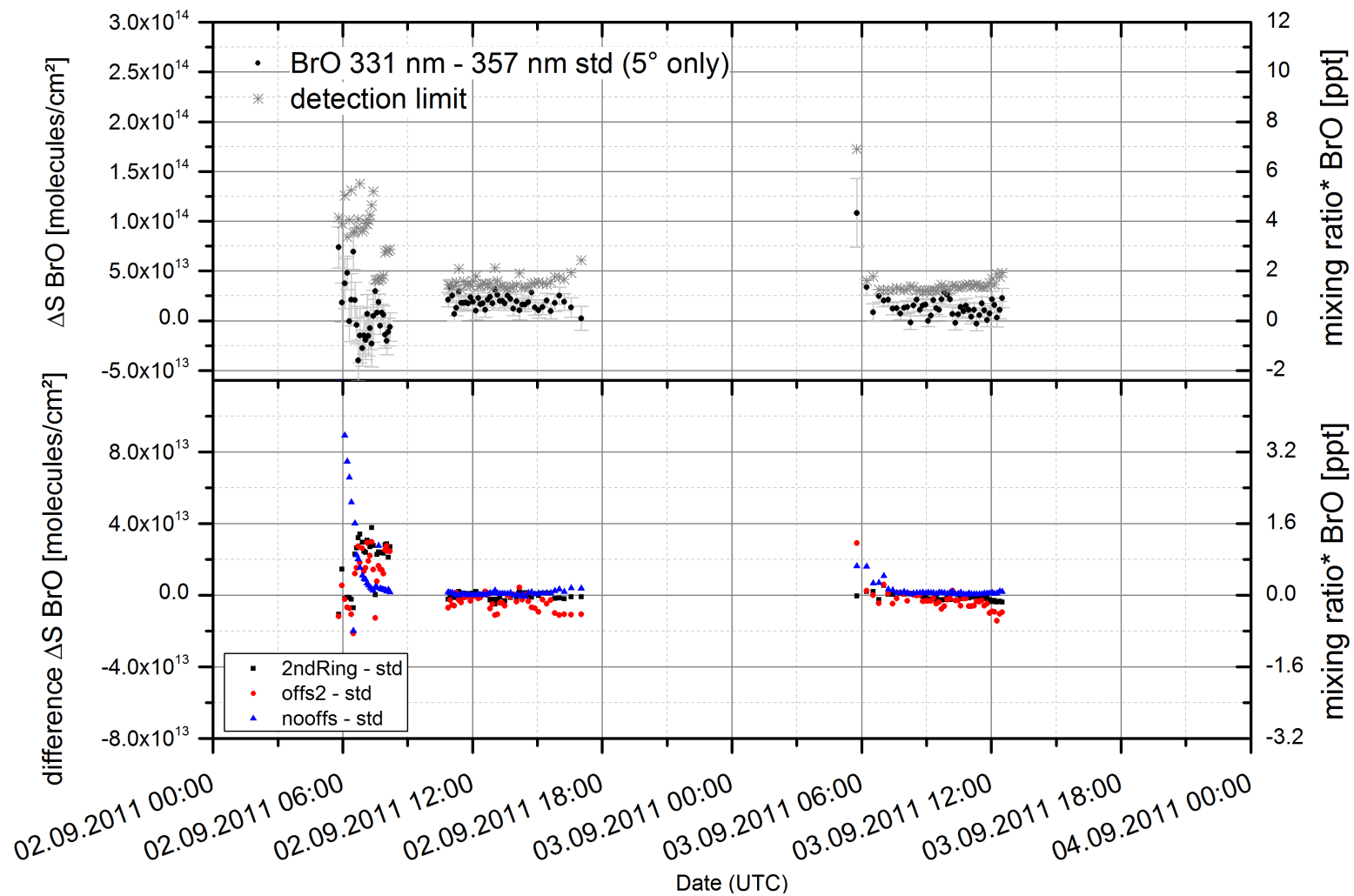


Figure A.26: BrO differential slant column density $\Delta S(\alpha = 5^\circ)$ retrieved from MAX-DOAS with fit scenario "BrO_331_357_std" (upper panel) and differences of $\Delta S(\alpha = 5^\circ)$ retrieved with other fit scenarios (see Table 8.2) to the standard fit scenario (lower panel) at the Bourtanger Moor, Germany.

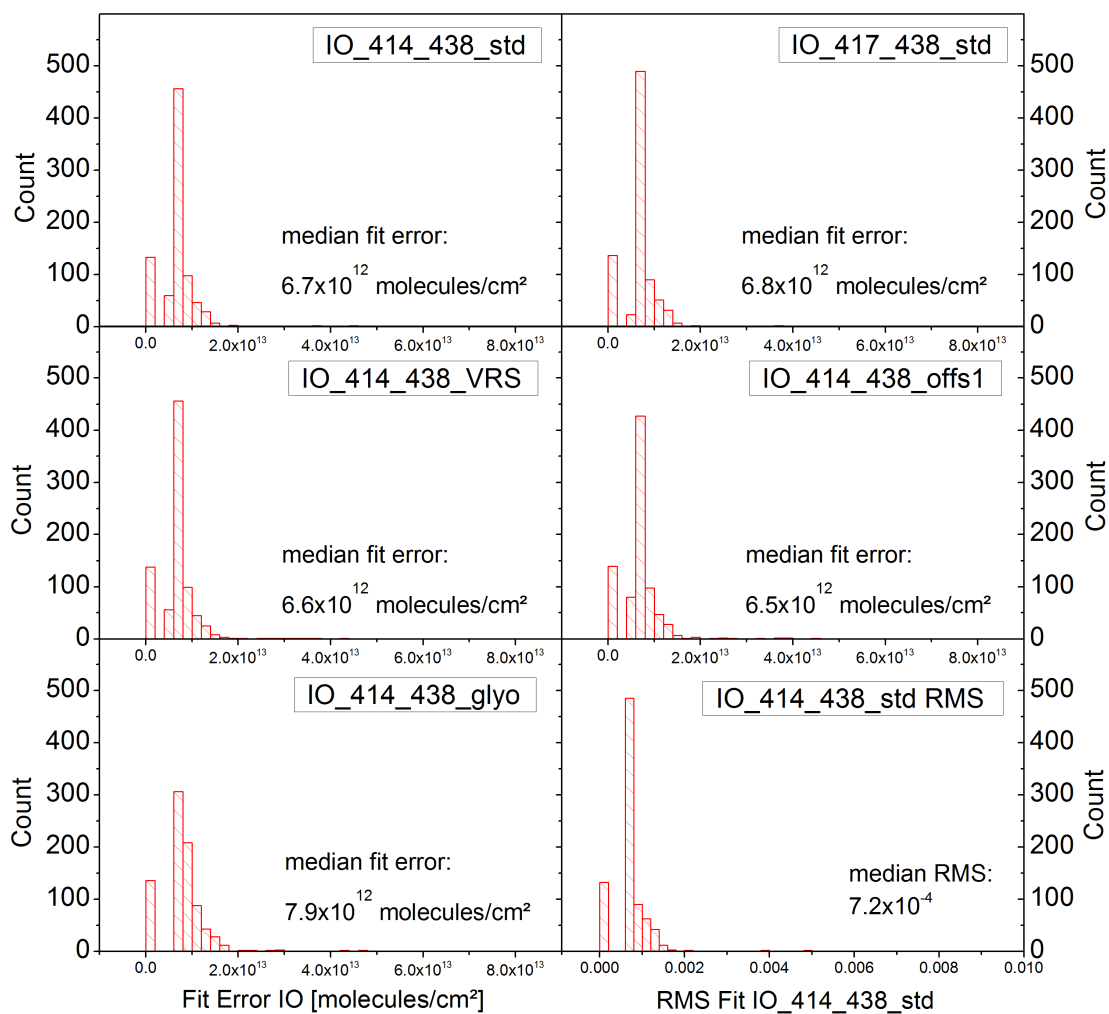


Figure A.27: Histograms of the fit errors (1-5) of different IO retrievals (see Table 8.2) and RMS from fitting scenario "IO_414_438_std" (6) at the Bourtangier Moor, Germany.

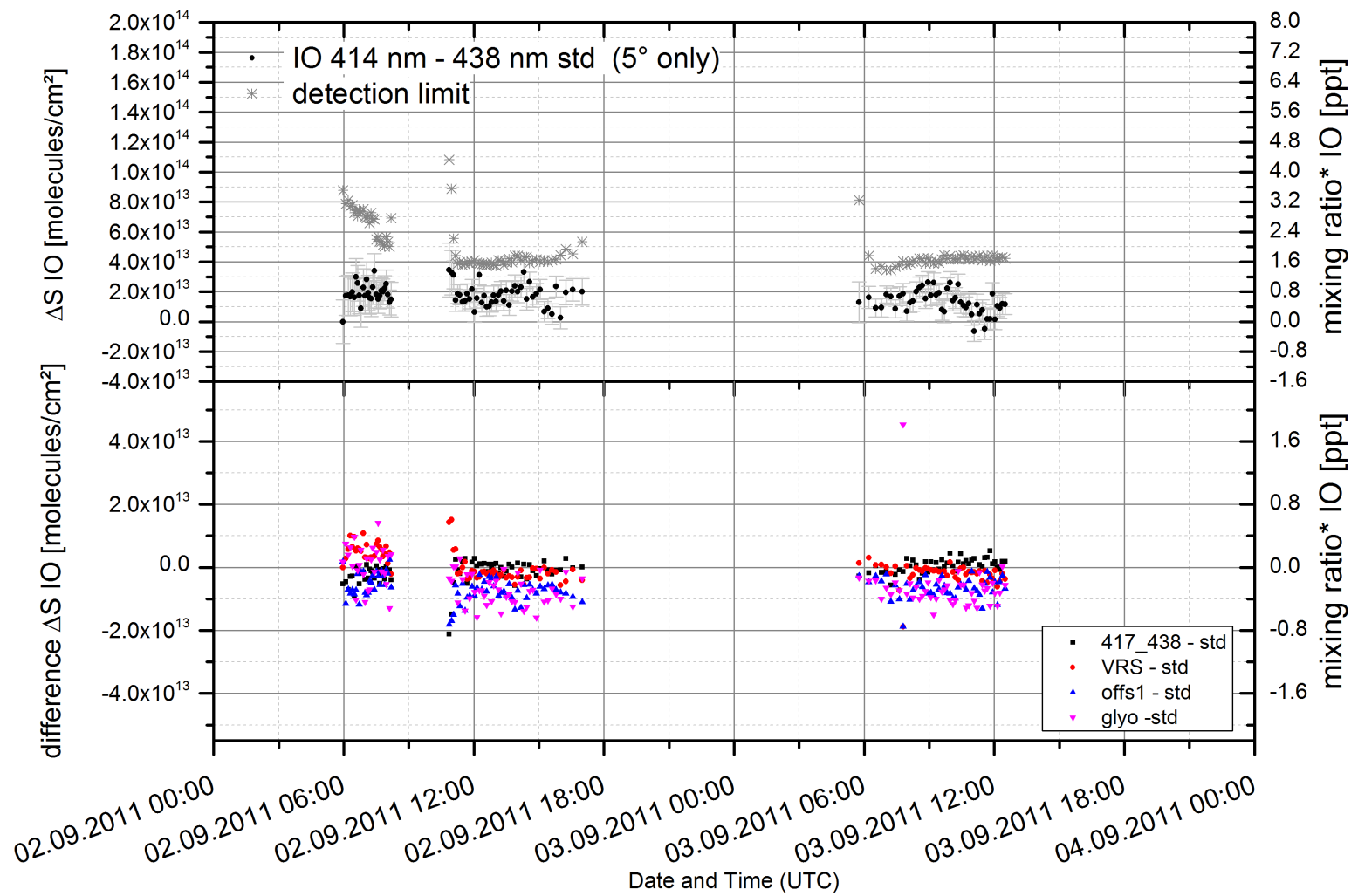


Figure A.28: IO differential slant column density $\Delta S(\alpha = 5^\circ)$ retrieved from MAX-DOAS with fit scenario "IO_414_438_std" (upper panel) and differences of $\Delta S(\alpha = 5^\circ)$ retrieved with other fit scenarios (see Table 8.2) to the standard fit scenario (lower panel) at the Bourtangier Moor, Germany.

List of Figures

1.1	Shaded areas indicate the distribution of salt lakes around the world. Salt lakes occur also outside of these areas, but less frequent. The circles indicate the locations of the salt lakes which were known to emit RHS prior to this work (green circles) and the salt lakes examined in the scope of this work (yellow circles), cf. Table 9.2. Adapted from Williams (2002).	2
2.1	Overview of the main atmospheric domains and processes involving halogens. Adapted from von Glasow (2007).	4
2.2	Sketch of important reactions of <i>Cl</i> and <i>Br</i> chemistry. Gas phase reactions, as well as aqueous phase are indicated by full arrows. Interaction with organics (grey arrows) possibly inhibits the release mechanisms by formation of soluble <i>HBr</i> and <i>HCl</i> . Dotted arrows show possible pathways for heterogeneous reactions. (Buxmann, 2012a)	10
3.1	Polar diagram of the Rayleigh phase function $\Phi_R(\vartheta)$ for unpolarized incoming light. The dotted line represents the contribution of light polarized parallel to the scattering plane and the dashed line shows the contribution of light polarized perpendicular to the scattering plane. Adapted from Hönninger (2002).	13
3.2	Mie scattering phase functions at 550 nm for water droplets with aerosol size parameters $x=1,3$ and 10. Left column: Phase function on logarithmic scale; Right column: Polar diagrams of the same phase functions on linear scale. It becomes apparent that forward scattering dominates with increasing particle size. Adapted from Sanghavi (2003). Ordinates give the scattering angle ϑ , abscissae the phase function $\Phi_{Mie}(\vartheta)$	15
4.1	Principle of DOAS: I_0 and σ are separated by an adequate filtering procedure into a narrow-band (D' and σ') and broad-band part (I'_0 and σ_b). (Platt and Stutz, 2008)	21
4.2	Sketch of a typical MAX-DOAS measurement in the single scattering case. Incoming sun light becomes scattered into the field of view of the instrument's telescope which is pointing sequentially at different elevation angles including the zenith.	22

5.1	Sketch of radiative transfer in the vicinity of a MAX-DOAS instrument. A small fraction of sunlight is transported to the instrument from a range of distances indicated by the weighting function (dashed blue line). The weighting function has a characteristic (wavelength dependent) length of several kilometers (indicated by the red line), see text for details. The instrument is most sensitive for trace gases in its close vicinity, but also trace gas clouds in a distance of several kilometers can be detected.	26
5.2	Example of an initial situation for the retrieval of a vertical profile of aerosol extinction or a trace gas, represented by the state vector \mathbf{x} . Adapted from Yilmaz (2012c).	27
5.3	Flow chart of the aerosol and trace gas profile retrieval procedure applied on MAX-DOAS measurements. (Yilmaz, 2012a)	30
6.1	Sketch of a spectrograph with Czerny-Turner configuration. Adapted from Zeiss.de	33
6.2	Sketch of the MAX-DOAS instrument used in South Russia and Mauritania.	34
6.3	Sketch of the configuration of the fiber of the MAX-DOAS instrument (cf. Figure 6.5) used for the measurements in South Russia and Mauritania.	34
6.4	Sketch of the MAX-DOAS instrument used for the measurements in South West Australia, on the Cape Verdian island Sal, at the Kali dump and at the Bourtanger Moor.	36
6.5	Sketch of the configuration of the fiber bundle of the MAX-DOAS instrument used for the measurements in South West Australia, on the Cape Verdian island Sal, at the Kali dump and at the Bourtanger Moor. Adapted from Tschritter (2012b).	37
6.6	Simplified sketch of the MAX-DOAS instrument used for the measurements at Masada, Dead Sea in 2002. (Hönninger, 2002)	38
6.7	Sketch of the MAX-DOAS instrument used at Masada, Dead Sea in 2012.	39
6.8	Sketch of the configuration of the fiber of the MAX-DOAS instrument used for the measurements at Masada, Dead Sea in 2012.	40
6.9	Offset (left panel) and Dark Current (right panel) signal of the UV spectrograph for a detector temperature of 20°C (operating temperature). Offset was recorded with 1000 scans à 3 ms exposure time. Dark Current was recorded with 1 scan and an exposure time of 60000 ms.	41
6.10	Offset (left panel) and Dark Current (right panel) signal of the Vis spectrograph for a detector temperature of 20°C (operating temperature). Offset was recorded with 1000 scans à 3 ms exposure time. Dark Current was recorded with 1 scan and an exposure time of 60000 ms.	41
6.11	Mercury emission line spectra measured by the UV spectrograph at 20°C optical bench temperature with a fitted Gaussian distribution.	42

6.12	Mercury emission line spectra measured by the Vis spectrograph at 20°C optical bench temperature with a fitted Gaussian distribution.	42
6.13	Vertical field of view for the spectrometers UV and Vis. The intensity is normalized to the maximum of the distribution.	43
6.14	Sketch of the MAX-DOAS instrument used in Ein Bokek, Dead Sea in 2012. Adapted from Grossmann (2010).	44
6.15	Sketch of the LP-DOAS measurement set up. Adapted from Tschritter (2012a).	45
6.16	Scheme of the LP-DOAS measurement sequence.	46
7.1	Position of MAX-DOAS measurements performed at Sua Pan, Botswana.	51
7.2	The sites where MAX-DOAS measurements were performed in South Russia.	53
7.3	The measurement site with positions of MAX-DOAS and LP-DOAS + retro reflector at Sebkhah N'Dramcha in Mauritania. The light path of the LP-DOAS was 4 km.	54
7.4	Salt crystals at the surface of Sebkhah N'Dramcha. Exposed crystalline surfaces were constrained on patches with diameters of several meters distributed over the whole basin shown in the picture on the lower right.	55
7.5	MAX-DOAS measurement sites on the Cape Verdian island Sal. Arrows indicate the orientation of the MAX-DOAS. (1) Punte Norte, (2) Caldera at Pedra Lume, (3) Evaporation ponds at Santa Maria.	56
7.6	MAX-DOAS measurement sites in South West Australia with geo coordinates of the instruments position. Arrows indicate the orientation of the MAX-DOAS.	58
7.7	Weather and ozone data during the DOAS measurements in South West Australia between 23 March and 2 April 2011.	59
7.8	Left: Topography of the Dead Sea and its environment. The Dead Sea Valley is encompassed by the Judean Mountains in the west and the Amman Plateau in the east. Data from SRTM and NOAA (2011). Right: Outline of the Dead Sea with the location of the measurement sites Masada and Ein Bokek. The viewing directions of the MAX-DOAS and the lightpath of the LP-DOAS are indicated by the colored lines. The dashed lines indicate the position of zonal cross sections at Masada and Ein Bokek shown in Figures 7.12,7.13, 9.23 and 9.24.	61
7.9	The diurnal thermal dynamics in valleys and the generation of LMCs. Adapted from Bendix (2004).	63
7.10	Wind roses of the years 2007 and 2008 at Masada Top (IMK) apportioned by day/night and summer/winter. Adapted from Schmitz (2009).	64
7.11	Overview of the measurement sites and instruments used during the campaign in May 2012.	66

7.12	Zonal cross section of the terrain at Masada (cf. Figure 7.8) with viewing geometry of the MAX-DOAS measurements in 2002. The colored lines indicate average δS on 29 June, 2002. In 2012 additionally the telescope elevation angles $+1^\circ$ and -1° were used. Vertical axis is multiplied by 30 compared to horizontal axis, angles are true.	67
7.13	Zonal cross section of the terrain at Ein Bokek (cf. Figure 7.8) with viewing geometry of the LP-DOAS and MAX-DOAS measurements. The telescope elevation of 80° used for reference and -5° are not shown. Vertical axis is multiplied by 30 compared to horizontal axis, angles are true.	68
7.14	Light path of the LP-DOAS Amundsen (blue), retro position and viewing direction of the MAX-DOAS Ein Bokek(orange) across the evaporation ponds at Ein Bokek.	69
7.15	Instrumental setup of the Car-DOAS during the measurements along the Dead Sea on Route 90. The orientation of the telescope was turned at the endpoints of the route so that it was facing the air over the Dead Sea.	69
7.16	Geometry of the MAX-DOAS measurements and frequency of different wind speeds in dependence of wind direction during the measurements on 2 and 3 September 2011 in the Bourtanger Moor.	70
7.17	Geometry of the MAX-DOAS and LP-DOAS measurements and main wind directions at the Kali Dump close to Heringen. Results from LP-DOAS did not yield significant signals of BrO and IO and are not presented in this work.	71
8.1	The diagram yields the correction factor $C(\tau, W)$ for a linear least-squares fit error depending on the width of absorption structures τ and the width of residual structures other than noise represented by W (Stutz and Platt, 1996).	78
8.2	Histograms of the measured absolute ΔS of BrO subtracted by their fit error weighted with correction factors C of 4, 5 and 6. A factor of $C=5$ agrees best with a confidence interval of 2σ	79
8.3	Typical averaging kernels of the aerosol extinction and BrO profile retrievals shown in Figures 9.6, 9.8 and 9.9. Colors refer to the altitudes of aerosol or BrO layers, indicated on the right.	82
8.4	Profiles of aerosol extinction and BrO volume mixing ratio both retrieved with exponential shape a priori profiles with characteristic heights of 2 km. Total retrieval errors are black, noise error blue and smoothing error orange (cf. section 5.2.4). Examples are from 26 July 2002 9:53 UTC, 12 May 2012 8:45 UTC, 12 May 13:08 UTC, respectively.	82
8.5	Profiles of aerosol extinction (left side) and BrO volume mixing ratio (right side) retrieved with different types of a priori profiles (rows) with characteristic heights of 1 km, 2 km and 3 km (columns), see text.	84

8.6	Typical profiles of the volume mixing ratio of <i>BrO</i> found at Masada and Ein Bokek convolved with the averaging kernel of the contrary instrument.	85
9.1	Back trajectories ending in the mid of the Dead Sea Valley in the evening on 26 June and 28 June 2002. Height levels above ground of 200 m, 600 m and 1000 m are indicated in different colors.	88
9.2	Differential slant column densities ΔS of <i>BrO</i> for a series of telescope elevation angles (color coded) between 25 June 2002, 9:03 UTC and 1 July, 12:45 UTC at Masada Top. Data provided by Zingler (2002). (*mixing ratios on the right y-axis are a rough estimate for a homogeneous distribution of the absorber along a characteristical light path of 10 km.)	89
9.3	Example of aerosol extinction vertical profiles retrieved from MAX-DOAS ΔS of O_4 in the course of the day on 28 June 2002. Times are given in UTC. The profiles were retrieved with a exponential a priori vertical profile (dashed line). Grid resolution is 50 m. Altitudes refer to ground (agl). (cf. Figure 9.6)	90
9.4	Left panel: The vertical profile of particle concentrations as measured by the CN counter during a flight above the Dead Sea valley on 29 April 1999, (starting at 09:45 and ending at 10:15LT); central panel: The vertical profile of temperature measured during a flight above the Dead Sea on 29 April 1999 (starting at 09:45 and ending at 10:15LT); right panel: Vertical profiles of average particle concentrations, measured on 31 July 1998. The dashed and solid curves represent the particle concentrations at 11:00LT and at 13:00LT, respectively. Altitudes refer to sea level (asl) with 0 m asl = 423 m agl. (Levin et al., 2005)	90
9.5	<i>BrO</i> versus simultaneous NO_2 mixing ratios retrieved from MAX-DOAS during the measurement period in 2002. The colorbar indicates the ratio between signal and retrieval error. <i>BrO</i> is observed only when NO_2 is below a threshold of 2-3 ppbv.	91
9.6	Diurnal profiles between 8:00 and 20:00 LT of aerosol extinction and mixing ratios of <i>BrO</i> and NO_2 retrieved from MAX-DOAS slant column densities, measured between 25 June and 30 June 2002 at Masada Top. The dashed line indicates the altitude of the instrument at Masada above the water level of the Dead Sea.	92
9.7	Aerosol extinction vertical profiles on 5 May 2012 and 7 May 2012. Times are given in UTC. The profiles were retrieved with a exponential a priori vertical profile (dashed line). Grid resolution is 50 m. (cf. Figure 9.8)	93

9.8	Diurnal profiles between 8:00 and 20:00 LT of aerosol extinction and mixing ratios of BrO and NO_2 retrieved from MAX-DOAS slant column densities, measured between 4 May and 15 May 2012 at Masada Top. The dashed line indicates the altitude of the instrument at Masada above the water level of the Dead Sea. Date on the x-axis refers to local time.	95
9.9	Diurnal profiles between 8:00 and 20:00 LT of aerosol extinction and mixing ratios of BrO and NO_2 retrieved from MAX-DOAS slant column densities, measured between 3 May and 15 May 2012 at Ein Bokek. The dashed line indicates the altitude of the instrument at Masada above the water level of the Dead Sea. Date on the x-axis refers to local time.	96
9.10	Mixing ratios of BrO and NO_2 measured with MAX-DOAS and LP-DOAS (Schmitt, 2012) between 2 May and 15 May 2012 at Ein Bokek and Masada. Wind data was kindly provided by IMK (Corsmeier and Kottmeier). Ozone was measured with LP-DOAS at Ein Bokek and with a mobile ozone monitor at Masada.	97
9.11	Mixing ratio of NO_2 measured with MAX-DOAS and LP-DOAS (Schmitt, 2012) on 3 May and 8 May 2012 at Ein Bokek and Masada.	98
9.12	Mixing ratios of BrO and NO_2 measured with MAX-DOAS and LP-DOAS (Schmitt, 2012) on 3 May and 8 May 2012 at Ein Bokek and Masada.	98
9.13	Diurnal profiles of aerosol extinction on 12 May, 2012 at Ein Bokek and Masada. The dashed line indicates the altitude of the instrument at Masada above the water level of the Dead Sea.	99
9.14	Diurnal profiles of the mixing ratios of BrO and NO_2 on 12 May, 2012 at Ein Bokek and Masada. The dashed line indicates the altitude of the instrument at Masada above the water level of the Dead Sea.	99
9.15	Horizontal and vertical wind speed and wind direction measured at weather station P88 (cf. Figure 7.11) on 12 May 2012 (Local Time).	101
9.16	Diurnal profiles of aerosol extinction on 13 May, 2012 at Ein Bokek and Masada. The dashed line indicates the altitude of the instrument at Masada above the water level of the Dead Sea.	101
9.17	Diurnal profiles of the mixing ratios of BrO and NO_2 on 13 May, 2012 and retrieval error of BrO at Ein Bokek and Masada. The dashed line indicates the altitude of the instrument at Masada above the water level of the Dead Sea.	102
9.18	Diurnal profiles of aerosol extinction at Ein Bokek and Masada on 14 May 2012. Below on the left the course of the total solar radiation (Corsmeier and Kottmeier) is shown. On the right hand side automatically recorded pictures at the measurement site Masada show the lighting conditions recognizable by the shadow of the walls. The vertical lines on the left hand side indicate the recording times of the photos.	104

- 9.19 Diurnal profiles of the mixing ratios of BrO and NO_2 on 14 May, 2012 and retrieval error of BrO at Ein Bokek and Masada. The dashed line indicates the altitude of the instrument at Masada above the water level of the Dead Sea. 105
- 9.20 View from Ein Bokek measurement site towards the retro reflector on three consecutive days (12, 13 and 14 May 2012). Left picture: On 12 May, like eleven days before, a whitish haze was present throughout the day. On some days only the ridge of the opposite Jordan mountains is recognizable. Central picture: Strong westerly winds bring dust into the valley resulting in reddish haze. The Jordan mountains are not visible until the evening. Right picture: Variable cloudy conditions alternate with short periods of sunshine. Structures of the opposite Jordan mountains can be seen clearly. 106
- 9.21 Differential slant column densities dS of BrO measured along *Route 90* (north to south) during the indicated times with cruise periods and main wind directions. Unit intervals correspond to 1×10^{14} molecules/cm². The telescope was orientated towards the Dead Sea with an elevation angle of 20° relative to the car. Highest relative levels were found from 10 May to 12 May in the south of Masada (cf. Figure 9.22). The dashed and dotted lines indicate the northern and southern map areas displayed in Figure 9.22, respectively. 108
- 9.22 Differential slant column densities dS of BrO in the course of *Route 90* on 11 May 2012. Numbers in brackets mark special events described in the text in chronological order. 109
- 9.23 A possible pattern of mountain induced thermal circulations in the Dead Sea Valley on days with elevated layers found with MAX-DOAS: Lower circulations compensate local slope winds, while upper circulations compensate the whole air mass transfer out of the valley by mesoscale valley winds. Thermal updraft winds can form convective inversion layers and opposed streams prevent vertical transport. . . . 113
- 9.24 Possible dynamics in the Dead Sea Valley under the influence of strong westerly winds, which dissolve circulations and/or inversion layers or prevent their formation. 113
- 9.25 Diurnal behavior of BrO , NO_2 and O_3 on 11 May 2012 measured with LP-DOAS at Ein Bokek. 117
- 9.26 BrO differential slant column density $\Delta S(\alpha = 5^\circ)$ retrieved from MAX-DOAS with fit scenario "BrO_331_357_std" (upper panel) and differences of $\Delta S(\alpha = 5^\circ)$ retrieved with other fit scenarios (see Table 8.2) to the standard fit scenario (lower panel) on Sal, Cape Verde. Significant levels are found on 8 and 9 June 2010. 119
- 9.27 Example of a DOAS fit using scenario "BrO_331_357_std" on Sal, Cape Verde, on 8 June 2010 16:40 (UTC) (=15:40 LT). The slant column density of BrO exceeds the detection limit (cf. Figure 9.26). . 121

9.28	Example of a DOAS fit using scenario "BrO_331_357_std" on Sal, Cape Verde, on 8 June 2010 16:40 (UTC) (=15:40 LT) using two normalized Ring spectra generated from the proximate FRS. The slant column density of <i>BrO</i> exceeds the detection limit.	122
A.1	Histograms of the fit errors of the <i>BrO</i> retrieval and RMS from fitting scenario "BrO_331_357_std" (see Table 8.2) at Masada, Dead Sea in 2012.	134
A.2	Histograms of the fit errors of the <i>BrO</i> retrieval and RMS from fitting scenario "BrO_331_357_std" (see Table 8.2) at Ein Bokek, Dead Sea in 2012.	134
A.3	Meteorological parameters from IMK weather station (Corsmeier and Kottmeier) at Masada Top (see 7.11) during the DOAS measurements 2012.	135
A.4	Meteorological parameters from IMK weather station (Corsmeier and Kottmeier) at the Dead Sea Works pumping station P88 (see 7.11) during the DOAS measurements 2012.	136
A.5	Histograms of the fit errors (1-4) of different <i>BrO</i> retrievals (see Table 8.2) and RMS from fitting scenario "BrO_331_357_std" (5) at Sua Pan.	137
A.6	<i>BrO</i> differential slant column density $\Delta S(\alpha = 5^\circ)$ retrieved from MAX-DOAS with fit scenario "BrO_331_357_std" (upper panel) and differences of $\Delta S(\alpha = 5^\circ)$ retrieved with other fit scenarios (see Table 8.2) to the standard fit scenario (lower panel) at Sua Pan.	138
A.7	Histograms of the fit errors (1-5) of different <i>IO</i> retrievals (see Table 8.2) and RMS from fitting scenario "IO_414_438_std" (6) at Sua Pan.	139
A.8	<i>IO</i> differential slant column density $\Delta S(\alpha = 5^\circ)$ retrieved from MAX-DOAS with fit scenario "IO_414_438_std" (upper panel) and differences of $\Delta S(\alpha = 5^\circ)$ retrieved with other fit scenarios (see Table 8.2) to the standard fit scenario (lower panel) at Sua Pan.	140
A.9	Histograms of the fit errors (1-4) of different <i>BrO</i> retrievals (see Table 8.2) and RMS from fitting scenario "BrO_331_357_std" (5) at locations in South Russia.	141
A.10	<i>BrO</i> differential slant column density $\Delta S(\alpha = 5^\circ)$ retrieved from MAX-DOAS with fit scenario "BrO_331_357_std" (upper panel) and differences of $\Delta S(\alpha = 5^\circ)$ retrieved with other fit scenarios (see Table 8.2) to the standard fit scenario (lower panel) at locations in South Russia.	142
A.11	Histograms of the fit errors (1-5) of different <i>IO</i> retrievals (see Table 8.2) and RMS from fitting scenario "IO_414_438_std" (6) at locations in South Russia.	143
A.12	<i>IO</i> differential slant column density $\Delta S(\alpha = 5^\circ)$ retrieved from MAX-DOAS with fit scenario "IO_414_438_std" (upper panel) and differences of $\Delta S(\alpha = 5^\circ)$ retrieved with other fit scenarios (see Table 8.2) to the standard fit scenario (lower panel) at locations in South Russia.	144

A.13	Histograms of the fit errors (1-4) of different <i>BrO</i> retrievals (see Table 8.2) and RMS from fitting scenario "BrO_331_357_std" (5) on Sal, Cape Verde.	145
A.14	<i>BrO</i> differential slant column density $\Delta S(\alpha = 5^\circ)$ retrieved from MAX-DOAS with fit scenario "BrO_331_357_std" (upper panel) and differences of $\Delta S(\alpha = 5^\circ)$ retrieved with other fit scenarios (see Table 8.2) to the standard fit scenario (lower panel) on Sal, Cape Verde.	146
A.15	Histograms of the fit errors (1-5) of different <i>IO</i> retrievals (see Table 8.2) and RMS from fitting scenario "IO_414_438_std" (6) on Sal, Cape Verde.	147
A.16	<i>IO</i> differential slant column density $\Delta S(\alpha = 5^\circ)$ retrieved from MAX-DOAS with fit scenario "IO_414_438_std" (upper panel) and differences of $\Delta S(\alpha = 5^\circ)$ retrieved with other fit scenarios (see Table 8.2) to the standard fit scenario (lower panel) on Sal, Cape Verde.	148
A.17	Histograms of the fit errors (1-4) of different <i>BrO</i> retrievals (see Table 8.2) and RMS from fitting scenario "BrO_331_357_std" (5) at locations in South West Australia.	149
A.18	<i>BrO</i> differential slant column density $\Delta S(\alpha = 5^\circ)$ retrieved from MAX-DOAS with fit scenario "BrO_331_357_std" (upper panel) and differences of $\Delta S(\alpha = 5^\circ)$ retrieved with other fit scenarios (see Table 8.2) to the standard fit scenario (lower panel) at locations in South West Australia.	150
A.19	Histograms of the fit errors (1-5) of different <i>IO</i> retrievals (see Table 8.2) and RMS from fitting scenario "IO_414_438_std" (6) at locations in South West Australia.	151
A.20	<i>IO</i> differential slant column density $\Delta S(\alpha = 5^\circ)$ retrieved from MAX-DOAS with fit scenario "IO_414_438_std" (upper panel) and differences of $\Delta S(\alpha = 5^\circ)$ retrieved with other fit scenarios (see Table 8.2) to the standard fit scenario (lower panel) at locations in South West Australia.	152
A.21	Histograms of the fit errors (1-4) of different <i>BrO</i> retrievals (see Table 8.2) and RMS from fitting scenario "BrO_331_357_std" (5) at the Kali dump in Heringen, Germany.	153
A.22	<i>BrO</i> differential slant column density $\Delta S(\alpha = 5^\circ)$ retrieved from MAX-DOAS with fit scenario "BrO_331_357_std" (upper panel) and differences of $\Delta S(\alpha = 5^\circ)$ retrieved with other fit scenarios (see Table 8.2) to the standard fit scenario (lower panel) at the Kali dump in Heringen, Germany.	154
A.23	Histograms of the fit errors (1-5) of different <i>IO</i> retrievals (see Table 8.2) and RMS from fitting scenario "IO_414_438_std" (6) at the Kali dump in Heringen, Germany.	155
A.24	<i>IO</i> differential slant column density $\Delta S(\alpha = 5^\circ)$ retrieved from MAX-DOAS with fit scenario "IO_414_438_std" (upper panel) and differences of $\Delta S(\alpha = 5^\circ)$ retrieved with other fit scenarios (see Table 8.2) to the standard fit scenario (lower panel) at the Kali dump in Heringen, Germany.	156

A.25	Histograms of the fit errors (1-4) of different <i>BrO</i> retrievals (see Table 8.2) and RMS from fitting scenario "BrO_331_357_std" (5) at the Bourtanger Moor, Germany.	157
A.26	<i>BrO</i> differential slant column density $\Delta S(\alpha = 5^\circ)$ retrieved from MAX-DOAS with fit scenario "BrO_331_357_std" (upper panel) and differences of $\Delta S(\alpha = 5^\circ)$ retrieved with other fit scenarios (see Table 8.2) to the standard fit scenario (lower panel) at the Bourtanger Moor, Germany.	158
A.27	Histograms of the fit errors (1-5) of different <i>IO</i> retrievals (see Table 8.2) and RMS from fitting scenario "IO_414_438_std" (6) at the Bourtanger Moor, Germany.	159
A.28	<i>IO</i> differential slant column density $\Delta S(\alpha = 5^\circ)$ retrieved from MAX-DOAS with fit scenario "IO_414_438_std" (upper panel) and differences of $\Delta S(\alpha = 5^\circ)$ retrieved with other fit scenarios (see Table 8.2) to the standard fit scenario (lower panel) at the Bourtanger Moor, Germany.	160

List of Tables

6.1	FWHM of the mercury emission lines measured by the UV and Vis spectrograph, see Figures 6.11 and 6.12.	43
7.1	Overview of the MAX-DOAS measurement sites in South Russia in Figure 7.2 with pH measured in soil samples by Huber et al. (2012). .	52
7.2	Overview of the MAX-DOAS measurement sites on Sal, Cape Verde.	56
7.3	Overview of the MAX-DOAS measurement sites in South West Australia shown in Figure 7.6.	57
8.1	Cross sections of trace gas absorption and inelastic scattering used in this work.	74
8.2	Applied fit scenarios used for the spectral retrieval of O_4 , NO_2 , BrO and IO from MAX-DOAS spectra.	76
8.3	Telescope elevation angles α and diurnal average of degrees of freedom d_s of signal (see section 5.2.2) with 1σ at the different measurement sites at the Dead Sea for aerosol, BrO and NO_2 retrievals (see text).	81
8.4	χ^2 of the retrievals shown in Figure 8.5.	83
9.1	Measurement periods during the campaign in Mauritania in 2009 (times are UTC) with average detection limits. For the detection limit of MAX-DOAS a light path with a length of 10 km through the absorbing layer is assumed.	123
9.2	Results from field campaigns performed in the scope of HaloProc at salt lakes (yellow) and other areas with high salt content (orange) in the context of previous RHS measurements at salt lakes (green). . .	124
9.3	Comparison of different properties and trace gas abundances found at salt lakes where RHS were measured potentially affecting the presence of BrO and IO	127

Bibliography

- AAFC, C. S. I. S.: Agriculture and Agri-Food Canada, URL <http://sis.agr.gc.ca/cansis/glossary/s/index.html>, 2011.
- AERONET: Aerosol Robotic Network, 2012.
- Aguzzi, A. and Rossi, M. J.: The kinetics of the heterogeneous reaction of BrONO with solid alkali halides at ambient temperature . A comparison with the interaction of ClONO on NaCl and KBr, *Phys. Chem. Chem. Phys.*, 1999.
- Akima, H.: A new method of interpolation and smooth curve fitting based on local procedures, *Journal of Assc. for Comp. Mach.*, 17, 589–602, 1970.
- Al-weshah, R. A.: The water balance of the Dead Sea : an integrated approach, *Hydrological Processes*, 154, 145–154, 2000.
- Alpert, P., Shafir, H., and Issahary, D.: Recent changes in the climate at the dead sea - a preliminary study, *Climatic Change*, 37, 513–537, 1997.
- Angström, A.: On the atmospheric transmission of sun radiation and on Dust in the Air, *Geografiska Annaler*, 11, 156–166, URL <http://www.jstor.org/stable/519399>, 1929.
- Ariya, P. a.: Atmospheric science: Mid-latitude mercury loss, *Nature Geoscience*, 4, 14–15, doi:10.1038/ngeo1048, URL <http://www.nature.com/doifinder/10.1038/ngeo1048>, 2011.
- Ashworth, S., Allan, B., and Plane, J.: High resolution spectroscopy of the OIO radical: Implications for the ozone-depleting potential of iodine, *Geophys. Res. Lett.*, 29, 2002.
- Atkinson, R., Baulch, D. L., Cox, R. A., Crowley, J. N., Hampson, R. F., Kerr, J. A., Rossi, M. J., and Troe, J.: Summary of Evaluated Kinetic and Photochemical Data for Atmospheric Chemistry, URL <http://www.iupac-kinetic.ch.cam.ac.uk/>, 2002.
- Atkinson, R., Baulch, D., Cox, R., Crowley, J., Hampson, R., Hynes, R., Jenkin, M., Rossi, M., and Troe, J.: Evaluated kinetic and photochemical data for atmospheric chemistry: Volume III - gas phase reactions of inorganic halogens, *Atmos. Chem. Phys.*, 7, 981–1191, 2007.

- Backus, G. and Gilbert, J.: Uniqueness in the inversion of inaccurate gross Earth data, *Trans. R. Soc.*, 266, 123–192, 1970.
- Barrie, L. and Platt, U.: Arctic tropospheric chemistry: an overview., *Tellus B*, 49, 449–454, 1997.
- Bendix, J.: *Geländeklimatologie*, Gebrüder Borntraeger Verlagsbuchhandlung Berlin Stuttgart, 2004.
- Bentor, Y. K.: Some geochemical aspects of the Dead Sea and the question of its age, *Geochimica et Cosmochimica Acta*, 25, 239–240, URL [http://dx.doi.org/10.1016/0016-7037\(61\)90061-8](http://dx.doi.org/10.1016/0016-7037(61)90061-8), 1961.
- Bitan, A.: The Influence of the Special Shape of the Dead-Sea and Its Environment on the Local Wind System, *Arch. Met. Geoph. Biokl., Ser. B*, 24, 283–301, 1977.
- Bobrowski, N.: Detection of bromine monoxide in a volcanic plume, *Nature*, 423, 273–276, doi:doi:10.1038/nature01625, 2003.
- Bobrowski, N.: *Volcanic Gas Studies by MAX-DOAS*, Dissertation, University of Heidelberg, 2005.
- Bogumil, K., Orphal, J., Homann, T., Voigt, S., Spietz, P., Fleischmann, O. C., Vogel, A., Hartmann, M., Kromminga, H. Bovensmann, H., Frerick, J., and Burrows, J. P.: Measurements of molecular absorption spectra with the SCIAMACHY pre-flight model: instrument characterization and reference data for atmospheric remote-sensing in the 230–2380 nm region, *Journal of Photochemistry and Photobiology A: Chemistry*, 157, 167–184, doi:doi:10.1016/S1010-6030(03)00062-5, 2003.
- Bowen, B. and Benison, K.: Geochemical characteristics of naturally acid and alkaline saline lakes in southern Western Australia, *Applied Geochemistry*, 24, 268–284, doi:10.1016/j.apgeochem.2008.11.013, URL <http://linkinghub.elsevier.com/retrieve/pii/S0883292708004034>, 2009.
- Brühl, C. and Crutzen, P.: MPIC two-dimensional model. In *The atmospheric effects of stratospheric aircraft*, NASA Ref. Publ., pp. 103–104, 1993.
- BUND Region Hannover: Kalihalden, URL http://region-hannover.bund.net/themen_und_projekte/bergbaufolgen/kalihalden/.
- Bussemer, M.: *Der Ring-Effekt: Ursachen und Einfluß auf die spektroskopische Messung stratosphärischer Spurenstoffe*, Diploma thesis, University of Heidelberg, 1993.
- Buxmann, J.: pers. comm. and performing measurements at Sua Pan, Botswana and Walfish Bay, Namibia, 2008.
- Buxmann, J.: 'Bromine and Chlorine Explosion' in a Simulated Atmosphere, Dissertation, Heidelberg, 2012a.

- Buxmann, J.: pers. comm., 2012b.
- Buxmann, J. and Holla, R.: Final Report SP Platt- HaloProc I Investigation of reactive halogen species in a smog chamber and in the field, Tech. rep., Institute of Environmental Physics, Heidelberg, 2011.
- Chance, K. and Spurr, R.: Ring effect studies: Rayleigh scattering, including molecular parameters for rotational Raman scattering, and the Fraunhofer spectrum, *Applied Optics*, 36, 5224–5230, doi:10.1364/AO.36.005224, 1997.
- Clémer, K., Van Roozendaal, M., Fayt, C., Hendrick, F., Hermans, C., Pinardi, G., Spurr, R., Wang, P., and De Mazière, M.: Multiple wavelength retrieval of tropospheric aerosol optical properties from MAXDOAS measurements in Beijing, *Atmospheric Measurement Techniques Discussions*, 3, 111–145, doi:10.5194/amtd-3-111-2010, URL <http://www.atmos-meas-tech-discuss.net/3/111/2010/>, 2010.
- Corsmeier, U. and Kottmeier, C.: Weather Stations IMK, URL <http://www.imk-tro.kit.edu/english/19.php><http://www.imk-tro.kit.edu>.
- Czerny, M. and Turner, A.: Czerny-Turner, *Z. Physik*, 61, 792, 1930.
- DAYAN, U., SHENHAV, R., and GRABER, M.: The spatial and temporal behavior of the mixed layer in Israel, *Journal of applied meteorology* (1988), 27, 1382–1394, URL <http://cat.inist.fr/?aModele=afficheN&cpsidt=7245372>, 1988.
- Deckker, P. D.: Australian salt lakes: their history, chemistry, and biota - a review, URL http://people.rses.anu.edu.au/dedeckker_p/pubs/120.pdf, 1983.
- Deters, B., Burrows, J., and Orphal, J.: UV-visible absorption cross sections of bromine nitrate determined by photolysis of BrONO₂/Br₂ mixtures, *Journal of Geophysical Research*, 103, 3563–3570, URL <http://scholar.google.com/scholar?hl=en&btnG=Search&q=intitle:determined+by+photolysis+of+BrONO2+/-+Br2+mixtures#1>, 1998.
- Deutschmann, T.: Atmospheric Radiative Transfer Modelling with Monte Carlo Methods, Diploma thesis, University of Heidelberg, 2009.
- Deutschmann, T., Beierle, S., Frieß, U., Grzegorski, M., Kern, C., Kritten, L., Platt, U., Prados-Roman, C., Pukite, J., Wagner, T., Werner, B., and Pfeilsticker, K.: The Monte Carlo atmospheric radiative transfer model McArtim: Introduction and validation of Jacobians and 3D features, *Journal of Quantitative Spectroscopy and Radiative Transfer*, 112, 1119–1137, doi:<http://dx.doi.org/10.1016/j.jqsrt.2010.12.009>, 2011.
- Dinter, T.: pers. comm., 2011.
- DiSalvo, F. J.: Thermoelectric Cooling and Power Generation, *Science*, 285, 703–706, doi:10.1126/science.285.5428.703, URL <http://www.sciencemag.org/cgi/doi/10.1126/science.285.5428.703>, 1999.

- Draxler, R. and Rolph, G.: HYSPLIT(HYbrid Single Particle Lagrangian Integrated Trajectory), 2003.
- EMC: Data Assimilation Team: GDAS (Global Data Assimilation System), URL <http://www.emc.ncep.noaa.gov/gmb/gdas/>.
- FAO: Food and Agricultural Organization of the United Nations, URL <http://www.fao.org/nr/aboutnr/nrl/en/>, 2012.
- Fayt, C. and Van Roozendaal, M.: WINDOAS, URL <http://bro.aeronomie.be/WINDOAS-SUM-210b.pdf>, 2001.
- Fickert, S., Adams, J. W., and Crowley, J. N.: Activation of Br₂ and BrCl via uptake of HOBr onto aqueous salt solutions, *Journal of Geophysical Research*, URL <http://www.agu.org/pubs/crossref/1999/1999JD900359.shtml>, 1999.
- Finlayson-Pitts: Chemistry of the Upper and Lower Atmosphere, ACADEMIC PRESS, Irvine, 2000.
- Finlayson-Pitts, Ezell, M., and Pitts Jr, J.: Formation of chemically active chlorine compounds by reactions of atmospheric NaCl particles with gaseous N₂O₅ and ClONO₂, *Nature*, 337, 241–244, 1989.
- Finlayson-Pitts, B. and Johnson, S.: The reaction of NO₂ with NaBr: Possible source of BrNO in polluted marine atmospheres, *Atmospheric Environment* (1967), 22, 1107–1112, doi:10.1016/0004-6981(88)90340-X, URL <http://linkinghub.elsevier.com/retrieve/pii/000469818890340X>, 1988.
- Finlayson-Pitts, B. J.: The tropospheric chemistry of sea salt: a molecular-level view of the chemistry of NaCl and NaBr., *Chemical reviews*, 103, 4801–22, doi:10.1021/cr020653t, URL <http://www.ncbi.nlm.nih.gov/pubmed/14664634>, 2003.
- Fleischmann, O., Hartmann, M., Burrows, J., and J., O.: New ultraviolet absorption cross-sections of BrO at atmospheric temperatures measured by a time-windowing Fourier transform spectroscopy, *Journal of Photochemistry and Photobiology A: Chemistry*, 168, 117–132, 2004.
- Friess, U.: Spectroscopic Measurements of Atmospheric Trace Gases at Neumayer-Station, Antarctica, Dissertation, University of Heidelberg, 2001.
- Friess, U.: MS-DOAS, 2008.
- Friess, U., Hollwedel, J., König-Langlo, G., Wagner, T., and Platt, U.: Dynamics and chemistry of tropospheric bromine explosion events in the Antarctic coastal region, *J. Geophys. Res.*, 109, 2004.
- Friess, U., Monks, P. S., Remedios, J. J., Rozanov, A., Sinreich, R., Wagner, T., and Platt, U.: MAX-DOAS O₄ measurements: A new technique to derive information on atmospheric aerosols: 2. Modeling studies, *Journal of Geophysical Research*, 111, D14 203, doi:10.1029/2005JD006618, URL <http://www.agu.org/pubs/crossref/2006/2005JD006618.shtml>, 2006.

- Friess, U., Sihler, H., Sander, R., Pöhler, D., Yilmaz, S., and Platt, U.: The vertical distribution of BrO and aerosols in the Arctic: Measurements by active and passive differential optical absorption spectroscopy, *Journal of Geophysical Research*, 116, D00R04, 2011.
- Gomer, T., Brauers, F., Heintz, F., Stutz, J., and Platt, U.: MFC User Manual Vers. 1.98, Institute of Environmental Physics, University of Heidelberg, URL <http://www2.fz-juelich.de/icg/icg-2/allgemeines/mfc>, 1993.
- Grabau, A. W.: *Geology of the NON-METALLIC MINERAL DEPOSITS OTHER THAN SILICATES*, vol. I, McGraw-Hill Book Co. Inc., New York, URL <http://www.ebooksread.com/authors-eng/amadeus-w-amadeus-william-1870-1946-grabau/geology-of-the-non-metallic-mineral-deposits-other-than-silicates--hci.shtml>, 1920.
- Grainger, J. and Ring, J.: Anomalous Fraunhofer Line Profiles, *Nature*, 193, 762–762, URL <http://dx.doi.org/10.1038/193762a0>, 1962.
- Greenblatt, G., Orlando, J., Burkholder, J., and Ravishankara, A.: Absorption Measurements of Oxygen Between 330 and 1140 nm, *Journal of Geophysical Research*, 95, 18 577–18 582, 1990.
- Gribble, G. W.: Natural Organohalogenes October 2004, 2004.
- Grossmann, K.: Reactive Halogen Species in the Western Pacific, Diploma thesis, University of Heidelberg, 2010.
- Grossmann, K., Friess, U., Peters, E., Wittrock, F., and Tschritter, J.: Iodine monoxide in the Western Pacific marine boundary layer (in rev.), *Atmos. Chem. Phys.*, 2012.
- Hanson, D. R., Ravishankara, A. R., and Lovejoy, E. R.: Reaction of BrONO₂ with H₂O on submicron sulfuric acid aerosol and the implications for the lower stratosphere, *Journal of Geophysical Research*, 101, 9063–9069, 1996.
- Haug, H.: Raman-Streuung von Sonnenlicht in der Erdatmosphäre, Diploma thesis, University of Heidelberg, 1996.
- Hausmann, M. and Platt, U.: Spectroscopic measurement of bromine oxide and ozone in the high Arctic during Polar Sunrise Experiments, *J. Geophys. Res.*, 99, 25 399–25 413, 1992.
- Hebestreit, K.: DOAS Measurements of Tropospheric Bromine Oxide in Mid-Latitudes, *Science*, 283, 55–57, doi:10.1126/science.283.5398.55, URL <http://www.sciencemag.org/cgi/doi/10.1126/science.283.5398.55>, 1999.
- Hecht, A. and Gertman, I.: Dead Sea Meteorological Climate, in: Biodiversity of Cyanoprocaryotes, Algae and Fungi of Israel. Fungal Life in the Dead Sea,

- edited by Nevo, E., Oren, A., and Wasser, S., International Center for Cryptogamic Plants and Fungi, Institute of Evolution, University of Haifa, Haifa, URL http://isramar.ocean.org.il/isramar2009/DeadSea/Hecht&Gertman_2003_DS_Climate_Chapter4.pdf, 2003.
- Heney, L. and Greenstein, J.: Diffuse radiation in the Galaxy, *Astrophys. J.*, 93, 70–83, 1941.
- Hermans, C., Vandaele, A. C., Fally, S., Carleer, M., Colin, R., Coquart, B., Jenouvrier, A., and Mérienne, M. F.: Absorption cross-section of the collision-induced bands of oxygen from the UV to the NIR, *Weakly Interacting Molecular Pairs: Unconventional Absorbers of Radiation in the Atmosphere*, 27, 193–200, 2003.
- Heue, K.-P.: Development of the Zeppelin MAX-DOAS, 2008.
- Hoch, D.: Resonator Verstärkte Differentielle Optische Absorptions Spektroskopie: Labormessungen von BrO, HCHO, HONO und O₃, Diploma thesis, University of Heidelberg, 2010.
- Hoffmann, T., O’Dowd, C. D., and Seinfeld, J. H.: Iodine oxide homogeneous nucleation: An explanation for coastal new particle production, *Geophysical Research Letters*, 28, 1949, doi:10.1029/2000GL012399, URL <http://www.agu.org/pubs/crossref/2001/2000GL012399.shtml>, 2001.
- Hönninger, G.: Halogen Oxide Studies in the Boundary Layer by Multi Axis Differential Optical Absorption Spectroscopy and Active Longpath-DOAS, Dissertation, University of Heidelberg, 2002.
- Hönninger, G. and Filsinger, F.: Jscript zur automatischen Auswertung mit WinDOAS bei wechselnder Referenz, URL <http://wiki.iup.uni-heidelberg.de/Doas/AutomatischeAuswertung>.
- Hönninger, G., Bobrowski, N., Palenque, E. R., Torrez, R., and Platt, U.: Reactive bromine and sulfur emissions at Salar de Uyuni, Bolivia, *Geophys. Res. Lett.*, 31, L04101, doi:10.1029/2003GL018818, URL <http://dx.doi.org/10.1029/2003GL018818>, 2004.
- Horbanski, M.: A Compact Resonator Based Instrument for DOAS Measurements of Ambient Nitrogen Dioxide, Diploma thesis, University of Heidelberg, 2010.
- Huber, S., Tubbesing, C., Krause, T., Rheinberger, S., and Kotte, K.: pers. comm., 2012.
- Huber, S. G., Kotte, K., Schöler, H. F., and Williams, J.: Natural abiotic formation of trihalomethanes in soil: results from laboratory studies and field samples., *Environmental science & technology*, 43, 4934–9, URL <http://www.ncbi.nlm.nih.gov/pubmed/19673288>, 2009.
- ILEC: ILEC Home Page - Data Summary Dead Sea, URL <http://web.archive.org/web/20071227155952/http://www.ilec.or.jp/database/asi/dsasi009.html>, 1999.

- ISRAMAR: Monitoring of the Dead Sea, URL <http://isramar.ocean.org.il/isramar2009/DeadSea/>.
- Jimenez, J. L.: New particle formation from photooxidation of diiodomethane (CH_2I_2), *Journal of Geophysical Research*, 108, doi:10.1029/2002JD002452, URL <http://www.agu.org/pubs/crossref/2003/2002JD002452.shtml>, 2003.
- Junkermann, W., Hacker, J., and Lyons, T.: Land use change suppresses precipitation, *Atmos. Chem. Phys.*, pp. 6531–6539, URL http://www.biodiversity.ru/programs/ecoservices/library/functions/water/doc/Junkermann_2009.pdf, 2009.
- Keppler, F., Eiden, R., Niedan, V., Pracht, J., and Schöler, H.: Halocarbons produced by natural oxidation processes during degradation of organic matter, *Nature*, 403, 298–301, 2000.
- Keppler, F., Biester, H., Putschew, A., Silk, P. J., Schjerve, H. F., and Müller, G.: Organoiodine formation during humification in peatlands, *Environmental Chemistry Letters*, 1, 219–223, doi:10.1007/s10311-003-0044-5, URL <http://www.springerlink.com/openurl.asp?genre=article&id=doi:10.1007/s10311-003-0044-5>, 2003.
- Kern, C.: Spectroscopic measurements of volcanic gas emissions in the ultra-violet wavelength region, Dissertation, University of Heidelberg, 2009.
- Kesner, M.: Bromine and Bromine Compounds from the Dead Sea, Israel Products in the Service of People, The Amos Dshalit Center for Science Education in Israel, Jerusalem, URL <http://www.weizmann.ac.il/sci-tea/Brombook/>, 1999.
- Kistemann, T. and Lauer, W.: Lokale Windsysteme in der Charazani-Talung (Bolivien), *Erdkunde*, Bd. 44, 46–59, URL <http://www.jstor.org/stable/25645455>, 1990.
- Klein, C. and Flohn, H.: Theoretical and Applied Climatology Contributions to the Knowledge of the Fluctuations of the Dead Sea Level, *Theoretical and Applied Climatology*, 38, 151–156, 1987.
- Kotte, K.: pers. comm., 2011.
- Kraus, S.: DOASIS: DOAS Intelligent System, 2004.
- Krumgalz, B.: Thermodynamic constraints on Dead Sea evaporation: can the Dead Sea dry up?, *Chemical Geology*, 165, 1–11, doi:10.1016/S0009-2541(99)00156-4, URL <http://linkinghub.elsevier.com/retrieve/pii/S0009254199001564>, 2000.
- Krumgalz, B. S. and Millero, F. J.: PHYSICO-CHEMICAL STUDY OF THE DEAD SEA WATERS I. Activity Coefficients of Major Ions in Dead Sea Water, *Marine Chemistry*, 11, 209–222, 1982.

- Kudish, A. I.: THE MEASUREMENT AND ANALYSIS OF UV RADIATION AND ITS USE IN OPTIMIZING TREATMENT PROTOCOLS FOR PHOTOCHEMOTHERAPY OF PSORIASIS AT THE DEAD SEA MEDICAL SPAS, *Journal of Dead-Sea and Arava Research* (2009), 1, 1–13, 2009.
- Kurucz, R., Furenlid, I., Brault, J., and Testerman, L.: *Solar Flux Atlas from 296 to 1300 nm*, Tech. rep., National Solar Observatory, New Mexico, U.S.A., 1984.
- Leser, H., Hönninger, G., and Platt, U.: MAX-DOAS measurements of BrO and NO₂ in the marine boundary layer, *Geophysical Research Letters*, 30, 1537, doi:10.1029/2003GL015811, 2003.
- Levenberg, K.: A method for the solution of certain non-linear problems in least squares, *Quart. Appl. Math.*, 2, 164–168, 1944.
- Levin, Z., Gershon, H., and Ganor, E.: Vertical distribution of physical and chemical properties of haze particles in the Dead Sea valley, *Atmospheric Environment*, 39, 4937–4945, doi:10.1016/j.atmosenv.2005.04.039, URL <http://linkinghub.elsevier.com/retrieve/pii/S1352231005004279>, 2005.
- Lyday, P. A.: BROMINE, URL <http://minerals.usgs.gov/minerals/pubs/commodity/bromine/130303.pdf>, 2003.
- Makarov, K. V. and Matalin, A. V.: Ground-beetle communities in the Lake Elton region, southern Russia: a case study of a local fauna (Coleoptera : Carabidae), *Festschrift towards the 75th Anniversary and a Laudatio in Honour of Academician Yuri Ivanovich Chernov*, pp. 357–384, 2009.
- Marquardt, D.: An Algorithm for Least-Squares Estimation of Nonlinear Parameters, *Journal of the Society for Industrial and Applied Mathematics*, 11, 431–441, 1963.
- Martin, M.: and Physics BrO measurements over the Eastern North-Atlantic, *Atmospheric Chemistry and Physics*, pp. 9545–9554, 2009.
- Martino, M., Mills, G. P., Woeltjen, J., and Liss, P. S.: A new source of volatile organoiodine compounds in surface seawater, *Geophysical Research Letters*, 36, 1–5, doi:10.1029/2008GL036334, URL <http://www.agu.org/pubs/crossref/2009/2008GL036334.shtml>, 2009.
- Matsubaya, O., Sakai, H., Torii, T., Burton, H., and Kerry, K.: Antarctic saline lakes-stable isotopic ratios , chemical compositions and evolution, *Geochimica et Cosmochimica Acta*, 43, 7–25, 1978.
- Matveev, V.: Bromine oxide - ozone interaction over the Dead Sea, *Journal of Geophysical Research*, 106, 2001.
- McFiggans, G.: Atmospheric science: marine aerosols and iodine emissions., *Nature*, 433, E13; discussion E13–4, doi:10.1038/nature03372, URL <http://www.ncbi.nlm.nih.gov/pubmed/15703706>, 2005.

- Meller, R. and Moortgat, G.: Temperature dependence of the absorption cross sections of formaldehyde between 223 and 323 K in the wavelength range 225–375 nm, *Journal of Geophysical Research*, 105, 7089–7101, URL <http://dx.doi.org/10.1029/1999JD901074>, 2000.
- Merten, A.: Neues Design von Langpfad-DOAS-Instrumenten basierend auf Faseroptiken und Anwendungen der Untersuchung der urbanen Atmosphäre, Ph.D. thesis, University of Heidelberg, 2008.
- Microsoft: JScript.net language reference, URL <http://msdn.microsoft.com/>, 2000.
- Molina, M. J. and Rowland, F.: Stratospheric sink for chlorofluoromethanes: chlorine atom-catalysed destruction of ozone, *Nature*, 249, 810–812, 1974.
- Möller, D.: Luft, de Gruyter, Cottbus, 2003.
- Muramatsu, Y.: The distribution of iodine in the earth's crust, *Chemical Geology*, 147, 201–216, doi:10.1016/S0009-2541(98)00013-8, URL [http://dx.doi.org/10.1016/S0009-2541\(98\)00013-8](http://dx.doi.org/10.1016/S0009-2541(98)00013-8), 1998.
- Niemi, T. M., Ben-Avraham, Z., and Gat, J. R.: THE DEAD SEA The Lake and Its Setting, OXFORD MONOGRAPHS ON GEOLOGY AND GEOPHYSICS NO. 36, 1997.
- NOAA: GSHHS high-resolution coastline database, URL <http://www.ngdc.noaa.gov/mgg/shorelines/data/gshhs/>, 2011.
- Obrist, D., Tas, E., Peleg, M., Matveev, V., Faïn, X., Asaf, D., and Luria, M.: Bromine-induced oxidation of mercury in the mid-latitude atmosphere, *Nature Geoscience*, 4, 22–26, doi:10.1038/ngeo1018, URL <http://www.nature.com/doifinder/10.1038/ngeo1018>, 2010.
- OceanOptics.com: Ocean Optics Website, URL <http://www.oceanoptics.com/Products/>.
- O'Dowd, C. D. and Hoffmann, T.: Coastal New Particle Formation: A Review of the Current State-Of-The-Art, *Environmental Chemistry*, 2, 245, doi:10.1071/EN05077, URL <http://www.publish.csiro.au/?paper=EN05077>, 2005.
- O'Dowd, C. D., Jimenez, J. L., Bahreini, R., Flagan, R. C., Seinfeld, J. H., Hämeri, K., Pirjola, L., Kulmala, M., Jennings, S. G., and Hoffmann, T.: Marine aerosol formation from biogenic iodine emissions., *Nature*, 417, 632–6, doi:10.1038/nature00775, URL <http://www.nature.com/nature/journal/v417/n6889/full/nature00775.html?free=2>, 2002.
- Orlando, J. and Tyndall, G.: Rate coefficients for the thermal decomposition of BrONO₂ and the heat of formation of BrONO₂, *J. Phys. Chem.*, 100, 19398–19405, 1996.

- Peleg, M., Matveev, V., Tas, E., Luria, M., Valente, R. J., and Obrist, D.: Mercury depletion events in the troposphere in mid-latitudes at the Dead Sea, Israel., *Environmental science & technology*, 41, 7280–5, URL <http://www.ncbi.nlm.nih.gov/pubmed/18044500>, 2007.
- Perliski, L.: The role of multiple Scattering in Twilight Zenith Sky Observations of Atmospheric Absorbers: Diurnal Photochemistry and Airmass Factors, Ph.D. thesis, Boulder, 1992.
- Perner, D., Ehhalt, D., Pätz, H., Platt, U., Röth, E., and Volz, A.: OH-radicals in the lower troposphere., *Geophys. Res. Lett.*, 3, 466–468, 1976.
- Platt, U.: pers. comm., 2009.
- Platt, U. and Stutz, J.: *Differential Optical Absorption spectroscopy Principles and Applications*, Springer, Heidelberg, 2008.
- Platt, U. and Zingler, J.: Investigation of Halogen Radicals on the Oxidation Capacity of the Atmosphere in the Dead-Sea Valley, Tech. rep., Institute of Environmental Physics, Heidelberg, 2004.
- Platt, U., Perner, D., and Pätz, H.: Simultaneous measurements of atmospheric CH₂O, O₃ and NO₂ by differential optical absorption., *J. Geophys. Res.*, 84, 6329–6335, 1979.
- Poehler, D. and Tschritter, J.: pers. comm. and operating of LP-DOAS, 2010.
- Pöhler, D.: Determination of two dimensional trace gas distributions using tomographic LP- DOAS measurements in the city of Heidelberg, Germany, Dissertation, University of Heidelberg, 2010.
- Quack, B., Atlas, E., Petrick, G., and Wallace, D. W. R.: Bromoform and dibromomethane above the Mauritanian upwelling: Atmospheric distributions and oceanic emissions, *Journal of Geophysical Research*, 112, 1–9, doi:10.1029/2006JD007614, URL <http://www.agu.org/pubs/crossref/2007/2006JD007614.shtml>, 2007.
- Read, K. a., Mahajan, A. S., Carpenter, L. J., Evans, M. J., Faria, B. V. E., Heard, D. E., Hopkins, J. R., Lee, J. D., Moller, S. J., Lewis, A. C., Mendes, L., McQuaid, J. B., Oetjen, H., Saiz-Lopez, A., Pilling, M. J., and Plane, J. M. C.: Extensive halogen-mediated ozone destruction over the tropical Atlantic Ocean., *Nature*, 453, 1232–5, doi:10.1038/nature07035, URL <http://www.ncbi.nlm.nih.gov/pubmed/18580948>, 2008.
- Risacher, F.: Bromine geochemistry of salar de Uyuni and deeper salt crusts, Central Altiplano, Bolivia, *Chemical Geology*, 167, 373–392, doi:10.1016/S0009-2541(99)00251-X, URL <http://linkinghub.elsevier.com/retrieve/pii/S000925419900251X>, 2000.
- Rodgers, C. D.: *INVERSE METHODS FOR ATMOSPHERIC SOUNDING Theory and Practice*, World Scientific, Oxford, 2000.

- Rodgers, C. D.: Intercomparison of remote sounding instruments, *Journal of Geophysical Research*, 108, doi:10.1029/2002JD002299, URL <http://www.agu.org/pubs/crossref/2003/2002JD002299.shtml>, 2003.
- Roedel, W.: *Physik unserer Umwelt*, Springer, Heidelberg, 3. auflage edn., 2000.
- Rothman, L., Gordon, I., Barbe, A., Benner, D., Bernath, P., Birk, M., Boudon, V., Brown, L., Campargue, A., Champion, J. P., Chance, K., Coudert, L. H., Dana, V., Devi, V. M., Fally, S., Flaud, J. M., Gamache, R. R., Goldman, A., Jacquemart, D., Kleiner, I., Lacombe, N., Lafferty, W. J., Y. M. J., Massie, S. T., Mikhailenko, S. N., Miller, C. E., Moazzen-Ahmadi, N., Naumenko, O. V., Nikitin, A. V., Orphal, J., Perevalov, V. I., Perrin, A., Predoi-Cross, A., Rinsland, C. P., Rotger, M., M. S., Smith, M. A. H., Sung, K., Tashkun, S. A., Tennyson, J., Toth, R. A., Vandaele, A. C., and Vander Auwera, J.: The HITRAN 2008 molecular spectroscopic database, *Journal of Quant. Spectrosc. Rad. Transfer*, 110, 533–572, doi:10.1016/j.jqsrt.2009.02.013, 2009.
- Rozanov, A., Rozanov, V., and Burrows, J.: A numerical radiative transfer model for a spherical planetary atmosphere: combined differential-integral approach involving the Picard iterative approximation, *Journal of Quantitative Spectroscopy and Radiative Transfer*, 69, 491–512, 2001.
- Rozanov, A., Rozanov, V., Buchwitz, M., Kokhanovsky, A., and Burrows, J.: SCIA-TRAN 2.0 - A new radiative transfer model for geophysical applications in the 175–2400 nm spectral region, in: *Atmospheric Remote Sensing: Earth's Surface, Troposphere, Stratosphere and Mesosphere - I, ADVANCES IN SPACE RESEARCH*, 36, 1015–1019, doi:doi:10.1016/j.asr.2005.03.012, 2005.
- Rozanov, A. V., Rozanov, V., and Burrows, J.: Combined differential-integral approach for the radiation field computation in a spherical shell atmosphere: Nonlimb geometry, *Journal of Geophysical Research*, 105, 22 937–22 942, doi: <http://dx.doi.org/10.1029/2000JD900378>, 2000.
- Saiz-Lopez, A. and von Glasow, R.: Reactive halogen chemistry in the troposphere., *Chemical Society reviews*, 41, 6448–72, doi:10.1039/c2cs35208g, URL <http://www.ncbi.nlm.nih.gov/pubmed/22940700>, 2012.
- Saiz-Lopez, A., Shillito, J., Coe, H., and Plane, J.: Measurements and modelling of I₂, IO, OIO, BrO and NO₃ in the mid-latitude marine boundary layer, *Atmospheric Chemistry and Physics*, 6, 1513–1528, 2006.
- Saiz-Lopez, A., Chance, K., Liu, X., Kurosu, T., and Sander, S.: First observations of iodine oxide from space, *Geophys. Res. Lett.*, 34, L12 812, doi:doi:10.1029/2007GL030111, URL <http://dx.doi.org/10.1029/2007GL030111>, 2007a.
- Saiz-Lopez, A., Mahajan, A., Salmon, R., Bauguitte, S., Jones, A., Roscoe, H., and Plane, J.: Boundary layer halogens in coastal Antarctica, *Science*, 317, 348–351, URL <http://www.sciencemag.org/cgi/content/abstract/317/5836/348>, 2007b.

- Saiz-Lopez, A., Plane, J. M. C., Baker, A. R., Carpenter, L. J., von Glasow, R., Martín, J. C. G., McFiggans, G., and Saunders, R. W.: Atmospheric chemistry of iodine., *Chemical reviews*, 112, 1773–804, doi:10.1021/cr200029u, URL <http://www.ncbi.nlm.nih.gov/pubmed/22032347>, 2012.
- Sanghavi, S.: An efficient Mie theory implementation to investigate the influence of aerosols on radiative transfer, Diploma thesis, University of Heidelberg, 2003.
- Schmitt, S.: pers. comm., operating of the LP-DOAS and evaluation, 2012.
- Schmitz, S.: Untersuchung thermisch induzierter Hang- und Talwindssysteme am Toten Meer und deren Kopplung an größere Skalen, Ph.D. thesis, University of Karlsruhe, 2009.
- Schöler, H. F.: Abiotic Formation of Organohalogens in the Terrestrial Environment, *CHIMIA, r+d in life sciences: Retrospective*, 57, 33–34, URL <http://www.rzuser.uni-heidelberg.de/~h05/pdf-files/SchoelerChimia2003.pdf>, 2003.
- Schöler, H. F. and Zetzsch, C.: Natural Halogenation Processes - Atmosphere, Soil, URL <http://www.rzuser.uni-heidelberg.de/~h05/haloproc/fg763/>, 2008.
- Schönhardt, A.: DOAS measurements of iodine monoxide from satellite, Dissertation, University of Bremen, 2009.
- Schroeder, W., Anlauf, K., Barrie, L., Lu, J., Steffen, A., Schneeberger, D., and Berg, T.: Arctic springtime depletion of mercury, *Nature*, 394, 331–332, 1998.
- Schulze, B.: *Climates of Africa*, vol. 10, Elsevier, Amsterdam, 1972.
- Segal, M., Mahrer, Y., and Pielke, R. a.: A study of meteorological patterns associated with a lake confined by mountains - the Dead Sea case, *Quarterly Journal of the Royal Meteorological Society*, 109, 549–564, doi:10.1002/qj.49710946107, URL <http://doi.wiley.com/10.1002/qj.49710946107>, 1983.
- Seitz, K.: The Spatial Distribution of Reactive Halogen Species at the Irish West Coast, Dissertation, University of Heidelberg, 2009.
- Seitz, K., Buxmann, J., Pöhler, D., Sommer, T., Tschritter, J., Neary, T., O’Dowd, C., and Platt, U.: The spatial distribution of the reactive iodine species IO from simultaneous active and passive DOAS observations, *Atmospheric Chemistry and Physics*, 10, 2117–2128, URL <http://www.atmos-chem-phys.net/10/2117/2010/>, 2010.
- Sihler, H.: Halogen Activation in the Polar Troposphere, Dissertation, University of Heidelberg, 2012.
- Simpson, W., von Glasow, R., Riedel, K., Anderson, P., Ariya, P., Bottenheim, J., Burrows, J., Carpenter, L., Frieß, U., and Goodsite, M.: Halogens and their role in polar boundary-layer ozone depletion., *Atmos. Chem. Phys*, 7, 4375–4418, 2007.

- Singer, A., Ganor, E., Dultz, S., and Fischer, W.: Dust deposition over the Dead Sea, *Journal of Arid Environments*, 53, 41–59, doi:10.1006/jare.2002.1023, URL <http://dx.doi.org/10.1006/jare.2002.1023>, 2003.
- Sinreich, R.: Multi-Axis Differential Optical Absorption Spectroscopy Measurements in Polluted Environments, Dissertation, University of Heidelberg, 2008.
- Sinreich, R., Frieß, U., Wagner, T., and Platt, U.: Multi axis differential optical absorption spectroscopy (MAX-DOAS) of gas and aerosol distributions, *Faraday Discussions*, 130, 153, doi:10.1039/b419274p, URL <http://xlink.rsc.org/?DOI=b419274p>, 2005.
- Sinreich, R., Coburn, S., Dix, B., and Volkamer, R.: Ship-based detection of glyoxal over the remote tropical Pacific Ocean, *Atmospheric Chemistry and Physics Discussions*, 10, 15 075–15 107, doi:10.5194/acpd-10-15075-2010, URL <http://www.atmos-chem-phys-discuss.net/10/15075/2010/>, 2010.
- Smoydzin, L.: Modelling Gas Phase and Aerosol Phase Chemistry in the Atmospheric Boundary Layer, Dissertation, University of Heidelberg, 2008.
- Smoydzin, L. and von Glasow, R.: Modelling chemistry over the Dead Sea: bromine and ozone chemistry, *Atmospheric Chemistry and Physics Discussions*, 9, 4525–4565, doi:10.5194/acpd-9-4525-2009, URL <http://www.atmos-chem-phys-discuss.net/9/4525/2009/>, 2009.
- Spietz, P., Gomez Martin, J., and Burrows, J.: Spectroscopic studies of the I₂/O₃ photochemistry. Part 2. Improved spectra of iodine oxides and analysis of the IO absorption spectrum, *Journal of Photochemistry and Photobiology A: Chemistry*, 176, 50–67, 2005.
- SRTM: Shuttle Radar Topography Mission, URL <http://www2.jpl.nasa.gov/srtm/http://dds.cr.usgs.gov/srtm/>.
- Stamnes, K., Tsay, S.-C., Wiscombe, W., and Jayaweera, K.: Numerically stable algorithm for discrete-ordinate-method radiative transfer in multiple scattering and emitting layered media, *Applied Optics*, 27, 2502–2509, 1988.
- Stutz, J. and Platt, U.: Numerical analysis and estimation of the statistical error of differential optical absorption spectroscopy measurements with least-squares methods, *Applied optics*, 35, 6041–6053, 1996.
- Stutz, J., Ackermann, R., Fast, J. D., and Barrie, L.: Atmospheric reactive chlorine and bromine at the Great Salt Lake, Utah, Great Salt Lake, Utah, *Geophys. Res. Lett.*, 291380doi, 101 029/, 2002.
- Tas, E.: Frequency and extent of bromine oxide formation over the Dead Sea, *Journal of Geophysical Research*, 110, 1–9, doi:10.1029/2004JD005665, URL <http://www.agu.org/pubs/crossref/2005/2004JD005665.shtml>, 2005.

- Tas, E.: Interactive comment on "Measurement-based modeling of bromine chemistry at the Dead Seaboundary layer - Part 2 : The influence of NO₂ on bromine chemistry at mid-latitude areas" by, Atmospheric Chemistry and Physics, 2008.
- Tas, E.: Interactive comment on "Modelling chemistry over the Dead Sea : bromine and ozone chemistry" by L . Smoydzin and R . von Glasow, Atmospheric Chemistry and Physics, 2009.
- Tas, E., Peleg, M., Pedersen, D. U., Matveev, V., Biazar, A. P., and Luria, M.: Measurement-based modeling of bromine chemistry in the boundary layer : 1 . Bromine chemistry at the Dead Sea, Atmos. Chem. Phys, 6, 4929–4971, 2006.
- Tas, E., Peleg, M., Pedersen, D. U., Matveev, V., Biazar, A. P., and Luria, M.: Measurement-based modeling of bromine chemistry in the Dead Sea boundary layer - Part 2 : The influence of NO₂ on bromine chemistry at mid-latitude areas, Atmospheric Chemistry and Physics, pp. 4811–4821, 2008.
- Tas, E., Obrist, D., Peleg, M., Matveev, V., Fain, X., Asaf, D., and Luria, M.: Measurement-based modeling of bromine-induced oxidation of mercury above the Dead Sea, Atmospheric Chemistry and Physics Discussions, 11, 24467–24502, doi:10.5194/acpd-11-24467-2011, URL <http://www.atmos-chem-phys-discuss.net/11/24467/2011/>, 2011.
- Tschritter, J.: Development of 3. generation DOAS-Optics and Comparison with conventional Techniques, Diploma thesis, University of Heidelberg, 2007.
- Tschritter, J.: pers. comm., 2012a.
- Tschritter, J.: PhD thesis in preparation, Dissertation, University of Heidelberg, 2012b.
- Van de Hulst, H.: Light scattering by small particles, 1981.
- Vergeiner, I. and Dreiseitl, E.: Meteorology and Atmospheric Physics Valley Winds and Slope Winds - Observations and Elementary Thoughts, Meteorology and Atmospheric Physics, 36, 264–286, 1987.
- Vogel, L.: Volcanic plumes: Evaluation of spectroscopic measurements, early detection, and bromine chemistry, Dissertation, University of Heidelberg, 2011.
- Voigt, S., Orphal, J., and Burrows, J.: The temperature and pressure dependence of the absorption cross-sections of NO₂ in the 250-800 nm region measured by Fourier-transform spectroscopy, Journal of Photochemistry and Photobiology A: Chemistry, 149, 1–7, 2002.
- Volkamer, R., Spietz, P., Burrows, J., and U., P.: High-resolution absorption cross-section of Glyoxal in the UV/vis and IR spectral ranges, Journal of Photochemistry and Photobiology A: Chemistry, 172, 35–46, 2005.

- von Friedeburg, C.: Derivation of Trace Gas Information combining Differential Optical Absorption Spectroscopy with Radiative Transfer Modelling, Dissertation, University of Heidelberg, 2003.
- von Glasow, R. .: Tropospheric Halogen Chemistry, in: The Atmosphere, edited by Keeling, R., 2007.
- Vountas, M., Richter, A., Wittrock, F., and Burrows, J.: Inelastic scattering in ocean water and its impact on trace gas retrievals from satellite data, *Atmospheric Chemistry and Physics*, 3, 1365–1375, 2003.
- Wagner, T., Ibrahim, O., Sinreich, R., Frieß, U., von Glasow, R., and Platt, U.: Enhanced tropospheric BrO over Antarctic sea ice in mid winter observed by MAX-DOAS on board the research vessel Polarstern, *Atmospheric Chemistry and Physics*, 7, 3129–3142, URL <http://www.atmos-chem-phys.net/7/3129/2007/>, 2007.
- Wagner, T., Beirle, S., and Deutschmann, T.: Three-dimensional simulation of the Ring effect in observations of scattered sun light using Monte Carlo radiative transfer models, *Atmospheric Measurement Techniques*, 2, 113–124, doi:10.5194/amt-2-113-2009, URL <http://www.atmos-meas-tech.net/2/113/2009/>, 2009.
- Williams, J., Gros, V., Atlas, E., Maciejczyk, K., Batsaikhan, a., Schöler, H. F., Forster, C., Quack, B., Yassaa, N., Sander, R., and Van Dingenen, R.: Possible evidence for a connection between methyl iodide emissions and Saharan dust, *Journal of Geophysical Research*, 112, 1–11, doi:10.1029/2005JD006702, URL <http://www.agu.org/pubs/crossref/2007/2005JD006702.shtml>, 2007.
- Williams, W.: Environmental threats to salt lakes and the likely status of inland saline ecosystems in 2025, *Environmental Conservation*, 29, doi:10.1017/S0376892902000103, URL http://www.journals.cambridge.org/abstract_S0376892902000103, 2002.
- Williams, W. D.: 1. Inland salt lakes: An introduction, *Hydrobiologia*, 81-82, 1–14, doi:10.1007/BF00048701, URL <http://www.springerlink.com/index/10.1007/BF00048701>, 1981.
- Wittrock, F., Müller, R., Richter, A., Bovensmann, H., and Burrows, J.: Measurements of iodine monoxide (IO) above Spitsbergen, *Geophys. Res. Lett.*, 27, 1471–1474, 2000.
- Yilmaz, S.: Retrieval of Atmospheric Aerosol and Trace Gas Vertical Profiles using Multi-Axis Differential Optical Absorption Spectroscopy, Dissertation, University of Heidelberg, 2012a.
- Yilmaz, S.: PROFILE RETRIEVAL, 2012b.
- Yilmaz, S.: Workshop PROFILE RETRIEVAL, 2012c.
- Yilmaz, S.: pers. comm., 2012d.

- Yohe, G., Lasco, R., Ahmad, Q., Arnell, N., Cohen, S., C., H., Janetos, A., and Perez, R.: Climate Change 2007: Impacts, Adaptation and Vulnerability. Contribution of Working Group II to the Fourth Assessment Report of the Intergovernmental Panel on Climate Change, in: IPCC Fourth Assessment Report: Climate Change 2007, edited by Parry, M., Canziani, O., Palutikof, J., van der Linden, P., and Hanson, C., chap. Perspectiv, pp. 811–841, Cambridge University Press, Cambridge, UK, 2007.
- Zeiss.de: Czerny-Turner, URL http://corporate.zeiss.com/country-page/de_de/home.html.
- Zingler, J.: MAX-DOAS measurements, 2002.
- Zingler, J. and Platt, U.: Antrag an die Deutsche Forschungsgemeinschaft auf Gewährung einer Beihilfe im Rahmen eines Normalverfahrens in Kooperation mit einem Partner in Israel - Fortsetzungsantrag - FORSCHUNGSVORHABEN: Investigation of Halogen Radicals on the Oxidation Capacity o, Tech. rep., Institute of Environmental Physics, Heidelberg, 2002.
- Zingler, J. and Platt, U.: Iodine oxide in the Dead Sea Valley: Evidence for inorganic sources of boundary layer IO, *Journal of Geophysical Research*, 110, D07307, URL [citeulike-article-id:9972753http://dx.doi.org/10.1029/2004JD004993](http://dx.doi.org/10.1029/2004JD004993), 2005.

Appendix B

Acknowledgements

An erster Stelle geht mein ganz besonderer Dank an meinen Betreuer Prof. Dr. Ulrich Platt, der mir diese Arbeit ermöglicht hat und mir auch in schwierigeren Momenten erleichtert hat, die Motivation aufrecht zu erhalten.

Herzlichen Dank auch an Dr. Udo Frieß, der immer ein offenes Ohr und gute Ratschläge parat hatte.

Sehr viel gelernt habe ich in allerlei Hinsicht außerdem von Jens, Selami, Denis, Joelle, Johannes, Holger, Martin und Stefan. Besonderen Dank an euch und vielen Dank an all die anderen, die zu der wunderbaren Arbeitsatmosphäre in der Gruppe beigetragen haben.

Für das Korrekturlesen bedanke ich mich bei Udo, Stefan, Joelle und Nicole. Meine Zimmergenossen Selami, Daniel, Luisa, Elke, Sanam und Christoph haben die Büroarbeit sehr angenehm gemacht.

Ich danke dem Team der Werkstatt um Ralph Pfeifer für die Beratung, die spontane Hilfe in einem Notfall und die zügige Bearbeitung meiner Aufträge.

Vielen Dank an die Verwaltung und das Sekretariat für die gute Zusammenarbeit, insbesondere danke ich Frau Clos-Lieffertz, Frau Thomas und Frau Weirich.

Ganz herzlicher Dank geht an Dr. Jutta Zingler, die mir bei Fragen stets unkompliziert und unglaublich engagiert mit Rat und Tat zur Seite stand und zum Gelingen der Kampagne am Toten Meer in Israel wesentlich beigetragen hat.

Many thanks to Eitan Campbell for the authorization to perform measurements at Masada and to your staff for the cordial support. Also many thanks to the Dead Sea Works for your exemplary support of our measurements at Ein Bokek.

Bei Dr. Karsten Kotte bedanke ich mich für die Leitung der Organisation der Salzsee-Kampagnen in Südrussland und auf Sal und den regen wissenschaftlichen Austausch. Danke auch an die restliche Arbeitsgruppe um Prof. Dr. Schöler:

Ines, Stefan, Torsten, Sabine und Christoph, für die Unterstützung während der Messkampagnen und die geochemischen Analysen.

Für die angenehmen Aufenthalte in Bayreuth bedanke ich mich bei Prof. Dr. Zetzsch, Prof. Dr. Andreas Held, Johannes, Matthias, Kathi, Nino und Sergej.

Ich bedanke mich auch für die Unterstützung durch meine Eltern und meine Oma. Mein allergrößter Dank aber geht natürlich an meine liebe Magdalena, auf deren Rückhalt ich mich immer verlassen kann.

